Computational exploration of the performances of mechanically constrained MOFs for hydrocarbon separation

Hengli Zhao

UNIVERSITÉ DE RENNES 1

THESE DE DOCTORAT DE

L'UNIVERSITE DE RENNES 1

ECOLE DOCTORALE N° 596
Matière, Molécules, Matériaux
Spécialité : « *Physique* »

Par
« Hengli ZHAO »

« Computational exploration of the performances of mechanically Constrained MOFs for hydrocarbon separation»

Thèse présentée et soutenue à « Rennes », le « 18/02/2022 »
Unité de recherche : Institut de Physique de Rennes (IPR)
Thèse N° :

Rapporteurs avant soutenance :

Jean-Marc Simon	Pr à l'université de Bourgogne
Armand Soldera	Pr à l'université de Sherbrooke

Composition du Jury :

Président :		
Examinateurs :		
	Nathalie Audebrand	Pr à l'université de Rennes 1
	Sandrine Bourrelly	MCF à l'Aix-Marseille Université
Dir. de thèse :	Aziz Ghoufi	MCF à l'université de Rennes 1
Co-dir. de thèse :	Guillaume Maurin	Pr à université de Montpellier I

Declaration

At this moment, I declare that the work presented in this thesis has not been submitted for any other degree or professional qualification and is the result of independent work.

Hengli ZHAO

Date: 09/01/2022

Publications associated with this research

(1) Henrique, A.; Maity, T.; Zhao, H.; Brântuas, P. F.; Rodrigues, A. E.; Nouar, F.; Ghoufi, A.; Maurin, G.; Silva, J. A. C.; Serre, C. Hexane Isomers Separation on an Isoreticular Series of Microporous Zr Carboxylate Metal Organic Frameworks. *J. Mater. Chem. A* **2020**, *8* (34), 17780–17789. https://doi.org/10.1039/D0TA05538G.

(2) Zhao, H.; Maurin, G.; Ghoufi, A. Tuning the Hexane Isomer Separation Performances of Zeolitic Imidazole Framework-8 Using Mechanical Pressure. *Journal of Chemical Physics* **2021**, *154* (8), 084702. https://doi.org/10.1063/5.0040469.

(3) Khudozhitkov, A. E.; Zhao, H.; Ghoufi, A.; Arzumanov, S. S.; Kolokolov, D. I.; Maurin, G.; Stepanov, A. G. Molecular Insight into the Slow Dynamics of C4 Hydrocarbons in the Zeolitic–Imidazole Framework (ZIF-8). *ACS Appl. Mater. Interfaces* **2021**, *13* (28), 33685–33692. https://doi.org/10.1021/acsami.1c08529.

(4) Zhao, H.; Maurin, G.; Ghoufi, Effective Separation of Hexane Isomers in the Zr-MIL-140B Metal-Organic Framework assisted by applying mechanical pressure (just submitted)

Table of contents

List of figures

List of figures

List of equations

List of equations

List of tables

Chapter I. Introduction

The petrochemical industry is gaining increasing attention on sustainable development, which critically depends on developing new innovative processes that consume less energy and more efficient material. Nowadays, in order to purify the mixtures, the processes with using heat, such as distillation, account for 10–15% of the world's energy consumption.[1,2] Overall separation/purification processes cost 45–55% of industrial consumption in the US.[3]

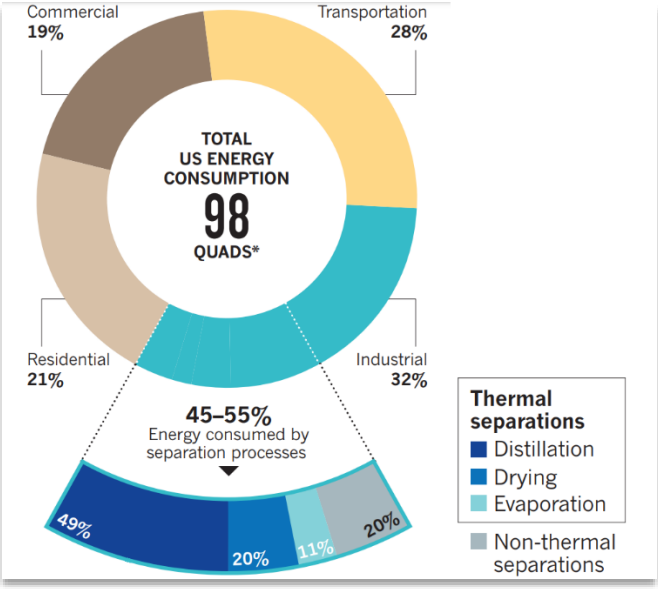

Figure I.1 *Pie chart for total energy consumption in US. *A quad is a unit of energy equal to 10^{15} British Thermal Units (1 BTU is about 0.0003 kilowatt-hours). Figure adapted from the Ref.*[3]

Hence, improving the separation/purification by using more non-thermal process can significantly reduce costs, energy use, and waste generation in order to increase profit, and more importantly, to preserve the earth. Gas separation by adsorption technology is a well-developed operation in chemical and petrochemical industries thanks to its efficiency in dealing with an extensive range of gas mixtures, including impurity removal, gas purification, and separation in recycling streams. The technology is not perfect, and improvements are required; the opportunities to expand its domain of applicability and improve its efficiency require a better understanding of physical phenomena as well as the in technological progress in materials and engineering. In this chapter, I will introduce briefly the basics of the separation by adsorption and use of porous materials.

I.1 Separation of molecules by adsorption

When gas or liquid molecules approach a solid, their concentration at the surface of this solid tends to increase with the interactions; this is the adsorption phenomenon. Two types of adsorptions are commonly studied: chemisorption (or chemical adsorption) and physisorption (or physical adsorption). Both adsorption types are illustrated in Figure I.1. This process involves separation of a compound or compounds accompanied by its accumulation or concentration at the surface of another. The adsorbing phase is defined as adsorbent, and the material adsorbed at the surface of that phase is defined as adsorbate. In the case of chemisorption, the molecules (adsorbates) are absorbed to the surface (adsorbent) thanks to the formation of chemical bonds, in general, covalent bonds or ionic

bonds by charge transfer. The molecules arrange for the sites to maximize their amount of coordination with the substrate. Chemisorbed molecules can even be cleaved to satisfy the valence of surface atoms. The arrangement of the adsorbed molecules mostly occurs in a single layer for the chemisorption.

In the case of physisorption, the adsorbed molecules are absorbed near the surface. The adsorbate-absorbent interactions in physisorption are weaker than in chemisorption. What's more, the arrangement of the adsorbed molecules occurs in several layers. Physisorption is a phenomenon qualified as reversible, unlike chemisorption, defined by its irreversibility.

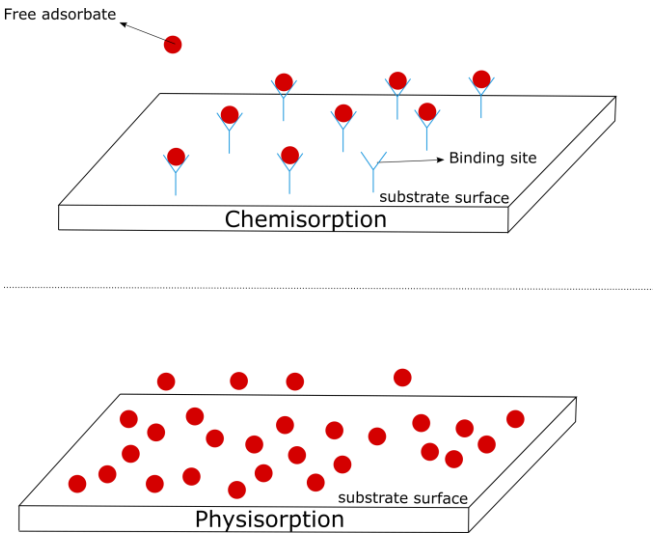

Figure I.2 *Illustration of chemisorption and physisorption, where red cycle dots represent the adsorbates. In the case of chemisorption, the free adsorbate interacts with binding site by establishing the chemical bonds. As for physisorption, the free adsorbate stay near the surface by the weak adsorbate-adsorbent interaction.*

I.1.1 Principle of separation by physisorption

In this study, we focused mainly on the case of physisorption. Which is illustrated on the second case in Figure I.2; let's consider a gas mixture composed of A and B injected into the adsorption column, which consists of an adsorbent that can separate the components A and B. At the outlet of the adsorption column, the gas after the physisorption can be captured. The concentration for a particular gas is hence increased. We can quantify the performance of the separation by the selectivity $\alpha_{A/B}$, which is defined as equation Eq. 1.1

$$\alpha_{A/B} = \frac{q_A \times C_A}{q_B \times C_B} \qquad \textit{Eq. I.1}$$

where q represents the adsorption quantity, and C represents the molar fraction of the gas. For equimolar binary mixture, $C_A = C_B = 0.5$. The selectivity $\alpha_{A/B}$ can evaluate the separation capacity of an adsorbent. Three scenarios are possible, for $\alpha_{A/B} > 1$, then the adsorbent can separate the gas mixture with the preferential adsorption for A; for $\alpha_{A/B} =$

1, then the adsorbent cannot separate the gas mixture of A and B; for $\alpha_{A/B} < 1$, then the adsorbent can separate the gas mixture with the preferential adsorption for B.

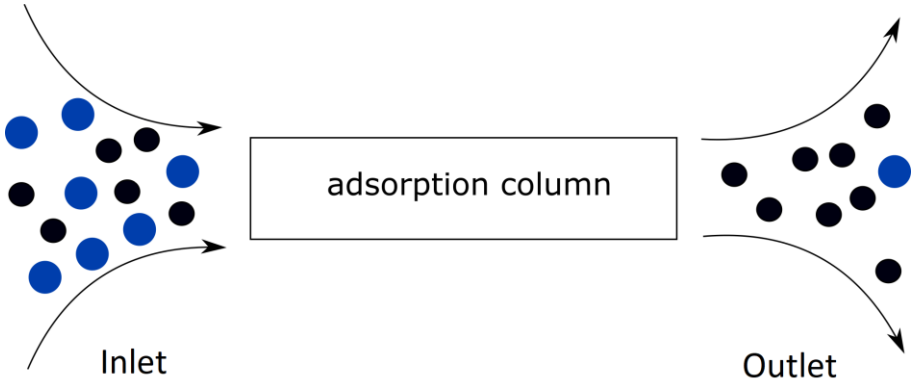

Figure I.3 *Illustration of separation by physisorption. The blue dots and black dots represent gas A and B, respectively, this adsorbent adsorbs more gas A than B, resulting in* $\alpha_{A/B} > 1$.

When the number of molecules adsorbed per surface or volume is very low (infinite dilution), only the adsorbate-adsorbent interactions are in play. With the increase of molecules adsorbed, not only adsorbent-adsorbate interactions are considered but also adsorbate-adsorbate interactions. These intermolecular interactions described can be classified in general into 2 types:

a) Ionic bond

Ionic bond, which is electrostatic intermolecular forces that from the electrostatic attraction between oppositely charged compounds.

b) Van der Waals force

Van der Waals forces appears when adjacent atoms come close enough in a way that their outer electron clouds just barely touch. This provokes the local fluctuations of the charge resulting in a nonspecific, nondirectional interaction. Van der Waals interactions exist between atoms regardless of their nature. Van der Waals forces consist of several contributions:

- Dispersion: attractive forces that arise between temporary dipoles and induced dipoles in atoms or molecules.
- Dipole-Dipole interaction: attractive forces between polar molecules. For example, the attraction between one H_2O to another H_2O molecule for the reason that H_2O is a polar molecule.
- A repulsive force due to the Pauli exclusion principle that prevents the overlaps of the atoms when the distance of the atoms is too close.

It is also common to have hydrogen bonds, it is a special form of dipole-dipole attraction which originated from the attractive force between a hydrogen atom and a pair of high electronegative atoms such as a Nitrogen (N), Oxygen (O), or Fluorine (F).

I.2 Porous materials

The previous subchapter illustrates the different interactions involved during the adsorption process. It is obvious that in order to achieve a high adsorption quantity inside the adsorbent, the interaction shall take place in the adsorbent with a high surface area. Porous materials feature void space inside which can facilize the adsorption process. Nature occurrent or synthetic design porous materials play important roles in many domains of human activities. They usually form their pore structure in the stages of crystallization or by subsequent treatment and comprise isolated or interconnected pores.

I.2.1 Standard porous materials

Standard adsorbents are mostly microporous (pore size smaller than 2nm) or mesoporous (pore diameters between 2nm and 50nm) materials and they split mostly into 4 families: zeolites, activated carbon, silica gel and activated alumina.

a) Zeolites

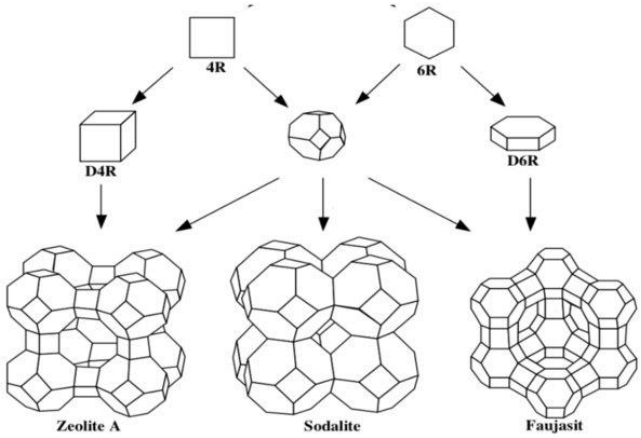

Figure I.4 *Illustration of LTA, SOD and FAU type Zeolite. Figure adapted from the Ref.*[4]

Zeolites are inorganic porous materials. There are 2 types of the occurrence, natural and synthetic zeolites.[5,6] More than 250 natural or synthetic zeolitic structures have been identified and recognised by International Zeolite Association (IZA) so far.[7] Currently, industrial important zeolites are produced synthetically. Their high specific surface area and high thermal stability make this family of materials of interest for a wide range of industrial applications including adsorption/separation and catalysis among others. The critical procedure in synthesizing industrial zeolites from natural aluminosilicate minerals is the effective activation. Typical procedures consist of heating aqueous solutions of alumina and silica with sodium hydroxide.

Synthetic zeolites keep the key advantages over their natural occurrence, but in a uniform, phase-pure state. Classical synthetic zeolites are aluminosilicates, but there are also other zeolites, such as germanate zeolites,[8] Silico Aluminophosphates (SAPO), Magnesium Aluminophosphates (MAPO), Titanium Aluminophosphates (TAPO), Vanadium Aluminophosphates (VAPO) and etc.[9,10] Take the aluminosilicates for example, it consists of silicon $[SiO_4]^{4-}$ and aluminium $[AlO_4]^{5-}$ tetrahedra, linked together by their corner oxygen atoms. Each aluminium tetrahedra introduces a net negative charge compensated by the incorporation of extra-framework cations (often alkalis or alkaline

earth metals such as Na^+, K^+, Li^+, Ca^{2+}…). The chemical formula of this aluminosilicate zeolite is expressed as $M_{x/n}$ [$Al_xSi_yO_{2(x+y)}$], z H_2O, where n is the valence of the cation M, x+y the total number of SiO_4 and AlO_4 tetrahedra per unit cell. For example, the natrolite has the formula of $Na_2(SI_3Al_2O_{10})$, $2H_2O$, and heulandite has the procedure of $(Ca, Na_2)_2(Si_7Al_2O_{18})$, $6H_2O$. The nature of the compensation cations and their positioning in the zeolite pores greatly affect the adsorption properties of the zeolites. The synthetic zeolites most used in separation are type A (LTA) or faujasite (FAU) topology. In the case of faujasite (FAU), there are two types based on the Si/Al molar ratio of the material: type X zeolites (1 <Si/Al <1.5) and type Y (Si/Al≥1.5).

b) Activated carbon

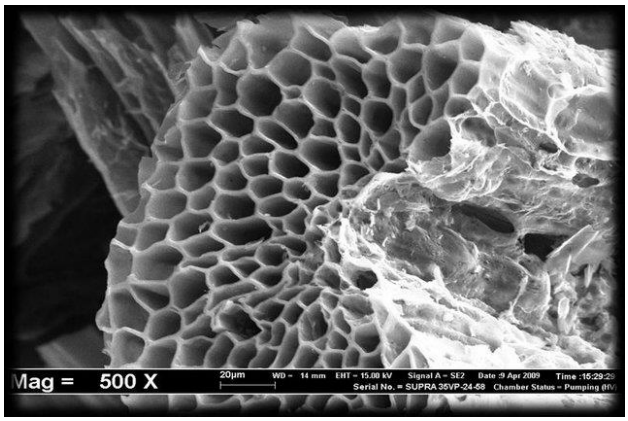

Figure I.5 *SEM image of banana leaf activated carbon prepared under optimum conditions. Figure adapted from the Ref.*[11]

Activated carbons or activated charcoal are adsorbents widely used industrially.[12,13] They can be obtained by carbonaceous materials such as wood, coal, coconuts and petroleum residue. There are two types of manufacturing processes: gas activation and chemical activation. The first one consisted of heating the materials without air at 400-500 °C to remove volatile compounds, forming pores. Then activation is carried out using steam with a temperature between 800-1000°C. As for the chemical activation, it can be carried out using zinc chloride or phosphoric acid.

Activated carbon comprises aromatic configurations of carbon atoms interconnected by random cross-linkages that develops a porous, three-dimensional graphite lattice structure. The size of the pores depends on the exact treatment, with different preparation methods, the pore sizes cover the range of micropores, mesopores and macropores. Functional groups and the internal surface determine the active surface properties, and the range of these areas vary from 500 m^2/g to 3000 m^2/g. Their relatively large pore size combined with the absence of polarity make this family of materials generally poorly selective for the adsorption of specific molecules. They are however widely used to recover solvent and hydrocarbon vapors, eliminate odour, and purify water, etc. To increase the selectivity, it is possible to prepare activated carbons with a very narrow pore size distribution by specific activation processes in post-treatment, such as cracking or polymerization of benzene or acetylene on their surface. These materials are used in particular to separate N_2 from air with a separation process based on kinetic selectivity. Activated carbon can be functionalized for the different target application. For example, by grafting different surface groups at appropriate oxidation states, we can achieve the

desired properties. Acid or basic carbons that are produced by grafting N, O, P, S, Ca, Ba, Na atoms or transition metals for the improvement of the adsorption capacity or served as catalyst.[14–24] The oxidation resistance of activated carbons was improved by doping with P, B, or Cl atoms,[25,26] whereas carbons containing N or O groups exhibited enhancement in electrochemical behaviors.[27,28]

c) Silica gel

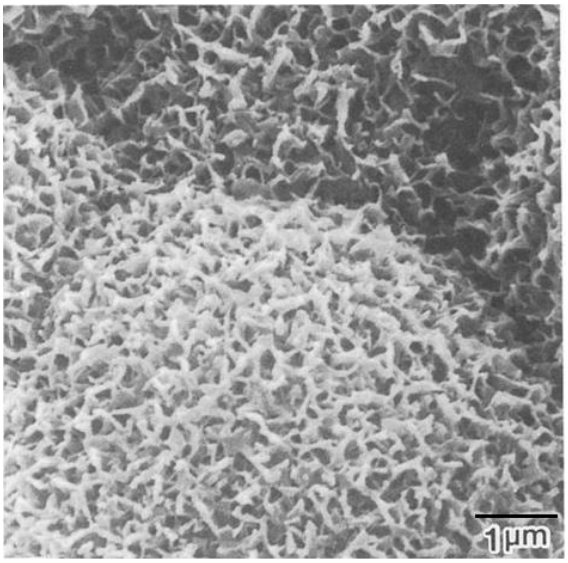

Figure I.6 *SEM Image of the surface of the silica gel. Figure adapted from the Ref.*[29]

Silica gel is a partially dehydrated polymeric form of colloidal silicic acid. The chemical formula of silica gel is expressed as: $SiO_2.nH_2O$. It can be obtained by hydrolysis of a sodium silicate solution with an acid. The silicic acid obtained polymerizes to form SiO_4 chains and then aggregate particles. As it dries, the particles agglomerate to form a microporous structure with pores whose size is primarily determined by the size of the initial particles.

In general, silica gel has a pore size in the range of 6-25nm. The presence of hydroxyl groups makes the material polar. It allows silica gels to dry gases or liquids, the separation of aromatic compounds, the treatment of natural gas, etc.

d) Activated Alumina

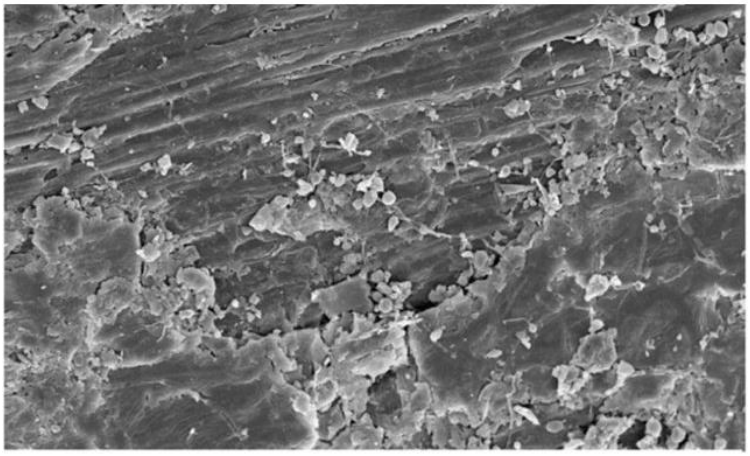

Figure I.7 *SEM image of activated alumina. Figure adapted from the Ref.*[30]

Activated alumina is a porous aluminium oxide; the chemical formula is expressed as: $Al_2O_3.nH_2O$. Activated alumina is generally prepared by dehydration and recrystallization of bauxite at elevated temperatures.

The surface of these compounds is more polar than silica gel and has both an acidic and basic character due to the amphoteric nature of the metal. Activated alumina is very hydrophilic and commonly used to dry gases or liquids.

I.2.1 Limitation of standard porous materials

Based on above examples, we concluded that the separation process by using porous materials is a compelling technology to lower the separation energy use. Standard porous materials have been extensively studied to improve their performance, and widely used in industrial scale thanks to their robustness. However, there are un-neglectable drawbacks on these materials that limit the furthermore increase of the separation efficiency. In general, the control of the porosity of the conventional porous materials is tough, which means it is difficulty to tune the porosity targeted for a certain adsorption application. Plus, the disadvantage of zeolite adsorbents is their high desorption temperatures which is above 470K. The disadvantage of silica gel in terms of process efficiency is the relatively low sorption capacity during the ad-/desorption cycles which requires large amounts of silica gel.

Compare to standard porous materials, Metal-Organic Frameworks (MOFs) are novel porous materials featuring exceptional porosity, high tunability and diverse functionality, which is very promising in addressing industrial important gas separation.

I.3 Metal-Organic Frameworks

I.3.1 General introduction

Early in 1965, nearly three decades ahead of the generally considered birth date of Metal-organic framework (MOFs), Tomic already reported a coordination polymer made of 1,5-Dihydroxynaphthalene-2,6-dicarboxylic acid (1,5-N-2,6) coordinated to Zn, Ni, Al, and Fe,[31] that would be called MOFs nowadays. In 1990, Hoskins and Robson reported the design of a new class of scaffolding-like materials comprising polymeric frameworks using Cu(I) centers.[32] The interest in these coordination polymers was carried on, S. Kitagawa and his team reported a three-dimensional framework which is a coordination polymer that featuring channelling cavities that can adsorb small gaseous molecules such as CH_4, N_2 and O_2.[33] In 1999, the group of O. M. Yaghi discovered MOF-5 (or IRMOF-1, illustrated in Figure I.8).[34]

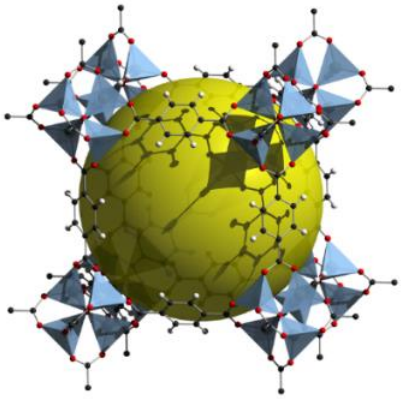

Figure I.8 *3D illustration of a unit cell structure of MOF-5. Oxygen, carbon and hydrogen are represented in red, black and white color. The yellow sphere represents the pore volume. Tetrahedrons represent the coordination of BDC to the Zinc ions centers.*

MOF-5 is formed from Zn_4O nodes connected by 1,4-benzodicarboxylic acid (BDC). The group of O. M Yaghi also pioneered and others MOFs by using the concept of reticular chemistry design, in 2002.[35–37]. In same year, prototypical MIL-53 series MOFs (MIL: Materials of Institut Lavoisier), were first synthesised by the group of Gérard Férey.[38] MIL-53(Cr) was the first MOF reported in this family of MOFs.[38,39] It is consisted of Cr^{3+} as metal ions center and terephthalate (benzene-1,4-dicarboxylate) as linker. From then to now, more MIL-53 family MOFs were synthesised: MIL-53(Al),[40] MIL-53(Fe),[41] MIL-53(In),[42] MIL-53(Co),[43] MIL-53(Ga),[44] MIL-53(Mn)[45] and etc, which brings a great contribution to the domain of MOFs. In 2007, G. Férey and his collaborators reported a novel MOF material, MIL-100(Fe), featuring a large accessible and permanent porosity.[46] As illustrated in Figure I.9.

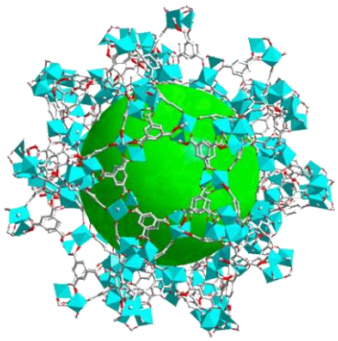

Figure I.9 *3D illustration of a unit cell structure of MIL-100(Fe). Oxygen, carbon and iron are represented in red, grey and dark orange color. Hydrogens atoms are omitted for clarity. The green sphere represents the pore volume. Tetrahedrons represent the coordination of benzenetricarboxylic acid (BDC) to the Iron ions centers.*

Nowadays, there are more than 100,000 MOFs synthesized,[47] according to the Cambridge Structural Database (CSD).[48] For the past decades, we witnessed a growth in research interesting trend of MOFs research as show in the Figure I.10.

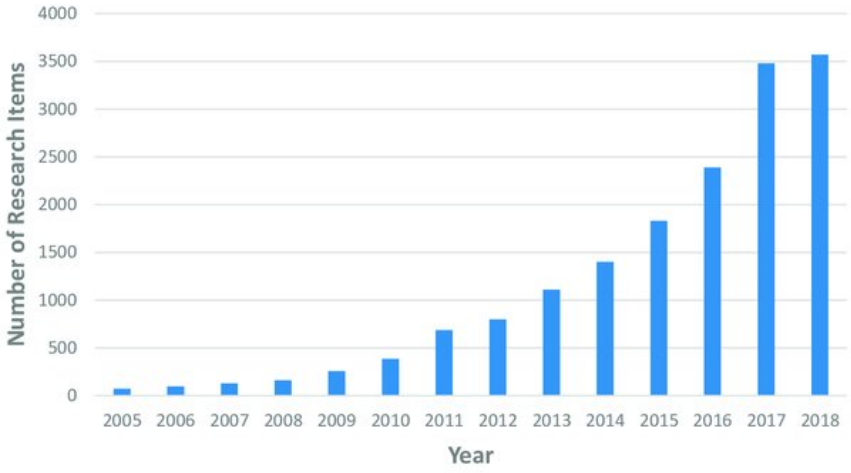

Figure I.10 *Trend in annually number of MOF research items published for the record between 2005 and 2018. Figure adapted from the Ref.*[49]

The recognized definition for MOFs is organic-inorganic hybrid crystalline porous material that consists of metal ions or clusters linked by organic ligands (also called linkers) that leads to the formation of channel or cage-like pore frameworks as represented in Figure I.11.

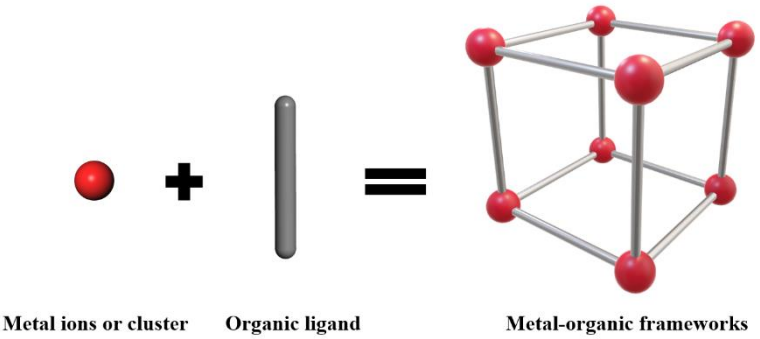

Figure I.11 *Simple illustration of the composition of MOFs, MOFs consists of metal ions or clusters and organic ligands.*

Depending on the nature of linkers and metal ions, the structural and chemical properties of MOFs are highly customizable. Yaghi et al. evidenced that it is possible to modulate the size of the pores without changing the topology of the structure.[35] One example is the MIL-140s MOF series, as shown in figure I.12,[50] this series includes MIL-140A, MIL-140B, MIL-140C, and MIL-140D; The nature of organic ligand is different among these 4 MOFs, with corresponding ligands are benzenedicarboxylic acid (BDC), naphthalene-2,6-dicarboxylic acid (NDC), biphenyl-4,4'-dicarboxylic acid (4,4'-BPDC) and 3,3'-dichloro-4,4'- azobenzenedicarboxylic acid (Cl_2AzoBDC), respectively. This resulting in different pore sizes of 3.2Å, 4.0Å, 5.7Å and 6.3Å, respectively for the triangular channels along the z-axis.[51]

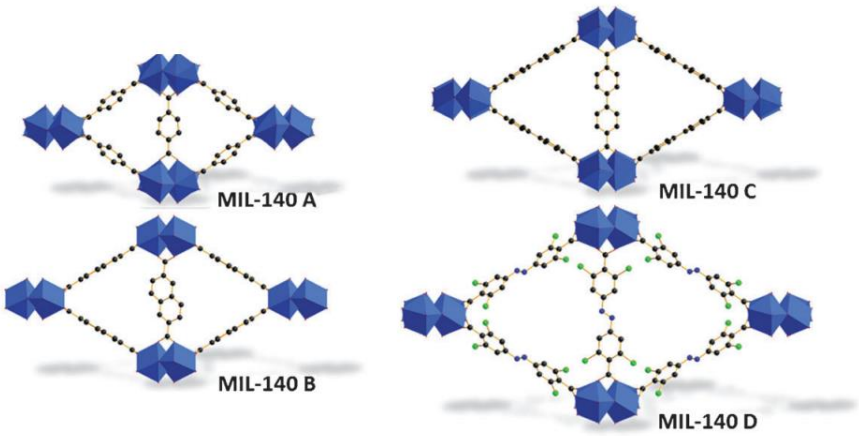

Figure I.12 *View from XY plane of the structure for MIL-140A, MIL-140B, MIL-140C, and MIL-140D. Figure cited from Ref.* [51]

I.3.2 Industrial important mixture separation

Thanks to the unprecedented structural and chemical versatility, MOFs have gained rising interest for various applications, including gas separation, storage, catalysis, sensors, inclusion, and drug delivery.[52–55]

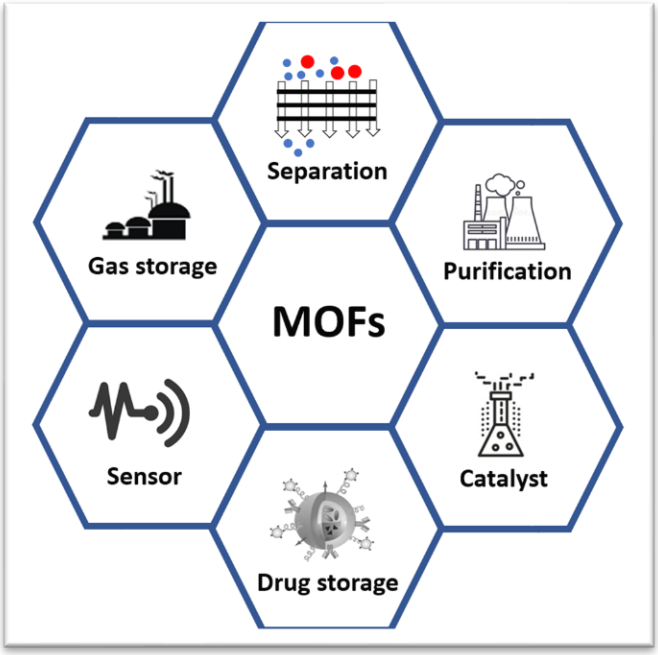

Figure I.13 *The various applications of the MOFs, include separation, purification, catalyst, drug storage, sensor and gas storage.*

Here in this thesis, we mainly concentrated on the gas separation application. As separations are highly important in particular for the petrochemical industry as mentioned in the beginning of the chapter.[3,56] The conventional processes to separate and purify industrial commodities that rely largely on heat-driven distillations, which are very energy intense processes, what's more this technology constitutes around 90–95% of all separations in chemicals and petroleum refining industries.[57] Therefore, it is necessary to find an alternative separation technology that is energy efficient.[58] Porous materials with the requisite metrics for effectively separating given molecules over others by adsorption present unambiguously a promising alternative solution to the energy-intensive fractional distillation techniques. Thanks to high tunability and versatility, MOFs are of great potential to be employed for gas separation technology.

In the petrochemical industry, in order to produce valuable chemical feedstocks, a sufficiently high purity has to be achieved. However, due to similar physical properties, separating these essential industrial mixtures is challenging. Below are discussed the three mixtures of interest in this thesis.

a) Propane/propylene separation

The separation of alkane/alkene gas mixtures is of great interest in industry. In propane/propylene separation, propene(propylene) is the main resource for the production of polymers, acids, alcohols, esters, ethers, and has been widely used for fibers, film, packaging, etc.[3] Figure I.14 illustrates the 3D model of propane and propene.

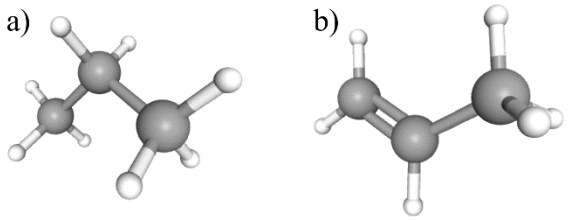

Figure I.14 *3D view of a) propane and b) propylene. Grey and white ball represents carbon and hydrogen atoms respectively.*

However due to similar physical properties as shown in Table I.1, it is extremely challenging to effectively separate this mixture. Conventional adsorbents such as carbon adsorbents[59] and zeolite 5A[60] have been investigated in separating alkane/alkene mixtures. Liang et al. reported the asphalt–based activated carbon can separate alkene over alkane with a selectivity of 3.2 at normal conditions. In order to achieve higher selectivity, MOFs are promising materials to innovate the separation.

Table I.1 *Physical properties of propane and propene.*

	Kinetic diameter (Å)	**Boiling point (K)**	**Freezing point (K)**
Propane	4.3	231.2	85.2
Propene	4.0	225.6	222.5

Dan and el. reported that JNU-3a (JNU; Jinan University), consisting of 5-(3-methyl-5-(pyridin-4-yl)-4H-1,2,4-triazol-4-yl)-1,3-benzenedicarboxylic acid (MPTBDC) linkers and Co^{2+} ions that forming 1D diffusion channel, is able to separating high-purity C_3H_6 (≥99.5%) from an equimolar C_3H_6/C_3H_8 mixture from breakthrough experiment, with an exceptional high Ideal Adsorbed Solution Theory (IAST) selectivity of 513 for propene over propane.[61] Figure I.15 illustrates the crystal structure of JNU-3a upon adsorption of propane and propene.

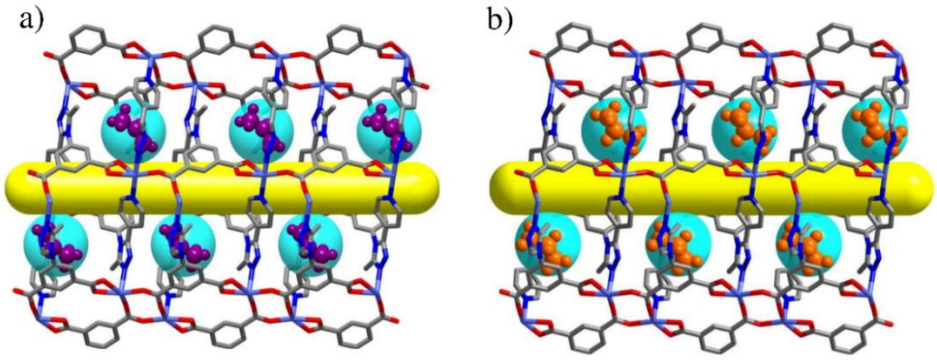

Figure I.15 *Binding sites of JNU upon adsorption of (a) propane and (b) propene(propylene). The arrangement of these two molecules is different inside the cage. Light blue, red, blue and grey nodes represent Co, O, N, H and C atoms, respectively. Hydrogen atoms are omitted for clarity. Yellow cylinder represents the 1D channel, and cyan sphere represents the contour of the molecules. Cited from Ref.* [61]

Chen et al. showed that $[Co(C_7O_5H_4)]\cdot 2H_2O$ (Co-gallate) MOFs could be used for high sieving separation of propene from propane, the IAST selectivity was calculated to be

330 at 1 bar and 298 K.[62] ZIF-8 (Zeolite imidazolate frameworks) was reported to exhibit notable diffusional limitations for propane while propene can enter its cages freely and diffuse, resulting in a propene/propane kinetic selectivity of more than 100.[63] Molecular simulation studied carried out on ZIF-8 evidenced that propene diffuses faster than propane for two orders, 1.6×10^{-12} m² s^{-1} and 5.1×10^{-14} m² s^{-1} at 310K, respectively.[63] Bae et al. reported the thermodynamic propene/propane selectivity of Co-MOF-74 reached 46 at normal conditions.[64] Serre et al. reported that MIL-100(Fe) can separate propane/propene with a separation factor up to 28.9, which is achieved from the breakthrough experiment at low pressure.[65] Wang et al. reported the fabrication of propane-selective MOFs, by compositing g-C_3N_4 and replacing ligand based on Zr-BPDC, yielding g-C_3N_4@Zr-BPDC(biphenyl-4,4'-dicarboxylate) and Zr-BPYDC(2,2'-bipyridine 5,5'-dicarboxylate). The selectivity observed for Zr-BPDC, g-C_3N_4@Zr-BPDC and Zr-BPYDC are 1.5, 1.8 and 2.8, respectively.[66]

Table I.2 *MOFs investigated in separation of propane/propene by adsorption.*

MOF	Capacity	Temperature (K)	Selectivity	Ref
JNU-3a	2.6 (mmol g^{-1})	303	513	61
$[Co(C_7O_5H_4)]\cdot 2H_2O$	66.6 (cm^3 cm^{-3} (STP))	298	330	62
ZIF-8	5 (mmol g^{-1})	310	100	63
Co-MOF-74	6.8 (mmol g^{-1})	308	46	64
MIL-100(Fe)	-	313	28.9	65
Zr-BPDC	-	298	1.5	66
g-C_3N_4@Zr- BPDC	8.79 (mmol g^{-1})	298	1.8	66
Zr-BPYDC	-	298	2.8	66

b) Xylene isomers/ethylbenzene separation

The separation of xylene isomers, para-xylene (PX), ortho-xylene (OX), and meta-xylene (MX), and Ethylbenzene (ETH) are of high importance in the industry. Among three isomers, PX is the most valuable isomer; it is an indispensable raw material for synthesizing polyethylene terephthalate (PET) and polybutylene terephthalate (PBT). OX is mainly used to produce phthalic anhydride, and MX is mostly used as a fuel additive or a co-monomer for the production of high-value resins. Figure I.16 illustrate the 3D models of xylene isomers and ETH. Xylene isomers and ETH have also close kinetic dimeters. (See Table I.2) Currently the adsorbent zeolite K-BaY is used to separate Xylene isomers and ETH, however a big drawback of this adsorbent is the sensitivity of the separation process to water contamination.[67]

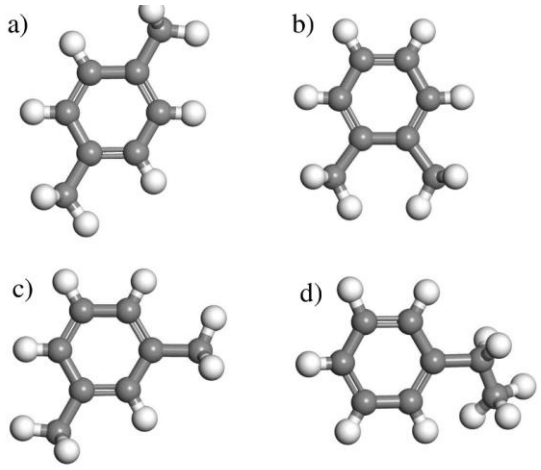

Figure I.16 *3D view of a) PX, b) OX, c) MX and d) Ethylbenzene. Grey and white ball represents carbon and hydrogen atoms respectively.*

Table I.3 *Physical properties of xylene isomers and ethylbenzene. PX, MX, OX et EB represent Para-Xylene, Meta-Xylene, Ortho-Xylene, and Ethylbenzene.*

	Kinetic diameter (Å)	**Boiling point (K)**	**Freezing point (K)**
PX	6.7	411.5	286.4
MX	7.1	412.3	222.5
OX	7.4	417.6	248
EB	6.7	409.3	178.2

MOFs also demonstrated the ability to separate relatively bulky molecules such as xylene isomers.[68] MIL-47 was investigated by Alerts et al. for the xylene separation.[69,70] Breakthrough experiments showed that PX can be adsorbed preferentially. The optimal arrangement is obtained with the PX positioned in a parallel fashion. The arrangement of OX is not exact in a parallel position compare to PX. On the other hand, the arrangement found for MX and EB does not allow optimal stacking of the molecules, which may explain why the adsorption of these two molecules is less favoured. This proved that thermodynamic separation is feasible for xylene isomers in MIL-47. Zinc-based MOFs MAF-X8 was also found prominent MOF for the separation of xylene isomers. It is a Zn(II) pyrazole-carboxylate framework featuring one-dimensional channels of 10 Å. At 433K, MAF-X8 exhibits the adsorption capacity of 2.1 $mmol.g^{-1}$, and the overall selectivity is estimated to be around 5.1.[71] JUC-77 was reported by Jin et el. exhibiting rhombus-shaped channels along with two directions. JUC-77 is able to separate PX from other isomers with a molecular sieving mechanism. At 433K, JUC-77 has an overall selectivity of 2.25.[72] MIL-53(Al), exhibiting flexibility between open pore and close pore, was proved in vapor-phase xylenes adsorption with two-step isotherms. At the open pore configuration, MIL-53(Al) is reported to have a OX/EB selectivity of 6.4.[73] The common scenario for xylene isomers is based on the preferential adsorption of PX. However, MOFs have a great variety that can be used for xylene separation based on the preferential adsorption of MX or OX. For example, $Ni(NCS)_2(isoquinoline)_2(4phenylpyridine)_2$

represents a separation factor of 4.7 for MX over PX at 321K.[74] Rodrigues reported the UiO-66 has favourable adsorption towards OX. UIO-66 featuring a cubic 3D structure with two types of microporous octahedral and tetrahedral cages, is evidenced to have a separation factor of 2.4 for OX over PX at 313K.[75] The Table I.3-I.5 is the summary of the MOFs for the xylene isomers separation. With MX adsorption preference, PX adsorption preference and OX adsorption preference. The table is adapted from the reference with minor update.[76]

Table I.4 *MOFs with MX adsorption preference applied in separation of xylene isomers by adsorption. "-" means N/A.*

MOF	Capacity (mmol g-1)	Temperature (K)	MX/PX	MX/OX	MX/EB	OX/PX	Ref
$Ni(NCS)_2(isoquinoline)_2(4\text{-phenylpyridine})_2$	-	321	4.7	2.6	1.9	1.8	74
HKUST-1	-	298	1.1	2.4	1.4	0.7	69

Table I.5 *MOFs with PX Preference Applied in Separation of Xylene Isomers by Adsorption, "-" represents N/A, (a) represents the number is overall selectivity, (b) represents the corresponding cannot separate the certain mixture.*

MOF	Capacity (mmol g-1)	Temperature (K)	PX/MX	PX/OX	PX/EB	MX/OX	Ref
$Zn_4O(L)_3$	2.73	298	1000*(a)*				77,78
Mg-CUK-1	1.18	298	15 (a)				79
MAF-X8	2.1	433	5.3*(a)*				71
JUC-77	0.55	433	2.25*(a)*				71
CoBDP	1.4	433	1.4*(a)*				71
$Ag_4(O_2CCF_3)_4(phenazine)_3$	-	298	14.2	9.13	-	-	80
Cu(CDC)	12 wt%	298	7	10	3.5-5	3	81
Nd(HTCPB)	2.21	383	6.33	-	-	-	82
Ce(HTCPB)	1.62	383	4.5	5.6	2.4	1.22	82
ZIF-8	1.5	398	1.15	1.5	1.1	-	83
	2.1	343	3.1	8.8	10	-	84
MIL-125(Ti)-NH2	1.2	298	3	2.2	1.6	1.03	71,85,86
	1.25	323	1.5	1.6	1.3	*(b)*	87

MOF	Capacity (mmol g-1)	Temperature (K)	PX/MX	PX/OX	PX/EB	MX/OX	Ref
MIL-47	4.55	323	1.1	0.6	1.7	-	[87]
	-	298	2.5	b	7.6	-	[69]
MOF-48	0.95	323	1.7	1.7	1.5	*(b)*	[87]
MIL-140B	1.2	323	1.6	1.8	2.1	*(b)*	[87]
MIL-125(Ti)	1.5	313	1.5	1.6	-	*(b)*	[71,88]
$Co_2L_2(AzoD)_2$	2.5	298	-	2.61	-	-	[89]

Table I.6 *MOFs with OX preference applied in separation of xylene isomers by adsorption. "-" represents N/A, (b) represents the corresponding cannot separate the certain mixture.*

MOF	Capacity (mmol g-1)	Temperature (K)	OX/PX	OX/MX	MX/PX	OX/EB	Ref
UiO-66	2.32	313	2.4	1.8	-	-	[75]
CAU-13	2	298	1.7	2.1	0.8	-	[90]
Zn(BDC)(Dabco)$_{0.5}$	3.3	398	1.83	1.64	*(b)*	1.77	[91]
HKUST-1	2.8	398	1.08-1.21	-	1.32	-	
CPO-27-Ni	2.1	398	3.3	1.7	2	-	[92]
MIL-53(Al)	3.37	298	3.5	2.7	*(b)*	10.9	[93]
	6.76	313	2.1	2.1	*(b)*	-	[94,95]
MIL-53(Fe)		323	2.53	1.57	1.83	-	[96]
CD-MOF	2.7	298	17.9	6.73	2.67	4.75	[97]
rho-ZMOF	0.92	398	1.3	-	-	-	[98]
ZIF-76	0.26	398	1.1	-	-	-	[98]
$Ni(NCS)_2(ppp)_4$		295	40.5	34.2	12.7	-	[99]
Co_2(dobdc)		306	3.9	2.5	1.6	1.21	[100]
MIL-101		408	-	1.5	-	1.4	[101]

c) Hexane isomers separation

Separation of linear paraffin and branched paraffins by the degree of branching is a critical process in enhancing octane number in gasoline fuels.[102] There are 5 hexane isomers as shown in Table I.6 which are *n*C6, 2MP, 3MP, 22DMB and 23DMB. Figure I.17 illustrate the 3D models of hexane isomers. The industrial value of a certain isomer in the gasoline pool is directly related to its research octane number (RON). Typically, the higher the RON, the more the fuel can be compressed and the better the performance will be. As we can see, the di-branched isomers have significant higher RON than linear isomer. However, the similar physical properties of hexane isomers bring a great difficulty on the separation process.

Table I.7 *Physical properties of hexane isomers. nC6, 2MP, 3MP, 23DMB et 22DMB represents n-hexane, 2-methyl pentane, 3methylpentane, 2,3-methylbutane, 2,2-methyl butane respectively.*

	Kinetic diameter (Å)	**RON**	**Boiling T (°C)**
*n*C6	4.3	30	68.7
2MP	5	74	60.3
3MP	5	75	63.3
23DMB	5.8	94	58
22DMB	6.2	105	49.7

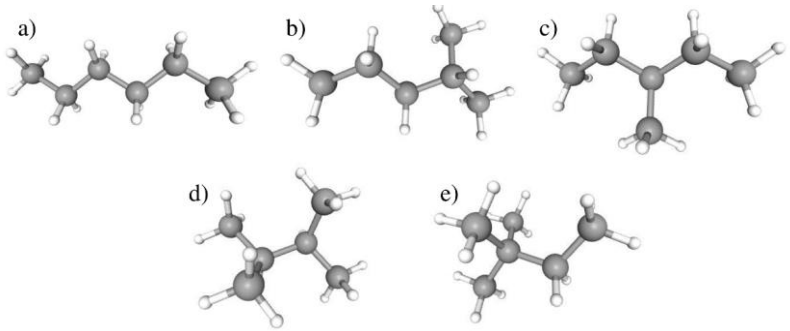

Figure I.17 *3D view of a) nC6, b) 2MP, c) 3MP, d) 23DMB and e) 22DMB. The Grey and white sphere represent carbon and hydrogen atoms respectively.*

In this context, the process of isomerization was used for the octane improvement of gasoline pools. During the process, normal paraffins are catalytically converted into their branched isomers with higher Research Octane Number. However, due to the limit of thermodynamic equilibrium, in the product, there are still around 50% of mono-branched and 10% of unreacted linear paraffins. In the industrial scale, the zeolite 5A is usually employed to separate the final product with a final RON around 87-90. In order to furthermore increase the RON, many efforts are being made to find alternative materials for the separation of hexane isomers. $Fe_2(BDP)_3$, which is a highly stable framework featuring triangular channels MOFs, is reported to separate the hexane isomers according to the degree of branching.[103] The separation ability of hexane isomers for $Fe_2(BDP)_3$ was evaluated with a breakthrough experiment. The Research Octane Number (RON) of the

eluted mixture rise to greater than 90, which is significantly higher than typical industrially refined hexane blends, which are 83.[104] The Table I.8 is the summary of the MOFs for the hexane isomers separation.

Table I.8 *MOFs Applied in Separation of Hexane Isomers by Adsorption*

MOF	Temperature (K)	*n*C6/22DMB	3MP/22DMB	*n*C6/2MP	*n*C6/3MP	nC6/23DMB	Ref
ZIF-8	453	*separation by inverse gas chromatography*					[105]
	373	25	4.5	4	-	-	[106]
	398	∞	∞	-	6.4	-	[107]
	373	16	-	1.2	-	1.8	[107]
	423	-	-	5.8	-	-	[108]
Fe2(BDP)3	433	2000*(a)*					[103]
IM-22	398	∞	∞	-	2	-	[109]
ZIF-76	398	0.7	0.8	-	0.8	-	[109]
ZIF-67	298	4.5	-	-	4.7	-	[110]
ZIF-68	298	-	-	-	3.5	-	[110]
ZIF-78	298	-	-	-	6	-	[110]
ZIF-81	298	-	-	-	6	-	[110]
$Zn(BDC)(dabco)_{0.5}$	313	33.15	5.35	-	-	-	[111]
UIO-66(Zr)	343	1.4	-	-	1.2	1.1	[112]
	423	6.3	-	-	2.7	5.8	[112]
UIO-66-OH	298	15	-	-	-	-	[110]
MIL-127(Fe)	343	7	-	-	5.6	-	[113]
	373	6.1	-	-	6	-	[113]
	423	16	-	-	9.6	-	[113]
MIL-125-NH2	373	2.6	1.8	-	-	-	[113]
	423	2.4	1.6	-	-	-	[113]
ZIF-69	423	-	-	-	3	-	[108]

MOF	Temperature (K)	*n*C6/22DMB	3MP/22DMB	*n*C6/2MP	*n*C6/3MP	nC6/23DMB	Ref
MOF-508	313-423	*separation by packed column gas chromatography*					[114]
MIL-140B		10.2	-	-	-	-	
Cu(hfipbb)(H2hfipbb)0.5	303	exclusion of 22DMB					[115]
MIL-100(Cr)	343	3	2.5	-	-	-	[112]

I.3.3 Gas separation mechanism

We can define four microscopic mechanisms at the origin of the separation performance of MOFs, i.e. driven by thermodynamic, kinetic, shape sieving and molecular sieving.

a) Thermodynamic separation

Thermodynamic separation mechanism is based on the equilibrium between the guest molecules and the adsorbent. It is defined as the separation of two or more components by a difference in adsorbate/MOF affinity. Two phenomena can be observed for a thermodynamic separation: i) the separation is based on guest-host affinity, when guest molecules can easily diffuse in the pores/cage of the MOFs, the interaction between the adsorbate and the adsorption sites is dominant for the preferential adsorption; ii) separation based on entropic effects: the selectivity of the MOF towards a guest molecule of a mixture depends on the ability to arrange and occupy the maximum volume.

b) Kinetic separation

The kinetics-driven separation can be defined as the capability of a porous material to separate two or more components in terms of diffusivity, *i.e.*, the ability/difficulty of the molecules to move along the cages/channels of the porous materials. Such a mechanism is generally encountered for molecules that display similar size and functionality, such as hydrocarbons. The larger molecule (with a higher kinetic diameter) naturally will diffuse more slowly through the adsorbent than the smaller molecule.

c) Shape sieving separation

This separation mechanism is based on the difference of the conformational behavior of guest molecules inside the adsorbent. In this scenario, the guest molecules have similar or smaller kinetic diameter than the pore size. The guest molecule that has the best spatial adaptability inside the pore of the adsorbent is more adsorbed.

d) Molecular sieving separation

This separation mechanism consists of using the adsorbent as a molecular sieve. Only molecules of kinetic diameters smaller than the dimension of the aperture of the adsorbent pores are able to enter in the porosity of the adsorbent. The molecules having a kinetic diameter much larger than the dimension of the pore are not be able to enter. Thus, the molecular sieving separation is not governed by thermodynamic equilibrium, and the

selectivity is almost infinite (one compound enters the pores and the other hardly adsorbed).

I.3.4 Flexibility of MOFs and external stimuli

The flexibility and dynamic behavior are unique feature that characteristics the MOFs. Stimuli-responsive MOFs which are currently at the forefront of the porous material research. It is of crucial importance thanks to their promising potential for diverse applications include the separation.[116] In this subchapter, I will introduce the common flexibility of the MOFs and external stimuli that can be used on MOFs.

a) MOFs flexibility

MOFs processes the flexibility depends on the nature of the linker materials and metal ions. The flexibility of the MOFs can be concluded in 4 categories: Breathing, swelling, linker rotation and subnetwork displacement.

i) Breathing

'Breathing' designate reversible transitions of MOFs, during which the substantial displacement of atoms of the framework resulting a variation in unit cell volume. One representative example for this kind of flexibility is the MIL-53(M) family ($[M(BDC)(OH)]_n$ (BDC = 1,4-benzenedicarboxylate) (M = Al,[40] Fe,[117] Cr[38,39], Sc,[118] Ga,[119] In[42]). It has a particular 'breathing' corresponds to a structural change between narrow pore (np) and large pore (lp) phases. Figure I.18 illustrated the breathing effect in MIL-53(Cr).

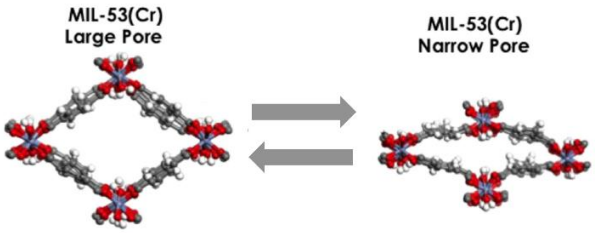

Figure I.18 *Large pore (lp) and narrow pore (np) phases of MIL-53(Cr). Light blue, red and grey nodes represent Cr, O, H and C atoms, respectively. Figure adapted from Ref.*[120]

ii) Swelling

Swelling flexibility designate an enlargement of the MOF unit cell volume without a modification in the unit cell shape and the space group. Note that swelling is often involved with linker rotation which will be explained in iii. I consider swelling as a specific flexibility for its conservation of unit cell shape and symmetry. One typical example is MIL-88.[121] The structure of the MIL-88 is based on a trimeric $M_3O(H_2O)_2X^{6+}$ (M = Fe^{3+}, Cr^{3+} ; X=F^-, OH^-) SBU (Secondary Building Unit) that consists of three truncated tetrahedra that are interconnected by dicarboxylic acids: fumaric acid (MIL-88A), BDC (MIL-88B), 2,6-NDC (MIL-88C) or BPDC (MIL-88D).[122] This swelling flexibility is illustrated in Figure I.19.

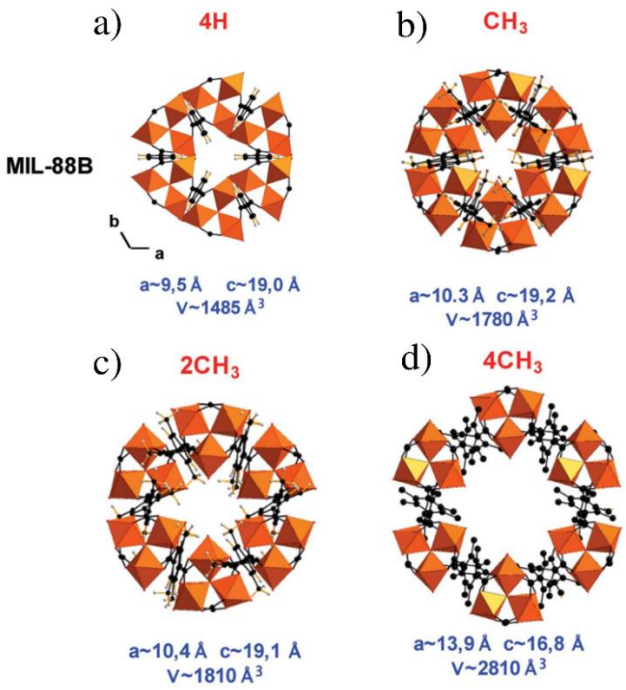

Figure I.19 *View along the c(z) axis of one pore of the dried a) MIL-88B, b) MIL-88(CH_3), c) MIL-88B($2CH_3$) and d) MIL-88B($4CH_3$). Orange, black, and grey represents Metal polyhedral, C, and H atoms respectively. Figure adapted from the Ref.*[123]

iii) Linker rotation

Linker rotation is defined as a (continuous) transition where the spatial alignment of a linker is changed by turning around a rotational axis. MIL-140 series MOFs; MIL-140A, MIL-140B, MIL-140C and MIL-140D with corresponding ligands BDC, NDC, BPDC and Cl_2AzoBDC processes this linker rotation flexibility with different degree of liberty. The linker rotation has an impact on the pore volume and size. The combined experimental and theoretical studies have led to the conclusion that the rotational linker movement causes the expansion of the pore windows and the adsorption of molecules larger than expected.[124,125] However, this conclusion was made for cage like MOFs, ZIF-8 and MOF-5, for 1D channel-structured with relatively small pore size MOFs such as MIL-140 series, the linker rotation can furthermore decrease the free volume, resulting a decrease in the adsorption uptake.[126] The linker rotation in MIL-140C is illustrated in Figure I.20.

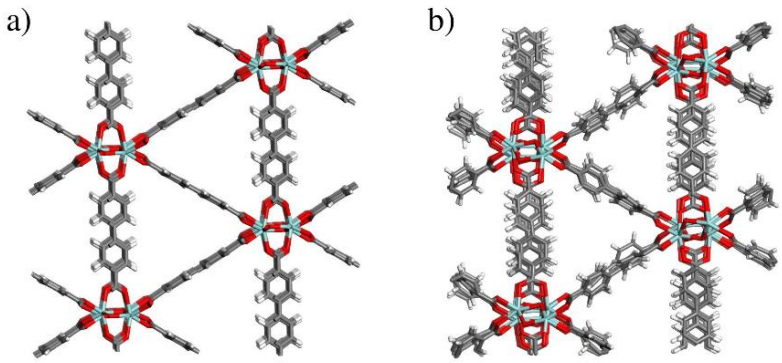

Figure I.20 *View along the c(z) axis of 1D channel-structured MOF a) snapshot of ideal MIL-140C from crystallographic information file (CIF), b) snapshot of MIL-140C in molecular dynamic simulation. Note the linker rotation decrease the accessible volume in the MOF. Cyan, red, grey and white represents Zr, O, C and H atoms respectively.*

iv) Subnetwork displacement

Subnetwork displacement refers to systems having individual frameworks, which are not connected by strong chemical bonds, but interact only by rather weak forces, resulting the relocation of the subnets. This phenomena can happen for interpenetrated three dimensional (3D) frameworks as well as interdigitated and stacked two dimensional (2D) frameworks.[127–130] 3-fold interpenetrated 3D microporous metal-organic coordination polymers (MOCPs) of Cu(II), $[Cu_3(bipy)_{1.5}(2,6\text{-}ndc)_3]_n$ (bipy = 4,40 -bipyridine), as illustrated in Figure I.21.

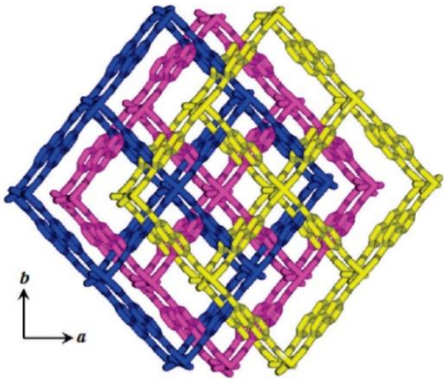

Figure I.21 *View along the c(z) axis of Crystal structure of 3D view of the α-Po type 3-fold interpenetrated framework. Figure adapted from the Ref.* [129]

b) External stimuli

Structural flexibility enables many MOFs to reversibly modulate their pore size or/and shape with respect to the external stimuli.[131] There are mainly 5 external stimuli such as light, temperature, electric field, guest molecules and mechanical pressure.[132,133]

i) Light

Certain organic molecules that are able to change their conformation or structure upon interaction with light are implemented into MOFs, rendering MOFs capable of changing

the pore size and shape, and hence the ability to adsorb specific guest molecules. For example, a photo-switchable linker was first given by Modrow et al.,[134] it was used to synthesis twofold interpenetrated MOF $[Zn_2(2,6\text{-ndc})_2\text{-(azo-bipy)}]_n$ (azo-bipy=3-azo-phenyl-4,4'-bipyridine). Exposure of the MOF to light of a wavelength of 365 nm triggers the transition from *trans* to the *cis*. A reversible switching back can be achived by either irradiation with light of a wavelength of 440 nm or by thermal treatment. This photoreactive induced phase transition is illustrated in Figure I.22.

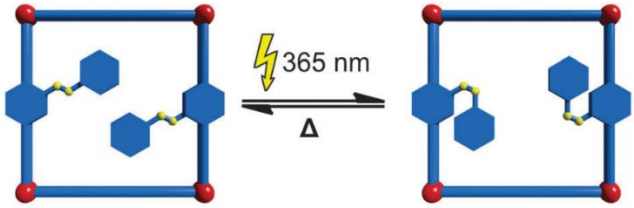

Figure I.22 *Illustration of the photochemically induced phase transitions in metal–organic frameworks. Figure adapted from the Ref.*[135]

ii) Temperature

Many MOFs are thermoresponsive, which display a reversible change in the lattice parameters after exposure to a thermal treatment without modifying the molecular composition. Some representative materials: MOF-5, HKUST-1, Ag(mIm), HMOF-1, FMOF-1, $Cd(CN)_2$, $Zn(CN)_2$, showed positive thermal expansion (PTE) or negative thermal expansion (NTE) during the heating/cooling from room temperature until the threshold temperature of the phase transition is reached.[136–141] One prominent example of a MOF that displays a np - lp phase transition is $[Zn_2(BME\text{-}bdc)_2(dabco)]_n$ (BME-bdc = 2,5-bis(2-methoxyethoxy)benzenedicarboxylate).[142] Initially at np phase after the activation, there are dangling side chains present inside the pore that can interact with each other. With the increase of the temperature, the thermal movement of the linkers' side chains is increased resulting the pore swelling and phase transition to the lp form at 493 K. This thermal induced structural change is illustrated in Figure I.23.

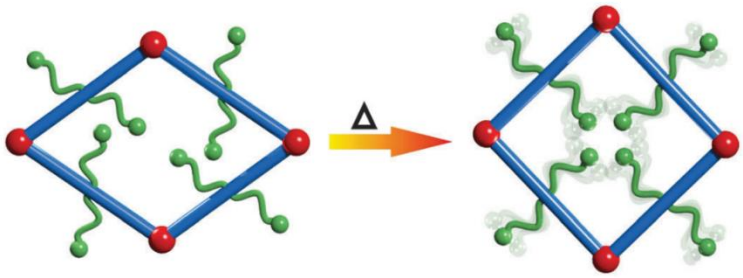

Figure I.23 *Illustration of np – lp transition for $[Zn_2(BME\text{-}bdc)_2(dabco)]_n$ with thermal treatment. Figure adapted from the Ref.*[135]

iii) Electric field

Electric field can also be used to induce the structure change of the MOFs. One great example is MIL-53(Cr),[120] this material is able to perform a reversible structural transition under electrical field. With the increase of the electric field, MIL-53(Cr) undergoes a phase transition from initial lp form to cp form that occurs at E = 1.75 V/nm. The aperture of the channel decrease from 12.8 to 7.9 Å accompanied with a unit cell volume

decreasing of 35%. This phase transition of MIL-53(Cr) in function of the electric field is illustrated in Figure I.24.

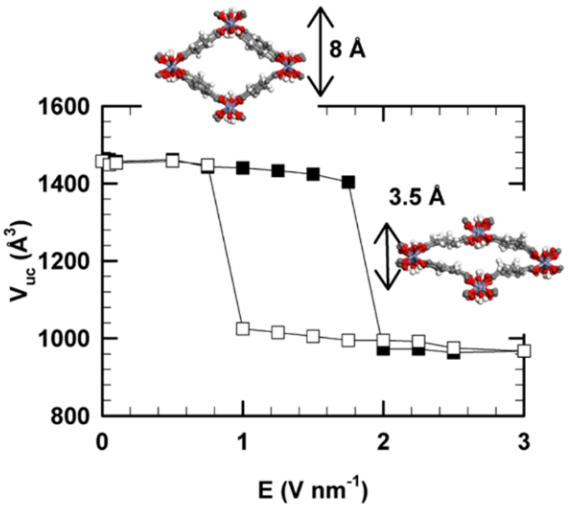

Figure I.24 *Phase transition between lp and cp of MIL-53(Cr) in function of the electrical field (E). Full and empty symbols correspond to increasing and decreasing electrical field range, respectively. Grey, white, light purple, and red spheres represent C, H, Cr, and O atoms, respectively. Figure adapted from the Ref.*[120]

iv) Guest molecules

The adsorption and desorption of guest molecules inside the MOF induce stress, which can be considered as internal pressure. This internal pressure can provoke breathing, ligand flip, pore gating, etc.[143–148] One interesting example to demonstrate this stimuli is the phase change of Co(BDP) upon adsorption/desorption of CO_2 is illustrated in Figure I.25,[149] Jeffrey R. Long and al. evidenced that both pure CO_2 at 3.6 bar and equimolar binary mixture CO_2/CH_4 at 7.2 bar can induce a phase change in Co(bdp), resulting in an expansion of the one-dimensional channels to an aperture ideally-sized to adsorb CO_2 but exclude CH_4.

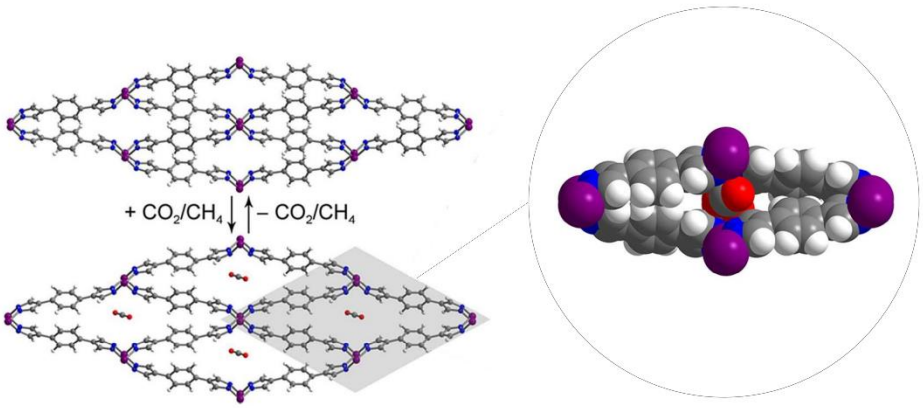

Figure I.25 *Phase transition of Co(BDP) upon adsorption/desorption of CO_2. Grey, blue, white, purple, and red spheres represent C, N, H, Co, and O atoms, respectively. Figure adapted from the Ref.*[149]

v) Mechanical pressure

External mechanical pressure can directly induce the transformation of the materials, Cheetham et al. investigated the mechanical properties on dense inorganic–organic frameworks and MOFs.[150] Pressure induced amorphization,[151,152] phase transitions to a new high pressure phase,[153] and pressure induced compressions[154–156] have been reported. MIL-53(Al)[157] and MIL-47(V)[158] can switch from a large pore to a closed pore phase. The variation of the unit cell volume of MIL-53(Al) between lp and cp is up to 37% accompanied by the change of the space group as illustrated in Figure I.26.

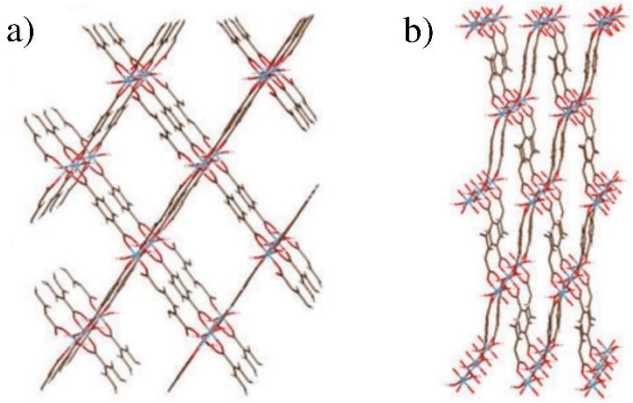

Figure I.26 *Illustration of the pressure induced phase transition of the MIL-53(Al) between the large pore form (a) and the closed pore form (b). Figure adapted from the Ref.*[157]

I.4 Motivation and aim

In this thesis, the stimuli investigated applied on the MOFs was external mechanical pressure. As mentioned before, the application of an external mechanical pressure on certain MOFs can induce either compression or phase transition which correspond to a decrease of their crystallinity due to a local disorder of the structure, while both structural changes being reversible.[159,160] This mechanical stimulus can be utilized as an alternative method to the current chemical synthesis/post-synthesis routes used for the creation of structural defects and their concentration control for both catalytic and adsorption purposes.[161,162] The external mechanical pressure can also be used to modulate the porosity of the MOFs for a fine tuning of adsorption. The mechanical pressure-induced loss of crystallinity/amorphization of the Zr-based cage-like carboxylate UiO-66(Zr) MOF and its mechanical properties has been investigated.[163,164]This decrease of crystallinity corresponds to ligand vacancy defects. Typically, a computational investigation evidenced that the presence of such defects makes this MOF more hydrophilic.[161] This agreement in the computational and experimental joint study suggests that modulating the affinity of the solid towards guest molecules is potentially feasible with the application of an external mechanical pressure. In most of the studies carried out regarding the flexibility of MOFs, there is always a control on the parameter, either the adsorption of guest molecules acting as an internal pressure, or the application of mechanical pressure acting as an external pressure. The thesis aims to successfully control both parameters simultaneously to fine-tune the pore structure of the MOF (pore size/shape, ligand orientation) optimal to pave the way towards novel approaches for the capture/storage or separation of guests. In the framework of the ANR project MeaCOPA,

the ultimate goal is to develop a novel concept that benefits from the control of the mechanical pressure to tune the MOF structures (pore size/shape, windows aperture, defects concentration…) and use this as novel tool to achieve sorption/separations that are difficult to attain using conventional approaches, in order to enhance the separation.
To achieve this objective, the porosity of the MOFs needs to be modulated throughout the gas adsorption/separation and this is feasible by using external mechanical pressure. Molecular Dynamic (MD) and Monte Carlo (MC), as well as Hybrid Osmotic Monte Carlo (HOMC) simulations, were used as the numerical approach. The novel HOMC simulation method enabled the ability to study the dynamics and structure of the global system involving guest molecules and MOFs. The molecular simulation will be explained in detail in Chapter II.

Throughout the thesis, we focused on the hydrocarbon mixture separation include hexane isomers. The external mechanical pressure was chosen as the external stimuli in order to enhance the separation ability via the mechanical fine-tuning of flexible MOFs. ZIF-8 was chosen thanks to its small opening gate which is around 3.4 Å that can be used for molecular sieving. There are already many studies carried out regarding the flexibility of ZIF-8, however, there isn't any systematic study on the impact of the mechanical pressure on the separation ability towards hexane isomers, our study will be one of the first that predict the selectivity as a function of mechanical pressure. MIL-140B was chosen for the same logic, it has 1D channel with small pore around 4.0 Å that can enable shape sieving towards hexane isomers, plus, our collaborators JA. C. Silva and his team experimentally proved that MIL-140B has the best selectivity among its MIL140 family. Our molecular simulation can assist the understanding on the performance of MIL-140B.

I.5 Structure of the thesis

Our work will be organised in six chapters. The Chapter I focus on the general introduction of the porous materials and the applications of the porous materials. The Chapter II provide the theoretical background for the molecular simulation. The Chapter III present the hexane isomers separation by the rigid MIL-140B. The Chapter IV is the pursuit of the Chapter III where we considered a flexible MIL-140B. Plus, we investigated the selectivity towards C6 isomers of MIL-140B with the application of external mechanical pressure. The Chapiter V bring out the investigation on the separation of C6 in ZIF-8. The Chapiter VI provide an atomistic level understanding of the slow C4 diffusion in ZIF-8.

Reference

(1) *Materials for Separation Technologies. Energy and Emission Reduction Opportunities*; Oak Ridge National Lab. (ORNL), Oak Ridge, TN (United States), 2005. https://doi.org/10.2172/1218755.
(2) Humphrey, J. L.; Keller, G. E. *Separation Process Technology*; McGraw-Hill: New York, 1997.
(3) Sholl, D. S.; Lively, R. P. Seven Chemical Separations to Change the World. *Nature* **2016**, *532* (7600), 435–437. https://doi.org/10.1038/532435a.
(4) Lecharlier, A. From Industrial Waste to Functional Materials, Development of Zeolite-Based Materials Using Non-Conventional Precursors, 2018. https://doi.org/10.13140/RG.2.2.26700.87682.
(5) Smith, J. V. Definition of a Zeolite. *Zeolites* **1984**, *4* (4), 309–310. https://doi.org/10.1016/0144-2449(84)90003-4.
(6) Earl, D. J.; Deem, M. W. Toward a Database of Hypothetical Zeolite Structures. *Ind. Eng. Chem. Res.* **2006**, *45* (16), 5449–5454. https://doi.org/10.1021/ie0510728.
(7) Simancas, R.; Chokkalingam, A.; Elangovan, S. P.; Liu, Z.; Sano, T.; Iyoki, K.; Wakihara, T.; Okubo, T. Recent Progress in the Improvement of Hydrothermal Stability of Zeolites. *Chem. Sci.* **2021**, *12* (22), 7677–7695. https://doi.org/10.1039/d1sc01179k.
(8) Cheng, J.; Xu, R.; Yang, G. Synthesis, Structure and Characterization of a Novel Germanium Dioxide with Occluded Tetramethylammonium Hydroxide. *J. Chem. Soc. Dalton Trans.* **1991**, No. 6, 1537–1540. https://doi.org/10.1039/DT9910001537.
(9) Li, J.; Corma, A.; Yu, J. Synthesis of New Zeolite Structures. *Chem. Soc. Rev.* **2015**, *44* (20), 7112–7127. https://doi.org/10.1039/C5CS00023H.
(10) Robson, H. *Verified Synthesis of Zeolitic Materials: Second Edition*; Gulf Professional Publishing, 2001.
(11) Kadhim, A.; Salman, J. Adsorption of Pesticides onto a Banana Leaf Activated Carbon: Optimization Study Using Response Surface Methodolog. **2017**.
(12) Marsh, H.; Reinoso, F. R. *Activated Carbon*; Elsevier, 2006.
(13) Bansal, R. C.; Goyal, M. *Activated Carbon Adsorption*; CRC Press: Boca Raton, 2005. https://doi.org/10.1201/9781420028812.
(14) Arrigo, R.; Hävecker, M.; Wrabetz, S.; Blume, R.; Lerch, M.; McGregor, J.; Parrott, E. P. J.; Zeitler, J. A.; Gladden, L. F.; Knop-Gericke, A.; Schlögl, R.; Su, D. S. Tuning the Acid/Base Properties of Nanocarbons by Functionalization via Amination. *J. Am. Chem. Soc.* **2010**, *132* (28), 9616–9630. https://doi.org/10.1021/ja910169v.
(15) Abe, M.; Kawashima, K.; Kozawa, K.; Sakai, H.; Kaneko, K. Amination of Activated Carbon and Adsorption Characteristics of Its Aminated Surface. *Langmuir* **2000**, *16* (11), 5059–5063. https://doi.org/10.1021/la990976t.
(16) Bautista-Toledo, I.; Rivera-Utrilla, J.; Ferro-García, M. A.; Moreno-Castilla, C. Influence of the Oxygen Surface Complexes of Activated Carbons on the Adsorption of Chromium Ions from Aqueous Solutions: Effect of Sodium Chloride and Humic Acid. *Carbon* **1994**, *32* (1), 93–100. https://doi.org/10.1016/0008-6223(94)90013-2.

(17) Song, X.; Liu, H.; Cheng, L.; Qu, Y. Surface Modification of Coconut-Based Activated Carbon by Liquid-Phase Oxidation and Its Effects on Lead Ion Adsorption. *Desalination* **2010**, *255* (1), 78–83. https://doi.org/10.1016/j.desal.2010.01.011.
(18) Moreno-Castilla, C.; Carrasco-Marín, F.; Parejo-Pérez, C.; López Ramón, M. V. Dehydration of Methanol to Dimethyl Ether Catalyzed by Oxidized Activated Carbons with Varying Surface Acidic Character. *Carbon* **2001**, *39* (6), 869–875. https://doi.org/10.1016/S0008-6223(00)00192-5.
(19) Bedia, J.; Barrionuevo, R.; Rodríguez-Mirasol, J.; Cordero, T. Ethanol Dehydration to Ethylene on Acid Carbon Catalysts. *Appl. Catal. B Environ.* **2011**, *103* (3), 302–310. https://doi.org/10.1016/j.apcatb.2011.01.032.
(20) Bedia, J.; Ruiz-Rosas, R.; Rodríguez-Mirasol, J.; Cordero, T. Kinetic Study of the Decomposition of 2-Butanol on Carbon-Based Acid Catalyst. *AIChE J.* **2010**, *56* (6), 1557–1568. https://doi.org/10.1002/aic.12056.
(21) Bedia, J.; Rosas, J. M.; Rodríguez-Mirasol, J.; Cordero, T. Pd Supported on Mesoporous Activated Carbons with High Oxidation Resistance as Catalysts for Toluene Oxidation. *Appl. Catal. B Environ.* **2010**, *94* (1), 8–18. https://doi.org/10.1016/j.apcatb.2009.10.015.
(22) Kiciński, W.; Szala, M.; Bystrzejewski, M. Sulfur-Doped Porous Carbons: Synthesis and Applications. *Carbon* **2014**, *68*, 1–32. https://doi.org/10.1016/j.carbon.2013.11.004.
(23) Calzado, M.; Valero-Romero, M. J.; Garriga, P.; Chica, A.; Guerrero-Pérez, M. O.; Rodríguez-Mirasol, J.; Cordero, T. Lignocellulosic Waste-Derived Basic Solids and Their Catalytic Applications for the Transformation of Biomass Waste. *Catal. Today* **2015**, *257*, 229–236. https://doi.org/10.1016/j.cattod.2014.06.038.
(24) Carabineiro, S. A. C.; Ramos, A. M.; Vital, J.; Loureiro, J. M.; Órfão, J. J. M.; Fonseca, I. M. Adsorption of SO2 Using Vanadium and Vanadium–Copper Supported on Activated Carbon. *Catal. Today* **2003**, *78* (1), 203–210. https://doi.org/10.1016/S0920-5861(02)00335-8.
(25) Rosas, J. M.; Ruiz-Rosas, R.; Rodríguez-Mirasol, J.; Cordero, T. Kinetic Study of the Oxidation Resistance of Phosphorus-Containing Activated Carbons. *Carbon* **2012**, *50* (4), 1523–1537. https://doi.org/10.1016/j.carbon.2011.11.030.
(26) Wu, X.; Radovic, L. R. Inhibition of Catalytic Oxidation of Carbon/Carbon Composites by Phosphorus. *Carbon* **2006**, *44* (1), 141–151. https://doi.org/10.1016/j.carbon.2005.06.038.
(27) Elmouwahidi, A.; Zapata-Benabithe, Z.; Carrasco-Marín, F.; Moreno-Castilla, C. Activated Carbons from KOH-Activation of Argan (Argania Spinosa) Seed Shells as Supercapacitor Electrodes. *Bioresour. Technol.* **2012**, *111*, 185–190. https://doi.org/10.1016/j.biortech.2012.02.010.
(28) Itoi, H.; Nishihara, H.; Ishii, T.; Nueangnoraj, K.; Berenguer-Betrián, R.; Kyotani, T. Large Pseudocapacitance in Quinone-Functionalized Zeolite-Templated Carbon. *Bull. Chem. Soc. Jpn.* **2014**, *87* (2), 250–257. https://doi.org/10.1246/bcsj.20130292.
(29) Li, P.; Ohtsuki, C.; Kokubo, T.; Nakanishi, K.; Soga, N.; Nakamura, T.; Yamamuro, T. Process of Formation of Bone-Like Apatite Layer on Silica-Gel. *J. Mater. Sci. Mater. Med.* **1993**, *4*, 127–131. https://doi.org/10.1007/BF00120381.
(30) Mandal, A.; Das, S. Adsorptive Removal of Phenol by Activated Alumina and Activated Carbon from Coconut Coir and Rice Husk Ash. *Water Conserv. Sci. Eng.* **2019**, *4*. https://doi.org/10.1007/s41101-019-00075-4.
(31) Tomic, E. A. Thermal Stability of Coordination Polymers. *J. Appl. Polym. Sci.* **1965**, *9* (11), 3745–3752. https://doi.org/10.1002/app.1965.070091121.

(32) Hoskins, B. F.; Robson, R. Design and Construction of a New Class of Scaffolding-like Materials Comprising Infinite Polymeric Frameworks of 3D-Linked Molecular Rods. A Reappraisal of the Zinc Cyanide and Cadmium Cyanide Structures and the Synthesis and Structure of the Diamond-Related Frameworks [N(CH3)4][CuIZnII(CN)4] and CuI[4,4',4'',4'''-Tetracyanotetraphenylmethane]BF4.XC6H5NO2. *J. Am. Chem. Soc.* **1990**, *112* (4), 1546–1554. https://doi.org/10.1021/ja00160a038.

(33) Kondo, M.; Yoshitomi, T.; Matsuzaka, H.; Kitagawa, S.; Seki, K. Three-Dimensional Framework with Channeling Cavities for Small Molecules: [M2(4, 4′-Bpy)3(NO3)4]·xH2On (M Co, Ni, Zn). *Angew. Chem. Int. Ed. Engl.* **1997**, *36* (16), 1725–1727. https://doi.org/10.1002/anie.199717251.

(34) Li, H.; Eddaoudi, M.; O'Keeffe, M.; Yaghi, O. M. Design and Synthesis of an Exceptionally Stable and Highly Porous Metal-Organic Framework. *Nature* **1999**, *402* (6759), 276–279. https://doi.org/10.1038/46248.

(35) Eddaoudi, M.; Kim, J.; Rosi, N.; Vodak, D.; Wachter, J.; O'Keeffe, M.; Yaghi, O. M. Systematic Design of Pore Size and Functionality in Isoreticular MOFs and Their Application in Methane Storage. *Science* **2002**, *295* (5554), 469–472. https://doi.org/10.1126/science.1067208.

(36) Yaghi, O.; Eddaoudi, M.; Li, H.; Kim, J.; Rosi, N. Isoreticular Metal-Organic Frameworks, Process for Forming the Same, and Systematic Design of Pore Size and Functionality Therein,with Application for Gas Storage, November 7, 2002.

(37) Chae, H. K.; Siberio-Pérez, D. Y.; Kim, J.; Go, Y.; Eddaoudi, M.; Matzger, A. J.; O'Keeffe, M.; Yaghi, O. M. A Route to High Surface Area, Porosity and Inclusion of Large Molecules in Crystals. *Nature* **2004**, *427* (6974), 523–527. https://doi.org/10.1038/nature02311.

(38) Millange, F.; Serre, C.; Férey, G. Synthesis, Structure Determination and Properties of MIL-53as and MIL-53ht: The First CrIII Hybrid Inorganic–Organic Microporous Solids: CrIII(OH)·{O2C–C6H4–CO2}·{HO2C–C6H4–CO2H}x. *Chem. Commun.* **2002**, No. 8, 822–823. https://doi.org/10.1039/B201381A.

(39) Serre, C.; Millange, F.; Thouvenot, C.; Noguès, M.; Marsolier, G.; Louër, D.; Férey, G. Very Large Breathing Effect in the First Nanoporous Chromium(III)-Based Solids: MIL-53 or CrIII(OH)·{O2C−C6H4−CO2}·{HO2C−C6H4−CO2H}x·H2Oy. *J. Am. Chem. Soc.* **2002**, *124* (45), 13519–13526. https://doi.org/10.1021/ja0276974.

(40) Loiseau, T.; Serre, C.; Huguenard, C.; Fink, G.; Taulelle, F.; Henry, M.; Bataille, T.; Férey, G. A Rationale for the Large Breathing of the Porous Aluminum Terephthalate (MIL-53) Upon Hydration. *Chem. – Eur. J.* **2004**, *10* (6), 1373–1382. https://doi.org/10.1002/chem.200305413.

(41) Whitfield, T. R.; Wang, X.; Liu, L.; Jacobson, A. J. Metal-Organic Frameworks Based on Iron Oxide Octahedral Chains Connected by Benzenedicarboxylate Dianions. *Solid State Sci.* **2005**, *7* (9), 1096–1103. https://doi.org/10.1016/j.solidstatesciences.2005.03.007.

(42) Anokhina, E. V.; Vougo-Zanda, M.; Wang, X.; Jacobson, A. J. In(OH)BDC·0.75BDCH2 (BDC = Benzenedicarboxylate), a Hybrid Inorganic−Organic Vernier Structure. *J. Am. Chem. Soc.* **2005**, *127* (43), 15000–15001. https://doi.org/10.1021/ja055757a.

(43) Munn, A. S.; Clarkson, G. J.; Millange, F.; Dumont, Y.; Walton, R. I. M(II) (M = Mn, Co, Ni) Variants of the MIL-53-Type Structure with Pyridine-N-Oxide as a Co-Ligand. *CrystEngComm* **2013**, *15* (45), 9679–9687. https://doi.org/10.1039/C3CE41268G.

(44) Vougo-Zanda, M.; Huang, J.; Anokhina, E.; Wang, X.; Jacobson, A. J. Tossing and Turning: Guests in the Flexible Frameworks of Metal(III) Dicarboxylates. *Inorg. Chem.* **2008**, *47* (24), 11535–11542. https://doi.org/10.1021/ic800008f.
(45) Xu, G.; Zhang, X.; Guo, P.; Pan, C.; Zhang, H.; Wang, C. MnII-Based MIL-53 Analogues: Synthesis Using Neutral Bridging M2-Ligands and Application in Liquid-Phase Adsorption and Separation of C6−C8 Aromatics. *J. Am. Chem. Soc.* **2010**, *132* (11), 3656–3657. https://doi.org/10.1021/ja910818a.
(46) Horcajada, P.; Surblé, S.; Serre, C.; Hong, D.-Y.; Seo, Y.-K.; Chang, J.-S.; Grenèche, J.-M.; Margiolaki, I.; Férey, G. Synthesis and Catalytic Properties of MIL-100(Fe), an Iron(Iii) Carboxylate with Large Pores. *Chem. Commun.* **2007**, *0* (27), 2820–2822. https://doi.org/10.1039/B704325B.
(47) Daglar, H.; Erucar, I.; Keskin, S. Recent Advances in Simulating Gas Permeation through MOF Membranes. *Mater. Adv.* *2* (16), 5300–5317. https://doi.org/10.1039/d1ma00026h.
(48) Groom, C. R.; Bruno, I. J.; Lightfoot, M. P.; Ward, S. C. The Cambridge Structural Database. *Acta Crystallogr. Sect. B Struct. Sci. Cryst. Eng. Mater.* **2016**, *72* (2), 171–179. https://doi.org/10.1107/S2052520616003954.
(49) Chedid, G.; Yassin, A. Recent Trends in Covalent and Metal Organic Frameworks for Biomedical Applications. *Nanomaterials* **2018**, *8*, 916. https://doi.org/10.3390/nano8110916.
(50) Guillerm, V.; Ragon, F.; Dan-Hardi, M.; Devic, T.; Vishnuvarthan, M.; Campo, B.; Vimont, A.; Clet, G.; Yang, Q.; Maurin, G.; Férey, G.; Vittadini, A.; Gross, S.; Serre, C. A Series of Isoreticular, Highly Stable, Porous Zirconium Oxide Based Metal-Organic Frameworks. *Angew. Chem. Int. Ed Engl.* **2012**, *51* (37), 9267–9271. https://doi.org/10.1002/anie.201204806.
(51) Gelb, L. D.; Gubbins, K. E. Pore Size Distributions in Porous Glasses: A Computer Simulation Study. *Langmuir* **1999**, *15* (2), 305–308. https://doi.org/10.1021/la9808418.
(52) Abánades Lázaro, I.; Forgan, R. S. Application of Zirconium MOFs in Drug Delivery and Biomedicine. *Coord. Chem. Rev.* **2019**, *380*, 230–259. https://doi.org/10.1016/j.ccr.2018.09.009.
(53) Wang, Y.; Li, B.; Zhang, B.; Tian, S.; Yang, X.; Ye, H.; Xia, Z.; Zheng, G. Application of MOFs-Derived Mixed Metal Oxides in Energy Storage. *J. Electroanal. Chem.* **2020**, *878*, 114576. https://doi.org/10.1016/j.jelechem.2020.114576.
(54) Zhao, X.; Zheng, M.; Gao, X.; Zhang, J.; Wang, E.; Gao, Z. The Application of MOFs-Based Materials for Antibacterials Adsorption. *Coord. Chem. Rev.* **2021**, *440*, 213970. https://doi.org/10.1016/j.ccr.2021.213970.
(55) Wiersum, A. D.; Giovannangeli, C.; Vincent, D.; Bloch, E.; Reinsch, H.; Stock, N.; Chang, J.-S.; Llewellyn, P. L. Experimental Screening of Porous Materials for High Pressure Gas Adsorption and Evaluation in Gas Separations: Application to MOFs (MIL-100 and CAU-10). *ACS Comb. Sci.* **2013**, *15* (2), 111–119. https://doi.org/10.1021/co300128w.
(56) Lin, J. Y. S. CHEMISTRY. Molecular Sieves for Gas Separation. *Science* **2016**, *353* (6295), 121–122. https://doi.org/10.1126/science.aag2267.
(57) Taylor, P. Energy Technology Perspectives 2010. 16.
(58) Chu, S.; Cui, Y.; Liu, N. The Path towards Sustainable Energy. *Nat. Mater.* **2016**, *16* (1). https://doi.org/10.1038/nmat4834.

(59) Liang, W.; Zhang, Y.; Wang, X.; Wu, Y.; Zhou, X.; Xiao, J.; Li, Y.; Wang, H.; Li, Z. Asphalt-Derived High Surface Area Activated Porous Carbons for the Effective Adsorption Separation of Ethane and Ethylene. *Chem. Eng. Sci.* **2017**, *162*, 192–202. https://doi.org/10.1016/j.ces.2017.01.003.
(60) Pure and binary adsorption isotherms of ethylene and ethane on zeolite 5A | SpringerLink https://link.springer.com/article/10.1007%2Fs10450-012-9423-1 (accessed 2021 -12 -30).
(61) Zeng, H.; Xie, M.; Wang, T.; Wei, R.-J.; Xie, X.-J.; Zhao, Y.; Lu, W.; Li, D. Orthogonal-Array Dynamic Molecular Sieving of Propylene/Propane Mixtures. *Nature* **2021**, *595* (7868), 542–548. https://doi.org/10.1038/s41586-021-03627-8.
(62) Liang, B.; Zhang, X.; Xie, Y.; Lin, R.-B.; Krishna, R.; Cui, H.; Li, Z.; Shi, Y.; Wu, H.; Zhou, W.; Chen, B. An Ultramicroporous Metal–Organic Framework for High Sieving Separation of Propylene from Propane. *J. Am. Chem. Soc.* **2020**, *142* (41), 17795–17801. https://doi.org/10.1021/jacs.0c09466.
(63) Krokidas, P.; Castier, M.; Moncho, S.; Brothers, E.; Economou, I. G. Molecular Simulation Studies of the Diffusion of Methane, Ethane, Propane, and Propylene in ZIF-8. *J. Phys. Chem. C* **2015**, *119* (48), 27028–27037. https://doi.org/10.1021/acs.jpcc.5b08554.
(64) Bae, Y.-S.; Lee, C. Y.; Kim, K. C.; Farha, O. K.; Nickias, P.; Hupp, J. T.; Nguyen, S. T.; Snurr, R. Q. High Propene/Propane Selectivity in Isostructural Metal–Organic Frameworks with High Densities of Open Metal Sites. *Angew. Chem. Int. Ed.* **2012**, *51* (8), 1857–1860. https://doi.org/10.1002/anie.201107534.
(65) Yoon, J. W.; Seo, Y.-K.; Hwang, Y. K.; Chang, J.-S.; Leclerc, H.; Wuttke, S.; Bazin, P.; Vimont, A.; Daturi, M.; Bloch, E.; Llewellyn, P. L.; Serre, C.; Horcajada, P.; Grenèche, J.-M.; Rodrigues, A. E.; Férey, G. Controlled Reducibility of a Metal–Organic Framework with Coordinatively Unsaturated Sites for Preferential Gas Sorption. *Angew. Chem. Int. Ed.* **2010**, *49* (34), 5949–5952. https://doi.org/10.1002/anie.201001230.
(66) Wang, S.; Zhang, Y.; Tang, Y.; Wen, Y.; Lv, Z.; Liu, S.; Li, X.; Zhou, X. Propane-Selective Design of Zirconium-Based MOFs for Propylene Purification. *Chem. Eng. Sci.* **2020**, *219*, 115604. https://doi.org/10.1016/j.ces.2020.115604.
(67) Jeffroy, M. Simulation moléculaire des propriétés des zéolithes cationiques : Propriétés thermodynamiques et propriétés structurales. phd thesis, Université Paris Sud - Paris XI, **2010**.
(68) Cannella, W. J. Xylenes and Ethylbenzene. In *Kirk-Othmer Encyclopedia of Chemical Technology*; John Wiley & Sons, Ltd, **2007**.
(69) Alaerts, L.; Kirschhock, C. E. A.; Maes, M.; van der Veen, M. A.; Finsy, V.; Depla, A.; Martens, J. A.; Baron, G. V.; Jacobs, P. A.; Denayer, J. F. M.; De Vos, D. E. Selective Adsorption and Separation of Xylene Isomers and Ethylbenzene with the Microporous Vanadium(IV) Terephthalate MIL-47. *Angew. Chem. Int. Ed Engl.* **2007**, *46* (23), 4293–4297. https://doi.org/10.1002/anie.200700056.
(70) Finsy, V.; Verelst, H.; Alaerts, L.; De Vos, D.; Jacobs, P. A.; Baron, G. V.; Denayer, J. F. M. Pore-Filling-Dependent Selectivity Effects in the Vapor-Phase Separation of Xylene Isomers on the Metal−Organic Framework MIL-47. *J. Am. Chem. Soc.* **2008**, *130* (22), 7110–7118. https://doi.org/10.1021/ja800686c.
(71) Torres-Knoop, A.; Krishna, R.; Dubbeldam, D. Separating Xylene Isomers by Commensurate Stacking of P-Xylene within Channels of MAF-X8. *Angew. Chem. Int. Ed Engl.* **2014**, *53* (30), 7774–7778. https://doi.org/10.1002/anie.201402894.

(72) Jin, Z.; Zhao, H.-Y.; Zhao, X.-J.; Fang, Q.-R.; Long, J. R.; Zhu, G.-S. A Novel Microporous MOF with the Capability of Selective Adsorption of Xylenes. *Chem. Commun.* **2010**, *46* (45), 8612–8614. https://doi.org/10.1039/C0CC01031F.
(73) Finsy, V.; Kirschhock, C. E. A.; Vedts, G.; Maes, M.; Alaerts, L.; De Vos, D. E.; Baron, G. V.; Denayer, J. F. M. Framework Breathing in the Vapour-Phase Adsorption and Separation of Xylene Isomers with the Metal–Organic Framework MIL-53. *Chem. – Eur. J.* **2009**, *15* (31), 7724–7731. https://doi.org/10.1002/chem.200802672.
(74) Wicht, M. M.; Báthori, N. B.; Nassimbeni, L. R. Enhanced Selectivity towards Xylene Isomers of a Mixed Ligand Ni(II) Thiocyanato Complex. *Polyhedron* **2016**, *C* (119), 127–133. https://doi.org/10.1016/j.poly.2016.08.022.
(75) Moreira, M. A.; Santos, J. C.; Ferreira, A. F. P.; Loureiro, J. M.; Ragon, F.; Horcajada, P.; Shim, K.-E.; Hwang, Y.-K.; Lee, U.-H.; Chang, J.-S.; Serre, C.; Rodrigues, A. E. Reverse Shape Selectivity in the Liquid-Phase Adsorption of Xylene Isomers in Zirconium Terephthalate MOF UiO-66. *Langmuir* **2012**, *28* (13), 5715–5723. https://doi.org/10.1021/la3004118.
(76) Yang, Y.; Bai, P.; Guo, X. Separation of Xylene Isomers: A Review of Recent Advances in Materials. *Ind. Eng. Chem. Res.* **2017**, *56* (50), 14725–14753. https://doi.org/10.1021/acs.iecr.7b03127.
(77) Mukherjee, S.; Joarder, B.; Manna, B.; Desai, A. V.; Chaudhari, A. K.; Ghosh, S. K. Framework-Flexibility Driven Selective Sorption of p-Xylene over Other Isomers by a Dynamic Metal-Organic Framework. *Sci. Rep.* **2014**, *4* (1), 5761. https://doi.org/10.1038/srep05761.
(78) Mukherjee, S.; Joarder, B.; Desai, A. V.; Manna, B.; Krishna, R.; Ghosh, S. K. Exploiting Framework Flexibility of a Metal–Organic Framework for Selective Adsorption of Styrene over Ethylbenzene. *Inorg. Chem.* **2015**, *54* (9), 4403–4408. https://doi.org/10.1021/acs.inorgchem.5b00206.
(79) Saccoccia, B.; Bohnsack, A. M.; Waggoner, N. W.; Cho, K. H.; Lee, J. S.; Hong, D.-Y.; Lynch, V. M.; Chang, J.-S.; Humphrey, S. M. Separation of P-Divinylbenzene by Selective Room-Temperature Adsorption Inside Mg-CUK-1 Prepared by Aqueous Microwave Synthesis. *Angew. Chem. Int. Ed.* **2015**, *54* (18), 5394–5398. https://doi.org/10.1002/anie.201411862.
(80) Wright, J. S.; Vitórica-Yrezábal, I. J.; Thompson, S. P.; Brammer, L. Arene Selectivity by a Flexible Coordination Polymer Host. *Chem. Weinh. Bergstr. Ger.* **2016**, *22* (37), 13120–13126. https://doi.org/10.1002/chem.201601870.
(81) Lannoeye, J.; Van de Voorde, B.; Bozbiyik, B.; Reinsch, H.; Denayer, J.; De Vos, D. An Aliphatic Copper Metal-Organic Framework as Versatile Shape Selective Adsorbent in Liquid Phase Separations. *Microporous Mesoporous Mater.* **2016**, *226*, 292–298. https://doi.org/10.1016/j.micromeso.2016.01.044.
(82) Warren, J. E.; Perkins, C. G.; Jelfs, K. E.; Boldrin, P.; Chater, P. A.; Miller, G. J.; Manning, T. D.; Briggs, M. E.; Stylianou, K. C.; Claridge, J. B.; Rosseinsky, M. J. Shape Selectivity by Guest-Driven Restructuring of a Porous Material. *Angew. Chem. Int. Ed.* **2014**, *53* (18), 4592–4596. https://doi.org/10.1002/anie.201307656.
(83) Peralta, D.; Chaplais, G.; Paillaud, J.-L.; Simon-Masseron, A.; Barthelet, K.; Pirngruber, G. D. The Separation of Xylene Isomers by ZIF-8: A Demonstration of the Extraordinary Flexibility of the ZIF-8 Framework. *Microporous Mesoporous Mater.* **2013**, *Complete* (173), 1–5. https://doi.org/10.1016/j.micromeso.2013.01.012.

(84) Peralta, D.; Barthelet, K.; Pirngruber, G.; CHAPLAIS, G.; SIMON-MASSERON, A.; Patarin, J. Method for Separating Paraxylenes Using an Adsorbent from the Family of Zifs of Sod Structure. WO2013011210A1, January 24, 2013.
(85) Vermoortele, F.; Maes, M.; Moghadam, P. Z.; Lennox, M. J.; Ragon, F.; Boulhout, M.; Biswas, S.; Laurier, K. G. M.; Beurroies, I.; Denoyel, R.; Roeffaers, M.; Stock, N.; Düren, T.; Serre, C.; De Vos, D. E. P-Xylene-Selective Metal–Organic Frameworks: A Case of Topology-Directed Selectivity. *J. Am. Chem. Soc.* **2011**, *133* (46), 18526–18529. https://doi.org/10.1021/ja207287h.
(86) Moreira, M. A.; Santos, J. C.; Ferreira, A. F. P.; Loureiro, J. M.; Ragon, F.; Horcajada, P.; Yot, P. G.; Serre, C.; Rodrigues, A. E. Effect of Ethylbenzene in P-Xylene Selectivity of the Porous Titanium Amino Terephthalate MIL-125(Ti)_NH2. *Microporous Mesoporous Mater.* **2012**, *158*, 229–234. https://doi.org/10.1016/j.micromeso.2012.03.039.
(87) Gee, J. A.; Zhang, K.; Bhattacharyya, S.; Bentley, J.; Rungta, M.; Abichandani, J. S.; Sholl, D. S.; Nair, S. Computational Identification and Experimental Evaluation of Metal–Organic Frameworks for Xylene Enrichment. *J. Phys. Chem. C* **2016**, *120* (22), 12075–12082. https://doi.org/10.1021/acs.jpcc.6b03349.
(88) A Moreira, M.; Carlos Santos, J.; F. P. Ferreira, A.; Miguel Loureiro, J.; Ragon, F.; Horcajada, P.; Yot, P.; Serre, C.; Egidio Rodrigues, A. Toward Understanding the Influence of Ethylbenzene in P-Xylene Selectivity of the Porous Titanium Amino Terephthalate MIL-125(Ti): Adsorption Equilibrium and Separation of Xylene Isomers. *Langmuir* **2012**, *28* (7), 3494–3502. https://doi.org/10.1021/la204969t.
(89) Dang, L.-L.; Zhang, X.-J.; Zhang, L.; Li, J.-Q.; Luo, F.; Feng, X.-F. Photo-Responsive Azo MOF Exhibiting High Selectivity for CO2 and Xylene Isomers. *J. Coord. Chem.* **2016**, *69* (7), 1179–1187. https://doi.org/10.1080/00958972.2016.1166359.
(90) Niekiel, F.; Lannoeye, J.; Reinsch, H.; Munn, A. S.; Heerwig, A.; Zizak, I.; Kaskel, S.; Walton, R. I.; de Vos, D.; Llewellyn, P.; Lieb, A.; Maurin, G.; Stock, N. Conformation-Controlled Sorption Properties and Breathing of the Aliphatic Al-MOF [Al(OH)(CDC)]. *Inorg. Chem.* **2014**, *53* (9), 4610–4620. https://doi.org/10.1021/ic500288w.
(91) Bárcia, P. da S.; Nicolau, M.; Gallegos, J.; Chen, B.; Rodrigues, A.; Silva, J. A. C. Modeling Adsorption Equilibria of Xylene Isomers in a Microporous Metal–Organic Framework. *Microporous Mesoporous Mater.* **2012**, No. 155, 220–226. https://doi.org/10.1016/j.micromeso.2012.01.033.
(92) Peralta, D.; Barthelet, K.; Pérez-Pellitero, J.; Chizallet, C.; Chaplais, G.; Simon-Masseron, A.; Pirngruber, G. D. Adsorption and Separation of Xylene Isomers: CPO-27-Ni vs HKUST-1 vs NaY. *J. Phys. Chem. C* **2012**, *116* (41), 21844–21855. https://doi.org/10.1021/jp306828x.
(93) Alaerts, L.; Maes, M.; Giebeler, L.; Jacobs, P. A.; Martens, J. A.; Denayer, J. F. M.; Kirschhock, C. E. A.; De Vos, D. E. Selective Adsorption and Separation of Ortho-Substituted Alkylaromatics with the Microporous Aluminum Terephthalate MIL-53. *J. Am. Chem. Soc.* **2008**, *130* (43), 14170–14178. https://doi.org/10.1021/ja802761z.
(94) Moreira, M. A.; Santos, J. C.; Ferreira, A. F. P.; Müller, U.; Trukhan, N.; Loureiro, J. M.; Rodrigues, A. E. Selective Liquid Phase Adsorption and Separation of Ortho-Xylene with the Microporous MIL-53(Al). *Sep. Sci. Technol.* **2011**, *46* (13), 1995–2003. https://doi.org/10.1080/01496395.2011.594481.

(95) Moreira, M. A.; Santos, J. C.; Ferreira, A. F. P.; Loureiro, J. M.; Rodrigues, A. E. Influence of the Eluent in the MIL-53(Al) Selectivity for Xylene Isomers Separation. *Ind. Eng. Chem. Res.* **2011**, *50* (12), 7688–7695. https://doi.org/10.1021/ie200206n.
(96) El Osta, R.; Carlin-Sinclair, A.; Guillou, N.; Walton, R. I.; Vermoortele, F.; Maes, M.; de Vos, D.; Millange, F. Liquid-Phase Adsorption and Separation of Xylene Isomers by the Flexible Porous Metal–Organic Framework MIL-53(Fe). *Chem. Mater.* **2012**, *24* (14), 2781–2791. https://doi.org/10.1021/cm301242d.
(97) Holcroft, J. M.; Hartlieb, K. J.; Moghadam, P. Z.; Bell, J. G.; Barin, G.; Ferris, D. P.; Bloch, E. D.; Algaradah, M. M.; Nassar, M. S.; Botros, Y. Y.; Thomas, K. M.; Long, J. R.; Snurr, R. Q.; Stoddart, J. F. Carbohydrate-Mediated Purification of Petrochemicals. *J. Am. Chem. Soc.* **2015**, *137* (17), 5706–5719. https://doi.org/10.1021/ja511878b.
(98) Peralta, D.; Chaplais, G.; Simon-Masseron, A.; Barthelet, K.; Chizallet, C.; Quoineaud, A.-A.; Pirngruber, G. D. Comparison of the Behavior of Metal–Organic Frameworks and Zeolites for Hydrocarbon Separations. *J. Am. Chem. Soc.* **2012**, *134* (19), 8115–8126. https://doi.org/10.1021/ja211864w.
(99) Lusi, M.; Barbour, L. J. Solid–Vapor Sorption of Xylenes: Prioritized Selectivity as a Means of Separating All Three Isomers Using a Single Substrate. *Angew. Chem. Int. Ed.* **2012**, *51* (16), 3928–3931. https://doi.org/10.1002/anie.201109084.
(100) Gonzalez, M.; Kapelewski, M.; Bloch, E.; Milner, P.; Reed, D.; Hudson, M.; Mason, J.; Barin, G.; Brown, C.; Long, J. Separation of Xylene Isomers through Multiple Metal Site Interactions in Metal–Organic Frameworks. *J. Am. Chem. Soc.* **2018**, *140*. https://doi.org/10.1021/jacs.7b13825.
(101) Gu, Z.-Y.; Yan, X.-P. Metal–Organic Framework MIL-101 for High-Resolution Gas-Chromatographic Separation of Xylene Isomers and Ethylbenzene. *Angew. Chem. Int. Ed.* **2010**, *49* (8), 1477–1480. https://doi.org/10.1002/anie.200906560.
(102) The chemistry and technology of petroleum, second edition, revised and expanded. By James G. Speight, Marcel Dekker, New York, 1991 - Gray - 1992 - AIChE Journal - Wiley Online Library https://aiche.onlinelibrary.wiley.com/doi/abs/10.1002/aic.690380820 (accessed 2021 -12 -06).
(103) Herm, Z. R.; Wiers, B. M.; Mason, J. A.; van Baten, J. M.; Hudson, M. R.; Zajdel, P.; Brown, C. M.; Masciocchi, N.; Krishna, R.; Long, J. R. Separation of Hexane Isomers in a Metal-Organic Framework with Triangular Channels. *Science* **2013**, *340* (6135), 960–964. https://doi.org/10.1126/science.1234071.
(104) *Handbook of Petroleum Refining Processes*; McGraw-Hill Education, 2016.
(105) Luebbers, M. T.; Wu, T.; Shen, L.; Masel, R. I. Effects of Molecular Sieving and Electrostatic Enhancement in the Adsorption of Organic Compounds on the Zeolitic Imidazolate Framework ZIF-8. *Langmuir ACS J. Surf. Colloids* **2010**, *26* (19), 15625–15633. https://doi.org/10.1021/la102582g.
(106) Zhao, H.; Maurin, G.; Ghoufi, A. Tuning the Hexane Isomer Separation Performances of Zeolitic Imidazole Framework-8 Using Mechanical Pressure. *J. Chem. Phys.* **2021**, *154* (8), 084702. https://doi.org/10.1063/5.0040469.
(107) Peralta, D.; Chaplais, G.; Simon-Masseron, A.; Barthelet, K.; Pirngruber, G. D. Separation of C6 Paraffins Using Zeolitic Imidazolate Frameworks: Comparison with Zeolite 5A. *Ind. Eng. Chem. Res.* **2012**, *51* (12), 4692–4702. https://doi.org/10.1021/ie202995g.
(108) Chen, L.; Yuan, S.; Qian, J.-F.; Fan, W.; He, M.-Y.; Chen, Q.; Zhang, Z.-H. Effective Adsorption Separation of N-Hexane/2-Methylpentane in Facilely

Synthesized Zeolitic Imidazolate Frameworks ZIF-8 and ZIF-69. *Ind. Eng. Chem. Res.* **2016**, *55* (40), 10751–10757. https://doi.org/10.1021/acs.iecr.6b02175.

(109) Peralta, D. Evaluation Des Metal-Organic Frameworks En Adsorption et Séparation Des Hydrocarbures. Theses, Université de Haute Alsace - Mulhouse, 2011.

(110) Dong, X.; Fan, Q.; Hao, W.; Chen, Y. Adsorption and Separation of Hexane Isomers in Metal-Organic Frameworks (MOFs): A Computational Study. *Comput. Theor. Chem.* **2021**, *1197*, 113164. https://doi.org/10.1016/j.comptc.2021.113164.

(111) Bárcia, P. S.; Zapata, F.; Silva, J. A. C.; Rodrigues, A. E.; Chen, B. Kinetic Separation of Hexane Isomers by Fixed-Bed Adsorption with a Microporous Metal−Organic Framework. *J. Phys. Chem. B* **2007**, *111* (22), 6101–6103. https://doi.org/10.1021/jp0721898.

(112) Mendes, P. A. P. Separation of Hexane Isomers in Metal-Organic Frameworks (MOFs). phdthesis, Université de Versailles-Saint Quentin en Yvelines, 2014.

(113) Mendes, P. A. P. M.; Rodrigues, A.; Horcajada, P.; Eubank, J.; Devic, T.; Serre, C.; Silva, J. Separation of Hexane Isomers on Rigid Porous Metal Carboxylate-Based Metal–Organic Frameworks. *Adsorpt. Sci. Technol.* **2014**, *32*. https://doi.org/10.1260/0263-6174.32.6.475.

(114) Chen, B.; Liang, C.; Yang, J.; Contreras, D. S.; Clancy, Y. L.; Lobkovsky, E. B.; Yaghi, O. M.; Dai, S. A Microporous Metal-Organic Framework for Gas-Chromatographic Separation of Alkanes. *Angew. Chem. Int. Ed Engl.* **2006**, *45* (9), 1390–1393. https://doi.org/10.1002/anie.200502844.

(115) Pan, L.; Olson, D. H.; Ciemnolonski, L. R.; Heddy, R.; Li, J. Separation of Hydrocarbons with a Microporous Metal–Organic Framework. *Angew. Chem. Int. Ed.* **2006**, *45* (4), 616–619. https://doi.org/10.1002/anie.200503503.

(116) Jin, H.; Li, Y. Flexibility of Metal-Organic Frameworks for Separations: Utilization, Suppression and Regulation. *Curr. Opin. Chem. Eng.* **2018**, *20*, 107–113. https://doi.org/10.1016/j.coche.2018.03.008.

(117) Millange, F.; Guillou, N.; Walton, R. I.; Grenèche, J.-M.; Margiolaki, I.; Férey, G. Effect of the Nature of the Metal on the Breathing Steps in MOFs with Dynamic Frameworks. *Chem. Commun.* **2008**, No. 39, 4732–4734. https://doi.org/10.1039/B809419E.

(118) Mowat, J. P. S.; Seymour, V. R.; Griffin, J. M.; Thompson, S. P.; Slawin, A. M. Z.; Fairen-Jimenez, D.; Düren, T.; Ashbrook, S. E.; Wright, P. A. A Novel Structural Form of MIL-53 Observed for the Scandium Analogue and Its Response to Temperature Variation and CO2 Adsorption. *Dalton Trans.* **2012**, *41* (14), 3937–3941. https://doi.org/10.1039/C1DT11729G.

(119) Volkringer, C.; Loiseau, T.; Guillou, N.; Férey, G.; Elkaïm, E.; Vimont, A. XRD and IR Structural Investigations of a Particular Breathing Effect in the MOF-Type Gallium Terephthalate MIL-53(Ga). *Dalton Trans.* **2009**, No. 12, 2241–2249. https://doi.org/10.1039/B817563B.

(120) Ghoufi, A.; Benhamed, K.; Boukli-Hacene, L.; Maurin, G. Electrically Induced Breathing of the MIL-53(Cr) Metal–Organic Framework. *ACS Cent. Sci.* **2017**, *3* (5), 394–398. https://doi.org/10.1021/acscentsci.6b00392.

(121) Mellot-Draznieks, C.; Serre, C.; Surblé, S.; Audebrand, N.; Férey, G. Very Large Swelling in Hybrid Frameworks: A Combined Computational and Powder Diffraction Study. *J. Am. Chem. Soc.* **2005**, *127* (46), 16273–16278. https://doi.org/10.1021/ja054900x.

(122) Surblé, S.; Serre, C.; Mellot-Draznieks, C.; Millange, F.; Férey, G. A New Isoreticular Class of Metal-Organic-Frameworks with the MIL-88 Topology. *Chem. Commun.* **2006**, No. 3, 284–286. https://doi.org/10.1039/B512169H.

(123) Horcajada, P.; Salles, F.; Wuttke, S.; Devic, T.; Heurtaux, D.; Maurin, G.; Vimont, A.; Daturi, M.; David, O.; Magnier, E.; Stock, N.; Filinchuk, Y.; Popov, D.; Riekel, C.; Férey, G.; Serre, C. How Linker's Modification Controls Swelling Properties of Highly Flexible Iron(III) Dicarboxylates MIL-88. *J. Am. Chem. Soc.* **2011**. https://doi.org/10.1021/ja206936e.

(124) Garberoglio, G.; Taioli, S. Modeling Flexibility in Metal–Organic Frameworks: Comparison between Density-Functional Tight-Binding and Universal Force Field Approaches for Bonded Interactions. *Microporous Mesoporous Mater.* **2012**, *163*, 215–220. https://doi.org/10.1016/j.micromeso.2012.07.026.

(125) Fairen-Jimenez, D.; Galvelis, R.; Torrisi, A.; Gellan, A. D.; Wharmby, M. T.; Wright, P. A.; Mellot-Draznieks, C.; Düren, T. Flexibility and Swing Effect on the Adsorption of Energy-Related Gases on ZIF-8: Combined Experimental and Simulation Study. *Dalton Trans.* **2012**, *41* (35), 10752–10762. https://doi.org/10.1039/C2DT30774J.

(126) Henrique, A.; Maity, T.; Zhao, H.; Brântuas, P. F.; Rodrigues, A. E.; Nouar, F.; Ghoufi, A.; Maurin, G.; Silva, J. A. C.; Serre, C. Hexane Isomers Separation on an Isoreticular Series of Microporous Zr Carboxylate Metal Organic Frameworks. *J. Mater. Chem. A* **2020**, *8* (34), 17780–17789. https://doi.org/10.1039/D0TA05538G.

(127) Kitagawa, S.; Kitaura, R.; Noro, S. Functional Porous Coordination Polymers. *Angew. Chem. Int. Ed.* **2004**, *43* (18), 2334–2375. https://doi.org/10.1002/anie.200300610.

(128) Maji, T. K.; Matsuda, R.; Kitagawa, S. A Flexible Interpenetrating Coordination Framework with a Bimodal Porous Functionality. *Nat. Mater.* **2007**, *6* (2), 142–148. https://doi.org/10.1038/nmat1827.

(129) Kanoo, P.; Matsuda, R.; Higuchi, M.; Kitagawa, S.; Maji, T. K. New Interpenetrated Copper Coordination Polymer Frameworks Having Porous Properties. *Chem. Mater.* **2009**, *21* (24), 5860–5866. https://doi.org/10.1021/cm9025683.

(130) Bureekaew, S.; Sato, H.; Matsuda, R.; Kubota, Y.; Hirose, R.; Kim, J.; Kato, K.; Takata, M.; Kitagawa, S. Control of Interpenetration for Tuning Structural Flexibility Influences Sorption Properties. *Angew. Chem. Int. Ed.* **2010**, *49* (42), 7660–7664. https://doi.org/10.1002/anie.201002259.

(131) Barthelet, K.; Marrot, J.; Riou, D.; Férey, G. A Breathing Hybrid Organic–Inorganic Solid with Very Large Pores and High Magnetic Characteristics. *Angew. Chem. Int. Ed.* **2002**, *41* (2), 281–284. https://doi.org/10.1002/1521-3773(20020118)41:2<281::AID-ANIE281>3.0.CO;2-Y.

(132) Coudert, F.-X. Responsive Metal–Organic Frameworks and Framework Materials: Under Pressure, Taking the Heat, in the Spotlight, with Friends. *Chem. Mater.* **2015**, *27* (6), 1905–1916. https://doi.org/10.1021/acs.chemmater.5b00046.

(133) Hazra, A.; Heerden, D. P. van; Sanyal, S.; Lama, P.; Esterhuysen, C.; Barbour, L. J. CO2-Induced Single-Crystal to Single-Crystal Transformations of an Interpenetrated Flexible MOF Explained by in Situ Crystallographic Analysis and Molecular Modeling. *Chem. Sci.* **2019**, *10* (43), 10018–10024. https://doi.org/10.1039/C9SC04043A.

(134) Modrow, A.; Zargarani, D.; Herges, R.; Stock, N. The First Porous MOF with Photoswitchable Linker Molecules. *Dalton Trans.* **2011**, *40* (16), 4217–4222. https://doi.org/10.1039/C0DT01629B.
(135) Schneemann, A.; Bon, V.; Schwedler, I.; Senkovska, I.; Kaskel, S.; A. Fischer, R. Flexible Metal–Organic Frameworks. *Chem. Soc. Rev.* **2014**, *43* (16), 6062–6096. https://doi.org/10.1039/C4CS00101J.
(136) Collings, I. E.; Goodwin, A. L. Metal–Organic Frameworks under Pressure. *J. Appl. Phys.* **2019**, *126* (18), 181101. https://doi.org/10.1063/1.5126911.
(137) Wu, Y.; Kobayashi, A.; Halder, G. J.; Peterson, V. K.; Chapman, K. W.; Lock, N.; Southon, P. D.; Kepert, C. J. Negative Thermal Expansion in the Metal-Organic Framework Material Cu3(1,3,5-Benzenetricarboxylate)2. *Angew. Chem. Int. Ed Engl.* **2008**, *47* (46), 8929–8932. https://doi.org/10.1002/anie.200803925.
(138) Ogborn, J. M.; Collings, I. E.; Moggach, S. A.; Thompson, A. L.; Goodwin, A. L. Supramolecular Mechanics in a Metal–Organic Framework. *Chem. Sci.* **2012**, *3* (10), 3011–3017. https://doi.org/10.1039/C2SC20596C.
(139) DeVries, L. D.; Barron, P. M.; Hurley, E. P.; Hu, C.; Choe, W. "Nanoscale Lattice Fence" in a Metal-Organic Framework: Interplay between Hinged Topology and Highly Anisotropic Thermal Response. *J. Am. Chem. Soc.* **2011**, *133* (38), 14848–14851. https://doi.org/10.1021/ja2032822.
(140) Yang, C.; Wang, X.; Omary, M. A. Crystallographic Observation of Dynamic Gas Adsorption Sites and Thermal Expansion in a Breathable Fluorous Metal-Organic Framework. *Angew. Chem. Int. Ed Engl.* **2009**, *48* (14), 2500–2505. https://doi.org/10.1002/anie.200804739.
(141) Goodwin, A. L.; Kepert, C. J. Negative Thermal Expansion and Low-Frequency Modes in Cyanide-Bridged Framework Materials. *Phys. Rev. B* **2005**, *71* (14), 140301. https://doi.org/10.1103/PhysRevB.71.140301.
(142) Henke, S.; Schneemann, A.; Fischer, R. A. Massive Anisotropic Thermal Expansion and Thermo-Responsive Breathing in Metal–Organic Frameworks Modulated by Linker Functionalization. *Adv. Funct. Mater.* **2013**, *23* (48), 5990–5996. https://doi.org/10.1002/adfm.201301256.
(143) Férey, G.; Serre, C. Large Breathing Effects in Three-Dimensional Porous Hybrid Matter: Facts, Analyses, Rules and Consequences. *Chem. Soc. Rev.* **2009**, *38* (5), 1380–1399. https://doi.org/10.1039/B804302G.
(144) Salles, F.; Ghoufi, A.; Maurin, G.; Bell, R. G.; Mellot-Draznieks, C.; Férey, G. Molecular Dynamics Simulations of Breathing MOFs: Structural Transformations of MIL-53(Cr) upon Thermal Activation and CO2 Adsorption. *Angew. Chem. Int. Ed.* **2008**, *47* (44), 8487–8491. https://doi.org/10.1002/anie.200803067.
(145) Ghoufi, A.; Maurin, G.; Férey, G. Physics Behind the Guest-Assisted Structural Transitions of a Porous Metal−Organic Framework Material. *J. Phys. Chem. Lett.* **2010**, *1* (19), 2810–2815. https://doi.org/10.1021/jz1011274.
(146) Boutin, A.; Coudert, F.-X.; Springuel-Huet, M.-A.; Neimark, A. V.; Férey, G.; Fuchs, A. H. The Behavior of Flexible MIL-53(Al) upon CH4 and CO2 Adsorption. *J. Phys. Chem. C* **2010**, *114* (50), 22237–22244. https://doi.org/10.1021/jp108710h.
(147) Ghoufi, A.; Subercaze, A.; Ma, Q.; Yot, P. G.; Ke, Y.; Puente-Orench, I.; Devic, T.; Guillerm, V.; Zhong, C.; Serre, C.; Férey, G.; Maurin, G. Comparative Guest, Thermal, and Mechanical Breathing of the Porous Metal Organic Framework MIL-53(Cr): A Computational Exploration Supported by Experiments. *J. Phys. Chem. C* **2012**, *116* (24), 13289–13295. https://doi.org/10.1021/jp303686m.

(148) Serre, C.; Bourrelly, S.; Vimont, A.; Ramsahye, N. A.; Maurin, G.; Llewellyn, P. L.; Daturi, M.; Filinchuk, Y.; Leynaud, O.; Barnes, P.; Férey, G. An Explanation for the Very Large Breathing Effect of a Metal–Organic Framework during CO2 Adsorption. *Adv. Mater.* **2007**, *19* (17), 2246–2251. https://doi.org/10.1002/adma.200602645.

(149) Taylor, M. K.; Runčevski, T.; Oktawiec, J.; Bachman, J. E.; Siegelman, R. L.; Jiang, H.; Mason, J. A.; Tarver, J. D.; Long, J. R. Near-Perfect CO2/CH4 Selectivity Achieved through Reversible Guest Templating in the Flexible Metal-Organic Framework Co(Bdp). *J. Am. Chem. Soc.* **2018**, *140* (32), 10324–10331. https://doi.org/10.1021/jacs.8b06062.

(150) Tan, J. C.; Cheetham, A. K. Mechanical Properties of Hybrid Inorganic–Organic Framework Materials: Establishing Fundamental Structure–Property Relationships. *Chem. Soc. Rev.* **2011**, *40* (2), 1059–1080. https://doi.org/10.1039/C0CS00163E.

(151) Chapman, K. W.; Sava, D. F.; Halder, G. J.; Chupas, P. J.; Nenoff, T. M. Trapping Guests within a Nanoporous Metal–Organic Framework through Pressure-Induced Amorphization. *J. Am. Chem. Soc.* **2011**, *133* (46), 18583–18585. https://doi.org/10.1021/ja2085096.

(152) Chapman, K. W.; Halder, G. J.; Chupas, P. J. Pressure-Induced Amorphization and Porosity Modification in a Metal−Organic Framework. *J. Am. Chem. Soc.* **2009**, *131* (48), 17546–17547. https://doi.org/10.1021/ja908415z.

(153) Moggach, S. A.; Bennett, T. D.; Cheetham, A. K. The Effect of Pressure on ZIF-8: Increasing Pore Size with Pressure and the Formation of a High-Pressure Phase at 1.47 GPa. *Angew. Chem. Int. Ed.* **2009**, *48* (38), 7087–7089. https://doi.org/10.1002/anie.200902643.

(154) Chapman, K. W.; Halder, G. J.; Chupas, P. J. Guest-Dependent High Pressure Phenomena in a Nanoporous Metal−Organic Framework Material. *J. Am. Chem. Soc.* **2008**, *130* (32), 10524–10526. https://doi.org/10.1021/ja804079z.

(155) Li, W.; Probert, M. R.; Kosa, M.; Bennett, T. D.; Thirumurugan, A.; Burwood, R. P.; Parinello, M.; Howard, J. A. K.; Cheetham, A. K. Negative Linear Compressibility of a Metal–Organic Framework. *J. Am. Chem. Soc.* **2012**, *134* (29), 11940–11943. https://doi.org/10.1021/ja305196u.

(156) Gagnon, K. J.; Beavers, C. M.; Clearfield, A. MOFs Under Pressure: The Reversible Compression of a Single Crystal. *J. Am. Chem. Soc.* **2013**, *135* (4), 1252–1255. https://doi.org/10.1021/ja311613p.

(157) Yot, P. G.; Boudene, Z.; Macia, J.; Granier, D.; Vanduyfhuys, L.; Verstraelen, T.; Speybroeck, V. V.; Devic, T.; Serre, C.; Férey, G.; Stock, N.; Maurin, G. Metal–Organic Frameworks as Potential Shock Absorbers: The Case of the Highly Flexible MIL-53(Al). *Chem. Commun.* **2014**, *50* (67), 9462–9464. https://doi.org/10.1039/C4CC03853C.

(158) Yot, P. G.; Ma, Q.; Haines, J.; Yang, Q.; Ghoufi, A.; Devic, T.; Serre, C.; Dmitriev, V.; Férey, G.; Zhong, C.; Maurin, G. Large Breathing of the MOF MIL-47(VIV) under Mechanical Pressure: A Joint Experimental–Modelling Exploration. *Chem. Sci.* **2012**, *3* (4), 1100–1104. https://doi.org/10.1039/C2SC00745B.

(159) Voorde, B. V. de; Stassen, I.; Bueken, B.; Vermoortele, F.; Vos, D. D.; Ameloot, R.; Tan, J.-C.; Bennett, T. D. Improving the Mechanical Stability of Zirconium-Based Metal–Organic Frameworks by Incorporation of Acidic Modulators. *J. Mater. Chem. A* **2014**, *3* (4), 1737–1742. https://doi.org/10.1039/C4TA06396A.

(160) Bennett, T. D.; Simoncic, P.; Moggach, S. A.; Gozzo, F.; Macchi, P.; Keen, D. A.; Tan, J.-C.; Cheetham, A. K. Reversible Pressure-Induced Amorphization of a

Zeolitic Imidazolate Framework (ZIF-4). *Chem. Commun.* **2011**, *47* (28), 7983–7985. https://doi.org/10.1039/C1CC11985K.

(161) Ghosh, P.; Colón, Y. J.; Snurr, R. Q. Water Adsorption in UiO-66: The Importance of Defects. *Chem. Commun.* **2014**, *50* (77), 11329–11331. https://doi.org/10.1039/C4CC04945D.

(162) Vandichel, M.; Hajek, J.; Vermoortele, F.; Waroquier, M.; Vos, D. E. D.; Speybroeck, V. V. Active Site Engineering in UiO-66 Type Metal–Organic Frameworks by Intentional Creation of Defects: A Theoretical Rationalization. *CrystEngComm* **2014**, *17* (2), 395–406. https://doi.org/10.1039/C4CE01672F.

(163) Bennett, T. D.; Todorova, T. K.; Baxter, E. F.; Reid, D. G.; Gervais, C.; Bueken, B.; Voorde, B. V. de; Vos, D. D.; Keen, D. A.; Mellot-Draznieks, C. Connecting Defects and Amorphization in UiO-66 and MIL-140 Metal–Organic Frameworks: A Combined Experimental and Computational Study. *Phys. Chem. Chem. Phys.* **2016**, *18* (3), 2192–2201. https://doi.org/10.1039/C5CP06798G.

(164) Yot, P. G.; Yang, K.; Ragon, F.; Dmitriev, V.; Devic, T.; Horcajada, P.; Serre, C.; Maurin, G. Exploration of the Mechanical Behavior of Metal Organic Frameworks UiO-66(Zr) and MIL-125(Ti) and Their NH2 Functionalized Versions. *Dalton Trans.* **2016**, *45* (10), 4283–4288. https://doi.org/10.1039/C5DT03621F.

Chapter II. Molecular Simulation

II.1 Introduction

For the last past decades, the molecular simulations have been used in a variety of domain of science for a better understanding in atomistic scale. Before the development of the modern computers since 1950s, physical sciences were described by the coupling between experiment and theory. From the experimental point of view, the physical observables are measured and can be expressed numerically. From the theoretical point of view, a physical model is applied to represent the physical system. The validation of the model depends on its ability to reproduce the experiments. Usually, the simplifications are considered due to the complexity from realistic system, thus, the physical model is constructed in ideal case.

With the development of the computers, numerical simulation became a powerful tool to probe the physical system and give a better understanding of real-life experiments. First numerical simulation example can be traced back to 1953,[1] carried out by Metropolis and al., which presents a general method of calculating the properties of any substance, based on a predetermined probability distribution. The Monte Carlo (MC) simulation was then elaborated from this work. Lately, in 1957, another MC simulation was carried out in order to compare between numerical simulation and model-derived thermodynamic data experiments, the Lennard Jones potential was examined by Wood and Parker.[2] The MC simulations are free from the restriction of solving Newton's equation of motion, which allow best sampling of the configurational space. MC simulation can probe structure and thermodynamic properties. In the same period, in 1957, Molecular Dynamics (MD) simulation which can reveal the dynamic properties was carried out by Alder and Wainwright.[3] In 1964, Rahman and al. solved the equation of motion for a set of Lennard Jones particles.[4] Within the time, the molecular simulations have advanced to be a reliable tool, researchers started to adopt this powerful tool for a various of applications, a series of study had been carried out. In 1969, MC simulations were performed in order to model liquid water.[5] In 1971, MD simulation were used to study liquid water.[6] Then in 1975, the first study on flexible hydrocarbons were carried out. Between 1982 and 2012, there was a series of simulations focus on the properties of water. Also, the early studies in the crystal formation dedicated to inorganic compounds can be date back to 1990s. Lately, there are many simulations achieved for proteins since 2010. With the advance for the past decades, molecular simulation has significantly improved efficiency and accuracy. As the continuous improvement and the further refinement of the algorithms on the calculation are ongoing, we can estimate that the numerical tool will play a more critical role in the understanding of the complex system. This chapter will deliver the basics of molecular simulation by introducing the fundamental theory and technical aspects.

II.2 Statistical ensembles

II.2.1 Partition function

A partition function describes the statistical properties of a system in thermodynamic equilibrium. For a system contains N particles and the temperature is far away from the 0 K, it can be considered as an approximation of a set of microstates. The total set of the microstates constitutes its 6N dimensional phase space, includes the coordinates of the position r_i and the momentum p_i of the N particles. The notion of phase space will be elaborated in the next subchapter. In classical mechanics, the positions and momentum

vary continuously, so the set of microstates is infinite, the partition function is then expressed as a sum:

$$Z = \frac{1}{h^3}\int exp\big(-\beta H(\boldsymbol{r},\boldsymbol{p})\big)d^3\boldsymbol{r}d^3\boldsymbol{p} \qquad \textit{Eq. II.1}$$

Where h is the Planck constant, β is the reverse temperature defined as $\frac{1}{k_B T}$, $H(\boldsymbol{r},\boldsymbol{p})$ is the Hamiltonian of the system, $\boldsymbol{r}$ is the positions and $\boldsymbol{p}$ is the momentum. For a gas of N identical classical particles in three dimensions, the partition function is:

$$Z = \frac{1}{N!\,h^{3N}}\int exp\left(-\beta\sum_{i=1}^{N} H(\boldsymbol{r_i},\boldsymbol{p_i})\right)d^3\boldsymbol{r}_1 \ldots d^3\boldsymbol{r}_N d^3\boldsymbol{p}_1 \ldots d^3\boldsymbol{p}_N \qquad \textit{Eq. II.2}$$

Where h^{3N} is introduced to make the partition function dimensionless.

II.2.2 Phase space

In classical mechanics, a phase space includes all possible configurations of a system, each configuration corresponds to one unique point in the phase space. The 'configuration' doesn't simply include the positions *r* of all particles in the system, but also their momenta *p*. For a system of N particles, each configuration is defined by the phase space of a 6N dimensional space with the positions *r* and momenta *p* ($\boldsymbol{r}_1,\ldots,\boldsymbol{r}_N, \boldsymbol{p}_1,\ldots,\boldsymbol{p}_N$), the phase space is defined as $\Gamma = (\boldsymbol{r}^{3N},\boldsymbol{p}^{3N})$. At a given time t, the configuration of the system is specified by a unique point in the phase space, with the evolution of time, the point can trace a trajectory over time.

II.2.3 Boltzmann's probability

The Maxwell-Boltzmann distribution is a probability distribution that gives the probability of a certain state as a function of that state's energy and temperature of the system where the distribution is applied. The expression for the Boltzmann probability is:

$$P_i \propto exp(-\beta\varepsilon_i) \qquad \textit{Eq. II.3}$$

Where P_i is the possibility of the system in state *i*, ε_i represents the energy of this state. and the partition function Z is expressed as:

$$Z = \frac{1}{N!\,h^{3N}}\int exp\left[-\beta H\big(\boldsymbol{r_1},\ldots,\boldsymbol{r_N},\boldsymbol{p_1},\ldots,\boldsymbol{p_N},\big)\right]d^3\boldsymbol{p_1}\ldots d^3\boldsymbol{p_N}d^3\boldsymbol{r_1}\ldots d^3\boldsymbol{r_N} \qquad \textit{Eq. II.4}$$

Where *N* represents the number of all accessible states. The Maxwell-Boltzmann distribution is often used to describe the distribution of particles with energy states accessible. In molecular dynamics simulation for example, without providing initial velocities or forces applied for each particle, the initial velocities will be taken at random from Maxwell-Boltzmann distribution.

II.2.4 Ensemble average

There are usually a large number of particles present in a physical system, in the magnitude of mol. Therefore, the macroscopic properties of a system, such as pressure, temperature and volume etc, is difficult to be obtained from microscopic characteristics of each particle. However, most of the macroscopic observables of a system are not sensitive to microscopic details of each particle, thus the macroscopic properties can be collectively calculated. The collection of the all the possible systems with different microscopic states but lead to a common set of macroscopic values is an ensemble. The ensemble average is a very important concept in statistical mechanics, it is defined as the average value taken over a large number of replicas of the system considered simultaneously. The ensemble average and its operational expression depend on the system's ensemble.

a) Classical statistical mechanics

For classical systems in thermal equilibrium with the environment, the partition function Z is expressed as:

$$Z = \iint exp\,[-\beta H(\boldsymbol{r}^N, \boldsymbol{p}^N)]\, d\boldsymbol{r}^N d\boldsymbol{p}^N \qquad \textit{Eq. II.5}$$

The ensemble average Q is expressed as:

$$< Q > = \frac{\iint Q exp\,[-\beta H(\boldsymbol{r}^N, \boldsymbol{p}^N)]\, d\boldsymbol{r}^N d\boldsymbol{p}^N}{Z} \qquad \textit{Eq. II.6}$$

where $Q(\boldsymbol{r}^N, \boldsymbol{p}^N)$ is the observable which can be expressed as a function of the positions $\boldsymbol{r}$ and the momenta $\boldsymbol{p}$.

The ensembles are defined by a series of parameters: the number of particles N, the pressure P, the volume V, the temperature T, the total energy E, etc. Only the ensembles which were used in this work are presented here.

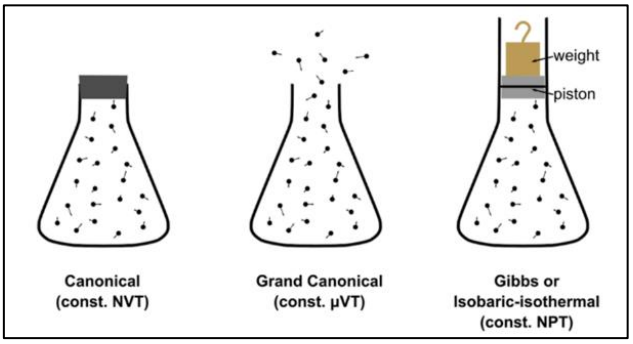

Figure II.1 *Illustration of different statistical ensembles: canonical, grand canonical, isobaric-isothermal ensemble.*

b) *Canonical ensemble: NVT*

This ensemble maintains a fixed temperature T and volume V as well as the number of particles N. This ensemble describes a closed system with no exchange of particles with

the external and a thermostat is in contact with the system to maintain the temperature. The Boltzmann's probability P $(\boldsymbol{r}^N, \boldsymbol{p}^N)$, can be expressed as:

$$P_{NVT}(\boldsymbol{r}^N, \boldsymbol{p}^N) = \frac{exp\big(-\beta H(\boldsymbol{r}^N, \boldsymbol{p}^N)\big)}{\int\int exp\big(-\beta H(\boldsymbol{r}^N, \boldsymbol{p}^N)\big) d\boldsymbol{r}^N d\boldsymbol{p}^N} = \frac{exp\big(-\beta H(\boldsymbol{r}^N, \boldsymbol{p}^N)\big)}{h^N N!\, Z(N,V,T)} \qquad \textit{Eq. II.7}$$

Where h is the Planck's constant, for the classical discrete system, the partition function Z is expressed as:

$$Z(N,V,T) = \frac{1}{h^N N!}\int\int exp(-\beta H(\boldsymbol{r}^N, \boldsymbol{p}^N)) d\boldsymbol{r}^N d\boldsymbol{p}^N \qquad \textit{Eq. II.8}$$

With $H(\boldsymbol{r}^N, \boldsymbol{p}^N)$ represents the Hamiltonian that describes these N particles, which is the sum of the total potential energy U and the total kinetic energy K. $H(\boldsymbol{r}^N, \boldsymbol{p}^N) = U(\boldsymbol{r}^N) + K(\boldsymbol{p}^N)$.With the definition of the ensemble average, a physical quantity Q can be expressed by:

$$< Q >_{NVT} = \frac{\int\int drdp\ exp(-\beta H(\boldsymbol{r}^N, \boldsymbol{p}^N)) Q}{\int\int drdp\ exp(-\beta H(\boldsymbol{r}^N, \boldsymbol{p}^N))} \qquad \textit{Eq. II.9}$$

c) *Isothermal-isobaric ensemble: NPT*

This ensemble maintains a fixed temperature T and pressure P as well as the number of particles N. This ensemble is well suited and has an important role in the molecular dynamics simulation to reproduce the normal laboratory conditions. Note that the volume can vary isotropically or anisotropically, which depends on the parameters of applied pressure as illustrated in Figure II.1. The probability to find a configuration throughout the positions and momenta can be written as:

$$P_{NPT} = \frac{exp(-\beta(H(\boldsymbol{r}^N, \boldsymbol{p}^N) + pV))}{V h^N N!\, Z(N,P,T)} \qquad \textit{Eq. II.10}$$

The partition function $Z\ (N, P, T)$ is:

$$Z(N,P,T) = \frac{1}{h^N N!\, V_0}\int dV \int exp(-\beta H(\boldsymbol{r}^N, \boldsymbol{p}^N, V) + PV) d\boldsymbol{r}^N d\boldsymbol{p}^N \qquad \textit{Eq. II.11}$$

Where V_0 is the unit cell volume.

d) *Grand canonical ensemble: μVT*

A grand canonical ensemble is also called μVT ensemble, it is used to represent the possible states of a system of particles in thermodynamic equilibrium with reservoirs. The system is open in the term that energy and particles exchange with a reservoir is possible, so the total energy and the total number of particles of the system can be varied. The partition function for each distinct microstate can be expressed as:

$$Z(\mu,V,T) = \sum_{N=0}^{\infty} \int \frac{d\boldsymbol{r}^N d\boldsymbol{p}^N}{h^N N!} exp\left(-\beta(H(\boldsymbol{r}^N,\boldsymbol{p}^N) - \mu N)\right) \qquad \textit{Eq. II.12}$$

Where μ represents the chemical potential, N represents the number of particles and E represents the total energy of the microstate. By using this ensemble, we are able to reproduce the adsorption isotherm, it describes quantitatively the adsorption of a gas by a porous material at a fixed temperature as a function of pressure. The adsorption isotherms curve reflects the adsorbate-adsorbent interactions. There are six types of isotherms that have been classified by the International Union of Pure and Applied Chemistry (IUPAC) as illustrated in Figure II.2.[7,8]

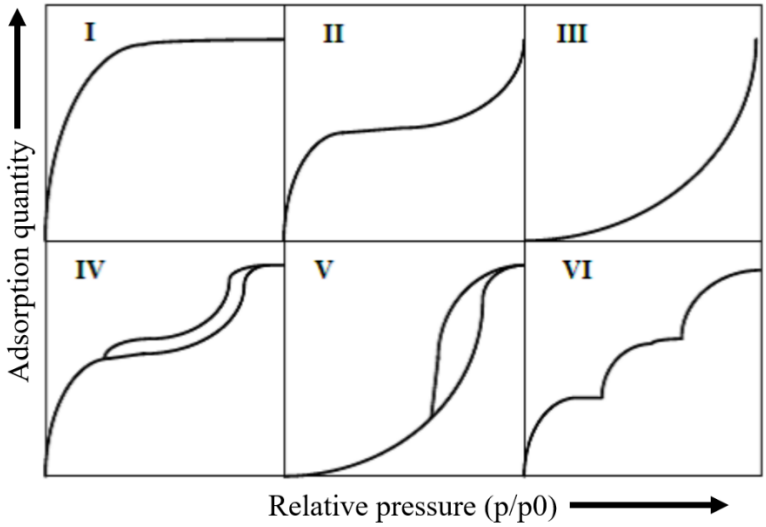

Figure II.2 *The classification of 6 types of adsorption isotherms according to IUPAC.*

The six types of adsorption isotherm are characteristic of adsorbents that are microporous (type I), nonporous or macroporous (types II, III, and VI) and mesoporous (types IV and V). In the case when the pore diameters of an adsorbent are narrow or when a strong adsorbate-adsorbent interaction is present, the adsorption isotherm is the type I. As for the Type II adsorption isotherms, 3 phases of the curve reflect the formation of a layer of adsorbed molecules whose thickness increases when the relative pressure increases. The adsorbed phase condenses at the end when the relative pressure reaches the saturated vapor pressure. For the type III, this specific curvature in the beginning of the adsorption isotherm is due to the adsorbent / adsorbate interactions are weaker than adsorbate / adsorbate interactions. The type IV adsorption isotherm has the same curve for the low relative pressure, at higher relative pressure, the capillary condensation occurs which resulting adsorption - desorption a hysteresis. The same reasoning is applied to the type V which is similar to type III. Type VI adsorption isotherm has a step-like behavior, it reflects a successive formation of layers on the surface of the adsorbent with the increase of relative pressure. It is worth to mention that the flexibility of certain MOFs could have a huge impact on the adsorption isotherm. For example, Co(BDP) is reported to exhibits a step like adsorption isotherm upon N_2 adsorption,[9] upon adsorption or desorption, Co(BDP) passes through 5 distinguished phases as illustrated in Figure II.3.

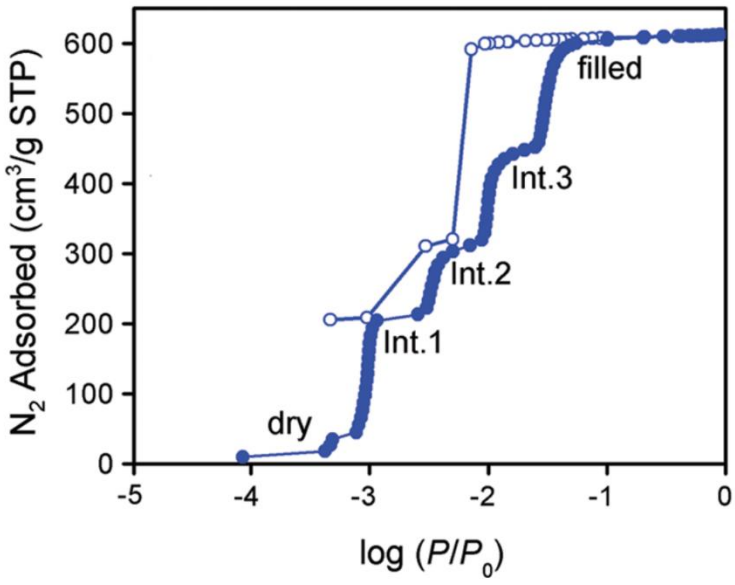

Figure II.3 *N_2 adsorption isotherm (bottom) measured at 77 K in Co(BDP), indicating the five pressure-dependent phases. Filled and empty symbols represent adsorption and desorption, respectively. Figure adapted from the Ref.*[10]

II.3 Molecular simulation

Thermodynamics and statistical mechanics create a bridge between the experimental macroscopic observations and the microscopic behavior of the simulated system. During the thesis, two molecular simulations methods were used for the simulation at molecular level, which are Molecular Dynamic and Monte Carlo simulation.

II.3.1 Molecular Dynamic Simulation

The concept of MD simulation consists in the numerical time-dependent integration of the Newtonian motion equations of the particles as

$$\boldsymbol{F_i} = m_i \boldsymbol{a_i}(t) = m_i \frac{d\boldsymbol{v_i}(t)}{dt} = m_i \frac{d^2\boldsymbol{r_i}(t)}{dt^2} = -\frac{\partial}{\partial \boldsymbol{r_i}} U \qquad \textit{Eq. II.13}$$

Where $\boldsymbol{F}$ represents the force applied on the particles, $\boldsymbol{v}_i$, m_i and $\boldsymbol{r}_i$ represent the velocity, the mass and the position of atom i respectively. U is the potential energy of the system. The interactions between atoms and molecules can be modelled via the potential energy by a set of empirical potential functions, which will be explained later. The numerical resolution can be performed from the Leapfrog algorithm, Beeman algorithm, Verlet algorithm and etc. The integration algorithms consist of discretizing the first or second order differential equations. A good integrator shall provide relatively good numerical stability and accuracy, and also a good compromise between the accuracy and the computational effort. Velocity Verlet algorithm, in this point of view, meets the argument and was used during the thesis. Based on a Taylor development, the positions of each atom at $t + \delta t$ is expressed as:

$$\boldsymbol{r_i}(t+\delta t) = \boldsymbol{r_i}(t) + \boldsymbol{v_i}(t)\,\delta t + \frac{\boldsymbol{F_i}(t)}{2m_i}\delta t^2 + O(\delta t^3) \qquad \textit{Eq. II.14}$$

The position of each atom at t is expressed as:

$$\boldsymbol{r_i}(t) = \boldsymbol{r_i}(t+\delta t) - \boldsymbol{v_i}(t+\delta t)\,\delta t + \frac{\boldsymbol{F_i}(t+\delta t)}{2m_i}\delta t^2 + O(\delta t^3) \qquad \textit{Eq. II.15}$$

the velocity can be then written as

$$\boldsymbol{v_i}(t+\delta t) = \boldsymbol{v_i}(t) + \frac{\boldsymbol{F_i}(t) + \boldsymbol{F_i}(t+\delta t)}{2m_i}\delta t^2 + O(\delta t^3) \qquad \textit{Eq. II.16}$$

This algorithm is very commonly used in Molecular Dynamic simulation because of its good numerical stability and performance/cost ratio.

II.3.2 Monte Carlo Simulation

Unlike Molecular Dynamic simulation, The Monte Carlo (MC) simulation generates random configuration using Metropolis algorithm to determine to accept/reject new configuration. This algorithm is a Markovian and is not time dependant. Each configuration is generated by a random trial move of atom or molecules, for example, the translation, rotation, insertion/deletion and etc. The MC moves will be explained in detail for the next chapter. The criteria of Metropolis method are used to ensure that the probability of obtaining a configuration is equal to its Boltzmann factor $e^{\frac{-U}{kT}}$. The low energy configurations are generated with higher probability than configurations with higher energy. If the energy of the new configuration is lower than the previous configuration, then the new configuration will be accepted. If the energy of the new configuration is higher than the previous configuration, then the Boltzmann factor, which is the ratio of probabilities of two configurations which depends only on the energy will be calculated:

$$\frac{p_i}{p_j} = e^{\frac{-\Delta U}{k_B T}} \qquad \textit{Eq. II.17}$$

The Boltzmann factor will be compared with a random number ranging from 0 and 1. If the Boltzmann factor is higher than the random generated number, then the new configuration will be accepted, in other case, the new configuration will be rejected, and the previous configuration is conserved for the next iteration. The measurable value Q can be calculated as:

$$< Q >= \frac{1}{N_{config}} \sum_{i}^{N_{config}} Q \qquad \textit{Eq. II.18}$$

The value Q is obtained by averaging the values over the number of configurations N_{config}.

II.4 Ergodic hypothesis

Molecular simulations enable the possibility to simulate the behaviour of the atoms or molecules in the scale and calculate the macroscopic properties thanks to statistical mechanics. The MD trajectory is described in phase space as [r^N(t), p^N(t)]. The measurement of a physical value from the MD simulation is then obtained as an arithmetic average. It is possible to calculate the value of *Q(t)*, as well as the experimental observable that can be regarded as the time average of *Q(t)* expressed as:

$$Q_{obs} = < Q(t) > = \lim_{\tau} \frac{1}{\tau} \int_{0}^{\tau} Q\big(\Gamma(t)\big)\, dt \qquad \textit{Eq. II.19}$$

Where τ is the observation time, and the brackets indicate the average value. Statistical mechanics calculate all macroscopic observable as averages over phase trajectories as well as averages over an ensemble of systems. As consequence, it is possible to calculate a macroscopic quantity Q by averaging directly over the whole of the thermodynamic ensemble, the ensemble average $<Q>_{ensemble}$ is defined as below:

$$< Q >_{ensemble} = \frac{1}{Z} \int Q(r,p)\, e^{-\beta E(r,p)} dr dp \qquad \textit{Eq. II.20}$$

Here, the partition functions *Z* are functions of the volume occupied by the system in phase space, this signifies the number of accessible microstates to the system in a given ensemble. E is the energy of the microstate. In other words, by considering an infinite number of configurations and an infinite sampling time, we have:

$$< Q >_{obs} = < Q >_{ensemble} = < Q(t) > \qquad \textit{Eq. II.21}$$

Eq. II.21 is ergodic hypothesis that indicates that any experimental observable is based on a long time on a molecular time scale, leading to the conclusion that time average equal to ensemble averages.

II.5 Force Field

II.5.1 Potential

The previous chapter highlighted the importance to know the energy to carry out the simulation. To be able to describe the energy of the system, a force field (FF) is required. A force field is an empirical function with a set of parameters which describe the potential.

Since 1950s when the first MC and MD simulations of model liquids carried out by Metropolis et al.,[1] a rapid growth in the computational study brought the development of force field into a new level. Up to date, it exists many force fields, such as AMBER,[11] COMPASS,[12] CHARMM,[13] DREDING,[14] UFF,[15] OPLS,[16] TraPPE, [17,18] and etc. Different force field has different complexity with different applicability and limitations. To carry out a reliable simulation, it is crucial to choose an appropriate force field. As said, there are many force fields available, however, a common force field for molecular simulation is composed of intra- and inter-molecular forces. A typical expression for an FF is expressed as:

$$U = \underbrace{(U_{bonds} + U_{angles} + U_{torsion})}_{\text{Intramolecular terms}} + \underbrace{(U_{vdw} + U_{elec})}_{\text{Intermolecular terms}} \qquad \textit{Eq. II.22}$$

Where U represents the potential energy of the system. U_{bonds} simulates the bonds of two atoms, U_{angles} contributes to the valence angle, $U_{torsion}$ contributes to torsional potentials. U_{vdw} and $U_{torsion}$ model van der Waals and electrostatic interactions respectively. The detailed mathematic formula of the interactions will be explained.

a) Intramolecular terms

Regarding to the bond contribution the length of the bond between two atoms oscillates around an average value. The harmonic potential is usually being used to describe the bond potential as:

$$U_{bond} = \sum_{bonds} K_r(r - r_0)^2 \qquad \textit{Eq. II.23}$$

Where K_r is the force constant in kJ mol / Å^{-2}, r is the distance between two atoms in Å, r_0 is the equilibrium bond length in Å, the schematic representation is as shown in Figure II.4.

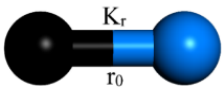

Figure II.4 *Illustration of the intermolecular bond potential, where K_r represents the force constant of the bond, and r_0 represents the equilibrium bond length.*

Similarly, in valence angle potential, the angle formed between three atoms is not constant and oscillate around the equilibrium value. The valence angle potential can be described as harmonic form, the mathematical formula is expressed as:

$$U_{angles} = \sum_{angles} K_\theta(\theta - \theta_0)^2 \qquad \textit{Eq. II.24}$$

Where K_θ represents the force constant of the angle in kJ/mol/°, θ is the valence angle between three atoms in degrees, θ_0 is the equilibrium angle in degrees, as illustrated in Figure II.5.

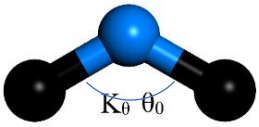

Figure II.5 *Illustration of the intermolecular bend potential, where K_θ represents the force constant of the angle, and θ_0 represents the equilibrium angle.*

The last element of intramolecular term is torsional potential, or dihedral potential which refers to 4 atoms, generally it is expressed as a cosine series expansion. The mathematical formula is expressed as:

$$U_{torsion} = \sum_{angles} \frac{V_n}{2}[1 + cos(n\phi - \gamma)] \qquad \textit{Eq. II.25}$$

Where V_n is the Fourier constant which correspond to the magnitude of torsion, n is the periodicity of the torsional potential, ϕ is the torsion angle between the plane formed by 4 atoms in degree, and γ is the phase factor, as illustrated in Figure II.6.

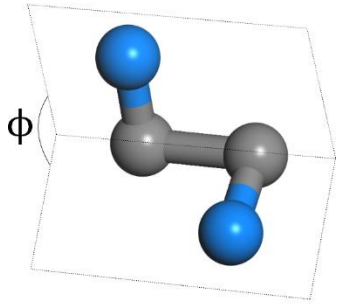

Figure II.6 *Illustration of the intermolecular dihedral potential, where ϕ is the torsion angle between the plane formed by 4 atoms.*

Note the relation to define the different potentials is not limited to one type, there are many others, depends on the force field and approximation. As an example, the valence angle can be described from a cosine form as:

$$U_{angles}^{Cos} = A[1 + cos(m\theta - \delta)] \qquad \textit{Eq. II.26}$$

Where m is a potential parameter and δ is the phase factor.

b) *Intermolecular terms*

i) *The Lennard-Jones potential*

Usually, intermolecular terms consist of mainly pairwise interactions, van der Waals and electrostatic potentials. Intermolecular terms are considered between all pairs of atoms of different molecules and between atoms which are separated by at least three bonds in the same molecule. The van der Waals potential functions is often modelled from the Lennard-Jones (LJ) potential.

$$U_{VDW} = \sum_{i}\sum_{j>i} 4\epsilon_{ij}\left[\left(\frac{\sigma_{ij}}{r_{ij}}\right)^{12} - \left(\frac{\sigma_{ij}}{r_{ij}}\right)^{6}\right] \qquad \textit{Eq. II.27}$$

This potential includes a repulsion term (r^{-12}) at short distances and an attractive term (r^{-6}) at long distance. To avoid expensive calculation, a cut-off radius is considered. It gives a limit on the calculation of the interactions, beyond the cut-off distance (r_c), the potential is neglected. In the mathematical expression, r is the distance between two particles in question, σ represents the collision parameter, at this distance, the intermolecular potential between two particles is zero while ϵ corresponds to the strength of the interaction. The LJ potential is short ranged and at long range, it tends to be 0. The schematic representation of LJ potential is in Figure II.7.

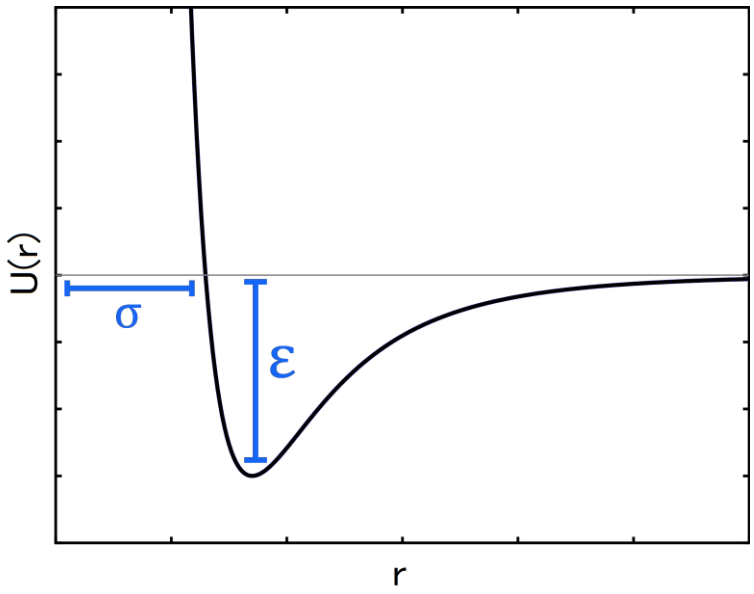

Figure II.7 *Schematic representation of Lennard-Jones potential, where σ is collision parameter and ϵ represents the strength of the interaction.*

The LJ potential parameters for the atoms with different types are calculated using Lorentz-Berthelot mixing rules. For atom A and atom B, their LJ parameters are:

$$\sigma_{AB} = \frac{\sigma_{AA} + \sigma_{BB}}{2} \qquad \epsilon_{AB} = \sqrt{\epsilon_{AA}\epsilon_{BB}} \qquad \textit{Eq. II.28}$$

ii) The electrostatic interactions

The electrostatic potential refers to the interactions between two electrically charged particles. Compared to the LJ potential, the electrostatic potential converges slow, and at the long-range electrostatic interaction cannot be neglected. The relation allowing us to calculate it as:

$$U_{elec} = \frac{1}{4\pi\epsilon_0}\sum_{ij}\frac{q_i q_j}{|r_{ij}|} \qquad \textit{Eq. II.29}$$

Where ϵ_0 (8.85E-12 $C^2J^{-1}mol^{-1}$) is the vacuum permittivity, q_i and q_j are the partial charge of two particles and r_{ij} is the separation distance. The sum is applied to all atomic pairs. As the matter of the fact that all atoms are under the periodic boundary conditions (PBC), which will be explained later in next subchapter. The simulation box is described by L_x, L_y and L_z. We can suppose the simulation box is cubic, which leads to $L_x = L_y = L_z = L$. As we have a pseudo infinite system with PBC, for a certain atom q_i with the corresponding location r_i, its images can be found at $r_i + n_xL + n_yL + n_zL$, with the same charge q_i, where n_x, n_y and n_z are arbitrary integers. With the consideration of PBC, the electrostatic potential can be rewritten as:

$$U_{elec} = \frac{1}{4\pi\epsilon_0}\sum_{n}\sum_{ij}\frac{q_i q_j}{|r_{ij} + nL|} \qquad \textit{Eq. II.30}$$

The above equation is the sum over all ij pairs, which can also be rewritten as the sums over all atoms:

$$U_{elec} = \frac{1}{2}\frac{1}{4\pi\epsilon_0}\sum_{n}\sum_{i}\sum_{j}\frac{q_i q_j}{|r_{ij} + nL|} \qquad \textit{Eq. II.31}$$

Where the $\frac{1}{2}$ term is to avoid the double-counting. There are different ways of proceeding this sum in the simulation with truncation methods, for example, spherical truncation, generalized reaction field, Wolf summation, Ewald summation.[19,20] The latter method, i.e., Ewald summation, will be discussed as it is the most commonly used in numerical simulation. Ewald summation rewrites the long-range interactions as the sum of the interaction energies of each charge of the primitive unit cell with all the periodic images. In order to improve the convergence, the function $\frac{1}{r}$ is converted into two series, as shown below in equation:

$$\frac{1}{r} = \frac{\phi(r)}{r} + \frac{1-\phi(r)}{r} \qquad \textit{Eq. II.32}$$

The function $\phi(r)$ need to be defined in a way that satisfy the rapid variations from 1 to *r* at short range and also the slow decay at long range of *r*, as the equation shown below:

$$\phi(r) \stackrel{\text{def}}{=} \phi_s(r) + \phi_l(r) \qquad \textit{Eq. II.33}$$

Where $\phi_s(r)$ represents the short-range term which converges rapidly in real space and $\phi_l(r)$ represents the long-range term which converges rapidly in Fourier space. The method assumes that the short-range term can be summed easily, and the problem becomes the sum for long-range term. Here, the most commonly used form for long-range term is a Gaussian distribution.

$$f_{gauss}(r) = \frac{z_{ia}\alpha^3}{\pi^{\frac{3}{2}}} exp(-\alpha^2 r^2) \qquad \textit{Eq. II.34}$$

Where α represents the gaussian distribution width. α is an empirical value. The total screened potential is calculated by summing over all the particles in the unit cell and all the periodic images in the real space of the images. The value of α which given by DLPOLY program is $\alpha = 3.2/(l_{min}/2)$, where l_{min} represents the smallest side length of the simulation box. The Ewald summation can be then expressed as:

$$U_{TOT} = U_S + U_L - U_{self}$$

$$U_{TOT} = \frac{1}{4\pi\epsilon_0}\frac{1}{2}\sum_n\sum_i\sum_j \frac{q_i q_j}{|r_i - r_j + nL|} erfc\left(\frac{|r_i - r_j + nL|}{\sqrt{2}\sigma}\right) + \frac{1}{2\epsilon_0}\sum_{k\neq 0}\frac{e^{\frac{-\sigma^2 k^2}{2}}}{k^2}|S(k)|^2 - \frac{1}{4\pi\epsilon_0}\frac{1}{\sqrt{2\pi}\sigma}\sum_{i=1}^{N} q_i^2 \qquad \textit{Eq. II.35}$$

Where $erfc\left(\frac{|r_i - r_j + nL|}{\sqrt{2}\sigma}\right)$ represents a complementary error function that tends to 0 with the increase of r. In summary, the Ewald summation method replace a set of point charges by a set of screened charges plus a set of Gaussian distribution. The interaction of the screened charges is summed in real space, the Gaussian distribution is summed in Fourier space.

II.5.2 Periodic Boundary Condition (PBC)

Usually, the simulation box is in general a closed system where atoms could come close to the boundary and eventually leave the box. It is obvious that the constraints on the boundary of the simulation need to be considered. In order to overcome this problem, the periodic boundary conditions are applied. This method consists of duplicating the simulation box in three directions, resulting a pseudo infinite system, so that the atoms inside the simulation box can interact with its images. The periodic image in each duplicated box also conserves the exactly the same moves. There are no walls at the boundary, for example, a particle which move through the top side extremity of the box will enter from the bottom side, as shown in the Figure II.8:

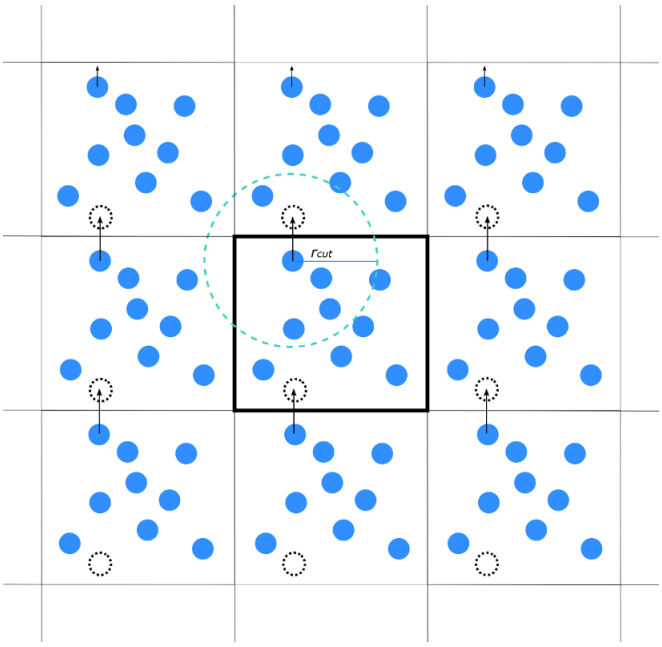

Figure II.8 *2D periodic system. The simulation boxes contain 9 atoms, their duplicated images contain the same atoms, the positions and movements are conserved.* r_{cut} *represents the cut off distance. The black dotted cycle is the ongoing position of the highlighted particle.*

With this approach, the density of the box is conserved and the problem with the boundary can be solved. Note that the simulation box is not limited to cubic, it is possible to use other types, such as rhombic, monoclinic and etc. As the central box is replicated for n times, the positions for one particle i can be represented as $r_i + nL$, where L represents the length of the box. The potential energy for a box contains n atoms can be represented as:

$$U(r_1, r_2, \ldots, r_n) = \sum_{i<j} U(r_{ij}) + \sum_{n} \sum_{i<j} U(|r_i - r_j + nL|) \qquad \textit{Eq. II.36}$$

It is obvious that it will take much computational effort and not realistic to include the interaction of each particle with all the images because the system is infinite, that's why a cut-off distance need to be considered, which means the interactions are limited to the radius of cut-off distance. The cut-off radius is indicated in Figure II.8 as dashed circle. In general, the cut-off distance obeys:

$$Ur_{cut-off} < \frac{L}{2} \qquad \textit{Eq. II.37}$$

With this approximation, we can still have a good compromise between the accuracy and the computational effort.

II.6 Hybrid Osmotic Monte Carlo Simulation

In this work, Hybrid Osmotic Monte Carlo (HOMC) simulation,[21] was adopted to investigate the adsorption and separation of hydrocarbon gas into the MOFs. The previous introduced simulation methods, molecular dynamics (MD) and grand canonical Monte Carlo (GCMC) simulations are not able to follow a guest-assisted structural phase transition, either the guest-assisted flexibility. The GCMC simulations allow a fluctuation of the guest molecules for a given chemical potential while generally considering the MOFs rigid. This approach can be used in a first approximation to calculate the quinary mixture adsorption isotherms of hexane isomers in MIL-140B,[22] or, another example, the CO_2 adsorption isotherms for both rigid narrow pore (Np) and large pore (Lp) forms of MIL-53(Cr). However, in order to rigorously reproduce the experimental conditions by considering the flexibility of the MOFs, this methodology is limited. To overcome such bottleneck, the hybrid osmotic Monte Carlo (HOMC) was adopted by coupling MD and GCMC simulation. To do so, there are two possible strategies. First strategy, the implementation of a GCMD method with osmotic ensemble ($\mu N_1 \sigma T$), [23,24] where μ represents the chemical potential of the guest molecules, N_1 represents the number of the MOFs or adsorbent, σ represents the target determinant of the anisotropic pressure tensor, and T represents the temperature. This method has been implemented to capture the dynamical properties such as diffusivity, viscosity and permeability.[25,26] Second strategy, create a MD move, which can be carried out in NVT or preferentially $N\sigma T$, in the Markov chain in a HOMC route. This enables the flexibility of the framework, which is crucial to capture guest-assisted structural changes. This method able to explore the configuration space efficiently. The latter strategy was chosen to perform the adsorption inside the flexible MOFs. Its working flow in detail is shown as in Figure II.9:

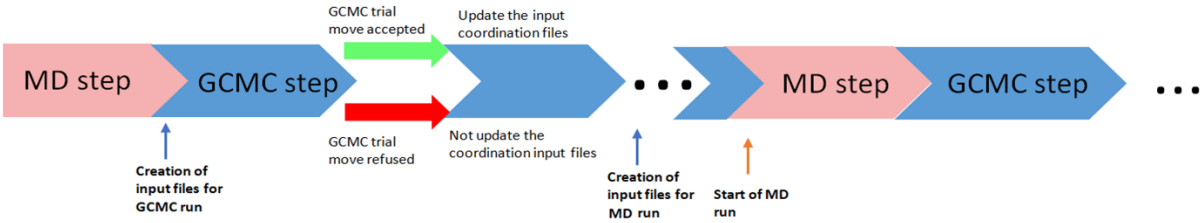

Figure II.9 *Illustration of how a HOMC simulation works. One HOMC step include MD -> MC -> MD steps in sequence.*

One HOMC run consists of many cycles, each cycle contains multiple HOMC step, and one HOMC step include one MD simulation run and one MC simulation run. The program starts with a MD simulation, with sufficient timesteps, the structure will reach equilibrium thermodynamically and energy will be converged. At the end of the MD simulation, the program converts the output files from MD simulation to the input files for MC simulation. This program is a home code that is developed in the IPR of the university of Rennes 1. Then an appropriate number of steps for MC simulation shall be considered in order to explore the configuration phase. A homogenization of the MC and MD partition functions was applied in order to ensure the coherence between the configuration and momentum spaces and to get a reliable probability of acceptance. At the end of MC simulations, this homogenization of partition function allows to determine if the newly generated configuration is accepted or not. If the configuration is accepted, the output file of MC simulations will be converted to input file for the next MD simulation, otherwise the

configuration will be conserved. Depends on the system, the computation time can vary. For our system involved with MOFs, usually supercell and guest molecules. One HOMC step is expected to take up to 200 minutes. The general expressions for MC and MD partition functions are shown as below:

$$Q_{\mu N_1 \sigma T}^{MC} = \sum_{i=1}^{i} \sum_{N=1}^{\infty} exp(\beta \mu N) \left[\frac{{q_i}^{N_i}}{N_i!}\right] \int |J^i|^{\frac{1}{2}} exp\big(-\beta(U(\boldsymbol{r}^N, \boldsymbol{p}^N) + [\sigma]V)\big) d\boldsymbol{r}^N dV \qquad \textit{Eq. II.38}$$

$$Q_{\mu N_1 \sigma T}^{MD} = \sum_{i=1}^{2} \sum_{N=1}^{\infty} exp(\beta \mu N) \int exp\big(-\beta(H(\boldsymbol{r}^N, \boldsymbol{p}^N) + [\sigma]V)\big) d\boldsymbol{r}^N dp^N dV \qquad \textit{Eq. II.39}$$

$$H(\boldsymbol{r}^N, p^N) = U(\boldsymbol{r}^N) + K(\boldsymbol{p}^N) + K'(\omega^{N_i}) \qquad \textit{Eq. II.40}$$

$$U(\boldsymbol{r}^N) = U^{INTRA}(\boldsymbol{r}^N) + U^{INTER}(\boldsymbol{r}^N) \qquad \textit{Eq. II.41}$$

Where $K'(\omega^{N_i}) = 0$ and $J^2 = 1$. β represents the reverse temperature, ω^{N_i} represents the angular velocity of the guest molecules. *U* and *H* represent the potential energy and Hamiltonian respectively. *K* and K' are translational and rotational kinetic energies respectively. U^{INTRA} and U^{INTER} represent intramolecular and intermolecular energies respectively.

As MC simulation is not time dependant. Its partition function has only the potential energy. For MD simulation, the total Hamiltonian needs to be considered. *N* represents the total number of atoms in the system which is the sum of the adsorbates and the framework, i represents the labels for the framework and guest molecules respectively. The total partition functions ${q_i}^{Ni}$ is shown as below:

$$q_i = {q_i}^{rot} {q_i}^{trans} {q_i}^{c} \qquad \textit{Eq. II.42}$$

Where rot, trans, and c represent the rotational, translational and constraints Jacobian constraint contributions. It is possible to have other contribution, such as internal rotation for long molecules, vibration, nuclear spin etc. A decomposition of the kinetic and the potential energy terms will not be possible because $\boldsymbol{r}^N$ and $\boldsymbol{p}^N$ are dependent. We need to considerate the determinant of the constraint matrix *J*. The partition function of MC is coherent with the reference for the osmotic ensemble.[27] There are other contributions in the MC partition function which can be considered in order to ensure the coherence between MC and MD part, i.e. translational, rotational, inter-rotational for long adsorbates, vibration and etc. We can replace q_i by these terms and we obtain the equation below:

$$Q_{\mu N_1 \sigma T}^{MC} = \sum_{i=1}^{i} \sum_{N=1}^{\infty} Z_i^t Z_i^r exp(\beta \mu N) \int Z_i^c exp\big(-\beta(U(\boldsymbol{r}^N, \boldsymbol{p}^N) + [\sigma]V)\big) d\boldsymbol{r}^N dV \quad \textit{Eq. II.43}$$

With $Z_i^t = \frac{V^{N_i}}{N_i! \Lambda^{3N_i}}$, $Z_2^r = \left(\frac{4\pi I_2 k_b T}{h}\right)^{\frac{N}{2}}$ and $Z_1^c = \frac{|J_1|^{\frac{1}{2}}}{|J_1^0|^{\frac{1}{2}}}$. Here, $Z_i^C = 1$ and we take the example of i = 2. The probability to accept the MD trial move is shown as below equation:

$$\rho_{\mu N_1 \sigma T}^{MC} = \frac{Z_i^t Z_i^r exp(\beta \mu N) exp\big(-\beta(U(\boldsymbol{r}^N) + [\sigma]V)\big)}{Q_{\mu N_1 \sigma T}^{MC}} \quad \textit{Eq. II.44}$$

The detailed balance is expressed as:

$$\pi(o \to n) = min\left(1, \frac{\rho(n)\alpha(o \to n)}{\rho(o)\alpha(n \to o)}\right) \quad \textit{Eq. II.45}$$

Where $\alpha(n \to o)$ represents the probability to generate a new trial configuration (n) from a previous old configuration (o). The translational and rotational contributions don't have effect in this acceptance function. In order to consider the rotational and Jacobian part at MD part, the detailed balance is then change to:

$$\pi(o \to n) = min\left(1, \left(\frac{V_n}{V_0}\right) exp(-\beta\big(\Delta U_{o\to n}(\boldsymbol{r}^N) + \Delta K_{o\to n}(\boldsymbol{p}^N) + \Delta K'_{o\to n}(\omega^{N_2}) + [\sigma]\Delta V_{o\to n} + \Delta G_{o\to n}(\boldsymbol{r}^{N_1}, \boldsymbol{p}^{N_1})\big)\right) \quad \textit{Eq. II.46}$$

Where $\Delta V_{o\to n}$ represents the volume variation between old configuration (o) and the new configuration (n), this volume variation is produced during MD move. For the trial insertion/deletion move, the insertion and orientation bias were considered. This method determines in a first place an appropriate location for the center of mass of the inserted guest molecules by *n* test insertions of a Lennard-Jones particle, considering only the *LJ* interactions. Then at the second place, m orientations are being considered for the selected appropriate location, and the electrostatic and LJ interactions are calculated. Finally, we obtain the probability of accepting the insertion and deletion as the expressions below:

$$\pi(N_2 \to N_2 + 1) = min\left(1, \frac{V}{\Lambda^3 (N_2 + 1)} \frac{4\pi^2 I_2 k_b T}{h^2} \frac{|J_1^2|^{\frac{1}{2}}}{|J_{1,o}^2|^{\frac{1}{2}}} exp(\beta\mu) W_i W_o \times exp(-\beta(U^{ext}(\boldsymbol{r}^N) + U^{LJ}(\boldsymbol{r}^N) + \Delta U^{corr}))\right) \quad \textit{Eq. II.47}$$

$$\pi(N_2 \to N_2 - 1) = min\left(1, \frac{\Lambda^3 N_2}{V} \frac{h^2}{4\pi^2 I_2 k_b T} \frac{|J_{1,o}^2|^{\frac{1}{2}}}{|J_1^2|^{\frac{1}{2}}} exp(-\beta\mu) \frac{exp(\beta(U^{ext}(\boldsymbol{r}^N) + U^{LJ}(\boldsymbol{r}^N) + \Delta U^{corr}))}{W_i W_o}\right) \quad \textit{Eq. II.48}$$

Where ΔU^{corr} represents the variation of the long-range corrections corresponding to the insertion of the molecule. W_i and W_o are the Rosenbluth factor of the statistical bias of insertion and orientation.[28]

II.7 Structural and dynamical analysis

Molecular simulation usually generates complex data with a considerable computational time. In order to extract the physical properties from the simple trajectories or configurations of the atoms, we need the programming tools for the post analysis. During the thesis, we mostly used Fortran 95 code for the post analyses program for the access to: Radial Distribution Function (RDF), Mean Square Displacement (MSD), total density, lecture of the system volume, lattice parameters, distribution of average bond length, distribution of average angle, distribution of dihedral angle and etc. Besides, we also used some commercial software; Visual Molecular Dynamics (VMD)[29] and OVITO[30] were used for the 3D visualization, Poreblazer[31] and zeo++[32,33] were used to extract the Pore Size Distribution (PSD).

Reference

(1) Metropolis, N.; Rosenbluth, A. W.; Rosenbluth, M. N.; Teller, A. H.; Teller, E. Equation of State Calculations by Fast Computing Machines. *J. Chem. Phys.* **1953**, *21* (6), 1087–1092. https://doi.org/10.1063/1.1699114.
(2) Wood, W. W.; Parker, F. R. Monte Carlo Equation of State of Molecules Interacting with the Lennard-Jones Potential. I. A Supercritical Isotherm at about Twice the Critical Temperature. *J. Chem. Phys.* **1957**, *27* (3), 720–733. https://doi.org/10.1063/1.1743822.
(3) Alder, B. J.; Wainwright, T. E. Phase Transition for a Hard Sphere System. *J. Chem. Phys.* **1957**, *27* (5), 1208–1209. https://doi.org/10.1063/1.1743957.
(4) Rahman, A. Correlations in the Motion of Atoms in Liquid Argon. *Phys. Rev.* **1964**, *136* (2A), A405–A411. https://doi.org/10.1103/PhysRev.136.A405.
(5) Barker, J. A.; Watts, R. O. Structure of Water; A Monte Carlo Calculation. *Chem. Phys. Lett.* **1969**, *3* (3), 144–145. https://doi.org/10.1016/0009-2614(69)80119-3.
(6) Rahman, A.; Stillinger, F. H. Molecular Dynamics Study of Liquid Water. *J. Chem. Phys.* **1971**, *55* (7), 3336–3359. https://doi.org/10.1063/1.1676585.
(7) Sing, K. S. W. Reporting physisorption data for gas/solid systems with special reference to the determination of surface area and porosity (Recommendations 1984). *Pure Appl. Chem.* **1985**, *57* (4), 603–619. https://doi.org/10.1351/pac198557040603.
(8) Broekhoff, J. C. P. Mesopore Determination from Nitrogen Sorption Isotherms: Fundamentals, Scope, Limitations. In *Studies in Surface Science and Catalysis*; Delmon, B., Grange, P., Jacobs, P., Poncelet, G., Eds.; Preparation of Catalysts II; Elsevier, 1979; Vol. 3, pp 663–684. https://doi.org/10.1016/S0167-2991(09)60243-3.
(9) Ishikawa, T.; Kodaira, N.; Kandori, K. Step-like Adsorption Isotherms of Molecules on γ-FeOOH and the Surface Homogeneity of γ-FeOOH. *J. Chem. Soc. Faraday Trans.* **1992**, *88* (5), 719–722. https://doi.org/10.1039/FT9928800719.
(10) Salles, F.; Maurin, G.; Serre, C.; Llewellyn, P. L.; Knöfel, C.; Choi, H. J.; Filinchuk, Y.; Oliviero, L.; Vimont, A.; Long, J. R.; Férey, G. Multistep N2 Breathing in the Metal−Organic Framework Co(1,4-Benzenedipyrazolate). *J. Am. Chem. Soc.* **2010**, *132* (39), 13782–13788. https://doi.org/10.1021/ja104357r.
(11) Cruzeiro, V. W. D.; Amaral, M. S.; Roitberg, A. E. Redox Potential Replica Exchange Molecular Dynamics at Constant PH in AMBER: Implementation and Validation. *J. Chem. Phys.* **2018**, *149* (7), 072338. https://doi.org/10.1063/1.5027379.
(12) Sun, H. COMPASS: An Ab Initio Force-Field Optimized for Condensed-Phase ApplicationsOverview with Details on Alkane and Benzene Compounds. *J. Phys. Chem. B* **1998**, *102* (38), 7338–7364. https://doi.org/10.1021/jp980939v.
(13) Momany, F. A.; Rone, R. Validation of the general purpose QUANTA ®3.2/CHARMm® force field. *J. Comput. Chem.* **1992**, *13* (7), 888–900. https://doi.org/10.1002/jcc.540130714.
(14) Mayo, S. L.; Olafson, B. D.; Goddard, W. A. DREIDING: A Generic Force Field for Molecular Simulations. *J. Phys. Chem.* **1990**, *94* (26), 8897–8909. https://doi.org/10.1021/j100389a010.

(15) UFF, a full periodic table force field for molecular mechanics and molecular dynamics simulations | Journal of the American Chemical Society https://pubs.acs.org/doi/10.1021/ja00051a040 (accessed 2021 -12 -07).
(16) Jorgensen, W. L.; Maxwell, D. S.; Tirado-Rives, J. Development and Testing of the OPLS All-Atom Force Field on Conformational Energetics and Properties of Organic Liquids. *J. Am. Chem. Soc.* **1996**, *118* (45), 11225–11236. https://doi.org/10.1021/ja9621760.
(17) Martin, M. G.; Siepmann, J. I. Transferable Potentials for Phase Equilibria. 1. United-Atom Description of n-Alkanes. *J. Phys. Chem. B* **1998**, *102* (14), 2569–2577. https://doi.org/10.1021/jp972543+.
(18) Martin, M. G.; Siepmann, J. I. Novel Configurational-Bias Monte Carlo Method for Branched Molecules. Transferable Potentials for Phase Equilibria. 2. United-Atom Description of Branched Alkanes. *J. Phys. Chem. B* **1999**, *103* (21), 4508–4517. https://doi.org/10.1021/jp984742e.
(19) Wolf, D.; Keblinski, P.; Phillpot, S. R.; Eggebrecht, J. Exact Method for the Simulation of Coulombic Systems by Spherically Truncated, Pairwise R−1 Summation. *J. Chem. Phys.* **1999**, *110* (17), 8254–8282. https://doi.org/10.1063/1.478738.
(20) Ewald, P. P. Die Berechnung Optischer Und Elektrostatischer Gitterpotentiale. *Ann. Phys.* **1921**, *369* (3), 253–287. https://doi.org/10.1002/andp.19213690304.
(21) Ghoufi, A.; Maurin, G. Hybrid Monte Carlo Simulations Combined with a Phase Mixture Model to Predict the Structural Transitions of a Porous Metal−Organic Framework Material upon Adsorption of Guest Molecules. *J. Phys. Chem. C* **2010**, *114* (14), 6496–6502. https://doi.org/10.1021/jp911484g.
(22) Henrique, A.; Maity, T.; Zhao, H.; Brântuas, P. F.; Rodrigues, A. E.; Nouar, F.; Ghoufi, A.; Maurin, G.; Silva, J. A. C.; Serre, C. Hexane Isomers Separation on an Isoreticular Series of Microporous Zr Carboxylate Metal Organic Frameworks. *J. Mater. Chem. A* **2020**, *8* (34), 17780–17789. https://doi.org/10.1039/D0TA05538G.
(23) Duane, S.; Kennedy, A. D.; Pendleton, B. J.; Roweth, D. Hybrid Monte Carlo. *Phys. Lett. B* **1987**, *195* (2), 216–222. https://doi.org/10.1016/0370-2693(87)91197-X.
(24) Mehlig, B.; Heermann, D. W.; Forrest, B. M. Hybrid Monte Carlo Method for Condensed-Matter Systems. *Phys. Rev. B* **1992**, *45* (2), 679–685. https://doi.org/10.1103/PhysRevB.45.679.
(25) DÜREN, T.; KEIL, F. J.; SEATON, N. A. Molecular Simulation of Adsorption and Transport Diffusion of Model Fluids in Carbon Nanotubes. *Mol. Phys.* **2002**, *100* (23), 3741–3751. https://doi.org/10.1080/0026897021000028429.
(26) Nagumo, R.; Takaba, H.; Nakao, S. A Methodology to Estimate Transport Diffusivities in 'Single-File' Permeation through Zeolite Membranes Using Molecular Simulations. *J. Chem. Eng. Jpn. - J CHEM ENG JPN* **2007**, *40*, 1045–1055. https://doi.org/10.1252/jcej.07WE170.
(27) Banaszak, B. J.; Faller, R.; de Pablo, J. J. Simulation of the Effects of Chain Architecture on the Sorption of Ethylene in Polyethylene. *J. Chem. Phys.* **2004**, *120* (23), 11304–11315. https://doi.org/10.1063/1.1751178.
(28) Gō, N.; Scheraga, H. A. Analysis of the Contribution of Internal Vibrations to the Statistical Weights of Equilibrium Conformations of Macromolecules. *J. Chem. Phys.* **1969**, *51* (11), 4751–4767. https://doi.org/10.1063/1.1671863.
(29) Humphrey, W.; Dalke, A.; Schulten, K. VMD: Visual Molecular Dynamics. *J. Mol. Graph.* **1996**, *14* (1), 33–38, 27–28. https://doi.org/10.1016/0263-7855(96)00018-5.

(30) Stukowski, A. Visualization and Analysis of Atomistic Simulation Data with OVITO–the Open Visualization Tool. *Model. Simul. Mater. Sci. Eng.* **2009**, *18* (1), 015012. https://doi.org/10.1088/0965-0393/18/1/015012.
(31) Sarkisov, L.; Bueno-Perez, R.; Sutharson, M.; Fairen-Jimenez, D. Materials Informatics with PoreBlazer v4.0 and the CSD MOF Database. *Chem. Mater.* **2020**, *32* (23), 9849–9867. https://doi.org/10.1021/acs.chemmater.0c03575.
(32) Martin, R. L.; Smit, B.; Haranczyk, M. Addressing Challenges of Identifying Geometrically Diverse Sets of Crystalline Porous Materials. *J. Chem. Inf. Model.* **2012**, *52* (2), 308–318. https://doi.org/10.1021/ci200386x.
(33) Willems, T. F.; Rycroft, C. H.; Kazi, M.; Meza, J. C.; Haranczyk, M. Algorithms and Tools for High-Throughput Geometry-Based Analysis of Crystalline Porous Materials. *Microporous Mesoporous Mater.* **2012**, *149* (1), 134–141. https://doi.org/10.1016/j.micromeso.2011.08.020.

Chapter III. Hexane isomers separation on an isoreticular series of microporous Zr carboxylate metal organic frameworks

III.1 Introduction and context

There is increasing demand to enhance fuel quality in order to minimize the negative impacts on the environment and public health.[1–3] Therefore, there are restrictions on the gasoline production, which limits the concentration of toxic additives.[4] The process of isomerization in petroleum processing is growing for the cleaner fuel. During this process, the linear paraffins are converted into their branched isomers catalytically in order to increase Research Octane Number (RON). The *n*C5 (linear pentane, RON: 61.8) is converted to iC5 (isopentane, RON: 92.3), while *n*C6 (linear hexane, RON: 24.8) is converted to 2MP, 3MP, 23DMB and 22DMB with RON equals to 73.4, 74.5, 101.7 and 91.8 respectively.[5,6] This isomerization method allows to increase the RON, however it has the limitation. The catalytic reaction is limited by thermodynamic equilibrium, there are still 10% of unreacted linear and 50% of mono-branched isomers.[7] In order to furthermore improve the RON, the Total Isomerization Process – TIP uses a classic porous material, Zeolite 5A to separate the final product, retain the branched isomers with RON around 87-90, and linear isomers will be recycled back to the reactors until they converted to branched isomers.[8] It is still possible to go further and improve the RON, if we can separate effectively of mono-branched hexane isomers (2MP, 3MP) and di-branched hexane isomers (22DMB, 23DMB). To do so, the petrochemical industry has been looking for alternatives which allow to effectively separate branched hexane isomers.

In this context, porous crystalline hybrid solids such as Metal Organic Frameworks (MOFs) comes into the sight. Since the past decades, MOFs have showed its great potential for a wide range of applications, including catalysis, sensing, drug delivery, adsorption and separation and so on. MIL-140 series MOFs are promising candidates for the effective separation of branched hexane isomers. This part of study is included in the study of a series of isoreticular Zr carboxylate MOFs, MIL-140A, B and C. Where the experimental parts were investigated by chromatographic breakthrough experiments by the collaborators.[9] Among all three Zr carboxylate MOFs, MIL-140B presents the highest selectivity, thus, our computational work was focused on MIL-140B. In this chapter, we will present the main result of the single component and equimolar quinary mixture adsorption and also the analysis.

III.2 Methodology

III.2.1 Alkane Model

TraPPE-UA[10,11] force field was used to describe all hexane isomers, each CH_x was considered as a single uncharged Lennard-Jones site. This united atom model allows to decrease the computational effort but still keeps a good accuracy, makes it a generally suitable force field to describe the hexane isomers.

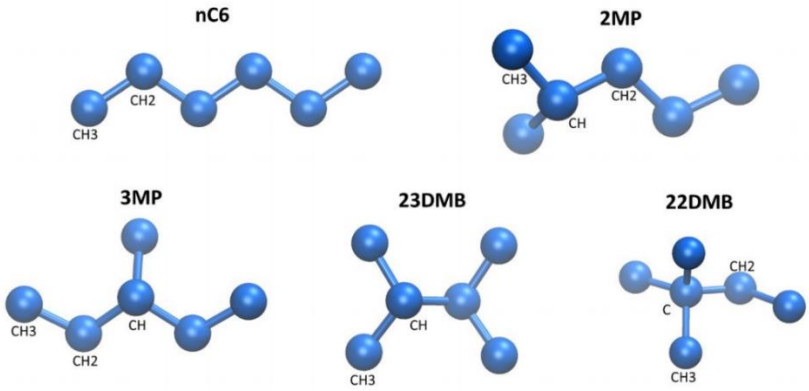

Figure III.1 *Illustration of hexane isomers with united atom (UA) model. Each methyl group is represented as a single pseudo atom. The UA model is applied for nC6, 2MP, 3MP, 23DMB and 22DMB.*

A harmonic cosine potential model describes the intra-molecular bond and bending contribution. The parameters summarized in the table below.

Table III.1 *Hexane isomers TraPPE force field parameters*

Pseudo atom	***Type***	***ϵ [K]***	***σ [Å]***
CH_3	CH_3-CH_x	98	3.75
CH_2	CH_2-CH_x	85	3.675
CH	CH_x=CH-CH_y	47	4.8
CH_2	CH_x-CH_2-CH_y	46	3.95
C	$(CH_x)3$-C-CHx	0.5	6.4

Bond	***r_0 [Å]***
CH_x-CH_x	1.54
CH_x=CH_x	1.33

Bending angle	***θ_0 (°)***	***K_θ/k_b [K/rad²]***
CH_x-CH_2-CH_y	114	62500
CH_x=CH-CH_x	119.7	70420

Dihedral angle	***c_0 [K]***	***c_1 [K]***	***c_2 [K]***	***c_3 [K]***
CH_x-CH_2-CH=CH_y	688.5	86.36	-109.77	-282.24
CH_x-CH_2-CH_2-CH_y	0	355.03	-68.19	791.32
CH_x-CH_2-C-CH_y	0	0	0	461.29
CH_x-CH-CH-CH_y	-251.6	428.73	-111.85	441.27

In the Table III.1, r_0 is the reference bond length in Å. K_θ/k_b is the bend energy constant in K/rad², θ_0 is the reference bend angle in degree. c_1, c_2, c_3, c_4 are torsion parameters in K. The inter-molecular interaction is described by Lennard-Jones interaction.

III.2.2 MIL-140B Model

The crystal structure was taken from the work of Thomas et al.[12] All atoms of the MIL-140B were treated as single uncharged LJ sites, only LJ parameters were taken from the UFF and DREIDING force fields for the Zr atoms and the rest of the atoms respectively. The force field is chosen in the way to describe the host-guest interactions. As the simulation method in this study was Monte Carlo in the first place, the structures were treated as rigid as represented in Figure III.2.

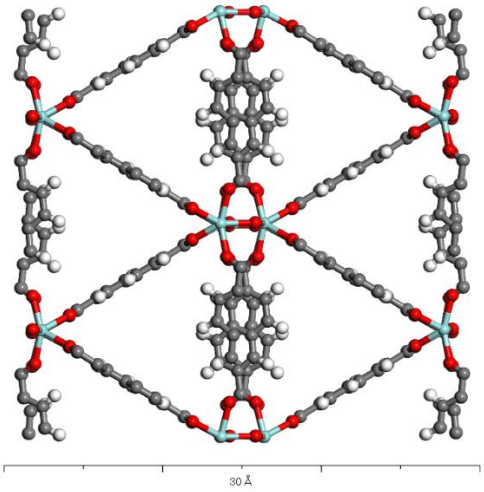

Figure III.2 *MIL-140B supercell of 1x2x4, with original configuration. Cyan, grey, red and white colour represents Zirconium, Carbon, Oxygen and Hydrogen atom respectively.*

III.2.3 Simulation method

Single-component and equimolar quinary mixture adsorption isotherms were calculated by grand canonical Monte Carlo (GCMC) simulation at 343K in order to compare with the experimental data. These calculations were carried out using a simulation box corresponding to a 1x2x4 supercell of MIL-140B with different linker rotation. The simulation consisted of $5x10^5$ Monte Carlo steps for equilibration and $4x10^4$ Monte Carlo steps for production. As conventional MC is too time consuming when it comes to adsorption of long molecules inside the MOFs, the configurational-bias MC (CBMC) was employed to improve the sampling rate, as this algorithm consists on 'growing' atom by atom to form a molecule rather than random insertion.[13,14] Several types of Monte Carlo moves were considered: translation move, rotation move, internal rotation move, and insertion/deletion move. The frequencies of these moves were respectively 0.3, 0.2, 0.2 and 0.3. The cut-off distance was set for 12 Å. The approximation that the fugacity is equal to gas pressure for the adsorption was also applied. The fugacity is a measure of the difference between its chemical potential in the system and in its hypothetical ideal-gas standard state, here, the fugacity is introduced as a convenient way to relate the chemical potential to the composition of the system.

III.3 Results and discussion

III.3.1 Adsorption Isotherms

a) Single component adsorption

The single component adsorption isotherm was carried out in the first place with pristine MIL-140B and was compared with experimental data as illustrated in Figure III. 3.

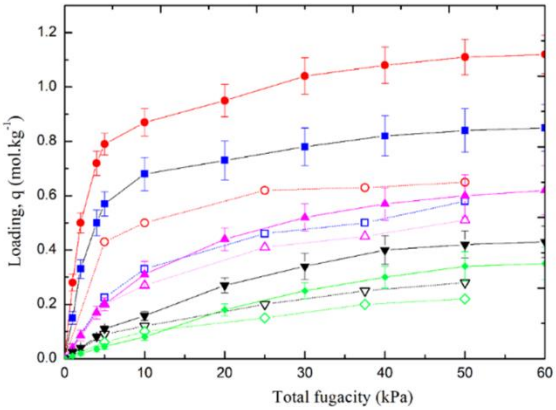

Figure III.3 *Single component adsorption isotherm vs experimental data. GCMC simulations nC6 (●), 2MP (—■—), 3MP, (—▲—) 23DMB (—▼—) and 22DMB (—◆—) and experimental data nC6 (○), 2MP (··□··), 3MP (·· △··), 23DMB (·· ▽··) and 22DMB (··◇··).*

Despite of the qualitative agreement regarding to the adsorption sequence between the simulation data and experimental data, the simulation overestimated the adsorption quantity. As suggested in the literature, the linker tilting plays a critical role in the sorption properties, it is expected to impact the adsorption uptakes.[13,14] However, the pristine rigid framework used in the simulations didn't consider any linker rotations, thus the pristine rigid MIL-140B structure presents more accessible volume for guest molecules resulting this over estimation. Indeed, a guest-induced reorientation of the linker has been already reported for many MOFs.[15,16] Especially for the MIL-140B which presents a tiny pore diameter, this becoming even more valid for the bulkier molecules as hexane isomers. In order to confirm the assumption, a series of MIL-140B configurations were generated by systematically tilting all the organic linkers by maximum 15°, the linker tilting was performed in a way that only the positions of atoms on the aromatic ring changes as illustrated in Figure III.4. As we do so, we obtained a pseudo flexible MIL-140B, the flexibility is artificial but it allows us to reveal the importance of the considering linker tilting in the small pore MOFs MIL-140B.

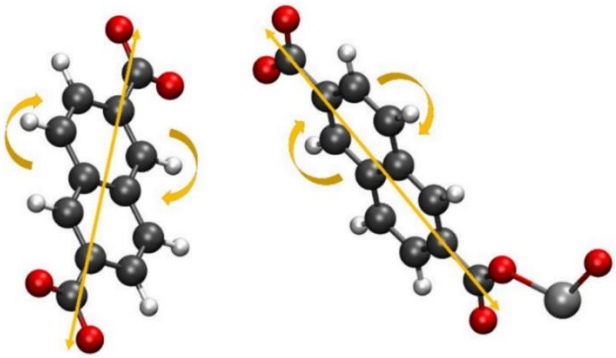

Figure III.4 *Examples of organic linker tilting in MIL-140B.* ⟷ *represents the axis of rotation.*

To probe the impact of the linker tilting effect on the sorption properties for rigid MIL-140B, we performed a series of linker tilting in order to obtain different configurations. Then MC simulations were then carried out on the different configurations to investigate the influence of the linker tilting.

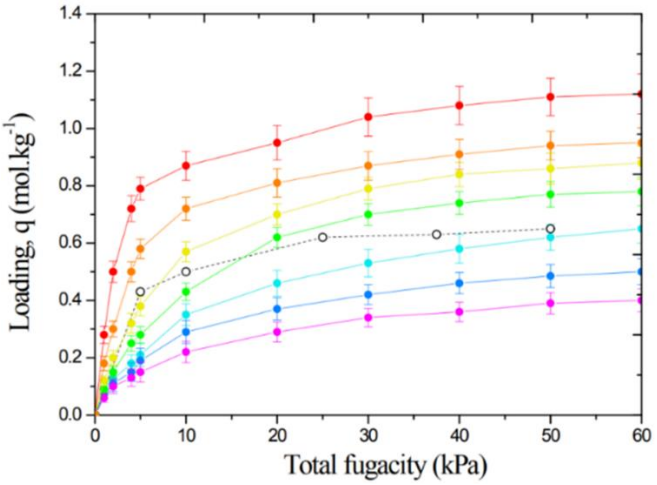

Figure III.5 *nC6 single component adsorption isotherm vs experimental data. experimental data (-- ○ --), 0° linker rotation (—●—), 2° linker rotation (—●—), 5° linker rotation (—●—), 7° linker rotation (—●—), 10° linker rotation (—●—), 12° linker rotation (—●—) and 15° linker rotation (—●—).*

The single component adsorption was performed on *n*C6 for different configurations, and compared with the experimental data. As evidenced in Figure III.5, with the increase of the linker, the adsorption uptake decreased as the accessible volume decreased. The best fitting of isotherm with experimental data corresponds to 5° and 7° linker rotation. The same trends were observed for other hexane isomers, 2MP, 3MP, 23DMB and 22DMB, as shown in Figure III.6 – Figure III.9.

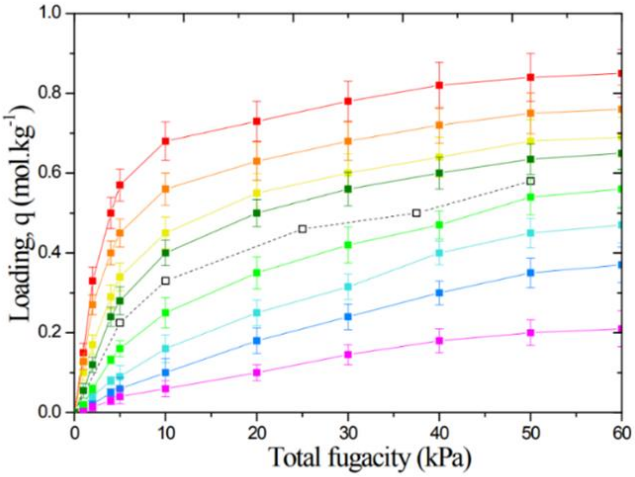

Figure III.6 *2MP single component adsorption isotherm vs experimental data. experimental data (-- □ --), 0° linker rotation (—■—), 2° linker rotation (—■—), 5° linker rotation (—■—), 6° linker rotation (—■—), 7° linker rotation (—■—), 10° linker rotation (—■—), 12° linker rotation (—■—) and 15° linker rotation (—■—).*

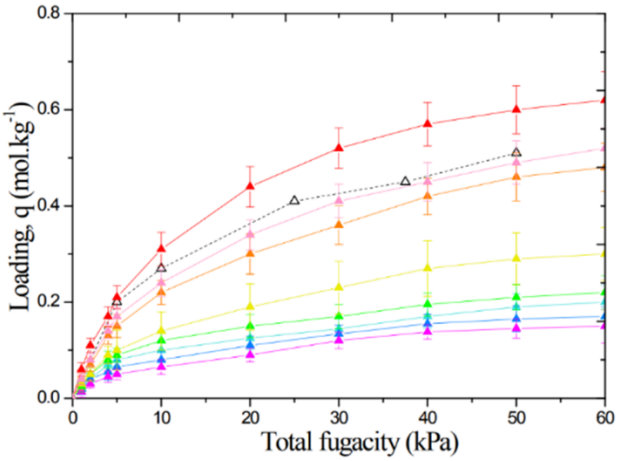

Figure III.7 *3MP single component adsorption isotherm vs experimental data, experimental data (-- △ --), 0° linker rotation (—▲—), 1° linker rotation (—▲—), 2° linker rotation (—▲—), 5° linker rotation (—▲—), 7° linker rotation (—▲—), 10° linker rotation (—▲—), 12° linker rotation (—▲—) and 15° linker rotation (—▲—).*

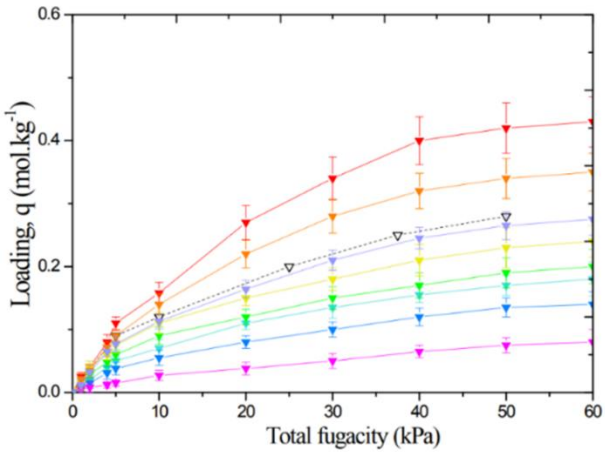

Figure III.8 *23DMB single component adsorption isotherm vs experimental data (--▽--), 0° linker rotation (—▼—), 2° linker rotation (—▼—), 4° linker rotation (—▼—), 5° linker rotation (—▼—), 7° linker rotation (—▼—), 10° linker rotation (—▼—), 12° linker rotation (—▼—) and 15° linker rotation (—▼—).*

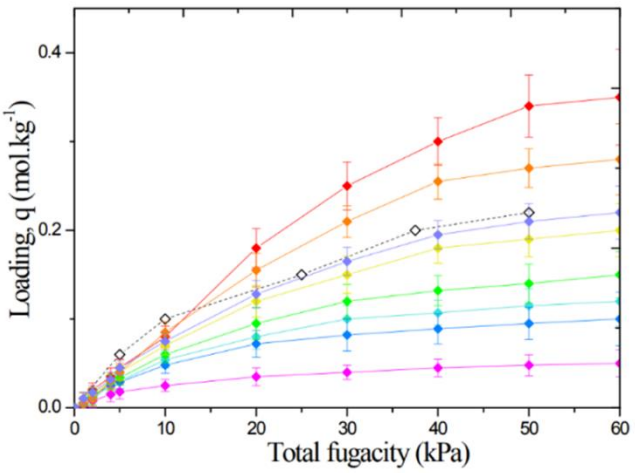

Figure III.9 *22DMB single component adsorption isotherm vs experimental data (--◇--), 0° linker rotation (—◆—), 2° linker rotation (—◆—), 4° linker rotation (—◆—), 5° linker rotation (—◆—), 7° linker rotation (—◆—), 10° linker rotation (—◆—), 12° linker rotation (—◆—) and 15° linker rotation (—◆—).*

In order to understand the origin of this difference of adsorption quantity, which is assumed to be thermodynamic driven assisted by shape sieving. Isosteric heat of adsorption, Radial distribution function (RDF) and Pore Size Distribution (PSD) were calculated. Figure III.10 further illustrates the preferential sittings of each isomer in the most representative tilted MIL-140B configurations. The molecules are arranged in such a way as to interact with the organic linkers preferentially via the methyl (-CH_3) united atoms. This implies relatively weak van der Waals interaction with characteristic separation MOF/hexane isomer distances over 3 Å.

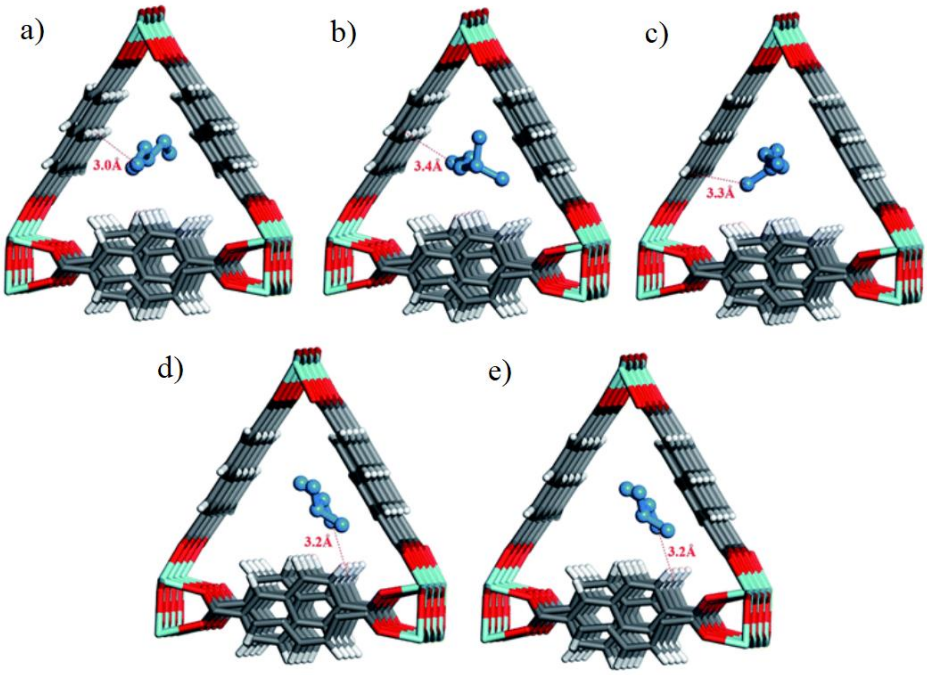

Figure III.10 *snapshots of one molecule inside the MIL-140B channel. With a,b,c,d and e represents nC6, 2MP, 3MP, 23DMB and 22DMB respectively.*

The observation of the snapshots which illustrate the distance between methyl group and the framework is confirmed by RDF, as evidenced in Figure III.11. The RDF corresponds to MOF/hexane isomer pairs. The figures a), b), c), d), and e) represent the case of adsorption of *n*C6, 2MP, 3MP, 23DMB, and 22DMB respectively. The loading for *n*C6, 2MP and 3MP corresponds to 1 molecule per unit cell while the loading for 22DMB and 23DMB corresponds to 0.5 molecule per unit cell. The MIL-140B linker tilting for *n*C6, 2MP, 3MP, 23DMB, and 22DMB were 10°, 7°, 2°, 4°, and 4°, which was evaluated by comparing with pristine linker position.

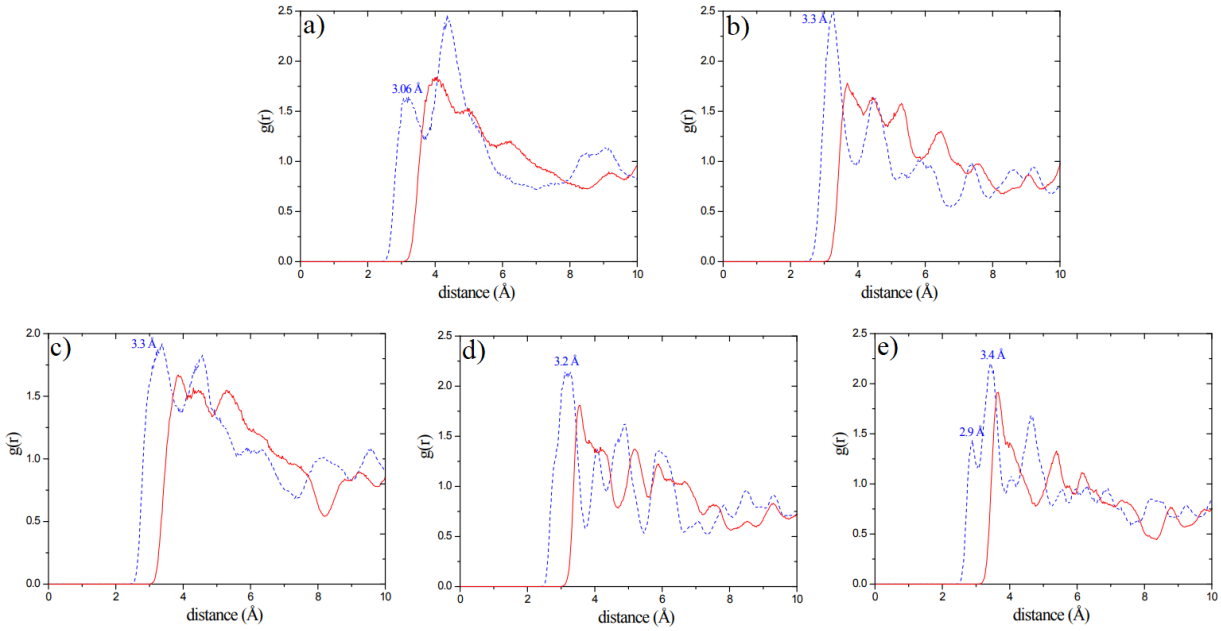

Figure III.11 *RDF for 5 isomers. a), b), c), d) and e) corresponds to nC6, 2MP, 3MP, 23DMB and 22DMB respectively. RDF between CH_3(UA) and C is represented in red line (———), between CH_3(UA) and H from MIL-140B aromatic ring is represented in blue dash line (- - - - - - -).*

The major peak position extracted from RDF indicated the order of the host-guest interaction strength is linear isomers > mono-branched isomers > di-branched isomers. We further calculated the isosteric heats of adsorption Q_{st} in order to quantitatively evaluate the strength of the host-guest interaction.

$$Q_{st} = RT - [\langle UN\rangle - \langle U\rangle\langle N\rangle]/[\langle N^2\rangle - \langle N\rangle^2] \qquad \textit{Eq. III.1}$$

where *U*, *N*, *R*, and *T* are the host–guest interactions, the number of molecules, the perfect gas constant, and the temperature, respectively). Q_{st} estimated is 54.6 kJ mol^{-1}, 51.2 kJ mol^{-1}, 47.5 kJ mol^{-1}, 44.4 kJ mol^{-1} and 41.3 kJ mol^{-1} for *n*C6, 2MP, 3MP, 22DMB and 23DMB, respectively. The value of Q_{st} followed the experimental trend for the adsorption uptakes at low pressure, and is consistent with the RDF. This suggested that the origin of the hexane separation in MIL-140B is thermodynamically driven.

b) Equimolar quinary mixture adsorption

Previous single component adsorption has shown that each hexane isomer corresponds to an optimised linker rotation, and by considering the organic linker rotation the simulation results are found in fair agreement with the experiment. Now we are interested in the separation ability of MIL-140B towards hexane isomers. By studying an equimolar quinary mixture adsorption, we can extract the selectivity as defined in Eq. III.2:

$$S = \frac{q_{nC6} + q_{2MP} + q_{3MP}}{q_{23DMB} + q_{22DMB}} \qquad \textit{Eq. III.2}$$

Where q represents the adsorption quantity of a hexane isomer. As previously, the calculation of hexane mixture adsorption isotherm was carried out firstly on pristine MIL-140B structure without linker rotation as presented in Figure III.12 and an overestimation

of adsorbed amount with respect to the experiment was found. Interestingly, the selectivity is found to be close to 24.7 at the saturation while the experimental selectivity is 10. This difference is the result of the dominant overestimation of *n*C6. Indeed, compared to other isomers, the adsorption uptake of *n*C6 is more pronounced in comparison with the experiment.

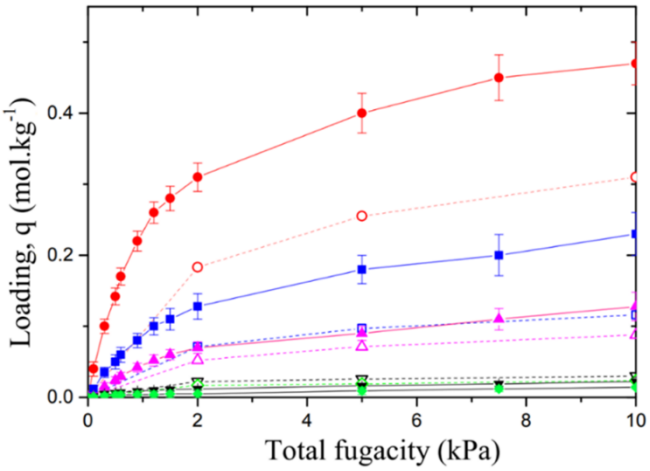

Figure III.12 *Quinary mixture adsorption isotherm with original MIL140B vs experimental data. GCMC simulations nC6 (●), 2MP (—■—), 3MP, (—▲—) 23DMB (—▼—) and 22DMB (—◆—) and experimental data nC6 (○), 2MP (··□··), 3MP (··△··), 23DMB (·· ▽··) and 22DMB (··◇··).*

In order to reproduce the experimental trend and selectivity, the linker rotation of MIL-140B need to be considered. Among all 5 hexane isomers, the *n*C6 adsorption quantity is more pronounced, hence we decided to perform 10° and 7° linker rotation which corresponds to the best fit for *n*C6. As shown in Figure III.13, the calculated selectivity for 10° and 7° linker rotation is 15.5 and 19. The simulated isotherms reproduce better the experimental data than the previous one with pristine MIL-140B, which underlined again the importance of considering the linker rotation as well as the flexibility of the MOFs to simulate the sorption properties in MIL-140B.

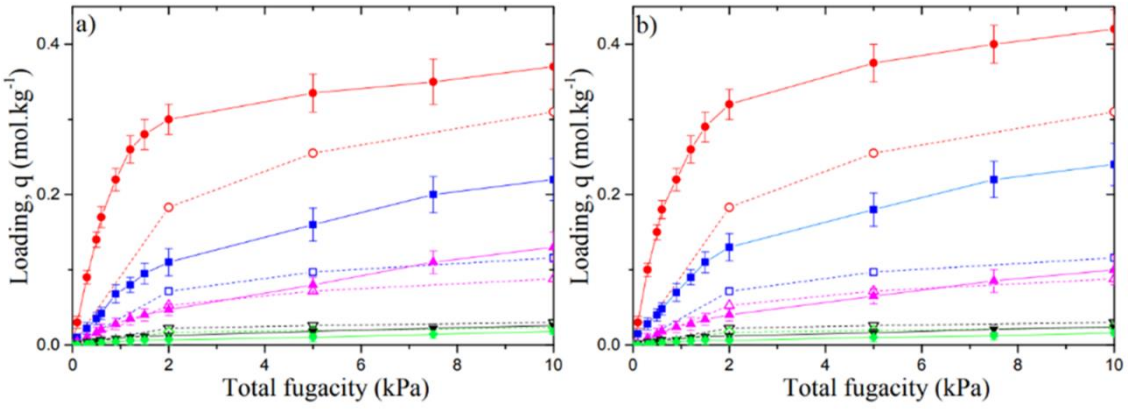

Figure III.13 *Quinary mixture adsorption isotherm vs experimental data. a) 10° linker rotation tilting, b) 7° linker rotation tilting. GCMC simulations nC6 (●), 2MP (—■—), 3MP, (—▲—) 23DMB (—▼—) and 22DMB (—◆—) and experimental data nC6 (○), 2MP (··□··), 3MP (··△··), 23DMB (·· ▽··) and 22DMB (··◇··).*

III.4 Conclusion

Our collaborators experimentally revealed that MIL-140B represents the highest selectivity which is up to 10, this point is further confirmed by our simulation result. Despite of the over estimation of adsorption quantity with original MIL-140B for the single component adsorption isotherm, we are able to reproduce the isotherm with the consideration of the linker rotation. However, the selectivity estimated from the quinary mixture adsorption is 15.5 for MIL-140B with 10° linker rotation, still much higher than the experimental data. This shift is because the framework is considered as rigid in GCMC simulation, and the linker rotation keeps a certain angle during the whole simulation too. This pseudo flexible MIL-140B lacks of the real interaction of guest-frameworks, as with the increase of the loading of molecules, the linker tilting could be affected thus the interaction of guest-framework could be affected as well. In order to overcome this difficulty, a fully flexible framework force field need to be considered. This flexible force field applied MIL-140B and results will be explained in chapter 4.

Reference

(1) The global experience with lead in gasoline and the lessons we should apply to the use of MMT - Walsh - 2007 - American Journal of Industrial Medicine - Wiley Online Library https://onlinelibrary.wiley.com/doi/abs/10.1002/ajim.20483 (accessed 2021 -12 -07).
(2) Shen, Y.; Shuai, S.; Wang, J.; Xiao, J. Optimization of Gasoline Hydrocarbon Compositions for Reducing Exhaust Emissions. *J. Environ. Sci.* **2009**, *21* (9), 1208–1213. https://doi.org/10.1016/S1001-0742(08)62405-5.
(3) Westphal, G. A.; Krahl, J.; Brüning, T.; Hallier, E.; Bünger, J. Ether Oxygenate Additives in Gasoline Reduce Toxicity of Exhausts. *Toxicology* **2010**, *268* (3), 198–203. https://doi.org/10.1016/j.tox.2009.12.016.
(4) Swick, D.; Jaques, A.; Walker, J. C.; Estreicher, H. Gasoline Toxicology: Overview of Regulatory and Product Stewardship Programs. *Regul. Toxicol. Pharmacol.* **2014**, *70* (2, Supplement), S3–S12. https://doi.org/10.1016/j.yrtph.2014.06.016.
(5) Handbook of Petroleum Refining Processes, Third Edition | McGraw-Hill Education - Access Engineering https://www.accessengineeringlibrary.com/content/book/9780071391092 (accessed 2021 -12 -07).
(6) *Handbook of Petroleum Refining Processes*; McGraw-Hill Education, 2016.
(7) Peralta, D.; Chaplais, G.; Simon-Masseron, A.; Barthelet, K.; Pirngruber, G. D. Separation of C6 Paraffins Using Zeolitic Imidazolate Frameworks: Comparison with Zeolite 5A. *Ind. Eng. Chem. Res.* **2012**, *51* (12), 4692–4702. https://doi.org/10.1021/ie202995g.
(8) Holcombe, T. C. (54) TOTAL SOMERIZATION PROCESS. 7.
(9) Henrique, A.; Maity, T.; Zhao, H.; Brântuas, P. F.; Rodrigues, A. E.; Nouar, F.; Ghoufi, A.; Maurin, G.; Silva, J. A. C.; Serre, C. Hexane Isomers Separation on an Isoreticular Series of Microporous Zr Carboxylate Metal Organic Frameworks. *J. Mater. Chem. A* **2020**, *8* (34), 17780–17789. https://doi.org/10.1039/D0TA05538G.
(10) Martin, M. G.; Siepmann, J. I. Transferable Potentials for Phase Equilibria. 1. United-Atom Description of n-Alkanes. *J. Phys. Chem. B* **1998**, *102* (14), 2569–2577. https://doi.org/10.1021/jp972543+.
(11) Martin, M. G.; Siepmann, J. I. Novel Configurational-Bias Monte Carlo Method for Branched Molecules. Transferable Potentials for Phase Equilibria. 2. United-Atom Description of Branched Alkanes. *J. Phys. Chem. B* **1999**, *103* (21), 4508–4517. https://doi.org/10.1021/jp984742e.
(12) Bennett, T. D.; Todorova, T. K.; Baxter, E. F.; Reid, D. G.; Gervais, C.; Bueken, B.; Voorde, B. V. de; Vos, D. D.; Keen, D. A.; Mellot-Draznieks, C. Connecting Defects and Amorphization in UiO-66 and MIL-140 Metal–Organic Frameworks: A Combined Experimental and Computational Study. *Phys. Chem. Chem. Phys.* **2016**, *18* (3), 2192–2201. https://doi.org/10.1039/C5CP06798G.
(13) Tang, J.; Chu, Y.; Li, S.; Xu, J.; Xiong, W.; Wang, Q.; Deng, F. Breathing Effect via Solvent Inclusions on the Linker Rotational Dynamics of Functionalized MIL-53. *Chem. – Eur. J.* **2021**, *27* (59), 14711–14720. https://doi.org/10.1002/chem.202102419.
(14) Gonzalez, A.; van der Veen, M. Rotational Dynamics of Linkers in Metal–Organic Frameworks. *Nanomaterials* **2019**, *9*, 330. https://doi.org/10.3390/nano9030330.

(15) Devautour-Vinot, S.; Maurin, G.; Serre, C.; Horcajada, P.; Paula da Cunha, D.; Guillerm, V.; de Souza Costa, E.; Taulelle, F.; Martineau, C. Structure and Dynamics of the Functionalized MOF Type UiO-66(Zr): NMR and Dielectric Relaxation Spectroscopies Coupled with DFT Calculations. *Chem. Mater.* **2012**, *24* (11), 2168–2177. https://doi.org/10.1021/cm300863c.

(16) Pires, J.; Fernandes, J.; Dedecker, K.; Gomes, J. R. B.; Pérez-Sánchez, G.; Nouar, F.; Serre, C.; Pinto, M. L. Enhancement of Ethane Selectivity in Ethane–Ethylene Mixtures by Perfluoro Groups in Zr-Based Metal-Organic Frameworks. *ACS Appl. Mater. Interfaces* **2019**, *11* (30), 27410–27421. https://doi.org/10.1021/acsami.9b07115.

Chapter IV. Effective separation of hexane isomers in the Zr-MIL-140B Metal-Organic Framework assisted by applying mechanical pressure

IV.1 Introduction and context

In the previous chapter, Grand canonical Monte Carlo (GCMC) simulations were performed to gain insight into the molecular separation mechanism. It highlighted the crucial need to consider a tiny tilting of the MOF organic linkers for capturing the experimental trend. A tilting angle of 5-7° was found to reproduce fairly the experimental single component adsorption isotherms for all hexane isomers at 343 K. However, this tilting angle was maintained fixed over the whole range of hexane pressure, and the flexibility of the MOF framework was not accounted for. To go beyond this preliminary study, there is a need to consider the guest-induced MOF flexibility that varies along with the pressure range with the implementation of a hybrid osmotic Monte Carlo (HOMC) simulation scheme.[1–3] Typically, we demonstrated that this HOMC approach is effective to describe the adsorption of different gases in a variety of breathing and flexible MOFs including MIL-53[1,2] and ZIF-8[3]. Herein, our first aim was to apply a HOMC strategy implementing a generic force field to describe the flexibility of the MIL-140B framework to gain insight into the interplay between ligand rotation and adsorption of hexane isomers as both single components and quinary mixture. Furthermore, recently, it has been delivered a proof-of-concept with an application of an external mechanical pressure to modulate the pore size/shape of MOFs upon guest adsorption[4,5] for tuning their separation performances. It was demonstrated that this mechanical control of the MOF porosity enables (i) a spectacular enhancement of the kinetics-driven propane/propylene separation by ZIF-8,[6] (ii) an infinite carbon dioxide selectivity over nitrogen and methane by the highly flexible 1D-channel like MIL-53 governed by a full-size exclusion mechanism[4] and iii) an enhancement of the thermodynamically-controlled selectivity of hexane isomers by ZIF-8 MOF.[3] Therefore, one of the objectives of this chapter is to explore the mechanical modulation of the pore size/shape of MIL-140B for boosting its C6 isomer separation performance. In this regard, HOMC simulations were carried out to predict the hexane isomers single components and mixture adsorption isotherms of the mechanically constrained MIL-140B.

IV.2 Computational details

All hexane (C6) isomer single-component and quinary mixture isotherms were calculated by using HOMC simulations. These calculations were carried out at 343 K (experimental condition) using a simulation box corresponding to a 1x2x4 supercell of the MIL-140B crystal structure.[7] All C6 isomers, *n*C6 (n-hexane), 2MP, 3MP, 23DMB and 22DMB, were described by means of the uncharged united-atom TraPPE model.[5,8] Illustrations of the atomistic models of the C6 isomers are provided in the previous chapter. The UFF[9] (inorganic node including Zirconium atoms) and DREIDING[10] (organic moieties) force fields were combined to describe the flexibility of the MIL-140B MOF framework. These force fields include bonds, bending, torsion and improper intra-molecular potential terms while the non-bonded interactions were described by Lennard-Jones (LJ) terms. LJ parameters of the MIL-140B are detailed in Table IV.1 while labels are described in Figure IV.1(a). The C6/MIL-140B LJ parameters were calculated using the Lorentz Berthelot mixing rule.[11,12] The detailed force field information can be found in Appendix, Table A.5 – Table A.8.

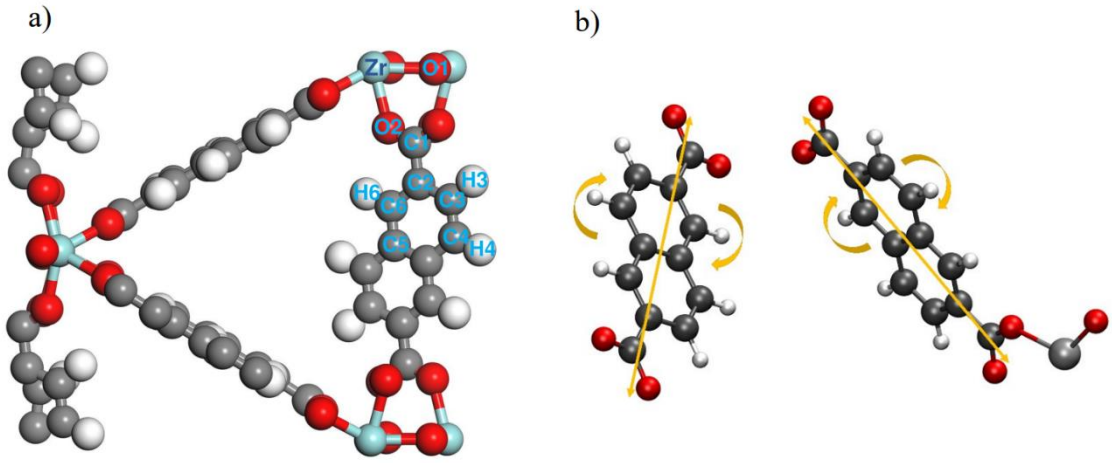

Figure IV.1 *a) Labels of atoms in the MIL-140B material. The carbon, hydrogen, oxygen and zirconium atoms are represented in grey, white, red and cyan respectively. b) Illustration of the tilting of organic linker along the axis connecting the carbon atoms C1.*

Table IV.1 *Lennard Jones and partial charges parameters of atoms of the MIL-140B force field.*

Type	***ϵ [kJ mol^{-1}]***	***σ[Å]***	***Charge[e]***
C1	0.3979	3.473	0.7965
C2	0.3979	3.473	-0.0278
C3	0.3979	3.473	-0.0309
C4	0.3979	3.473	-0.3556
C5	0.3979	3.473	0.236
C6	0.3979	3.473	-0.233
H3	0.0636	2.846	0.1339
H4	0.0636	2.846	0.1339
H6	0.0636	2.846	0.1339
O1	0.4004	3.033	-1.2585
O2	0.4004	3.033	-0.688
Zr	0.2301	4.045	2.437

All calculated LJ interactions were truncated with a cut-off radius of 12 Å. MD simulations were performed by using DLPOLY software.[13] HOMC simulations consist of introducing a Molecular Dynamics (MD) step in a Monte Carlo scheme through the osmotic statistical ensemble.[1] Theoretical background ruling the HOMC method is detailed in chapter II.[1,3] In the HOMC simulation step, we considered a MD run of 10^5 steps using a time-step of 0.001 ps, i.e. a total of 100 ps, in order to ensure that the thermodynamic equilibrium was achieved.[3] In the GCMC simulations, the fugacity, temperature, and volume were fixed. All simulations consisted of 10^5 Monte Carlo (MC) steps. Insertion/deletion, translation, rotation and internal rotation trial moves with the following frequency, 0.4, 0.2, 0.2 and 0.2 were considered. For the quinary mixture, additional swapping trial move was involved with a frequency of 0.1. MD steps were performed in the NσT (N: number of particles, σ: pressure constraint and T: temperature=343 K) ensemble where the thermostat (relaxation time of 0.1ps) and the

barostat (relaxation time of 0.5ps) were both considered by means of the Nose-Hoover algorithm.[14,15] Each MD step was accepted following the Metropolis criterion.[1] The mechanical pressure was considered by fixing the pressure through the MD step such as p=0.1 MPa, 0.5 and 1 GPa. The selectivity was calculated in the same way as presented in previous chapter. Additional MD simulations were carried out in the NσT ensemble to identify the preferential distribution and conformation of hexane isomers as well as to explore their interactions with the MIL-140B channel through the calculation of the radial distribution functions between hexane isomers/MIL-140B atom pairs. Furthermore, at low coverage the isosteric heat of adsorption for all C6 isomers was calculated from the fluctuations of number of molecules and the energy.[16]

IV.3 Results and discussion

IV.3.1 Preliminary force field validation for MIL-140B

We report in Table IV.2 the simulated unit cell parameters (a, b, c, α, β, γ) of MIL-140B in its empty form by means of a MD run of 10 ns in the NσT ensemble implementing the flexible force field described above. A good concordance was obtained with the corresponding experimental data[7] with a maximum deviation of 4.4 % for the cell parameters and 2.3 % for the total unit cell volume. Interestingly, the unit cell volume reported previously from first principle calculations showed a higher deviation (6.6%).

Table IV.2 *Calculated and experimental lattice parameters of the empty MIL-140B at 0.1 MPa and 298 K.*

	a(Å)	***b(Å)***	***c(Å)***	***α (°)***	***β (°)***	***γ (°)***	***V (Å^3)***
This work	27.99± 0.02	13.26± 0.01	7.98 ± 0.01	90.00± 0.08	95.58± 0.07	89.99± 0.07	3003.4 ± 3.0
Ref.	27.95	13.46	7.91	90	93.34	90	2764.77
Exp.	26.71	13.3	7.79	90	93.82	90	2963.3

Figure IV.2 that reports an illustration of the equilibrated configuration of the empty MIL-140B, confirms that the guest-free framework remains intact with only a slight tilting of the organic linkers. Bond distances and bending angles for the MOF framework averaged over the MD runs are reported in the appendix. These geometric characteristics are in excellent agreements with the corresponding data reported for the crystal structure of MIL-140B.

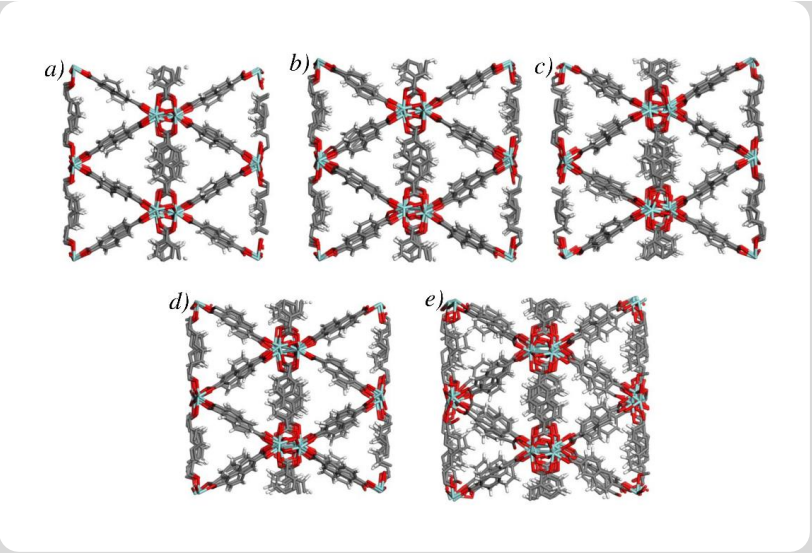

Figure IV.2 *Snapshot of MIL-140B structure under mechanical pressure, view from xy plane. Cyan, red, grey and white color represents Zirconium, Oxygen, Carbon and Hydrogen atoms, respectively.*

To ensure that the structure maintains its crystallinity and that no bonds are broken. Bond distances and bending angles for the MOF framework averaged over the MD runs are calculated and reported in Table IV.3 and IV.4.

Table IV.3 *Average bond length calculated in MIL-140B for the force field validation with and without mechanical pressure.*

	Average bond length (Å)	
Bonds type	0.1 MPa	1GPa
C-H	1.02 ± 0.01	1.02 ± 0.01
C1-C2	1.38 ± 0.01	1.38 ± 0.01
C1-O2	1.35 ± 0.01	1.34 ± 0.02
Or-Zr	2.27 ± 0.02	2.20± 0.07
O2-Zr	2.37 ± 0.02	2.22 ± 0.09
Zr-Zr	3.58 ± 0.01	3.42± 0.10

Table IV.4 *Average bending angle calculated in MIL-140B for the force field validation.*

	Average angles (°)	
Angles type	0.1 MPa	1GPa
C2-C3-C4	119.8 ± 1.9	122.1 ± 3.9
C2-C3-H3	120.3 ± 2.2	121.5 ± 4.7
Zr-O1-Zr	91.8 ± 1.7	82.6 ± 5.2
O1-Zr-O2	63.9 ± 1.4	51.8 ± 3.8
O1-Zr-O1	137.3 ± 2.4	131.9 ± 4.7
C1-O2-Zr	122.8 ± 4.5	125.4 ± 9.3

We also looked at the bond length distribution and the bending angle distribution, which are shown in Figures IV.3 and Figure IV.4.

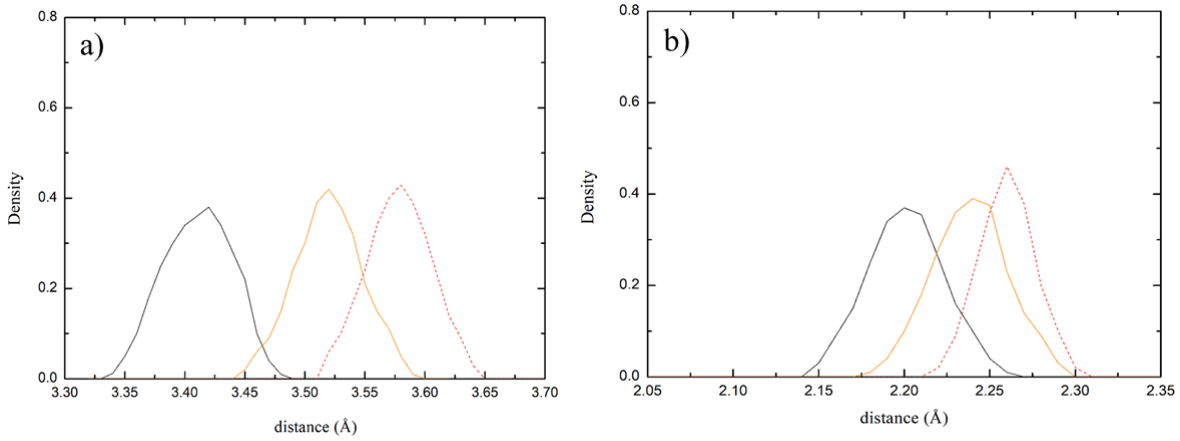

Figure IV.3 *Distribution of bond length calculated in MIL-140B for the force field validation. a) Zr-Zr, b) Zr-Or. For different mechanical pressure: 0.1 MPa (--------), 500MPa (———) and 1 GPa (———).*

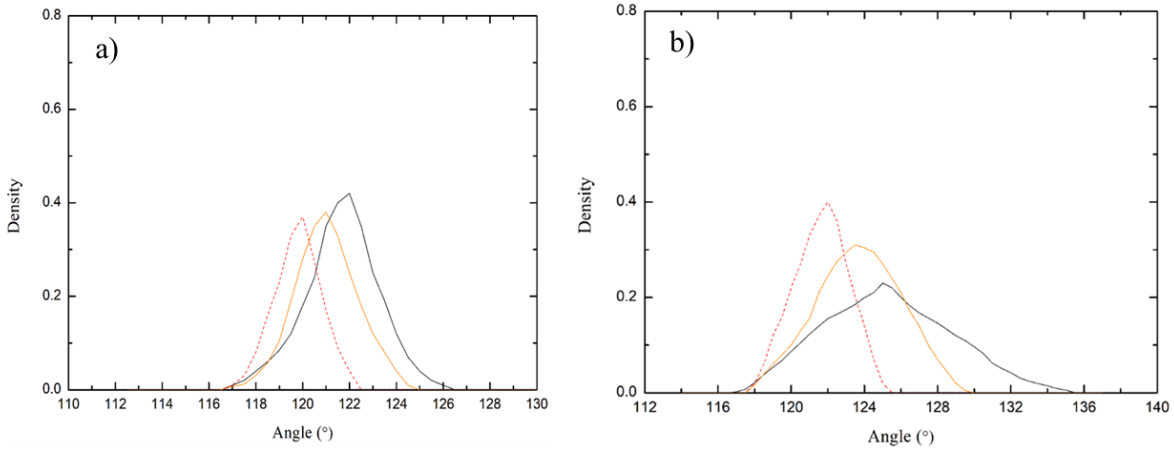

Figure IV.4 *Distribution of bending angle calculated in MIL-140B for the force field validation. a) C2-C3-C4, b) C1-O2-Zr. For different mechanical pressure: 0.1 MPa (--------), 500MPa (———) and 1 GPa (———).*

The structure's crystallinity is stable, as evidenced by the comparison of lattice volume with experimental data and other references, as well as the verification of average bonds length and average bending angle. This observation supports that the combination of UFF/DREIDING force field is suitable to accurately capture the structural dynamics of MIL-140B.

IV.3.2 Adsorption Isotherms

a) Adsorption of single component hexane isomers and equimolar quinary mixture

Single component adsorption experiment and simulation were performed for *n*C6, 2MP, 3MP, 23DMB and 22DMB in MIL-140B at 343K, 0.1 MPa by HOMC simulation method as illustrated in Figure IV.5. One can observe that these predicted data are in agreement with the experimental adsorption isotherms.[17] This emphasizes that the flexible force field use for MIL-140B describes well the structural response of the MOF framework to the adsorption. The adsorption equilibrium hierarchy of hexane isomers on MIL-140B is as linear > mono-branched > di-branched: *n*C6 > 2MP > 3MP > 23DMB > 22DMB, which is in line with the sequence of the isosteric heat of adsorptions, calculated at low coverage; 55.1 kJ mol^{-1}, 52.8 kJ mol^{-1}, 44.3 kJ mol^{-1}, 43.5 kJ mol^{-1}, and 40.1 kJ mol^{-1} for *n*C6, 2MP, 3MP, 23DMB and 22DMB, respectively. The single component adsorption isotherms show that the di-branched alkane 22DMB is almost fully excluded mostly due to a steric hindrance since its kinetic diameter (6.2 Å) significantly exceeds the pore size of MIL-140B (3.9 Å). One note that the HOMC simulations slightly overestimate the amounts adsorbed for all C6 isomers. This observation is consistent with the fact that the HOMC simulated unit cell volume of MIL-140B is about 2.3 % higher than the corresponding experimental value[7] as shown in Table IV.2.

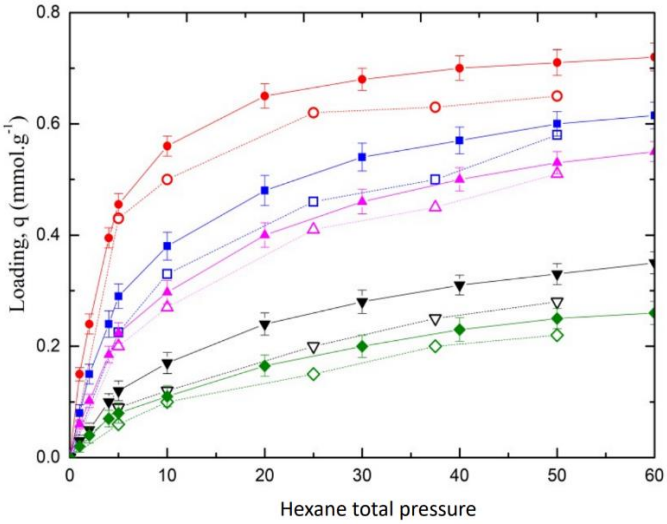

Figure IV.5 *Calculated and experimental single component adsorption isotherms of hexane isomers in MIL-140B at 343 K: HOMC simulations nC6 (●), 2MP (—■—), 3MP, (—▲—) 23DMB (—▼—) and 22DMB (—◆—) and experimental data nC6 (○), 2MP (··□··), 3MP (·· △··), 23DMB (·· ▽··) and 22DMB (··◇··).*

HOMC simulations were further performed for the equimolar quinary mixture. Figure IV.6 first shows a fair agreement between the HOMC and experimental multicomponent adsorption isotherms, the preferential adsorption sequence being the same that obtained from the single component isotherms (Figure IV.5).

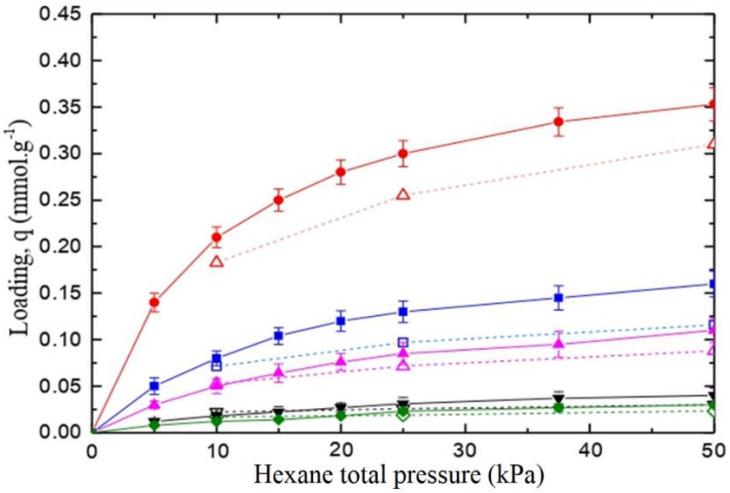

Figure IV.6 *Calculated and experimental equimolar quinary mixture adsorption isotherms of hexane isomers in MIL-140B at 343 K: HOMC simulations nC6 (●), 2MP (—■—), 3MP, (—▲—) 23DMB (—▼—) and 22DMB (—◆—) and experimental data nC6 (○), 2MP (--□--), 3MP (--△--), 23DMB (--▽--) and 22DMB (--◇--).*

The maximum of selectivity was found to be 10.9 for a hexane total pressure of 10 kPa in line with the experimental value of 10.2.[3] Interestingly, we report in Figure IV.7 the tilting angle corresponding to the linker rotation as a function of the total hydrocarbon partial pressure. This figure shows that the degree of reorientation of the organic linker slightly changes upon incremental adsorption, from 10.2° to 7.8°. This emphasizes that the experimental profile cannot be reproduced by considering a single tilted configuration as evoked in the study[3] and that the tilting is impacted by the host/guest and guest/guest interactions. As shown in Figure IV.7, the decrease of the tilting angle as a function of the hexane total pressure is accompanied by a slight increase in the unit cell volume of the MOF (about 0.9 %).

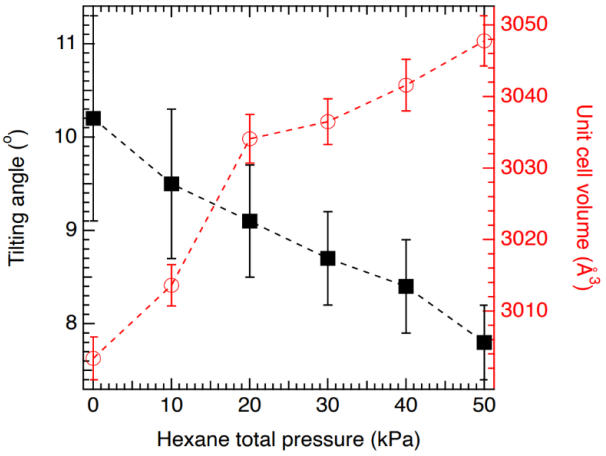

Figure IV.7 *Tilting angle (black square, left axis and black color) and unit cell volume (red circle, right axis and red color) as a function of hydrocarbon partial pressure in quinary mixture at 343 K at 0.1 MPa.*

Compared with the rigid framework, by using the fully flexible force field, the simulation has a satisfying agreement with experimental data. This result confirmed the precision of

HOMC simulation and the hybrid flexible force field of UFF and DREIDING allows reproducing the flexibility of the framework as well as the isotherms.

b) Adsorption and separation of hexane isomers by the mechanical-constrained MIL-140B

We further assessed the impact of the mechanical pressure on the separation performance of MIL-140B for the quinary mixtures. Figure IV.8 a) and Figure IV.8 b) reveal a global decrease of the adsorbed amount for the five components as the mechanical pressure increases from 0.7 GPa et 1 GPa. Interestingly, the amount adsorbed of di-branched isomers decreases more than that of the linear and mono-branched isomers once the mechanical pressure is applied.

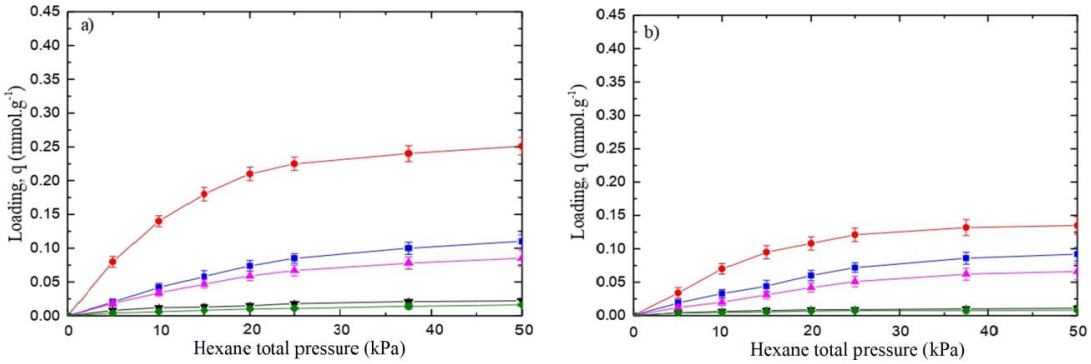

Figure IV.8 *Calculated equimolar quinary mixture adsorption isotherms of hexane isomers in MIL-140B at 343 K at a) 0.7 GPa and b) 1.0 GPa: HOMC simulations nC6 (●), 2MP (—■—), 3MP, (—▲—) 23DMB (—▼—) and 22DMB (—◆—).*

Figure IV.9 shows that this translates into a substantial increase of the overall selectivity by 80% (from 10.9 to 21.5) for a hexane total pressure of 10 kPa (maximum of selectivity). This trend is explained by a pressure-induced reduction of the unit cell volume of the hexane isomers loaded MIL-140B that restricts the accessibility of the pores to the di-branched molecules.

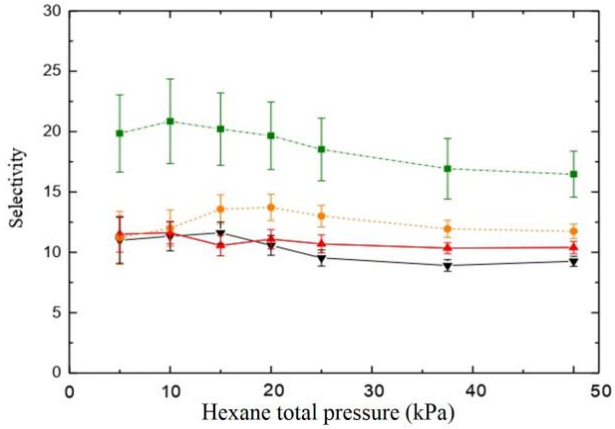

Figure IV.9 *Calculated Selectivity at 0.1 MPa (—▼—), 0.5 GPa (—▲—), 0.7 GPa (—●—) and 1.0 GPa (—■—).*

Typically, the fully hexane isomer quinary mixture loaded MIL-140B under 1 GPa exhibits a unit cell volume of 2644 $Å^3$ vs 3034 $Å^3$ at 0.1 MPa. This unit cell volume

change is accompanied by a decrease of the channel dimension by 0.5 Å as exhibited in Figure IV.10 a) that reports the hexane pressure dependence of channel dimension in pristine and mechanically constrained MIL-140B framework. As shown in Figure IV.10 b) one also observes that the averaged tilting angle of the organic linkers for the hexane loaded MIL-140B is substantially increased under the application of a mechanical pressure of 1 GPa shifting from 9° (mechanically unconstrained material) to 26.8° at for an hexane total pressure of 10 kPa corresponding to the maximum of selectivity suggesting an increase in their rotational degrees of freedom as illustrated in Figure IV.2 where an increase in disorder of the organic linkers as a function of the mechanical pressure is observed.

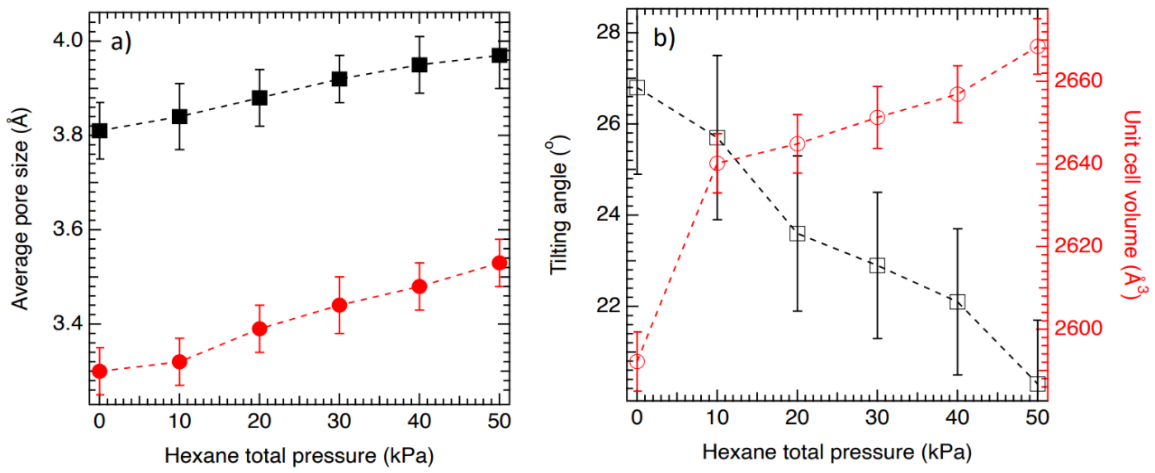

Figure IV.10 *a) Average pore size as a function of hexane total pressure for 0.1Mpa (– ■ –) and 1 Gpa (–●–) b) Titling angle (– □ –, left axis) and unit cell volume (–○–, right axis) as a function of the hexane total pressure for a mechanical pressure of 1 Gpa.*

The origin of the decrease in adsorbed amount when the mechanical pressure is applied can be explained by the increase in the tilting angle of the organic linker combined with the decrease in pore dimension of MIL-140B. Figure IV.10(b) further shows that the tilting angle decreases as the hexane total pressure increases and this decrease is more pronounced than for the mechanically unconstrained MOF (Figure IV.7). Indeed, a drop of 6.8° and 2.2° are observed for the mechanically constrained and unconstrained MIL-140B in the range of hexane total pressure of 50 kPa. Figure IV.11 further evidences that the increase of the mechanical pressure (from 0.1 MPa to 1 GPa) for an hexane total pressure of 10 kPa induces a shortening of the end-to-end distances of mono-branched and di-branched (change between 0.3-0.4 Å) isomers while the length of the linear C6 isomer remains almost unchanged. This highlights that the mono- and di-branched molecules significantly change their conformations in the channels under mechanical pressure while *n*C6 maintains its linear geometry. These results show a pressure-induced cooperative deformation of the channels (Figure IV.11 a) and Figure IV.11 b)) and a distortion of the molecules in the case of 2MP, 3MP, 22DMB and 23DMB. 23DMB and 22DMB amounts decrease more than the 2MP, 3MP and *n*C6 due to their more rigid backbones and the steric hindrance created by the pore size of MIL-140B (3.2 Å) at 1 GPa as shown in Figure IV.11.

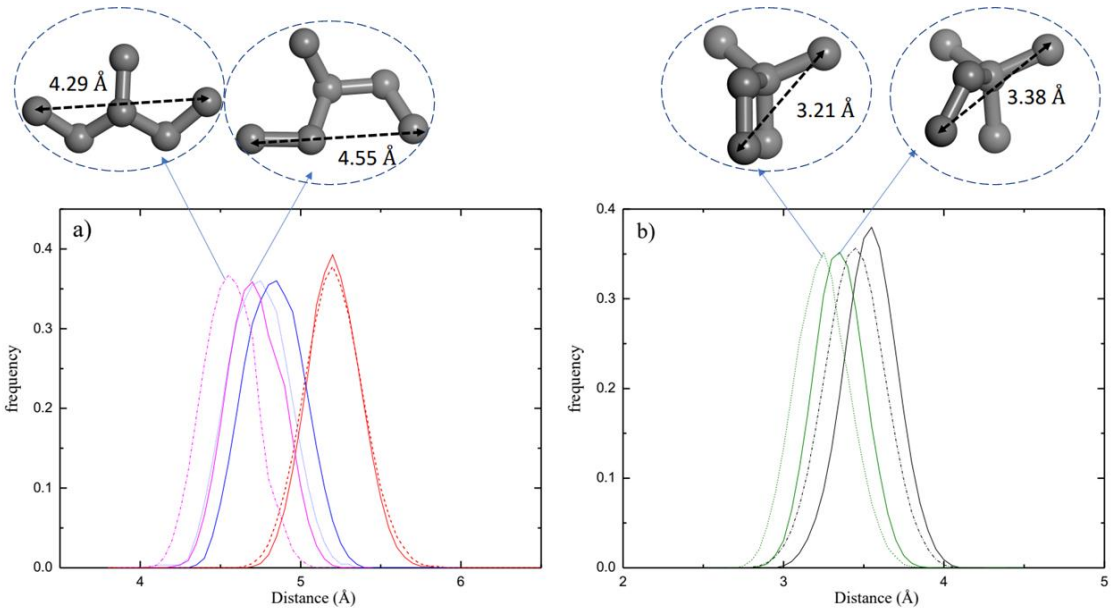

Figure IV.11 *Distribution of the end-to-end distance for a) nC6 (–), 2MP (–), and 3MP (–) b) 23DMB (–) and 22DMB (–) at 0.1 MPa. Distribution of end-to-end distance for a mechanical pressure of 1 GPa are represented in dashed line.*

IV.4 Conclusion

To summarize, HOMC simulations were performed to gain microscopic insight into the separation performance of hexane isomers in the MIL-140B MOF material. We first revealed that a combination of the generic UFF and DREIDING forcefields to describe the flexibility of the MOF was capable to capture the structural features of MIL-140B and to reproduce its C6 isomers single component and quinary mixture adsorption isotherms. We evidenced that the adsorption of the hexane isomers induces a significant tilting of the MOF organic linkers. This tilting angle varies in the range of 7.8°-10.2° upon increase of the hydrocarbon vapor pressure. This highlights that the consideration of a single configuration of the MOF with a fixed tilting angle is not valid to account for the adsorption behavior of MIL-140B in the whole domain of pressure. We further demonstrated that the application of a mechanical pressure leads to a decrease of the adsorbed amount of all hexane isomers resulting from a contraction of the pore dimension and a more pronounced tilting of the organic linkers for the MOF framework. Interestingly, 22DMB and 23DMB are more strongly impacted by the mechanical pressure than *n*C6, 2MP and 3MP due to steric hindrance thus leading to a substantial enhancement of the C6 isomer separation performance of MIL-140B by 80%. This molecular simulation study reveals that the channel dimension of MIL-140B as well as the dynamics of its organic linkers can be controlled by applying mechanical pressure to boost the hexane isomer separation performance of this narrow channel MOF.

Reference

(1) Ghoufi, A.; Maurin, G. Hybrid Monte Carlo Simulations Combined with a Phase Mixture Model to Predict the Structural Transitions of a Porous Metal−Organic Framework Material upon Adsorption of Guest Molecules. *J. Phys. Chem. C* **2010**, *114* (14), 6496–6502. https://doi.org/10.1021/jp911484g.
(2) Zhang, C.; Koros, W. J. Tailoring the Transport Properties of Zeolitic Imidazolate Frameworks by Post-Synthetic Thermal Modification. *ACS Appl. Mater. Interfaces* **2015**, *7* (42), 23407–23411. https://doi.org/10.1021/acsami.5b07769.
(3) Zhao, H.; Maurin, G.; Ghoufi, A. Tuning the Hexane Isomer Separation Performances of Zeolitic Imidazole Framework-8 Using Mechanical Pressure. *J. Chem. Phys.* **2021**, *154* (8), 084702. https://doi.org/10.1063/5.0040469.
(4) Chanut, N.; Ghoufi, A.; Coulet, M.-V.; Bourrelly, S.; Kuchta, B.; Maurin, G.; Llewellyn, P. L. Tailoring the Separation Properties of Flexible Metal-Organic Frameworks Using Mechanical Pressure. *Nat. Commun.* **2020**, *11* (1), 1216. https://doi.org/10.1038/s41467-020-15036-y.
(5) Martin, M. G.; Siepmann, J. I. Novel Configurational-Bias Monte Carlo Method for Branched Molecules. Transferable Potentials for Phase Equilibria. 2. United-Atom Description of Branched Alkanes. *J. Phys. Chem. B* **1999**, *103* (21), 4508–4517. https://doi.org/10.1021/jp984742e.
(6) Zheng, B.; Maurin, G. Mechanical Control of the Kinetic Propylene/Propane Separation by Zeolitic Imidazolate Framework-8. *Angew. Chem.* **2019**, *131* (39), 13872–13876. https://doi.org/10.1002/ange.201906245.
(7) Guillerm, V.; Ragon, F.; Dan-Hardi, M.; Devic, T.; Vishnuvarthan, M.; Campo, B.; Vimont, A.; Clet, G.; Yang, Q.; Maurin, G.; Férey, G.; Vittadini, A.; Gross, S.; Serre, C. A Series of Isoreticular, Highly Stable, Porous Zirconium Oxide Based Metal-Organic Frameworks. *Angew. Chem. Int. Ed Engl.* **2012**, *51* (37), 9267–9271. https://doi.org/10.1002/anie.201204806.
(8) Martin, M. G.; Siepmann, J. I. Transferable Potentials for Phase Equilibria. 1. United-Atom Description of n-Alkanes. *J. Phys. Chem. B* **1998**, *102* (14), 2569–2577. https://doi.org/10.1021/jp972543+.
(9) UFF, a full periodic table force field for molecular mechanics and molecular dynamics simulations | Journal of the American Chemical Society https://pubs.acs.org/doi/10.1021/ja00051a040 (accessed 2021 -12 -07).
(10) Mayo, S. L.; Olafson, B. D.; Goddard, W. A. DREIDING: A Generic Force Field for Molecular Simulations. *J. Phys. Chem.* **1990**, *94* (26), 8897–8909. https://doi.org/10.1021/j100389a010.
(11) Lorentz, H. A. Ueber Die Anwendung Des Satzes Vom Virial in Der Kinetischen Theorie Der Gase. *Ann. Phys.* **1881**, *248* (1), 127–136. https://doi.org/10.1002/andp.18812480110.
(12) Berthelot, D. *Sur Le Mélange de Gaz*; Comptes rendus hebdomadaires des séances de l'Académie des Sciences; 1703; 1898.
(13) Smith, W.; Forester, T. R. DL_POLY_2.0: A General-Purpose Parallel Molecular Dynamics Simulation Package. *J. Mol. Graph.* **1996**, *14* (3), 136–141. https://doi.org/10.1016/S0263-7855(96)00043-4.

(14) Nosé, S. A Unified Formulation of the Constant Temperature Molecular Dynamics Methods. *J. Chem. Phys.* **1984**, *81* (1), 511–519. https://doi.org/10.1063/1.447334.
(15) Hoover, W. G. Canonical Dynamics: Equilibrium Phase-Space Distributions. *Phys. Rev. A* **1985**, *31* (3), 1695–1697. https://doi.org/10.1103/PhysRevA.31.1695.
(16) Ghoufi, A.; Gaberova, L.; Rouquerol, J.; Vincent, D.; Llewellyn, P. L.; Maurin, G. Adsorption of CO2, CH4 and Their Binary Mixture in Faujasite NaY: A Combination of Molecular Simulations with Gravimetry–Manometry and Microcalorimetry Measurements. *Microporous Mesoporous Mater.* **2009**, *119* (1), 117–128. https://doi.org/10.1016/j.micromeso.2008.10.014.
(17) Henrique, A.; Rodrigues, A. E.; Silva, J. A. C. Separation of Hexane Isomers in ZIF-8 by Fixed Bed Adsorption. *Ind. Eng. Chem. Res.* **2019**, *58* (1), 378–394. https://doi.org/10.1021/acs.iecr.8b05126.

Chapter V. Tuning the hexane isomer separation performances of Zeolitic Imidazole Framework-8 using mechanical pressure

V.1 Introduction and context

As previously underlined, the separation of hexane isomers according to the degree of branching is very important in the petrochemical industry to produce high-octane gasoline.[1] For past decades, researchers are looking for the alternatives porous materials for the effective separation to replace zeolite 5A. Metal Organic Frameworks (MOFs)[2–5] have been considered to achieve hexane isomer separation based on complementary mechanisms. We have seen previously that MIL-140B material enable to separate hexane isomers by degrees of branching. Besides MIL-140B, Zeolitic Imidazole Frameworks (ZIFs)[2,3,6–8] is also a prominent candidates, as both MOFs feature small aperture of the pores that can be used for the molecular sieving.

ZIFs show a unique chemical/structural diversity as compared to other reference porous materials such as active carbons, mesoporous silica, and zeolites.[9–13] Indeed, they are highly tunable in terms of pore size/shape and chemical functionality, which make them attractive for molecular separation driven by not only molecular sieving but also thermodynamics, entropic(shape-selectivity), or kinetics.[14] More specifically, among the family of ZIFs, Dubbeldam et al. proposed the zinc-imidazole ZIF-77 as a promising candidate to separate the alkane isomers according to the degree of branching. This computational work assigned the unique separation capability of the ZIF-77 to its 2D-channel architecture; the larger channels allowing to confine the linear and mono-branched isomers, while the smaller channels enable a size-exclusion of the mono- and di-branched molecules.[4] The zinc-methyl imidazole ZIF-8 made of sodalite cages of 11.4 Å connected by a six membered ring with a free pore aperture of 3.4 Å also appears as an attractive candidate for the separation of hexane isomers. The pioneer work reported by Chang et al. revealed by breakthrough experiments that this ZIF can sieve 22DMB from *n*C6[6] as also confirmed later. Silva et al. revealed a complete kinetics-driven separation of nC6 from the branched paraffins by means of ternary *n*C6/3MP/22DMB breakthrough mixture experiments.[15] These studies collected under dynamic modes were completed by a series of experimental works performed under static conditions. Ferreira et al. evidenced that only 22DMB is not adsorbed in ZIF-8 owing to a size exclusion, and Chen et al.[16] observed that *n*C6 is more adsorbed than 2MP allowing a partial separation of the two isomers most probably due to stronger host/guest interactions in the case of the linear alkane.[8] Indeed, so far ZIF-8 has been demonstrated as an excellent selective adsorbent allowing a full separation from *n*C6 to 22DMB; however, its level of performance is far from optimal to separate both linear branched from mono-branched isomers and mono-branched from di-branched isomers, which still remains a challenge for any types of porous adsorbents. Therefore, there is a need to envisage possible routes to boost the C6 isomer separation performance of this ZIF-8 platform.

Our research group delivered a proof-of-concept of an innovative strategy consisting of applying an external mechanical pressure to modulate the pore size/shape of MOFs upon adsorption.[17,18] This pioneered work revealed that a mechanical control of the pore size/shape of the MOFs enables (i) a spectacular enhancement of the kinetics-driven propane/propylene separation by ZIF-8 and (ii) an infinite carbon dioxide selectivity over nitrogen and methane by the highly flexible 1D-channel-like MIL-53 governed by a full-

size exclusion. [17] More recently, this innovative strategy was tested on MIL-140B, which provided a great understanding of separation mechanism on C6 isomers. Therefore, the same approach was implemented to modulate the cage size/shape and pore aperture of ZIF-8 upon adsorption of hexane isomers. This synergistic combination of stimuli (mechanical pressure/guest adsorption) is expected to optimize the separation performance of ZIF-8 for the two challenging linear branched/mono-branched and mono-branched/di-branched isomer mixtures. To that purpose, molecular simulations combining grand canonical Monte Carlo (GCMC) and Molecular Dynamics (MD) techniques into a hybrid osmotic Monte Carlo (HOMC) scheme have been deployed to predict the C6 isomer single component and binary mixture adsorption performance of the mechanically constrained ZIF-8. This computational effort based on a previously validated flexible force field for ZIF-8 [19] reveals an enhancement of both *n*C6/2MP and 2MP/23DMB selectivity under the application of a mechanical pressure above 1 GPa. The microscopic origin of this phenomenon is further elucidated by a careful exploration of the pressure-induced structural changes of the ZIF-8 framework upon adsorption and their consequences on the pore filling mechanism of the C6 isomers.

V.2 Methodology

V.2.1 ZIF-8 and C6 isomers Models

The simulation box corresponding to a 2 × 2 × 2 supercell of ZIF-8, starting with the crystal structure reported.[20] The ZIF-8 force field was developed by the charged flexible force field developed by Zheng et al.[19] The bonds, bending, torsion and improper intramolecular potential terms were described in the force field.

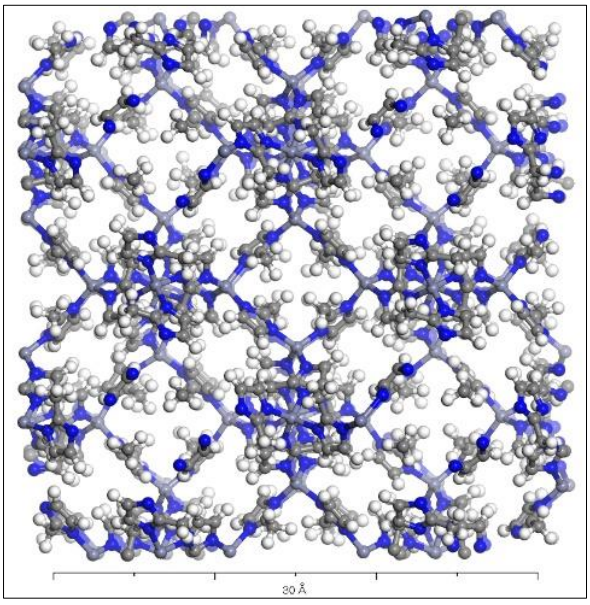

Figure V.1 *Snapshot of 2x2x2 supercell of ZIF-8, view from xy plane. Light purple, blue, grey and white color represent Zinc, Nitrogen, Carbon and Hydrogen atoms, respectively.*

The detailed force field information for ZIF-8 can be found below, Figure V.2 represents the 6 membered ring window in ZIF-8. The detailed ZIF-8 force field information can be found in Appendix, from Table A.1 – Table A.4.

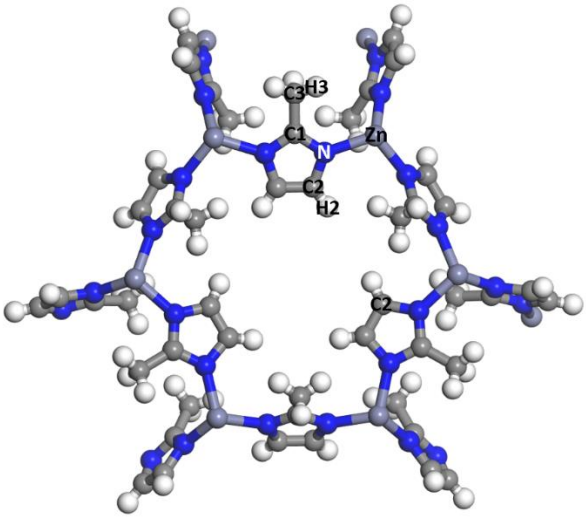

Figure V.2 *ZIF-8 6 membered ring window, with different atom types (C2, H2, C1, C3, H3, N and Zn) indicated in the snapshot. Light purple, blue, grey and white color represent Zinc, Nitrogen, Carbon and Hydrogen atoms, respectively.*

For hexane isomers, TraPPE UA force field was employed which is consistent with previous study on MIL-140B, the force field information of hexane isomers was presented in Chapter III, Table III.1.

V.2.2 Computational details and validation

HOMC simulations on the C6 isomers/ZIF-8 systems were carried out at 373 K. The HOMC simulation method couples GCMC and MD simulations. Theoretical background behind the HOMC method is detailed in chapiter II. In the HOMC simulation step, the MD part consisted of a run of 10^5 steps, with a time step of 0.001 ps. In the GCMC simulations, the chemical potential, temperature, and volume were fixed. All simulations consisted of 10^5 Monte Carlo (MC) steps. The frequencies of insertion/deletion, translation, rotation, and internal rotation trial moves are 0.4, 0.2, 0.2, and 0.2, respectively. For binary mixture additional swapping, the trial move was considered with a frequency, of 0.1 and 0.3 for the insertion/deletion move. A cavity bias (CBMC) was employed to avoid the insertion of the molecules in the sodalite cages as it was previously achieved.[8] To that purpose, we blocked these cages with the use of a dummy atom associated with the following LJ parameters, i.e., ϵ = 10 K and σ = 5 Å. The accessibility to these cages throughout the small pore aperture was only possible during the MD steps by removing the dummy atom. MD steps were performed in the NsT (N: number of particles, s: anisotropic pressure, and T: temperature = 373 K) ensemble where the thermostat (relaxation time of 0.1 ps) and the barostat (relaxation time of 0.5 ps) were both considered by means of Nose–Hoover algorithms.[21,22] Each MD step was accepted following the Metropolis criterion.[23] The mechanical pressure was considered by fixing the pressure through the MD step such as p = 0.1 MPa, 1.0 GPa, and 1.5 GPa. The selectivity of the equimolar mixtures was calculated from the ratio of adsorbed amounts such as $S_{(nC6/2MP)} = q_{nC6}/q_{2MP}$. Additional MC simulations were considered to identify

the preferential distribution and conformation of hexane isomers as well to explore their interactions with the ZIF-8 pore wall through the calculation of the radial distribution functions between hexane isomers/ZIF-8 atom pairs. Furthermore, at a low coverage, the isosteric heat of adsorption for all C6 isomers was calculated from the fluctuations of number of molecules and the energy.[24] Each MD step was performed for 100 ps to reach the thermodynamic equilibrium the convergence of the adsorbed amount of *n*C6 in the case of *n*C6/ZIF-8, the information is presented in Figure V.3.

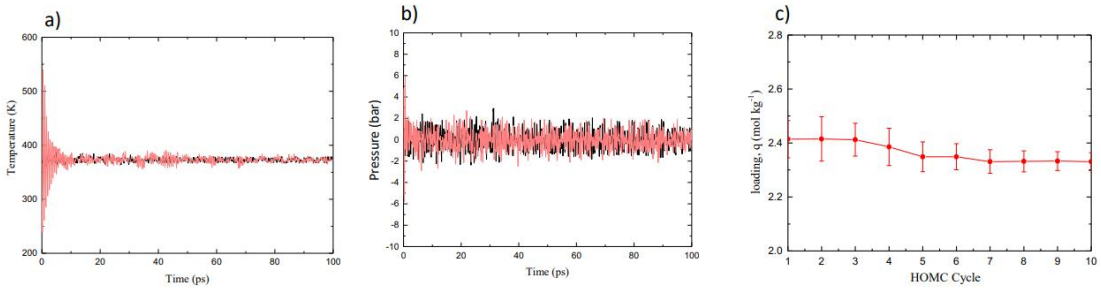

Figure V.3 *Temperature a) and pressure b) time evolution during one MD step, c) nC6 adsorbed as a function of a HOMC cycle.*

The MD simulations were extended to 200 ps in the case that 100 ps was long enough to attain the thermodynamic equilibrium. Regarding the cage blocking, all the C6 isomers fit in the cages of 11.6 Å; however, the cages are only accessible by crossing small pore gate of 3.4 Å. Since the GCMC simulations can randomly insert a molecule inside these cages, all C6 isomers could be directly loaded in these cages. To prevent this, we blocked the cages artificially by considering dummy atoms at their centres. Typically, Figure V.4 clearly evidenced that no blocking of the cages leads to a dramatic overestimation of the experimental 23DMB amount adsorbed, while simulations performed by blocking the cages lead to a good agreement with the experimental values. This validates the use of dummy atoms in our GCMC simulations.

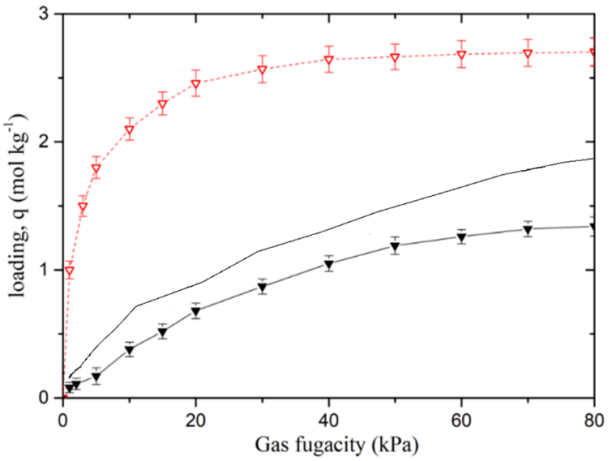

Figure V.4 *HOMC simulated single component adsorption isotherms of 23DMB isomers in ZIF-8 at 373 K with (—▼—), without (··▽··) blocking cages and experimental data (——).*

MD steps however allow the molecules to diffuse through the gate to access the cages. The analyse confirmed also that all cages are homogeneously sampled. This demonstrates that the MD steps allow these molecules to diffuse through the gate to access the cages. Detailed information can be found in Figure V.5.

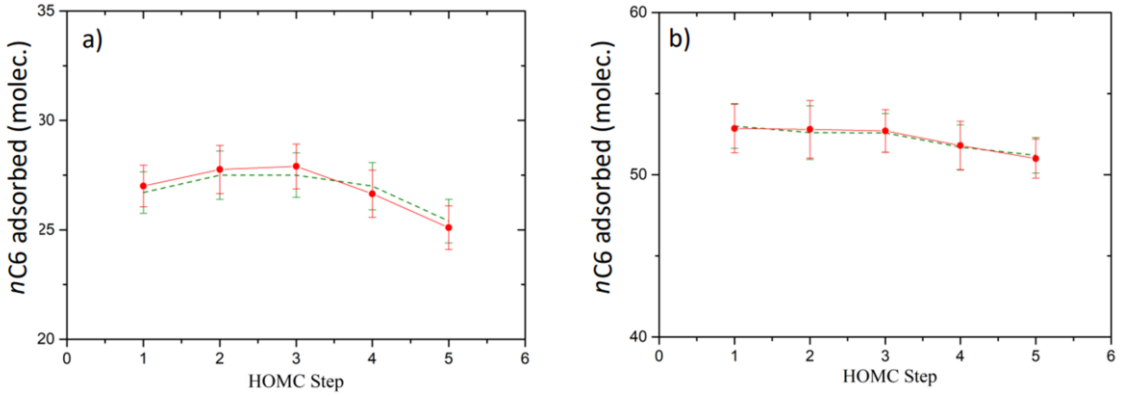

Figure V.5 *nC6 adsorbed as a function of the HOMC steps for two different equilibration time, 100 ps (filled symbols) and 200 ps (dashed line) for a gas fugacity of a) 5 kPa and b) 80kPa.*

We also examined the variation in unit cell volume as a function of simulation time up to 1ns to ensure that the structure maintained its crystallinity even under high mechanical pressure. Figure V.6 presented the unit cell volume variation with and without mechanical pressure upon adsorption of different hexane isomers.

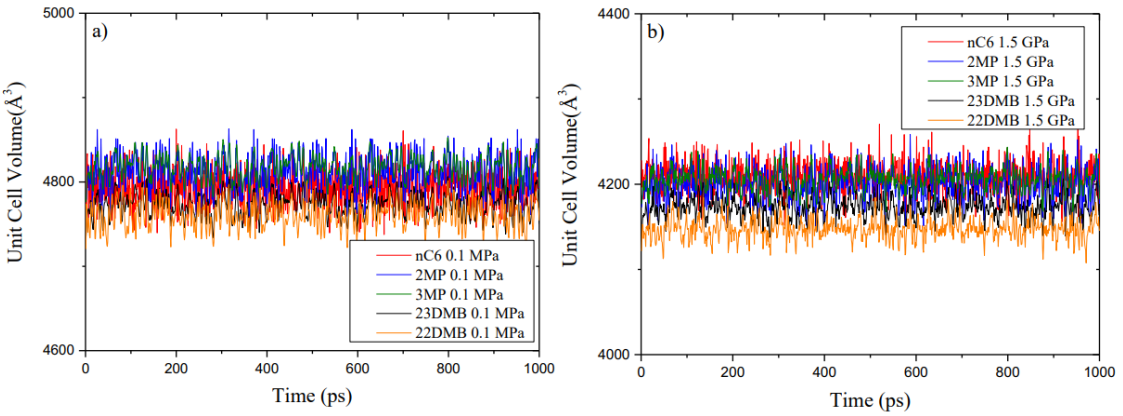

Figure V.6 *Unit cell volume of the fully hexane isomers loaded ZIF-8 as a function of time at 373 K for two pressures at 0.1 MPa and 1.5 GPa.*

V.3 Results and discussion

V.3.1 Adsorption/separation of hexane isomers in ZIF-8

Figure V.7 displays the simulated single component adsorption isotherms for *n*C6, 2MP, 3MP, 22DMB, and 23DMB in ZIF-8. The predicted isotherms are in fair agreement with the previously reported experimental adsorption isotherms,[8,15] which validates the force field parameters used to describe the flexibility of ZIF-8 as well as the ZIF-8/alkanes interactions. It is to be noted that the HOMC simulations slightly underestimate the

amounts adsorbed for all C6 isomers. This observation is consistent with the general shrinking of the unit cell volume during the simulations. First of all, the unit cell volume of ZIF-8 is about 1% lower than the corresponding experimental value,[20] secondly, the cage dimension (at *n*C6 saturation) (10.5 Å) is slightly below the experimental value (10.9 Å).

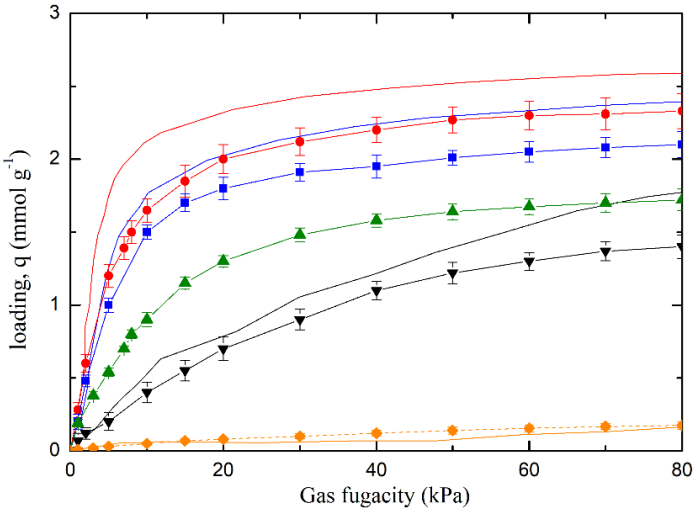

Figure V.7 *Calculated and experimental single component adsorption isotherms[8,15] of C6 isomers in ZIF-8 at 373 K: HOMC simulations nC6 (—●—), 2MP (—■—), 3MP (—▲—), 23DMB (—▼—), and 22DMB (—◆—) and experimental data[8,15] nC6 (———), 2MP (———), 23DMB (———), and 22DMB (———).*

The simulated sorption hierarchy *n*C6 > 2MP > 3MP > 23DMB > 22DMB is found in excellent agreement with the previous adsorption data.[8] This trend is in line with the sequence of the isosteric heat of adsorption calculated at a low coverage: 57.8 (51) kJ mol^{-1}, 53.6 (42.5) kJ mol^{-1}, 51.1 kJ mol^{-1}, 38.5 (35) kJ mol^{-1}, and 31.4 (30.5) kJ mol^{-1} for *n*C6, 2MP, 3MP, 23DMB, and 22DMB, respectively. Although the calculated values slightly differ from the corresponding experimental data (values in bracket), the force field employed enables to capture the energetic trend. The single component adsorption isotherms suggest that the di-branched alkane 22DMB is expected to be almost fully excluded mostly due to a steric hindrance since its kinetic diameter (6.2 Å) largely exceeds the gate size of ZIF-8 (3.4 Å).

As a further stage, HOMC simulations were performed for the three binary mixtures *n*C6/22DMB, *n*C6/2MP, and 2MP/23DMB. The corresponding adsorption isotherms are presented as Figure V.8 – Figure V.10. These scenarios are considered to illustrate the ability of ZIF-8 to separate (i) linear *n*C6 from its mono- and di-branched isomers as well as (ii) mono-branched from di-branched isomers. Figure V.8 first confirms that ZIF-8 sieves the branched 22DMB from the linear isomer. Figure V.9 and Figure V.10 show that *n*C6 is more adsorbed than 2MP and 2MP more than 23DMB in their respective binary mixtures following the sequence of the isosteric heat of adsorption.

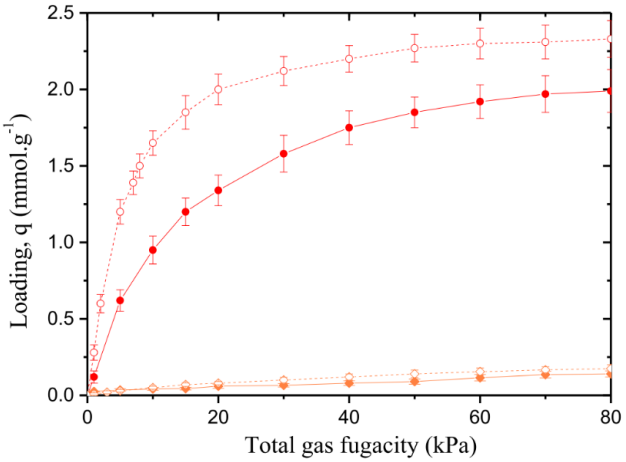

Figure V.8 *HOMC simulated binary mixtures isotherms: nC6 (—●—)/22DMB (—◆—) represented in solid lines and full symbols. nC6 (—○—)/22DMB (—◇—) represent the data simulated for the single component for comparison.*

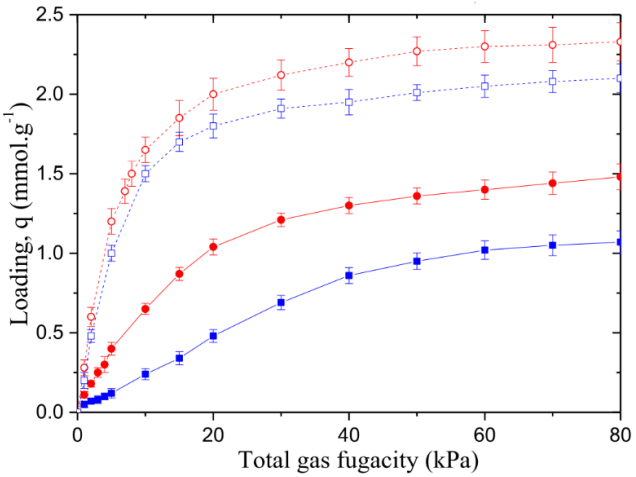

Figure V.9 *HOMC simulated binary mixtures isotherms: nC6 (—●—)/2MP (—■—) represented in solid lines and full symbols. The open symbols and dashed lines: nC6 (—○—)/2MP (—□—) represent the data simulated for the single component for comparison.*

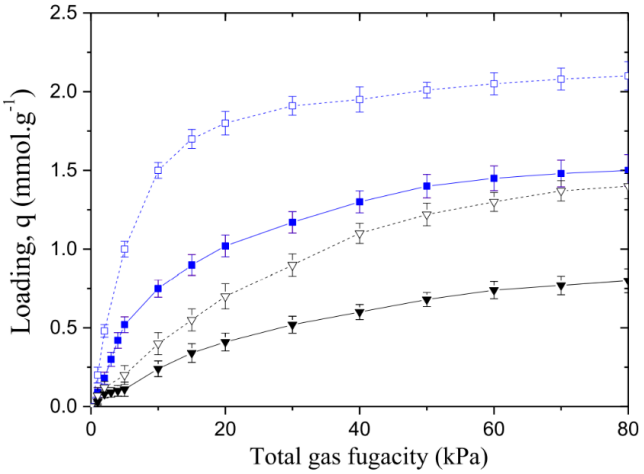

Figure V.10 *HOMC simulated binary mixtures isotherms: 2MP (—■—)/23DMB (—▼—) represented in solid lines and full symbols. The open symbols and dashed lines: 2MP (—□—)/23DMB (—▽—) represent the data simulated for the single component for comparison.*

This observation emphasizes that the two separations are thermodynamically driven although the resulting selectivity is far from optimal, e.g., S(*n*C6/2MP) = 2.5 and S(2MP/23DMB) = 4.7 for a total gas fugacity of 10 kPa.

V.3.2 Adsorption/separation of hexane isomers in mechanical-constrained ZIF-8

As a further step in this study, the mechanical pressure was applied on ZIF-8 in order to investigate its influence on the separation performance. We focused on the two binary mixtures, *n*C6/2MP and 2MP/23DMB to simulate the scenario of linear/mono-branched and mono-branched/di-branched mixtures. First of all, the single component adsorption simulations for *n*C6, 2MP and 23DMB in the mechanically constrained ZIF-8 were performed, with the external pressures of 1 GPa and 1.5 GPa, see Figure V.11 – Figure V.13. Similar to other MOFs under huge mechanical pressure, a general decrease of the adsorbed quantity is observed. This decrease is explained by a pressure-induced decrease of the unit cell volume of the hexane isomers loaded in ZIF-8. Indeed, the fully *n*C6 loaded ZIF-8 under 1.5 GPa pressure shows a unit cell volume of 4104 $Å^3$, versus 4840 $Å^3$ for the empty simulated structure (See Figure V.6). Note that this value is lower than the reported values for propane/propylene,[17] which are 4346 $Å^3$ and 4388 $Å^3$ respectively, as well as oxygen and argon which are 4782 $Å^3$ and 4720 $Å^3$ respectively under similar mechanical pressure. This decrease of the unit cell volume is accompanied by a decrease of the cage dimension by 1 Å, and of the gate size by 0.25 Å. One also observes a change of the gate shape, at 1.5 GPa, the swing angle for the fully *n*C6 loaded ZIF-8 is 40°. This value is similar to the value previously reported for open-gate HP ZIF-8 configuration which is 42°. The same magnitude value is observed for the mechanically constrained 2MP and 23DMB which is 40° and 41°, respectively.

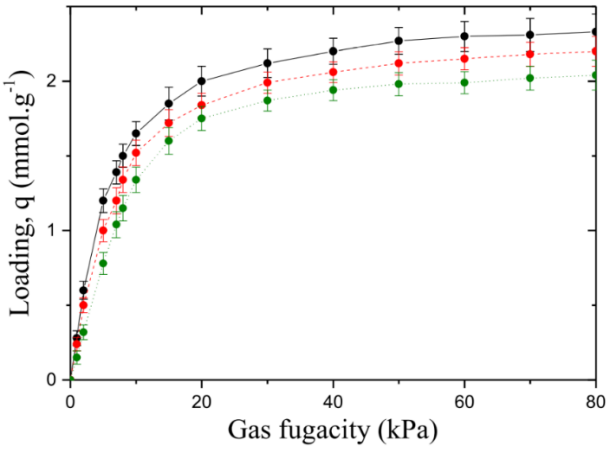

Figure V.11 *HOMC simulated single component adsorption isotherms of nC6 in ZIF-8 at 373 K. Black (—●—), red (---●---), and green (---●---) symbols correspond to a mechanical pressure of 0.1 MPa, 1 GPa, and 1.5 GPa, respectively.*

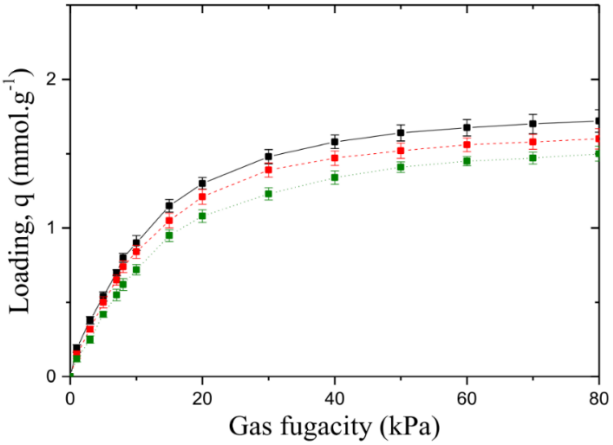

Figure V.12 *HOMC simulated single component adsorption isotherms of 2MP in ZIF-8 at 373 K. Black (—■—), red (---■---), and green (---■---) symbols correspond to a mechanical pressure of 0.1 MPa, 1 GPa, and 1.5 GPa, respectively.*

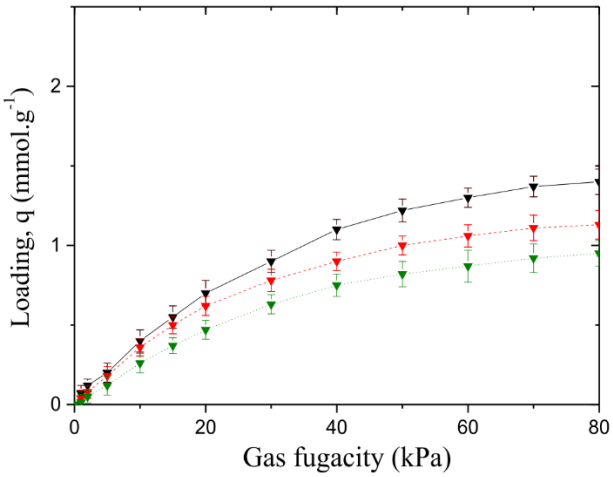

Figure V.13 *HOMC simulated single component adsorption isotherms of 23DMB in ZIF-8 at 373 K. Black (—▼—), red (---▼---), and green (---▼---) symbols correspond to a mechanical pressure of 0.1 MPa, 1 GPa, and 1.5 GPa, respectively.*

It is worth to mention that from the adsorption isotherm obtained, the 23DMB uptake is more affected by the mechanical pressure than 2MP and subsequently than *n*C6. Typically, at 60 kPa, we observe a decrease of the uptake by 44%, 28%, and 14% for 23DMB, 2MP, and *n*C6, respectively, when the pressure goes from 0.1 MPa to 1.5 GPa. This observation indicates that the cage size reduction is more detrimental to the adsorption of the branched isomers due to their bulkiness. Indeed, Figure V.14 – Figure V.16 show that while the end-to-end distance for the linear isomer remains almost unchanged under the application of the mechanical pressure from 0.1 MPa to 1.5 GPa, this geometric feature significantly changes for both 2MP and 23DMB with an associated shortening of the corresponding distance of 0.7 Å and 0.2 Å, respectively, in this range of applied pressure. This highlights that the mono- and di-branched molecules significantly change their conformations in the cages under mechanical pressure, while *n*C6 maintains its linear geometry.

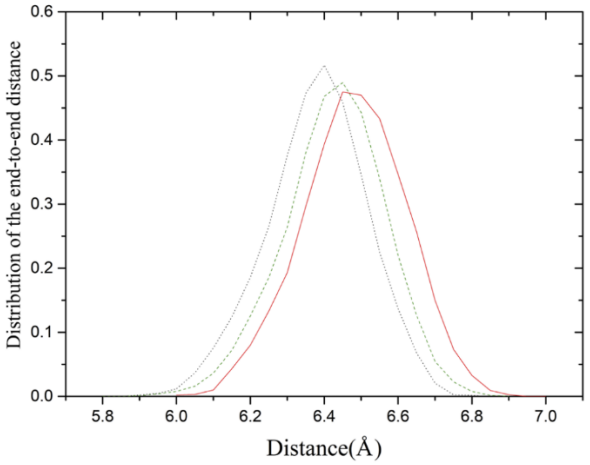

Figure V.14 *Distribution of the end-to-end distance for nC6 at 0.1 MPa (———) and under mechanical pressures of 1 GPa (- - - - - - - -) and 1.5 GPa (·····) for a representative loading of 0.78 mmol/g in the case of single component adsorption.*

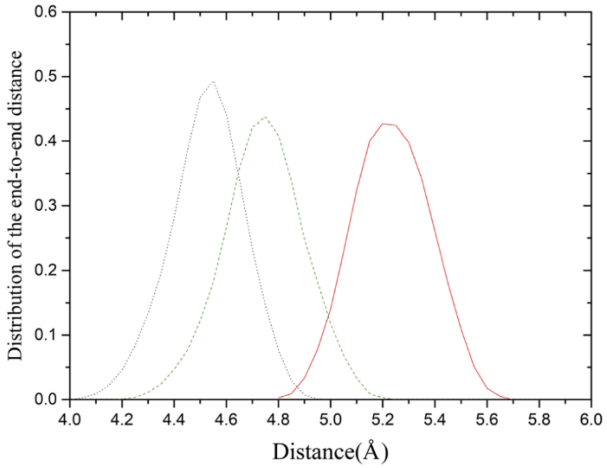

Figure V.15 *Distribution of the end-to-end distance for 2MP nC6 at 0.1 MPa (———) and under mechanical pressures of 1 GPa (- - - - - - - -) and 1.5 GPa (·····) for a representative loading of 0.78 mmol/g in the case of single component adsorption.*

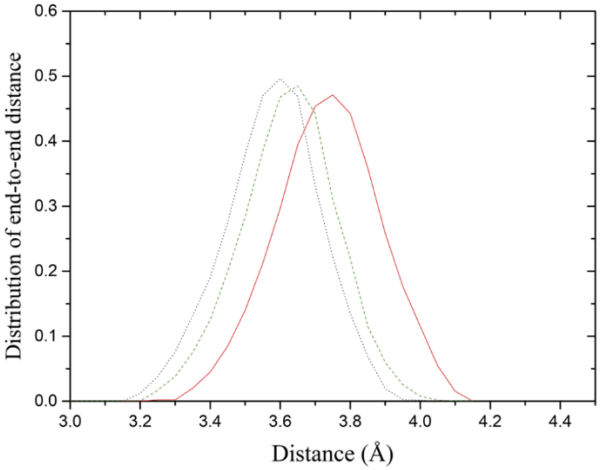

Figure V.16 *Distribution of the end-to-end distance for 23DMB nC6 at 0.1 MPa (———) and under mechanical pressures of 1 GPa (- - - - - - - -) and 1.5 GPa (·····) for a representative loading of 0.78 mmol/g in the case of single component adsorption.*

This is corroborated by the calculation of the dihedral angle distributions for the three isomers, as illustrated in Figure V.17, while we do not observe any changes in the dihedral angle distribution for *n*C6 under 1.5 GPa vs 0.1 MPa, the first peak is shifted for both 2MP and 23DMB and accompanied by the appearance of a second contribution that corresponds to a distortion of their chains. Interestingly, as Figure V.18 shows, the more pronounced structural changes (dihedral angle and end-to-end distance) for 2MP than both *n*C6 and 23DMB is concomitant with a higher shrinkage of the cages of ZIF-8 under mechanical pressure.

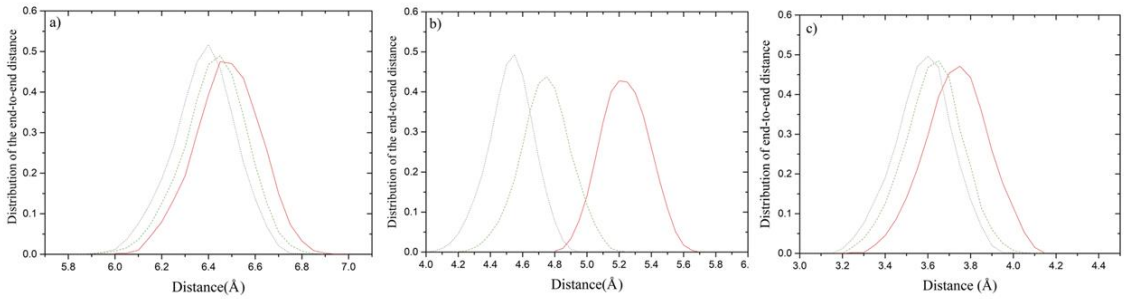

Figure V.17 *Distribution of the end-to-end distance for (a) n-C6, (b) 2MP, and (c) 23DMB at 0.1 MPa (———) and under mechanical pressures of 1 GPa (- - - -) and 1.5 GPa (· · · · · ·) for a representative loading of 0.78 mmol/g for all isomers in the case of single component adsorption.*

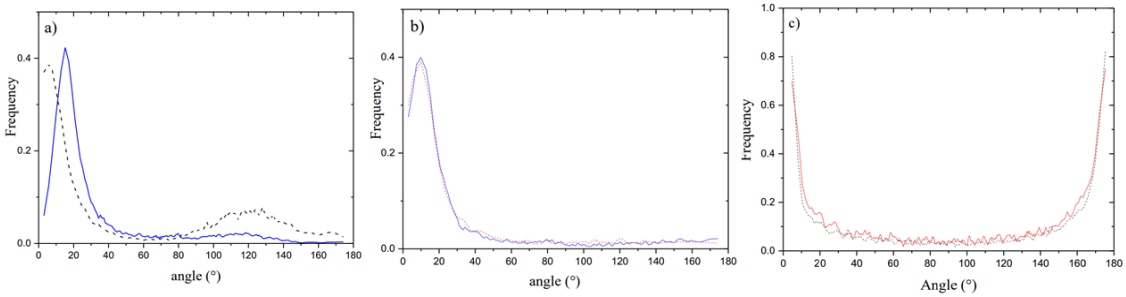

Figure V.18 *Angular distributions of the dihedral angles: a) CH3-CH2-CH2-CH of 2MP CH3- CH2-CH2-CH2, b) nC6 and c) CH3-CH2-CH2-CH2 of 23DMB for the fully loaded ZIF-8 at T= 373 K. 2MP at 0.1 MPa (·····), 2MP at 1.5 GPa (———), nC6 at 0.1 MPa (- - - - - -), nC6 at 1.5 GPa (———), 23DMB at 0.1 MPa (- - - - - -) and 23DMB at 1.5 GPa (———),*

Figure V.19 – Figure V.21 show that the application of the mechanical pressure leads to a higher increase in swing motion of the ZIF-8 linker in the case of 2MP (broader swing angle distribution and maximum located at 40°) than in *n*C6 and 23DMB where the maximum of the swing angle distribution is located at 36°. These results show a pressure induced cooperative deformation of the cages and a distortion of the molecules in the case of 2MP and 23DMB, while the structural local changes of the ZIF-8 framework in the presence of *n*C6 are smaller.

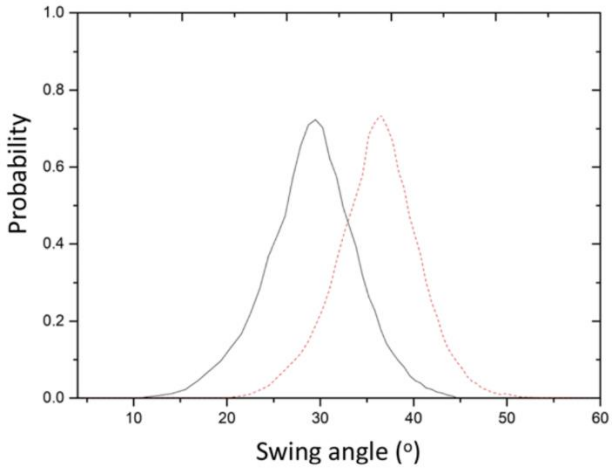

Figure V.19 *Swing angle distribution for nC6 of loaded ZIF-8 (0.78 mmol/g) at 0.1 MPa (- - - - - -), 1 GPa (———), at 373 K.*

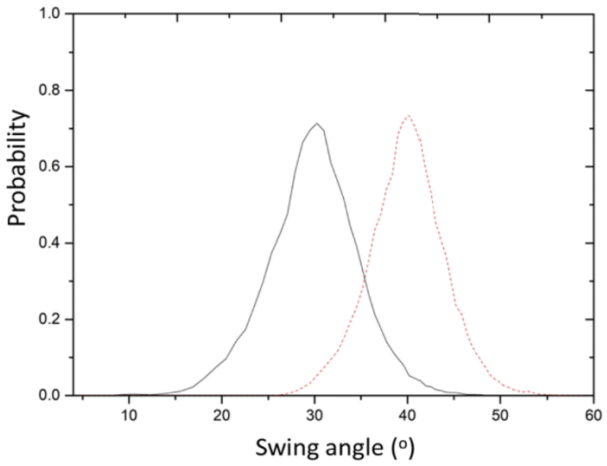

Figure V.20 *Swing angle distribution for 2MP of loaded ZIF-8 (0.78 mmol/g) at 0.1 MPa (--------), 1 GPa (———), at 373 K.*

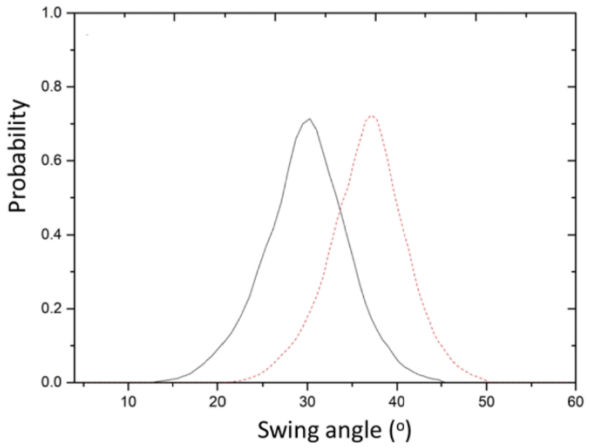

Figure V.21 *Swing angle distribution for 23DMB of loaded ZIF-8 (0.78 mmol/g at 0.1 MPa (--------), 1 GPa (———), at 373 K.*

This result highlights the host/guest interactions interplay on the mechanical response of the hexane isomers loaded ZIF-8. The analyse of the simulation evidenced that the application of the mechanical pressure makes even more pronounced the preferential adsorption of the three isomers in the corners of the cages owing to the shrinkage of the cages, as illustrated in 2D density from Figure V.22.

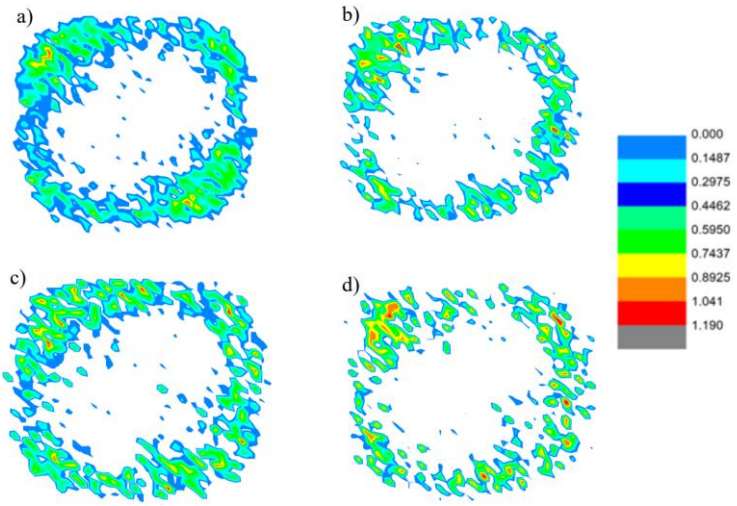

Figure V.22 *Two-dimensional density of a) 2MP at 0.1 MPa, b) 2MP at 1.5 GPa, c) 23 DMB at 0.1 MPa and d) 23 DMB at 1.5 GPa at saturation.*

The above observations pointed out that 2MP is able to change its conformation more easily than 23DMB in response to the pressure-induced contraction of the ZIF-8 porosity. This better adaptability to the mechanical constraint is at the origin of the lowest decrease of the uptake for 2MP vs 23DMB in the whole range of applied mechanical pressure. As ZIF-8 is able to discriminate di-branched C6 hexane isomers, even almost exclude di-branched isomers, so the focus on the separation ability shifts to linear and mono-branched isomers. Figure V.23(a) reports the calculated equimolar binary *n*C6/2MP mixture adsorption isotherms for the mechanically constrained ZIF-8. The application of the mechanical pressure leads to a more pronounced decrease of the 2MP uptake as compared with *n*C6, consistent with the behaviour described above for the corresponding single components. This translates into an increase of the *n*C6/2MP selectivity as reported in Figure V.23(b). Typically, the maximum of the *n*C6/2MP selectivity observed at 10 kPa vapor pressure increases from 2.5 to 4 when the mechanical pressure varies from 0.1 MPa to 1.5 GPa.

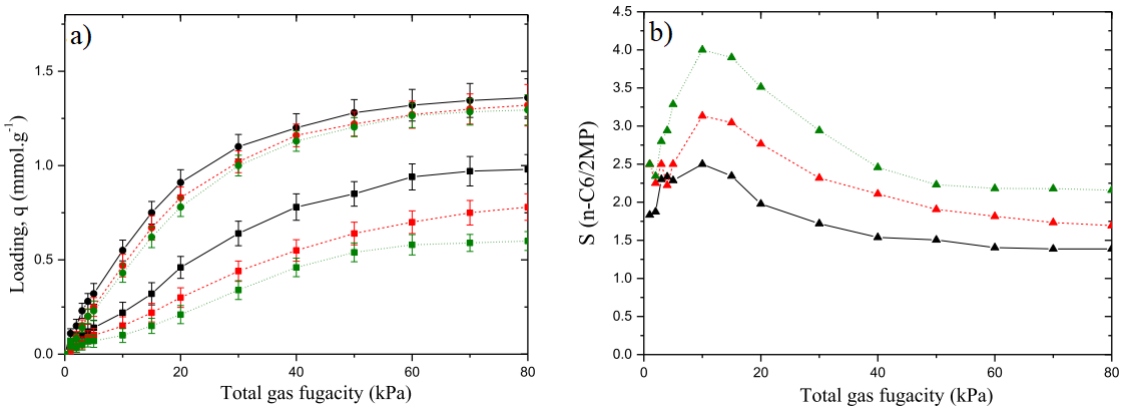

Figure V.23 *HOMC simulated (a) nC6/2MP equimolar binary mixture adsorption isotherms in ZIF-8 at 373 K and (b) selectivity as a function of the total gas fugacity. nC6 (—●—) and 2MP (—■—) at 0.1 MPa; nC6 (---●---) and 2MP (---■---) at 1 GPa pressure; nC6 (····●····) and 2MP (····■····) at 1.5 GPa pressure. (b) nC6/2MP (—▲—) selectivity at 0.1 MPa; nC6/2MP (---▲---) selectivity at 1 GPa pressure; and nC6/2MP (····▲····) selectivity at 1.5 GPa pressure.*

Regarding the 2MP/23DMB mixture, Figure V.24 a) shows that the mechanical pressure affects the uptake of both components in a similar way than for the single adsorption isotherm. Figure. V.24 b) reveals that the gain in terms of selectivity [S(2MP/23DMB)] is not as substantial as it in the case of *n*C6/2MP, the selectivity varying from 3.5 to 4.5 at 10 kPa when the mechanical pressure increases from 0.1 MPa to 1.5 GPa.

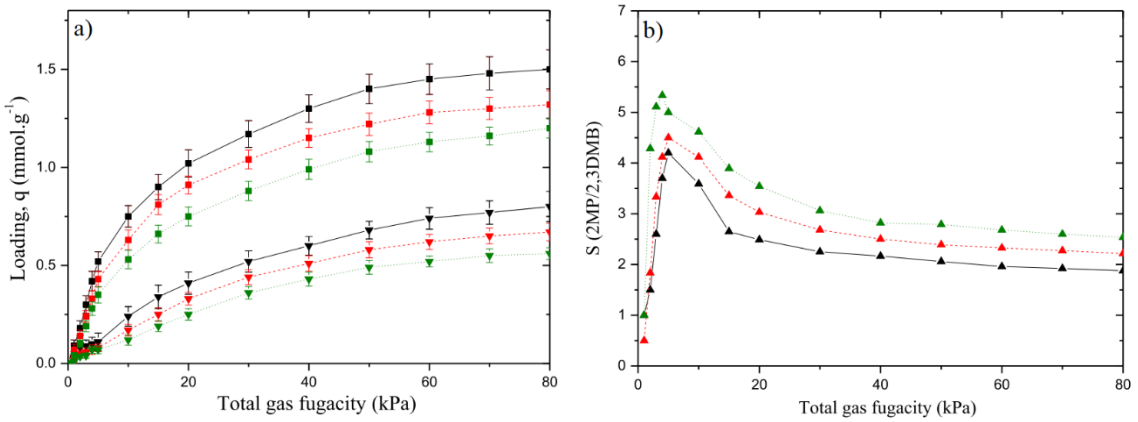

Figure V.24 *(a) 2MP/23DMB equimolar binary mixture adsorption isotherms. (b) Calculated selectivity as a function of the total gas fugacity. 2MP (—■—) and 23DMB (—▼—) at 0.1 MPa; 2MP (···■···) and 23DMB (···▼···) at 1 GPa pressure; 2MP (···■···) and 23DMB (···▼···) at 1.5 GPa pressure; 2MP/23DMB (—▲—) selectivity at 0.1 MPa; 2MP/23DMB (···▲···) selectivity at 1 GPa pressure; and 2MP/23DMB (···▲···) selectivity at 1.5 GPa pressure.*

V.4 Conclusion

In summary, the impact of the mechanical pressure on the adsorption of hexane isomers in ZIF-8 was assessed by HOMC simulations. We validated the force field of ZIF-8 by reproduced the adsorption isotherm and compared with the experimental data. *n*C6/2MP was chosen as the binary mixture of high interest to simulate the scenario of linear/mono-branched isomers mixture. By comparing the selectivity of *n*C6/2MP at different mechanical pressure, we obtained an increase of the selectivity by 30% from 0.1 MPa to 1.5 GPa. We also evidenced that the application of a mechanical pressure above 1 GPa leads to a decrease of the adsorption uptake for all single component hexane isomers in ZIF-8. This results from the shrinkage of the ZIF-8 cage and a reduction of the gate opening leading to a decrease of the accessible porosity, which is proved by the PSD and distribution of swing angle for six membered rings of the gate. The conformation analyses for the adsorbates evidenced that *n*C6 remains linear under the mechanical pressure, both mono- and di-branched molecules show significant conformational changes resulting in a more pronounced pressure-induced decrease of their uptakes. We further revealed that the mechanical pressure induces a significant improvement of the selective behaviour of ZIF-8 with respect to the *n*C6/2MP mixture and in a lesser extent to the 2MP/23DMB mixture. This computational work highlights that the mechanical pressure enables a control of the size/shape of both the gate and cavity of ZIF-8 to optimize its C6 isomer separation performance. We successfully controlled both guest molecules and the application of mechanical pressure simultaneously to tune the pore size and gate shape.

Reference

(1) *Handbook of Petroleum Refining Processes*; McGraw-Hill Education, 2016.
(2) Chen, B.; Liang, C.; Yang, J.; Contreras, D. S.; Clancy, Y. L.; Lobkovsky, E. B.; Yaghi, O. M.; Dai, S. A Microporous Metal-Organic Framework for Gas-Chromatographic Separation of Alkanes. *Angew. Chem. Int. Ed Engl.* **2006**, *45* (9), 1390–1393. https://doi.org/10.1002/anie.200502844.
(3) Bárcia, P. S.; Zapata, F.; Silva, J. A. C.; Rodrigues, A. E.; Chen, B. Kinetic Separation of Hexane Isomers by Fixed-Bed Adsorption with a Microporous Metal−Organic Framework. *J. Phys. Chem. B* **2007**, *111* (22), 6101–6103. https://doi.org/10.1021/jp0721898.
(4) Dubbeldam, D.; Krishna, R.; Calero, S.; Yazaydın, A. Ö. Computer-Assisted Screening of Ordered Crystalline Nanoporous Adsorbents for Separation of Alkane Isomers. *Angew. Chem. Int. Ed.* **2012**, *51* (47), 11867–11871. https://doi.org/10.1002/anie.201205040.
(5) Duerinck, T.; Denayer, J. F. M. Unusual Chain Length Dependent Adsorption of Linear and Branched Alkanes on UiO-66. *Adsorption* **2014**, *2–3* (20), 251–259. https://doi.org/10.1007/s10450-013-9568-6.
(6) Chang, N.; Gu, Z.-Y.; Yan, X.-P. Zeolitic Imidazolate Framework-8 Nanocrystal Coated Capillary for Molecular Sieving of Branched Alkanes from Linear Alkanes along with High-Resolution Chromatographic Separation of Linear Alkanes. *J. Am. Chem. Soc.* **2010**, *132* (39), 13645–13647. https://doi.org/10.1021/ja1058229.
(7) Peralta, D.; Chaplais, G.; Simon-Masseron, A.; Barthelet, K.; Pirngruber, G. D. Separation of C6 Paraffins Using Zeolitic Imidazolate Frameworks: Comparison with Zeolite 5A. *Ind. Eng. Chem. Res.* **2012**, *51* (12), 4692–4702. https://doi.org/10.1021/ie202995g.
(8) P. Ferreira, A. F.; C. Mittelmeijer-Hazeleger, M.; Angelo Granato, M.; Duarte Martins, V. F.; E. Rodrigues, A.; Rothenberg, G. Sieving Di-Branched from Mono-Branched and Linear Alkanes Using ZIF-8: Experimental Proof and Theoretical Explanation. *Phys. Chem. Chem. Phys.* **2013**, *15* (22), 8795–8804. https://doi.org/10.1039/C3CP44381G.
(9) Férey, G.; Serre, C. Large Breathing Effects in Three-Dimensional Porous Hybrid Matter: Facts, Analyses, Rules and Consequences. *Chem. Soc. Rev.* **2009**, *38* (5), 1380–1399. https://doi.org/10.1039/B804302G.
(10) Horike, S.; Shimomura, S.; Kitagawa, S. Soft Porous Crystals. *Nat. Chem.* **2009**, *1* (9), 695–704. https://doi.org/10.1038/nchem.444.
(11) Férey, G.; Serre, C.; Devic, T.; Maurin, G.; Jobic, H.; L. Llewellyn, P.; Weireld, G. D.; Vimont, A.; Daturi, M.; Chang, J.-S. Why Hybrid Porous Solids Capture Greenhouse Gases? *Chem. Soc. Rev.* **2011**, *40* (2), 550–562. https://doi.org/10.1039/C0CS00040J.
(12) Schneemann, A.; Bon, V.; Schwedler, I.; Senkovska, I.; Kaskel, S.; A. Fischer, R. Flexible Metal–Organic Frameworks. *Chem. Soc. Rev.* **2014**, *43* (16), 6062–6096. https://doi.org/10.1039/C4CS00101J.
(13) Kitagawa, S.; Kitaura, R.; Noro, S. Functional Porous Coordination Polymers. *Angew. Chem. Int. Ed.* **2004**, *43* (18), 2334–2375. https://doi.org/10.1002/anie.200300610.

(14) Adil, K.; Belmabkhout, Y.; S. Pillai, R.; Cadiau, A.; M. Bhatt, P.; H. Assen, A.; Maurin, G.; Eddaoudi, M. Gas/Vapour Separation Using Ultra-Microporous Metal–Organic Frameworks: Insights into the Structure/Separation Relationship. *Chem. Soc. Rev.* **2017**, *46* (11), 3402–3430. https://doi.org/10.1039/C7CS00153C.
(15) Henrique, A.; Rodrigues, A. E.; Silva, J. A. C. Separation of Hexane Isomers in ZIF-8 by Fixed Bed Adsorption. *Ind. Eng. Chem. Res.* **2019**, *58* (1), 378–394. https://doi.org/10.1021/acs.iecr.8b05126.
(16) Chen, L.; Yuan, S.; Qian, J.-F.; Fan, W.; He, M.-Y.; Chen, Q.; Zhang, Z.-H. Effective Adsorption Separation of N-Hexane/2-Methylpentane in Facilely Synthesized Zeolitic Imidazolate Frameworks ZIF-8 and ZIF-69. *Ind. Eng. Chem. Res.* **2016**, *55* (40), 10751–10757. https://doi.org/10.1021/acs.iecr.6b02175.
(17) Zheng, B.; Maurin, G. Mechanical Control of the Kinetic Propylene/Propane Separation by Zeolitic Imidazolate Framework-8. *Angew. Chem.* **2019**, *131* (39), 13872–13876. https://doi.org/10.1002/ange.201906245.
(18) Chanut, N.; Ghoufi, A.; Coulet, M.-V.; Bourrelly, S.; Kuchta, B.; Maurin, G.; Llewellyn, P. L. Tailoring the Separation Properties of Flexible Metal-Organic Frameworks Using Mechanical Pressure. *Nat. Commun.* **2020**, *11* (1), 1216. https://doi.org/10.1038/s41467-020-15036-y.
(19) Zheng, B.; Sant, M.; Demontis, P.; Suffritti, G. B. Force Field for Molecular Dynamics Computations in Flexible ZIF-8 Framework. *J. Phys. Chem. C* **2012**, *116* (1), 933–938. https://doi.org/10.1021/jp209463a.
(20) Park, K. S.; Ni, Z.; Côté, A. P.; Choi, J. Y.; Huang, R.; Uribe-Romo, F. J.; Chae, H. K.; O'Keeffe, M.; Yaghi, O. M. Exceptional Chemical and Thermal Stability of Zeolitic Imidazolate Frameworks. *Proc. Natl. Acad. Sci.* **2006**, *103* (27), 10186–10191. https://doi.org/10.1073/pnas.0602439103.
(21) Nosé, S. A Unified Formulation of the Constant Temperature Molecular Dynamics Methods. *J. Chem. Phys.* **1984**, *81* (1), 511–519. https://doi.org/10.1063/1.447334.
(22) Hoover, W. G. Canonical Dynamics: Equilibrium Phase-Space Distributions. *Phys. Rev. A* **1985**, *31* (3), 1695–1697. https://doi.org/10.1103/PhysRevA.31.1695.
(23) Ghoufi, A.; Maurin, G. Hybrid Monte Carlo Simulations Combined with a Phase Mixture Model to Predict the Structural Transitions of a Porous Metal−Organic Framework Material upon Adsorption of Guest Molecules. *J. Phys. Chem. C* **2010**, *114* (14), 6496–6502. https://doi.org/10.1021/jp911484g.
(24) Zhao, H.; Maurin, G.; Ghoufi, A. Tuning the Hexane Isomer Separation Performances of Zeolitic Imidazole Framework-8 Using Mechanical Pressure. *J. Chem. Phys.* **2021**, *154* (8), 084702. https://doi.org/10.1063/5.0040469.

Chapter VI. Molecular Insight into the Slow Dynamics of C4 Hydrocarbons in the Zeolitic−Imidazole Framework ZIF-8

VI.1 Introduction and context

Previously in chapter 5, we evidenced that ZIF-8 is capable of separating hexane isomers, the origin is thermodynamic separation assisted by molecular sieving for di-branched isomers thanks to its narrow gate size of 3.4 Å. However, many systematic studies[1–4] have demonstrated that ZIF-8 is capable to host a variety of large molecules with kinetic diameters up to 7 Å, e.g., xylenes.[5] The mechanism behind such anomalous adsorption behaviour was assigned to a dynamical guest-induced gate opening that occurs due to the pronounced flexibility of the imidazolate linkers, leading to significant gate size fluctuations to enable the molecules to enter the cages.[6–10] Specifically, this porous material was found to be highly attractive for the kinetic-driven separation of short hydrocarbons,[11,12] e.g., ethane/ethene, propane/propene mixtures. Notably, ZIF-8 has been one of the most investigated MOFs for membrane-based hydrocarbons separation over the last few years.[2,13–17] At the same time, despite the practical importance and the growing number of experimental and computational studies, the microscopic mechanisms related to the adsorption/separation of most of the hydrocarbons in ZIF-8 are still not fully understood.

Indeed, all conventional experimental techniques used to directly measure the microscopic diffusivities, such as quasi-elastic neutron scattering (QENS),[18] pulsed-field gradient (PFG)-NMR,[19,20] and IR microscopy,[21] have failed to determine the diffusivities of molecules longer than propane in ZIF-8 due to their very slow mobility and characteristic time. Furthermore, molecular dynamics (MD) simulations applied to such complex systems mostly led to calculated self-diffusivity that underestimates the experimental values even for the shortest hydrocarbons.[22–25] Recently, Alexander E. Khudozhitkov et al established a robust strategy to probe slow inter-cage molecular diffusion in ZIF-8 and similar porous solids based on a ^{2}H NMR spin relaxations analysis.[26] The main idea of this method is to consider the gates of the ZIF-8 cage as potential adsorption sites[8,26] and the translational motion for any guests confined in ZIF-8 decomposed into two events: motions inside the cage, i.e., intra-cage dynamics, and migrations from one cage to another one, i.e., intercage dynamics. It turns out that the two possible location sites, i.e., in the center of the cage (state I) and in the neighbourhood of the gates (state II), are characterized by drastically different dynamics patterns. The molecules within the cage have enough freedom to rapidly rotate in an isotropic manner, while the molecules localized next to the gates perform only local anisotropic motions, e.g., librational motions. In order to gain a complete atomistic picture of the intra- and intercage motions of butane and butene in ZIF-8, MD simulations with flexible force field were carried out.

VI.2 Methodology

The ZIF-8 model used is the same with the one used in chapiter 6. The simulation box corresponding to a 2 × 2 × 2 supercell of ZIF-8. The ZIF-8 force field was developed by the charged flexible force field developed by our collaborator Bin Zheng. The bonds, bending, torsion and improper intramolecular potential terms were described in the force field. The detailed force field information can be found in appendix. TraPPE UA[27,28] force field is employed to model the butane and butene. The detailed information of the force field can be found in the appendix.

MD simulations are performed to explore the translational dynamics of both *n*-butane and 1-butene in ZIF-8 at a loading of 2 molecules per cage to be in line with the NMR conditions. ZIF-8 was treated as fully flexible with the force field parameters taken from our previous work, while the guests were described by the TraPPE-UA flexible model as previously mentioned too. The ZIF-8/guest interactions were evaluated by a Lennard-Jones (LJ) potential term, with cross LJ terms calculated using the Lorentz−Berthelot mixing rule and by considering a cut-off distance set to 12 Å. The initial guest-loaded ZIF-8 configurations were generated by preliminary Monte-Carlo (MC) simulations in the canonical ensemble with the use of 1×10^6 steps. The MD simulations were performed in the NpT ensemble, where N is the number of particles, p is the mechanical pressure (1 bar), and T is the temperature. We used the Nose−Hoover algorithm[29] with the associated relaxation times of 0.5 ps (thermostat) and 0.1 ps (barostat), and the velocity−Verlet integration algorithm as implemented in the DLPOLY 2.2 program.[30]

As the butane and butene diffusion inside ZIF-8 is expected to be very slow at 600K according the experimental value carried out by Alexander E. Khudozhitkov, the probability to capture the intercage motion is low, which translate to a huge computational effort. Therefore, four temperatures were considered: 600, 700, 800, and 1000 K to increase the translational/rotational motions and to increase the probability of the intercage motions. We carefully checked that the guest-loaded ZIF-8 maintains its structural integrity and shows only a small increase of window size in this range of temperature. Three independent MD trajectories for 100 ns were considered to extract averaged values of both the self-diffusion coefficient D_S using Einstein's expression, the cage-to-cage transition time labelled as τ_{tr} and the jump rates (k_{jump}) as well as their corresponding activation energies from the Arrhenius plots.

VI.3 Results and discussion

VI.3.1 ^{2}H NMR relaxation analyses

^{2}H NMR spectra of deuterated *n*-butane and versus temperature for *n*-butane and 1-butene are shown in Figure VI.1(a), (b). The relaxation times for both guests exhibit qualitatively similar behaviour. Temperature dependence of T_1 exhibits a single slope, thus implying a single fast motion of the adsorbed guests. Remarkably, the temperature dependence of T_2 shows an unusual pattern with two regimes: a low-temperature region (labelled as a in Figure VI.1), where T_2 remains almost unchanged, and a high-temperature region (marked as b in Figure VI.1) with a steep decrease-growth pattern. As demonstrated in earlier studies on benzene[31] and propane/propene in ZIF-8,[26] such behaviour is a fingerprint of chemical exchange of guest species between two adsorption states, i.e., state I (in the center of the cage) and state II (in the neighborhood of the gate) exhibiting different individual mobilities.

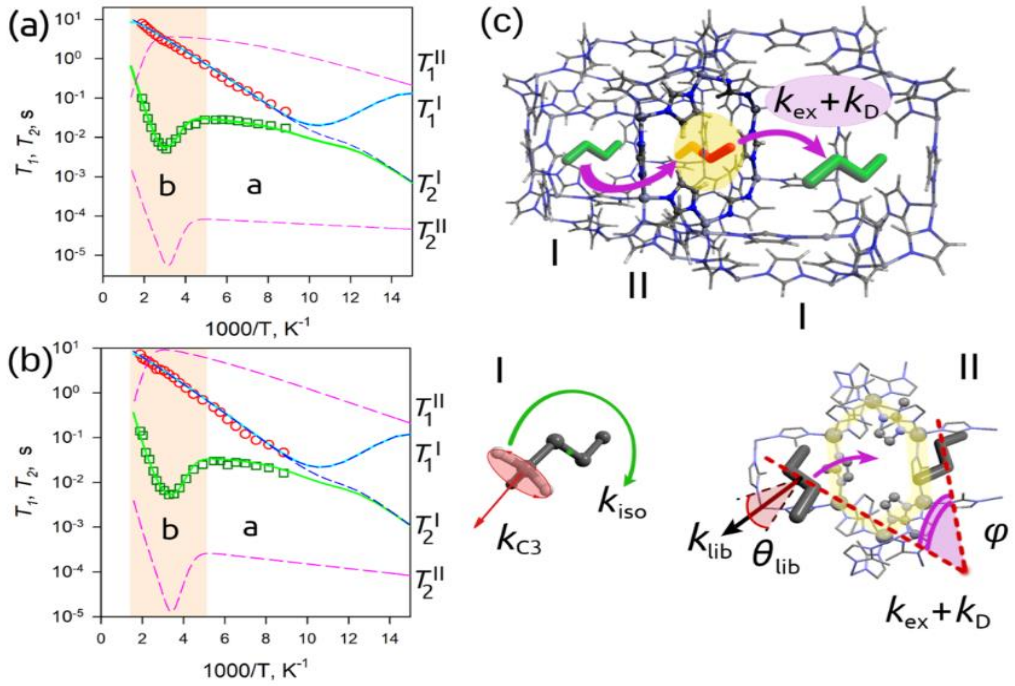

Figure VI.1 *Experimental temperature dependences of T_1 (○) and T_2 (□) with numerical fitting results for n-butane-1,4-d6 (a) and 1-butene-d8 (b) in ZIF-8. K_{ex} and K_D are equilibrium constants. Numerical simulations with elaborated motion models are presented in solid or dashed lines: individual T_1, T_2 I for state I (blue dashed); individual T_1 II, T_2 II for state II (pink dashed); and effective T_1, T_2 after the exchange (solid lines). (c) The guests can migrate between two dynamically different states I and II within the ZIF-8 framework. State I is populated by relatively mobile molecules localized at the center of the cage. State II represents the guest confined at the cage gate and restricted in its dynamics. Here, the ki are the rate constants of the i-th motional process and are related to the corresponding correlation times by $\tau_i = 1/(2\pi ki)$. Figure adapted from the Ref.*[32]

The resulting fits to relaxation curves evidence that the model gives a proper description of the experimental relaxations for both *n*-butane and 1-butene. All corresponding kinetic diameters of the molecular motions are summarised in the Table VI.1.

Table VI.1 *Fitting parameters for T1 and T2 relaxation time (spin-lattice T1 and spin-spin T2 relaxation time) versus temperature dependences of n-butane-1, 4-d6 and 1-butene-d8 adsorbed on ZIF-8. With τ_{iso} represents the fast isotropic reorientation of the molecule and E_{iso} is the corresponding energy, τ_{C3} represents characteristic time of fast internal rotation of the methyl groups and E_{C3} is the corresponding energy. τ_{lib} is characteristic time of restricted libration, E_{lib} is the corresponding energy, τ_{ex} is the time until the size of the gate fluctuates owing to the intrinsic mobility of the linkers and E_{ex} is the corresponding energy, E_D is the activation energy, and τ_D is the characteristic time.*

	***n*-butane**	**1-butene**
E_{iso} (kJ mol^{-1})	6.8 ± 0.5	6.5 ± 0.5
τ_{iso_0} (s)	(3 ± 1) × 10^{-13}	(4 ± 1) × 10^{-13}
E_D (kJ mol^{-1})	34 ± 3	32 ± 3
τ_{D_0} (s)	(8 ± 4) × 10^{-11}	(6 ± 3) × 10^{-11}
E_{C_3} (kJ mol^{-1})	3 ± 1	3 ± 1
τ_{C30} (s)	(3 ± 2) × 10^{-14}	(3 ± 2) × 10^{-14}
E_{lib_1} (kJ mol^{-1})	0.5 ± 0.1	1 ± 0.2
$\tau_{lib_{10}}$ (s)	(4 ± 2) × 10^{-7}	(4 ± 2) × 10^{-7}
E_{ex} (kJ mol^{-1})	1.5 ± 0.2	1 ± 0.2
τ_{ex_0} (s)	(8 ± 2) × 10^{-6}	(3 ± 1) × 10^{-5}

The kinetic parameters for the diffusion of *n*-butane (E_D = 34 kJ mol^{-1}; $\tau_{D_0} = 8 \times 10^{-11}$ s) and 1-butene (E_D = 32 kJ mol^{-1}; $\tau_{D_0} = 6 \times 10^{-11}$ s) are similar. While the ^{2}H NMR provides directly only the correlation time of the motion and its activation barrier, we can nevertheless compute the diffusivities based on the correlation time τ_D and the framework geometry using the Einstein equation to isotropic diffusion model: $D = \langle l^2 \rangle / 6\tau$. Here, l = 1 nm is the average jump length corresponding to the distance between two neighbouring ZIF-8 cage centers, and $\tau = (1/\tau_{ex} + 1/\tau_D)^{-1}$ is a characteristic time between jumps. Thus, the estimated diffusivities D can be calculated: 1.5×10^{-14} and 1.4×10^{-14} m^2 s^{-1} at 308 K for *n*-butane and 1-butene, respectively. These computed diffusivities can be related to those previously derived only for *n*-butane using the gravimetric uptake curves conducted at this same temperature (308 K) by Eum et al.,[3] which afforded a value of transport diffusivity of 2.5×10^{-14} m^2 s^{-1} and a Maxwell−Stefan diffusivity of 1.5×10^{-14} m^2 s^{-1}.

Table VI.2 *Diffusion Coefficients (D) and Activation Barriers (E_D) for n-Butane, 1-Butene, n-Propane,* [26] *and Propene in ZIF-8 Measured by ^{2}H NMR at 243 K.*

	***n*-propane**	**propene**	***n*-butane**	**1-butene**
D (m² s-1) 308K	6.1×10^{-15}	1.3×10^{-12}	1.5×10^{-14}	1.4×10^{-14}
E_D (kJ mol^{-1})	38	13.5	34	32

The thermal activation process for the two hydrocarbons dominates above 330 K. Typically, at 343 K, the estimated diffusivities D are 2.6×10^{-14} and 4.1×10^{-14} m^2 s^{-1} for *n*-butane and 1-butene, respectively. At the same time, the intercage transport driven by the dynamics fluctuation of the gate's aperture dominates at lower temperatures and leads to D values of 1.0×10^{-14} and 0.37×10^{-14} m^2 s^{-1} for *n*-butane and 1-butene at 243 K, respectively. These values are summarized in Table VI.2 and compared to those we previously derived by the same approach for *n*-propane and propene.[26]

VI.3.2 Molecular Dynamic simulation

In order to gain more microscopic insight, the molecular dynamic simulations were carried out. The simulations were performed on relatively high temperature in order to increase the intercage motion observed. 4 temperatures were considered, 1000K, 800K, 700K and 600K. MSD was then calculated as shown in Eq. VI.1:

$$MSD(t) = \frac{\langle \sum_{t_0} \sum_{i=1}^{N} [r_{c,i}(t_0 + t) - r_{c,i}(t_0)] \rangle}{N N_0 t} \qquad \text{Eq. VI.1}$$

Where $r_{c,i}$ is the position of the centre of mass for atom i, t_0 is the time origin, and N is the number of the molecules and N_0 is the number of the time origin. The Figure VI.2 below presents the calculated Mean Squared Displacement (MSD) for *n*-butane and 1-butene.

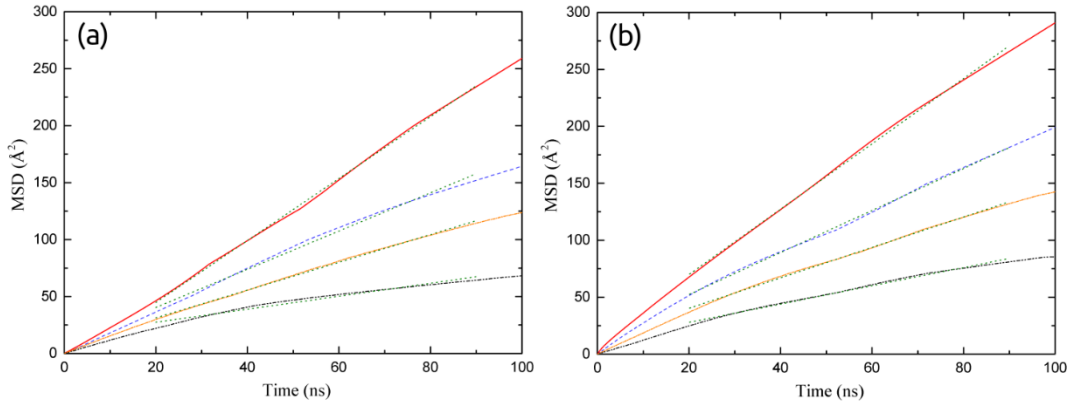

Figure VI.2 *Averaged MSD calculated for (a) n-butane and (b) 1-butene at different temperatures. 1000K, 800K, 700K, 600K. Dotted lines represent the linear fit.*

The self-diffusivity D_s was calculated using the Einstein's equation:

$$D_s = \frac{MSD}{6t} \qquad \text{Eq. VI.2}$$

The self-diffusivity D_s for *n*-butane and 1-butene were then extracted. The intercage transition time can also be extracted thanks to the analysis of the trajectory file from the variation of the coordinates of the atoms. In order to evaluate the self-diffusivity and transition time at 308K, the Arrhenius plots were plotted in Figure VI.3 in order to extrapolate the value.

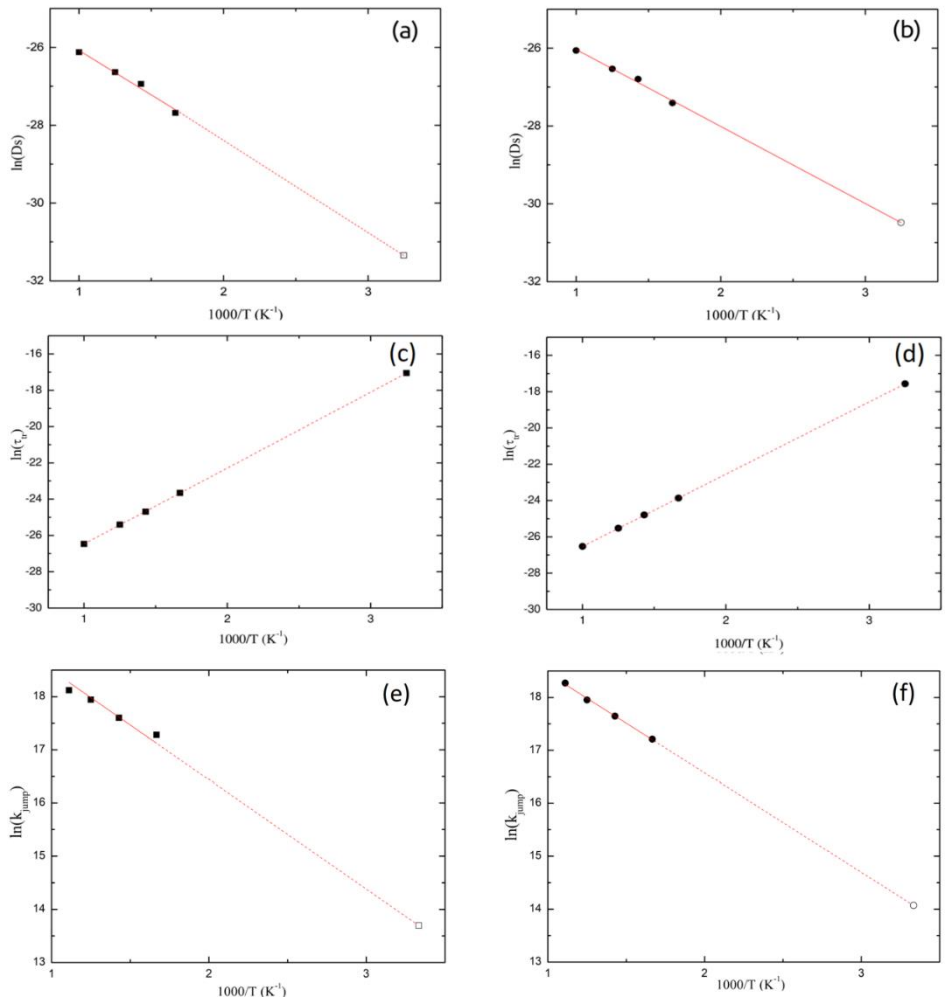

Figure VI.3 *Arrhenius plots for (1) the simulated self-diffusion coefficients (D_S) for (a) n-butane and (b) 1-butene, (2) the transition time τ_{tr} for the intercage jump for (c) n-butane and (d) 1-butene and (3) jump rate k_{jump} (calculated by counting the number of jumps per MD simulation time) for (e) n-butane and (f) 1-butene. Filled and empty symbols represent the simulated data and the extrapolated point at 308 K, respectively. Dotted line corresponds to the linear fit.*

The self-diffusivity D_s calculated and intercage transition τ_{tr} are summarised in the Table VI.3.

Table VI.3 *MD-Simulated Self-Diffusion Coefficients (D_S) and Intercage Transition Times (τ_{tr}) for n-Butane and 1-Butene at Different Temperatures and Extrapolated at 308 K.*

	***n*-butane**		**1-butene**	
T (K)	D_s (m^2 s^{-1})	τ_{tr} (s)	D_s (m^2 s^{-1})	τ_{tr} (s)
308	2.4×10^{-14}	3.9×10^{-18}	3.3×10^{-14}	2.35×10^{-8}
600	9.5×10^{-13}	5.3×10^{-11}	1.4×10^{-12}	4.3×10^{-11}
700	2.0×10^{-13}	1.9×10^{-11}	2.3×10^{-12}	1.7×10^{-11}
800	2.7×10^{-12}	9.2×10^{-12}	3.0×10^{-12}	8.2×10^{-12}
1000	4.5×10^{-12}	3.2×10^{-12}	4.8×10^{-12}	3.0×10^{-12}

These calculated values are equivalent to those predicted by Verploegh et al. at the same temperature and 1.01 bar (1-butene: 7.00×10^{-14} m^2 s^{-1} and *n*-butane: 6.45×10^{-14} m^2 s^{-1}) using biased MD simulations implementing the DFT-derived intra ZIF-FF force field.[33] From our work, the simulated D_S overestimates the experimental values by a factor of ~2; this magnitude of deviation is lower than that classically observed for the diffusion of molecules in highly confined zeolites/MOFs when characterized by very slow dynamics.[22–25] Here, the overestimation of the diffusivity by our MD simulations is in line with a lower predicted activation barrier for the self-diffusion compared to the value obtained for the experimental diffusivity: 18.9 vs 34 kJ mol^{-1} for *n*-butane and 16.4 vs 32 kJ mol^{-1} for 1-butene. MD trajectories were analysed carefully to grasp the microscopic diffusion mechanism. Figure VI.3 shows that the trajectory implies intracage motions followed by a much less frequent intercage jump event. By counting the number of jumps in the MD trajectories for all temperatures, we evaluated the jump rates (k_{jump}) of 8.85×10^5 and 1.02×10^6 s^{-1} at 308 K for *n*-butane and 1-butene, respectively. A detailed inspection shows that at all temperatures, this cage-to-cage transition is associated with a fast displacement over ~0.8 nm, see Figure VI.4, which is consistent with the averaged jump length of 1 nm we considered for the evaluation of the experimental diffusivity as stated above.

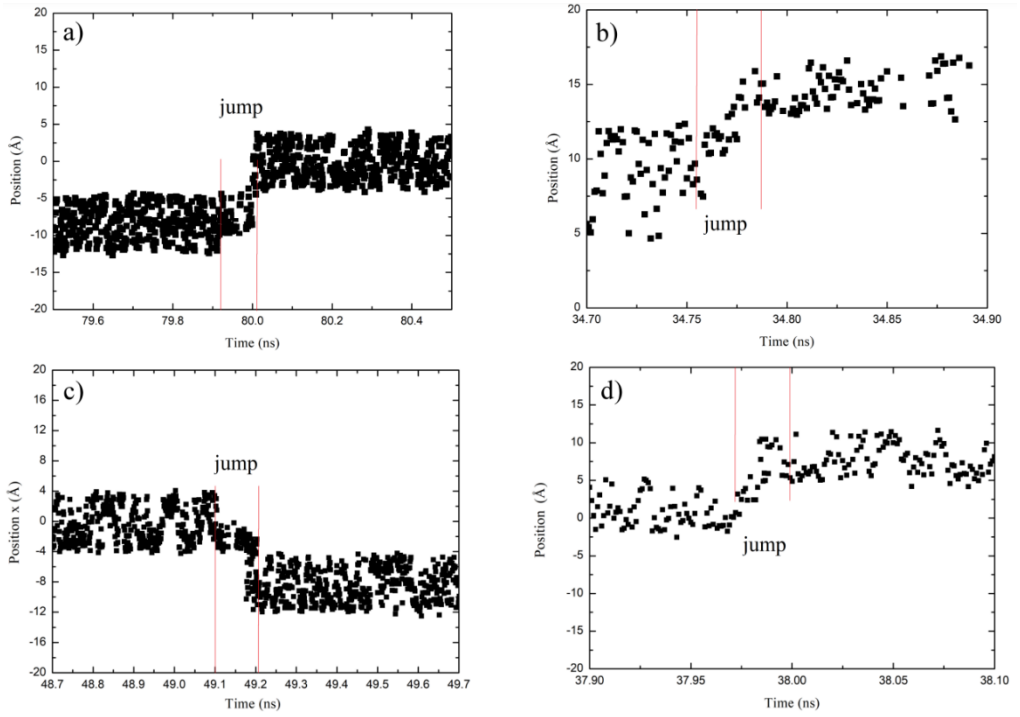

Figure VI.4 *Time-evolution of the center of mass of the molecule along x axis. (a) n-butane at 600K, (b) n-butane at 1000K, (c) 1-butene at 600K and (d) 1-butene at 1000K. The intercage jump event is shown with the vertical red lines.*

Temperature dependence of the time required for the jump, i.e., transition time labelled as τ_{tr}, shows an Arrhenius-type behaviour, which leads to activation barriers of 34.7 kJ mol^{-1} for *n*-butane and 33.1 kJ mol^{-1} for 1-butene, in excellent agreement with the experimental values (34 and 32 kJ mol^{-1} respectively).The simulated transition time value τ_{tr} for 1-butene (2.35×10^{-8} s) is slightly shorter than that for *n*-butane (3.9×10^{-8} s) extrapolated at 308 K, consistent with lower activation energy for 1-butene again in good agreement with the NMR findings.

Thanks to the trajectory generated by MD simulation, which offer us the opportunity to visualise the process of the gate crossing. As illustrated in Figure VI.5.

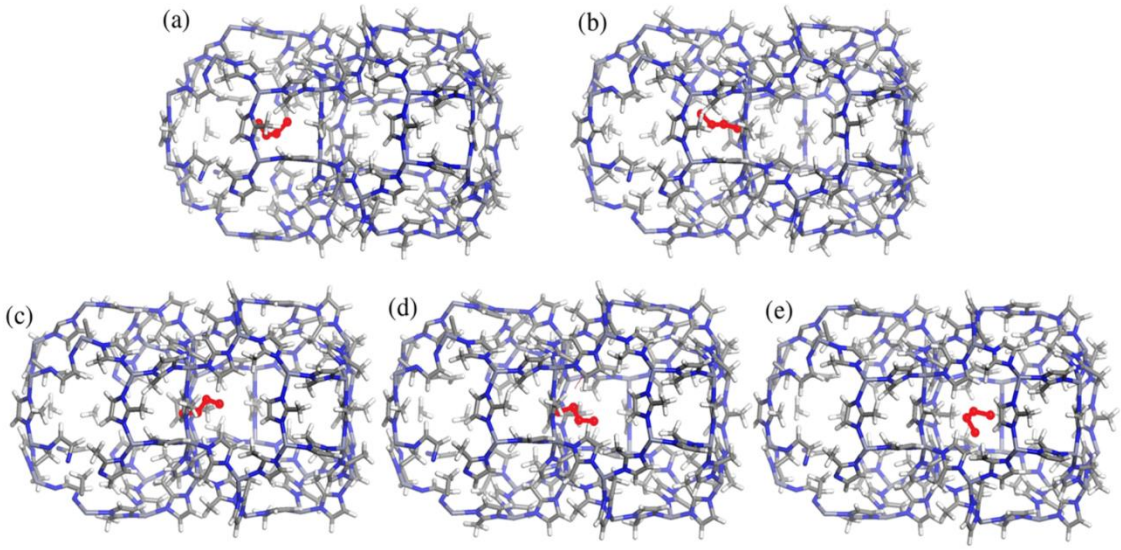

Figure VI.5 *Illustration of the progressive crossing of the ZIF-8 gate by n-butane from the center of the cage (a) to the neighbor cage (e) extracted from the MD trajectory recorded at 600 K. The alkane adapts its conformation (b, c) prior to crossing the gate (d); the time required for this alkane rearrangement and gate crossing is about 150 ps.*

After the comparison of the simulated and experimental results, the following question arises: why is the activation barrier for the simulated self-diffusivity notably lower than the value obtained for the cage-to-cage transition time? The answer is hidden in the complexity of the diffusion mechanism in such a confined system since the self-diffusivity calculated by MD simulations corresponds to an averaged value over the whole trajectory time, which implies two distinct diffusion events, the intracage diffusion and cage-to-cage transition. The intracage diffusion is governed by the same energy barrier as the in-cage isotropic rotation monitored by ^{2}H NMR for the mobile state I and is expected to be notably smaller than the barrier needed to overcome the cage gate for the jump from one cage to another. Moreover, as mentioned above, the intercage jump event is a rare event along the MD trajectory and the molecules need to adapt an optimal arrangement before crossing the windows. The self-diffusion coefficients extracted from such MD trajectories provide a certain weighted average of the two elementary steps of the dynamics process, i.e., diffusion in the cage and intercage jump, associated with the characteristic time for the intracage diffusion and intercage motion labeled as τ_s and τ_{tr}, both of which have a fixed displacement length limited by the dimension of the cage and the aperture of the gate windows. Normally, the slowest process should be the limiting one and thus governing the activation barrier, but not at conditions when the frequency of the intracage diffusion events is much higher than the one corresponding to the intercage jumps. Thus, the presented approach to investigate the transition event provides a robust protocol to elucidate the long-range diffusion in systems with a cage topology, such as ZIF-8. This overall accordance with experimental results served to validate our computational findings for further exploring in-depth the microscopic mechanism that governs the dynamics of both guests in ZIF-8. Figure VI.4 shows that the gate crossing is very fast (about 3 ps at 1000 K and 30−40 ps at 600 K) and progressive for both guests

without any evidence of an abrupt translational jump. Figure VI.6 reveals that there is a significant expansion of the window size (from 3.35 to 3.6− 3.65 Å) once both *n*-butane and 1-butene cross the gate, consistent with the simulated data reported previously for diverse guests.[23]

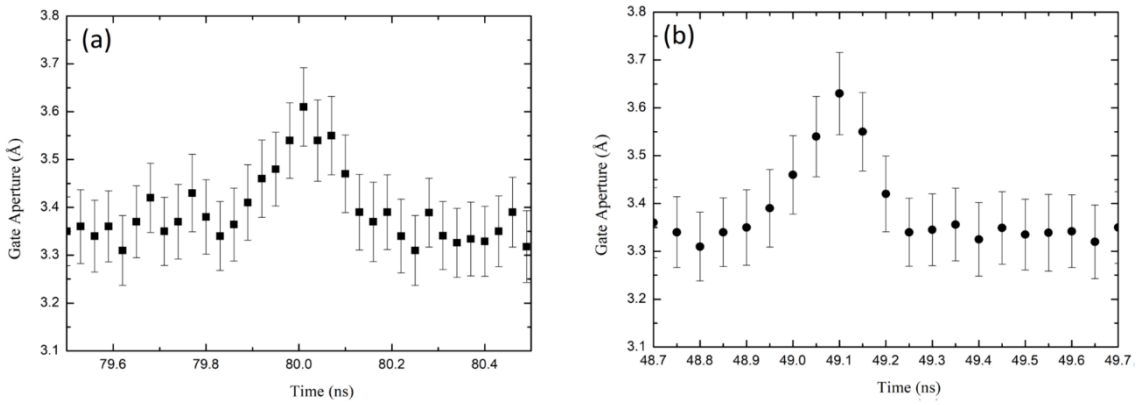

Figure VI.6 *Time-evolution of the window size for (a) n-butane at 600K and (b) 1-butene at 600 K.*

Typically, the transition from one cage to another is illustrated for *n*-butane in Figure VI.5 from an MD trajectory recorded at 600 K. This shows that *n*-butane needs to adopt a linear conformation in the cages prior to slide through the gate. The small size of the gate aperture implies an interacting distance of 3.1 Å between the terminal CH_3 groups of both guests and the H-atom of the methyl-imidazolate linker as shown in the radial distribution function plots reported in for both *n*-butane and 1-butenebetween the two guests and the methyl-imidazolate linker when crossing Figure VI.7. One can however notice that the intensity of the RDF peak present around 5 Å for CH_3 groups/C-atom of the linker pair is significantly more pronounced for *n*-butane as compared to 1-butene (Figure VI.7). This observation suggests that a higher degree of a steric hindrance (excluded volume) is felt by *n*-butane once crossing the gate in line with its larger kinetic diameter vs 1-butene (4.68 vs 4.46 Å) resulting in a lower simulated diffusivity for the alkane. This orientation change during the squeezing through the gate is responsible for the specific behavior of the ^2H NMR T_2 relaxation curve of the diffusing species. In conclusion, the MD results support the mobility mechanism inferred from the ^2H NMR data.

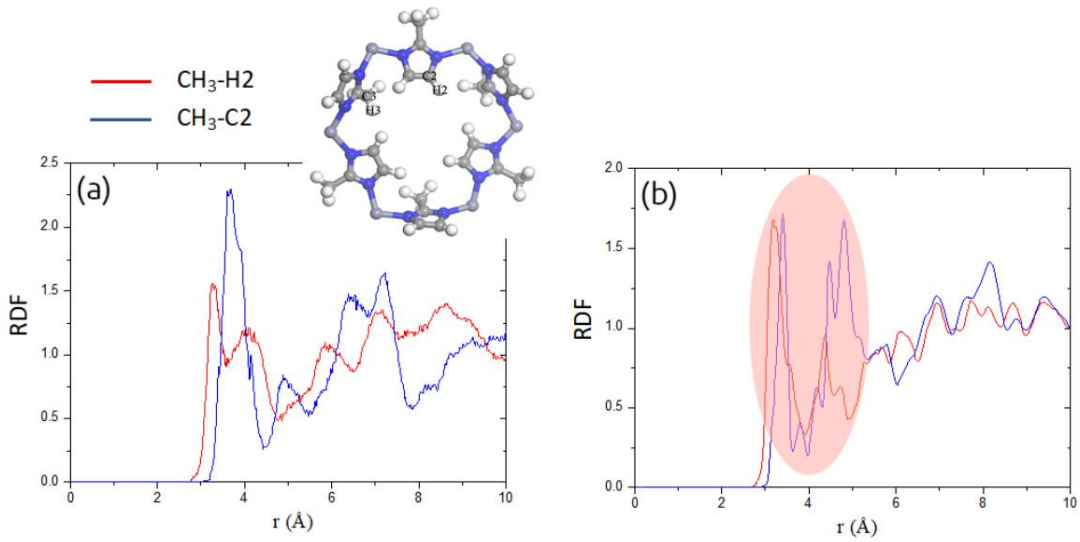

Figure VI.7 *Radial distribution functions calculated between the terminal methyl groups of 1-butene (a) and n-butane (b) and the atoms of the ZIF-8 gate (H2 and C2 represented in upper panel) of (a)).*

VI.4 Conclusion

We have performed a computational (MD) work to support the experimental (^{2}H NMR) study of the C4 hydrocarbons diffusion mechanism through ZIF-8. The numerical fit of the ^{2}H NMR T1 and T2 relaxation times vs temperature dependences yielded a detailed mechanism of the *n*-butane and 1-butene mobility in ZIF-8. These guest molecules were found to populate two dynamic states, localized in the central part of the cage and on the cage wall nearby the windows. Both C4 hydrocarbons are primarily involved in a fast isotropic reorientation inside the cage, whereas in the vicinity of the windows these guests can perform only intramolecular rotations and confined librations. These librational motions are associated with the molecule orientational change during the transition of the molecule from one cage to another. This motion thus reflects the lifetime of the state localized at the gate of the cage. We have further provided the first experimental evaluation of the microscopic diffusivity and activation barriers for *n*-butane and 1-butene in ZIF-8. The diffusion of 1-butene was found to be only slightly faster than *n*-butane, thus suggesting that the kinetics-driven separation of this mixture by ZIF-8 is hardly feasible. The computational results fully support the proposed dynamics picture for both *n*-butane and 1-butene and are capable to derive the diffusivity and energy barriers for long-range diffusion within the ZIF-8 framework. We showed that our combined NMR-modelling method provides a robust tool to probe molecular mobility at an atomistic level even for slowly diffusing species in ordered cagelike porous frameworks. This work is another perfect example of how molecular simulation assisted the understanding on the experiments, and evidenced the experimental model.

Reference

(1) Gee, J. A.; Chung, J.; Nair, S.; Sholl, D. S. Adsorption and Diffusion of Small Alcohols in Zeolitic Imidazolate Frameworks ZIF-8 and ZIF-90. *J. Phys. Chem. C* **2013**, *117* (6), 3169–3176. https://doi.org/10.1021/jp312489w.

(2) Zhang, K.; Lively, R. P.; Zhang, C.; Chance, R. R.; Koros, W. J.; Sholl, D. S.; Nair, S. Exploring the Framework Hydrophobicity and Flexibility of ZIF-8: From Biofuel Recovery to Hydrocarbon Separations. *J. Phys. Chem. Lett.* **2013**, *4* (21), 3618–3622. https://doi.org/10.1021/jz402019d.

(3) Eum, K.; Jayachandrababu, K. C.; Rashidi, F.; Zhang, K.; Leisen, J.; Graham, S.; Lively, R. P.; Chance, R. R.; Sholl, D. S.; Jones, C. W.; Nair, S. Highly Tunable Molecular Sieving and Adsorption Properties of Mixed-Linker Zeolitic Imidazolate Frameworks. *J. Am. Chem. Soc.* **2015**, *137* (12), 4191–4197. https://doi.org/10.1021/jacs.5b00803.

(4) Kolokolov, D. I.; Diestel, L.; Caro, J.; Freude, D.; Stepanov, A. G. Rotational and Translational Motion of Benzene in ZIF-8 Studied by 2H NMR: Estimation of Microscopic Self-Diffusivity and Its Comparison with Macroscopic Measurements. *J. Phys. Chem. C* **2014**, *118* (24), 12873–12879. https://doi.org/10.1021/jp5026834.

(5) Peralta, D.; Chaplais, G.; Paillaud, J.-L.; Simon-Masseron, A.; Barthelet, K.; Pirngruber, G. The Separation of Xylene Isomers by ZIF-8: A Demonstration of the Extraordinary Flexibility of the ZIF-8 Framework. *Microporous Mesoporous Mater.* **2013**, *173*, 1–5. https://doi.org/10.1016/j.micromeso.2013.01.012.

(6) Kolokolov, D. I.; Stepanov, A. G.; Jobic, H. Mobility of the 2-Methylimidazolate Linkers in ZIF-8 Probed by 2H NMR: Saloon Doors for the Guests. *J. Phys. Chem. C* **2015**, *119* (49), 27512–27520. https://doi.org/10.1021/acs.jpcc.5b09312.

(7) Knebel, A.; Geppert, B.; Volgmann, K.; Kolokolov, D. I.; Stepanov, A. G.; Twiefel, J.; Heitjans, P.; Volkmer, D.; Caro, J. Defibrillation of Soft Porous Metal-Organic Frameworks with Electric Fields. *Science* **2017**, *358* (6361), 347–351. https://doi.org/10.1126/science.aal2456.

(8) Ueda, T.; Yamatani, T.; Okumura, M. Dynamic Gate Opening of ZIF-8 for Bulky Molecule Adsorption as Studied by Vapor Adsorption Measurements and Computational Approach. *J. Phys. Chem. C* **2019**, *123* (45), 27542–27553. https://doi.org/10.1021/acs.jpcc.9b07239.

(9) Ueda, T.; Nakai, M.; Yamatani, T. A Solid-State 1H-NMR Study of the Dynamic Structure of ZIF-8 and Its Role in the Adsorption of Bulky Molecules. *Adsorption* **2017**, *23* (6), 887–901. https://doi.org/10.1007/s10450-017-9902-5.

(10) Polyukhov, D. M.; Poryvaev, A. S.; Gromilov, S. A.; Fedin, M. V. Precise Measurement and Controlled Tuning of Effective Window Sizes in ZIF-8 Framework for Efficient Separation of Xylenes. *Nano Lett.* **2019**, *19* (9), 6506–6510. https://doi.org/10.1021/acs.nanolett.9b02730.

(11) Pan, Y.; Li, T.; Lestari, G.; Lai, Z. Effective Separation of Propylene/Propane Binary Mixtures by ZIF-8 Membranes. *J. Membr. Sci.* **2012**, *390–391*, 93–98. https://doi.org/10.1016/j.memsci.2011.11.024.

(12) Comparison of the Behavior of Metal–Organic Frameworks and Zeolites for Hydrocarbon Separations | Journal of the American Chemical Society https://pubs.acs.org/doi/abs/10.1021/ja211864w (accessed 2021 -12 -08).
(13) Hou, Q.; Wu, Y.; Zhou, S.; Wei, Y.; Caro, J.; Wang, H. Ultra-Tuning of the Aperture Size in Stiffened ZIF-8_Cm Frameworks with Mixed-Linker Strategy for Enhanced CO2/CH4 Separation. *Angew. Chem. Int. Ed.* **2019**, *58* (1), 327–331. https://doi.org/10.1002/anie.201811638.
(14) Zhou, S.; Wei, Y.; Li, L.; Duan, Y.; Hou, Q.; Zhang, L.; Ding, L.-X.; Xue, J.; Wang, H.; Caro, J. Paralyzed Membrane: Current-Driven Synthesis of a Metal-Organic Framework with Sharpened Propene/Propane Separation. *Sci. Adv. 4* (10), eaau1393. https://doi.org/10.1126/sciadv.aau1393.
(15) Bae, T.-H.; Lee, J. S.; Qiu, W.; Koros, W. J.; Jones, C. W.; Nair, S. A High-Performance Gas-Separation Membrane Containing Submicrometer-Sized Metal-Organic Framework Crystals. *Angew. Chem. Int. Ed Engl.* **2010**, *49* (51), 9863–9866. https://doi.org/10.1002/anie.201006141.
(16) Zhang, C.; Koros, W. J. Zeolitic Imidazolate Framework-Enabled Membranes: Challenges and Opportunities. *J. Phys. Chem. Lett.* **2015**, *6* (19), 3841–3849. https://doi.org/10.1021/acs.jpclett.5b01602.
(17) Zhang, C.; Koros, W. J. Tailoring the Transport Properties of Zeolitic Imidazolate Frameworks by Post-Synthetic Thermal Modification. *ACS Appl. Mater. Interfaces* **2015**, *7* (42), 23407–23411. https://doi.org/10.1021/acsami.5b07769.
(18) Jobic, H.; Kolokolov, D. I.; Stepanov, A. G.; Koza, M. M.; Ollivier, J. Diffusion of CH4 in ZIF-8 Studied by Quasi-Elastic Neutron Scattering. *J. Phys. Chem. C* **2015**, *119* (28), 16115–16120. https://doi.org/10.1021/acs.jpcc.5b04259.
(19) Chmelik, C.; Freude, D.; Bux, H.; Haase, J. Ethene/Ethane Mixture Diffusion in the MOF Sieve ZIF-8 Studied by MAS PFG NMR Diffusometry. *Microporous Mesoporous Mater.* **2012**, *1* (147), 135–141. https://doi.org/10.1016/j.micromeso.2011.06.009.
(20) Kärger, J.; Freude, D.; Haase, J. Diffusion in Nanoporous Materials: Novel Insights by Combining MAS and PFG NMR. *Processes* **2018**, *6* (9), 147. https://doi.org/10.3390/pr6090147.
(21) Chmelik, C. Characteristic Features of Molecular Transport in MOF ZIF-8 as Revealed by IR Microimaging. *Microporous Mesoporous Mater.* **2015**, *216*, 138–145. https://doi.org/10.1016/j.micromeso.2015.05.008.
(22) Bukowski, B. C.; Keil, F. J.; Ravikovitch, P. I.; Sastre, G.; Snurr, R. Q.; Coppens, M.-O. Connecting Theory and Simulation with Experiment for the Study of Diffusion in Nanoporous Solids. *Adsorption* **2021**, *27* (5), 683–760. https://doi.org/10.1007/s10450-021-00314-y.
(23) Verploegh, R. J.; Nair, S.; Sholl, D. S. Temperature and Loading-Dependent Diffusion of Light Hydrocarbons in ZIF-8 as Predicted Through Fully Flexible Molecular Simulations. *J. Am. Chem. Soc.* **2015**, *137* (50), 15760–15771. https://doi.org/10.1021/jacs.5b08746.
(24) Zheng, B.; Maurin, G. Mechanical Control of the Kinetic Propylene/Propane Separation by Zeolitic Imidazolate Framework-8. *Angew. Chem.* **2019**, *131* (39), 13872–13876. https://doi.org/10.1002/ange.201906245.
(25) Krokidas, P.; Castier, M.; Moncho, S.; Brothers, E.; Economou, I. G. Molecular Simulation Studies of the Diffusion of Methane, Ethane, Propane, and Propylene in ZIF-8. *J. Phys. Chem. C* **2015**, *119* (48), 27028–27037. https://doi.org/10.1021/acs.jpcc.5b08554.

(26) E. Khudozhitkov, A.; S. Arzumanov, S.; I. Kolokolov, D.; Freude, D.; G. Stepanov, A. Dynamics of Propene and Propane in ZIF-8 Probed by Solid-State 2 H NMR. *Phys. Chem. Chem. Phys.* **2020**, *22* (10), 5976–5984. https://doi.org/10.1039/D0CP00270D.
(27) Martin, M. G.; Siepmann, J. I. Transferable Potentials for Phase Equilibria. 1. United-Atom Description of n-Alkanes. *J. Phys. Chem. B* **1998**, *102* (14), 2569–2577. https://doi.org/10.1021/jp972543+.
(28) Martin, M. G.; Siepmann, J. I. Novel Configurational-Bias Monte Carlo Method for Branched Molecules. Transferable Potentials for Phase Equilibria. 2. United-Atom Description of Branched Alkanes. *J. Phys. Chem. B* **1999**, *103* (21), 4508–4517. https://doi.org/10.1021/jp984742e.
(29) Hoover, W. G. Canonical Dynamics: Equilibrium Phase-Space Distributions. *Phys. Rev. A* **1985**, *31* (3), 1695–1697. https://doi.org/10.1103/PhysRevA.31.1695.
(30) Smith, W.; Forester, T. R. DL_POLY_2.0: A General-Purpose Parallel Molecular Dynamics Simulation Package. *J. Mol. Graph.* **1996**, *14* (3), 136–141. https://doi.org/10.1016/S0263-7855(96)00043-4.
(31) Khudozhitkov, A. E.; Arzumanov, S. S.; Kolokolov, D. I.; Stepanov, A. G. Mobility of Aromatic Guests and Isobutane in ZIF-8 Metal–Organic Framework Studied by 2H Solid State NMR Spectroscopy. *J. Phys. Chem. C* **2019**, *123* (22), 13765–13774. https://doi.org/10.1021/acs.jpcc.9b03081.
(32) Khudozhitkov, A. E.; Zhao, H.; Ghoufi, A.; Arzumanov, S. S.; Kolokolov, D. I.; Maurin, G.; Stepanov, A. G. Molecular Insight into the Slow Dynamics of C4 Hydrocarbons in the Zeolitic–Imidazole Framework (ZIF-8). *ACS Appl. Mater. Interfaces* **2021**, *13* (28), 33685–33692. https://doi.org/10.1021/acsami.1c08529.
(33) Verploegh, R. J.; Kulkarni, A.; Boulfelfel, S. E.; Haydak, J. C.; Tang, D.; Sholl, D. S. Screening Diffusion of Small Molecules in Flexible Zeolitic Imidazolate Frameworks Using a DFT-Parameterized Force Field. *J. Phys. Chem. C* **2019**, *123* (14), 9153–9167. https://doi.org/10.1021/acs.jpcc.9b00733.

Conclusion and perspectives

Conclusion of current works

In this work, several molecular simulation methods: Molecular dynamics, Monte Carlo, and Hybrid Osmotic Monte Carlo simulation were used to investigate the adsorption of guest molecules inside the MOFs assisted by external mechanical pressure. We are thus able to modulate simultaneously the gas pressure and mechanical pressure induced structure flexibility. Our results deliver a novel concept of adsorption/separation processes of MOFs.

The adsorbate investigated in this thesis was hydrocarbon, include hexane isomers mixture and butane/butene mixture. Two MOFs were chosen as the objectives: MIL-140B and ZIF-8. We investigated the impact of mechanical pressure on ZIF-8 and MIL-140 series MOFs upon adsorption of hexane isomers. We first evidenced that the application of a mechanical pressure above 1 GPa leads to a decrease of the adsorption uptake for all single component hexane isomers in ZIF-8 as well as MIL-140B which is explained by microscopic analysis. PSD analysis pointed out the decrease of the adsorption quantity in ZIF-8 is due to the compressing of the cage at high mechanical pressure. The distribution of linker rotation and PSD provoked the decrease of free volume in MIL-140B. The effect is enhanced by the local disorder which conducts to the decrease of the adsorption uptake. We further revealed that the mechanical pressure brings a significant improvement of the selective behaviour on MIL-140B and ZIF-8. The increase of 70% for the overall selectivity of MIL-140B was recorded. In ZIF-8, the binary mixture of *n*C6/2MP had an increase of selectivity by 30%. The isosteric heat of adsorption and RDF proved this separation is thermodynamically drive. By coupling Monte Carlo and molecular dynamic simulation, our works provide a microscopic level understanding of the adsorption of hexane isomers into flexible porous MOFs ZIF-8 and MIL-140B.

We also improve the molecular understanding of the slow dynamics diffusion of *n*-butane and 1-butene in the ZIF-8, which is a great example that illustrates how the molecular simulation assist in validating a theoretical model.
The most important advantage of simulations is the ability to reach the experimental condition which is hard even impossible. However, this is a double-edged sword, while we explored the properties of the MOFs at high mechanical pressure up to 1 GPa, experimentally it is very difficult to reach such pressure. For example, our collaborators, the team from MADIREL developed their experimental set up to apply the mechanical pressure on MOFs as shown in Figure CP.1, the maximum mechanical pressure that can be applied by this fairly sophisticated device is 400 MPa, which is far lower than theoretical simulation condition. What's more, the mechanical pressure that can be applied in this device is uniaxial, while in the simulation the anisotropic pressure was considered. This kind of detachment between experiments and simulation at high mechanical pressure is a serious limitation.

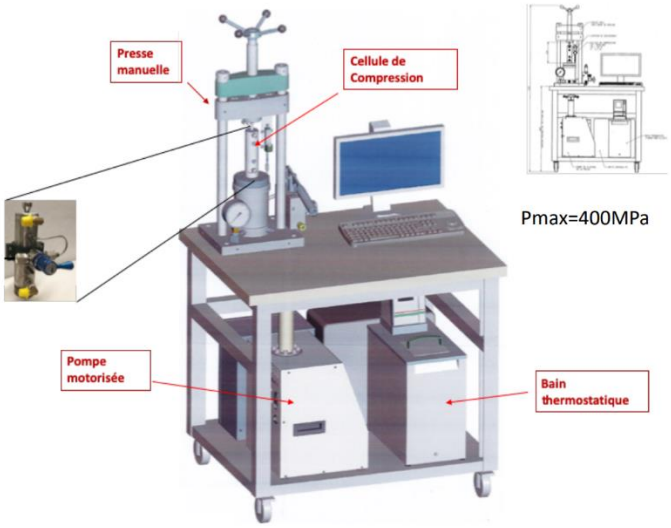

Figure CP. 1 *Experimental set up from MADIREL team to investigate the adsorption in MOFs.*

The mechanical flexibility of the MOFs between the experiments and simulation also brings another challenge. Force field is not universal, it is very hard to fellow the flexibility of MOFs especially with multiple phase transitions in the point of view from the simulation.

To bring this discussion to industrial level, despite of the great potential of MOFs, they aren't being used in a large scale yet. Although some companies propose the using of MOFs materials for the industrial applications, for example, ProfMOF, NovoMOF. The main stumbling point that blocks the industrial application actually is the durability of the MOFs during the industrial standard process. To address this issue, the MOFs based membrane could help to improve the durability. This domain is still the forefront of the research.

Despite the limitations, our simulation methods provide a novel concept to investigate the adsorption properties of MOFs in the condition the closest to laboratory condition, rendering this method much more precise than conventional methods. With the successful scenarios achieved on MIL-140B and ZIF-8. We can apply this method to a wider range of MOFs and even other non-MOFs porous materials. With further implementation of the electric field application, we can simultaneously control multiple parameters, mechanical pressure, electric field, temperature, and adsorption of guest molecules. This would be a bottleneck-breaking concept that brings the simulation methods to a higher level.

Perspectives

The work carried out in this thesis can be pursued in different directions. Firstly, we want to investigate the inversion of the selectivity for *n*C6 and 3MP, which is observed in MIL-140B and MIL-140C from equimolar quinary hexane isomers mixture breakthrough experiment. In order to explain the mechanism of this inversion, we already carried out the molecular dynamic simulation to probe the diffusion of hexane isomers inside the two MOFs in question. However, the long diffusion process is currently a bottleneck and it should be resolved in order to explain the selectivity inversion for *n*C6/3MP.

We also want to investigate a larger set of MOFs with different pore size/shape and functionality. For example, $Fe_2(BDP)_3$, which is also a 1D triangular form channel-structured MOF as MIL-140 series MOFs, it is reported to have a very high overall hexane

selectivity up to 2000. The idea is to boost even higher the selectivity with external stimuli. Another example is UIO-66, it is reported to have reverse shape selectivity towards xylene isomers, but the microscopic mechanisms is not yet fully understood. The precise description of the flexibility of the UIO-66 is crucial to successfully reveal the origin and mechanism for this reverse shape selectivity. The main challenge here is the validation of the force field for new MOFs and automatization of the simulation programs.

Another theme is the investigation on other porous system, for example, mesoporous silica. Molecular simulation provides the possibility to investigate the rotational dynamics of nanoconfined water in this type of mesoporous materials. The challenge on this project is the modeling of the mesoporous system with the addition of the additional bridging unit.

Finally, there are still room to improve the simulation code. The generalization of the program can make it more user friendly, for example, implement a single interface to enter the parameters of the simulation. The possibility to couple between different molecular dynamics simulation package and Monte Carlo packages will make this method more universal and appealing.

Appendix

ZIF-8 Force Field

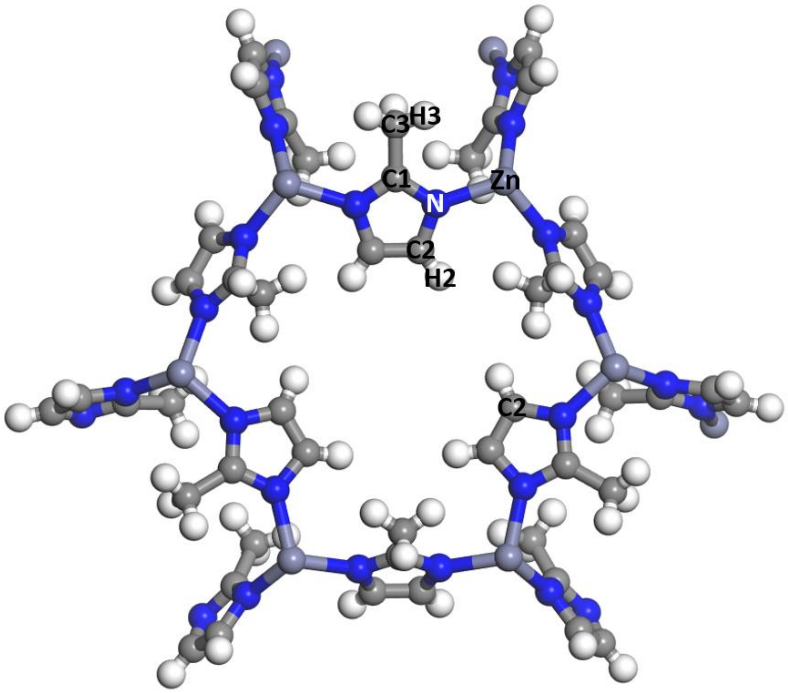

Figure A. 1 *Snapshot of a six membered ring on ZIF-8.*

Table A. 1 *Atoms types in the ZIF-8 force field.*

Atom type	ϵ [K]	σ [Å]	Partial Charge [e]
C1	43.28	3.40	0.4339
C2	43.28	3.40	-0.1924
C3	55.0	3.40	-0.6042
H1	7.54	2.51	0.1585
H2	7.89	2.47	0.1572
N	85.47	3.25	-0.3008
Zn	6.28	5.96	0.7362

Table A. 2 *Description of bonds in ZIF-8 force field.*

$$U_{bond} = \sum_{bonds} K_r(r - r_0)^2$$

Bonds	K_r [kcal. mol^{-1}]	r_0 [Å]
C1-C3	346.543	1.49
C1-N	488.00	1.335
C2-N	440.210	1.370
C2-H1	367.000	1.080
C2-C2	540.249	1.350
C3-H2	340.000	1.090
Zn-N	78.500	2.011
C2-C2 (on the six-ring window)	1.839	5.146

Table A. 3 *Description of bendings in ZIF-8 force field.*

$$U_{angles} = \sum_{angles} K_\theta(\theta - \theta_0)^2$$

Bending	K_θ [kcal. mol^{-1}]	θ_0 [degree]
N-C1-N	75.4840	112.16
C3-C1-N	66.0150	123.92
C2-C2-N	73.7500	108.65
C2-C2-H1	49.4510	125.67
H1-C2-N	49.9540	125.68
C1-C3-H2	48.0880	109.32
C1-N-C2	71.2540	105.27
C1-N-Zn	48.6800	128.33
C2-Zn-C1	32.4770	126.40
C1-Zn-N	35.2400	109.48
H2-C3-H2	35.000	109.50

Table A. 4 *Description of dihedrals in ZIF-8 force field.*

$$U_{torsion} = \sum_{angles} \frac{V_n}{2}[1 + cos(n\phi - \gamma)]$$

Dihedral	V_n [kcal. mol^{-1}]	n	γ (integer value of degrees)
H1-C2-N-Zn	2.325	2	180
C2-C2-N-Zn	2.325	2	180
H1-C2-N-C1	2.325	2	180
C2-C2-N-C1	2.325	2	180
H1-C2-C2-H1	5.150	2	180
H1-C2-C2-N	5.150	2	180
N-C2-C2-N	5.150	2	180
C3-C1-N-Zn	5.000	2	180
N-C1-N-Zn	5.000	2	180

C3-C1-N-C2	5.000	2	180
N-C1-N-C2	5.000	2	180

MIL-140B Force field

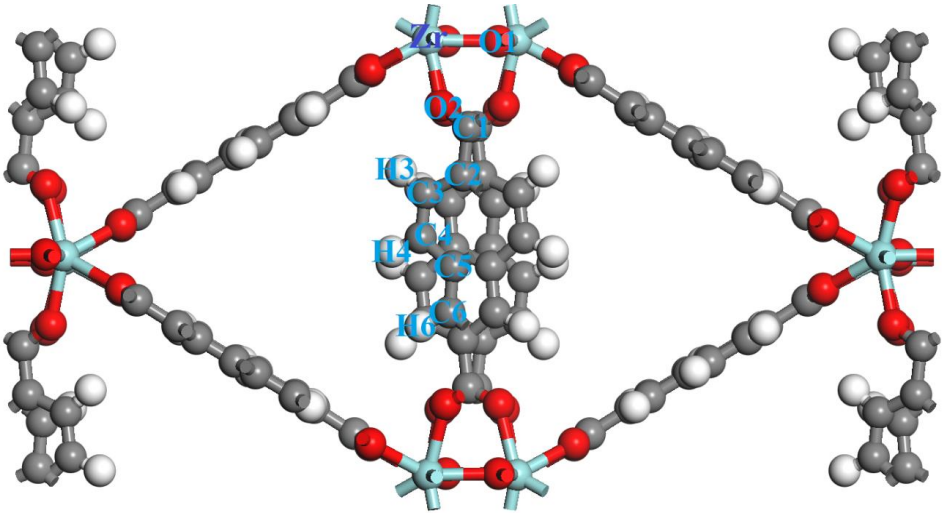

Figure A. 2 *Snapshot of the unit cell with the label of the atom types of MIL-140B.*

Table A. 5 *Atoms types in the MIL-140B force field.*

Atom type	ϵ [kJ mol^{-1}]	σ [Å]	Partial Charge [e]
C1	0.3979	3.473	0.7965
C2	0.3979	3.473	-0.0278
C3	0.3979	3.473	-0.0309
C4	0.3979	3.473	-0.3556
C5	0.3979	3.473	0.236
C6	0.3979	3.473	-0.233
H3	0.0636	2.846	0.1339
H4	0.0636	2.846	0.1339
H6	0.0636	2.846	0.1339
O1	0.4004	3.033	-1.2585
O2	0.4004	3.033	-0.688
Zr	0.2301	4.045	2.437

Table A. 6 *Description of bonds in ZIF-8 force field.*

$$U_{bond} = \sum_{bonds} K_r(r - r_0)^2$$

Bonds	K_r [kJ. mol^{-1}]	r_0 [Å]
C-C	2197	1.39
C1-N	1464	1.02
C1-O2	2196	1.35
Zr-O2	1464	2.33
Zr-O1	1464	2.23
Zr-Zr	1464	3.35

Table A. 7 *Description of bendings in ZIF-8 force field.*

$$U_{angles} = \sum_{angles} K_\theta(\theta - \theta_0)^2$$

Bending	k_θ [kJ. mol^{-1}]	θ_0 [degree]
C-C-C	279	120
C-C-O	279	120
C-C-H	279	120
O1-Zr-O1	235	109
O1-Zr-O2	235	109
O2-Zr-O2	235	109

Table A. 8 *Description of dihedrals in ZIF-8 force field.*

$$U_{torsion} = \sum_{angles} \frac{V_n}{2}[1 + cos(n\phi - \gamma)]$$

Dihedral	V_n [kcal. mol^{-1}]	*n*	γ *(integer value of degrees)*
C-C-C-C	13.07	2	540
H-C-C-C	13.07	2	540
C-C-C-O	5.23	2	540
C-C-O-Zr	26.15	2	540

Butane and butene Force field

TraPPE-UA (united atoms) flexible force field was used to describe *n*-butane and 1-butene. Each CH_x was considered as a single uncharged Lennard-Jones (LJ) site.

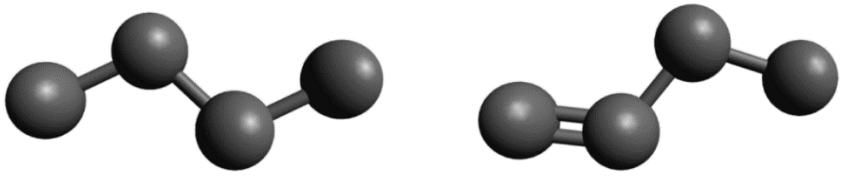

Figure A. 3 *Snapshot of butane(left) and butene(right).*

Table S. 9 *Force field used to describe butane and butene.*

Bond	r_0 [Å]
CH_x-CH_x	1.54
CH_x=CH_x	1.33

Bending angle	θ_0 (°)	K_θ/k_b [K/rad²]
CH_x-CH_2-CH_y	114	62500
CH_x=CH-CH_x	119.7	70420

Dihedral angle	c_0 [K]	c_1 [K]	c_2 [K]	c_3 [K]
CH_x-CH_2-CH=CH_y	688.5	86.36	-109.77	-282.24
CH_x-CH_2-CH_2-CH_y	0	355.03	-68.19	791.32

LJ Pair	Type	ϵ [K]	σ [Å]
CH_3	CH_3-CH_x	98	3.75
CH_2	CH_2-CH_x	85	3.675
CH	CH_x=CH-CH_y	47	4.8
CH_2	CH_x-CH_2-CH_y	46	3.95

Titre : Exploration informatique des performances des MOFs contraints mécaniquement pour la séparation des hydrocarbures

Mots clés : Metal-organic frameworks, Simulation Moléculaire, Séparation de l'hydrocarbure, diffusion.

Résumé étendu de la thèse

Cette thèse a débuté en octobre 2018 et je l'ai soutenue en février 2022. Elle a été codirigée par Aziz Ghoufi (MCF, Université de Rennes 1) et Guillaume Maurin (PR, Université de Montpellier). Elle est intitulée « Exploration informatique des performances des MOFs contraints mécaniquement pour la séparation des hydrocarbures ». Elle a été réalisée au sein de IPR (Institut Physique de Rennes) à l'université de Rennes 1. Cette thèse s'appuie sur l'étude de la séparation des hydrocarbures par les MOFs avec l'aide des différentes méthodes de simulation.

I. MOFs

Les Metal-Organic Frameworks (MOFs) sont des solides organiques/inorganiques qui sont micro- ou mésoporeux. La définition du MOF est un matériau poreux cristallin hybride organique-inorganique constitué d'ions métalliques liés par des ligands organiques. Illustré dans la Figure R.1.

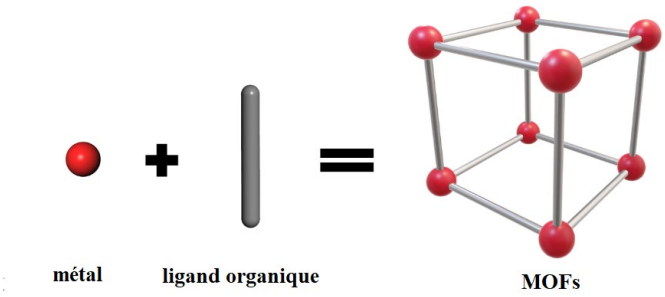

Figure R.1 *Illustration simple de MOFs.*

Ces matériaux possèdent une grande diversité chimique et structurelle. L'étude sur MOFs ne cesse de croitre depuis des dizaines d'années grâce à leurs forts potentiels. La première trace des MOFs remonte au début de 1965, près de trente ans avant la date de naissance généralement considérée de la MOFs, Tomic a déjà synthétisé un polymère de coordination composé de l'acide 1,5-dihydroxynaphtalène-2,6-dicarboxylique (1,5-N- 2,6) coordonné à Zn, Ni, Al et Fe,[1] qui serait appelé MOFs de nos jours. En 1990, Hoskins et Robson ont rapporté la conception d'une nouvelle classe de matériaux de type échafaudage comprenant des charpentes polymères utilisant des centres Cu (I).[2] L'intérêt pour ces polymères de coordination s'est accru. Plus récemment, S. Kitagawa et son équipe ont rapporté un matériau qui est un polymère de coordination comportant des cavités qui peuvent adsorber de petites molécules gazeuses telles que CH4, N2 et O2. [3] En 1999, le groupe d'O. M. Yaghi a découvert le MOF-5 (ou IRMOF-1, illustré dans la Figure R.2) .[4]

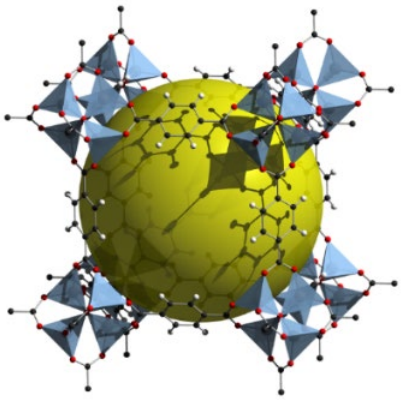

Figure R.2 *Illustration 3D d'une structure de cellule unitaire de MOF-5. L'oxygène, le carbone et l'hydrogène sont représentés en rouge, noir et blanc. La sphère jaune représente le volume poreux. Les tétraèdres représentent la coordination du BDC(linker) aux centres des ions zinc.*

Avec la croissance des études sur MOFs, il y a de plus en plus de MOFs qui ont été synthétisés. Aujourd'hui, il existe plus de 100 000 MOF synthétisés, selon la Cambridge Structural Database (CSD).

II. Méthode de simulation

Avec le développement de la technologie informatique, la simulation numérique est devenue un outil puissant pour sonder le système physique et comprendre les expériences réelles. Le premier exemple de simulation numérique remonte à 1953,[5] réalisé par Metropolis et al., qui a proposé une méthode générale de calcul des propriétés de toute substance, basée sur une distribution de probabilité prédéterminée.

Avec les progrès réalisés au cours des dernières décennies, la simulation moléculaire a considérablement amélioré son efficacité et sa précision. Comme l'amélioration et le raffinement des algorithmes sur le calcul et hardware sont en cours, nous pouvons estimer que l'outil numérique jouera un rôle plus en plus important dans la compréhension du système complexe. Dans ma thèse, j'ai utilisé principalement 3 méthodes de simulation, Simulation Dynamique Moléculaire (MD), Simulation Monte Carlo (MC), et Simulation Hybrid Osmotique Monte Carlo (HOMC).

a) Simulation Dynamique Moléculaire

Le concept de simulation MD consiste en l'intégration numérique dépendante du temps des équations de mouvement newtoniennes des particules. Comme illustré dans l'équation:

$$\boldsymbol{F_i} = m_i \boldsymbol{a_i}(t) = m_i \frac{d\boldsymbol{v_i}(t)}{dt} = m_i \frac{d^2\boldsymbol{r_i}(t)}{dt^2} = -\frac{\partial}{\partial \boldsymbol{r_i}} U$$

Où F représente la force exercée sur les particules, v_i, m_i et r_i représentent respectivement la vitesse, la masse et la position de l'atome i. U est l'énergie potentielle du système. Les interactions entre atomes et molécules peuvent être modélisées via l'énergie potentielle par un ensemble de fonctions potentielles empiriques. La résolution numérique peut se faire avec des algorithme différents: Leapfrog algorithm, Beeman algorithm, Verlet algorithm, etc.

Avec la simulation MD, nous pouvons avoir accès à la trajectoire des atomes dans le système, et ainsi, extraire les propriétés physiques.

b) Simulation Monte Carlo

Contrairement à la simulation MD, la simulation Monte Carlo consiste à la génération des configurations aléatoires à l'aide de l'algorithme Metropolis pour déterminer s'il faut accepter/rejeter une nouvelle configuration. Cet algorithme est un Markovien et n'est pas dépendant du temps. Chaque configuration est générée par un mouvement d'essai aléatoire d'atomes ou de molécules, par exemple, la translation, la rotation, l'insertion/la suppression, etc.

Les critères de la méthode Metropolis permettent de s'assurer que la probabilité d'obtenir une configuration est égale à son facteur de Boltzmann.
Les configurations à faible énergie sont générées avec une probabilité plus élevée que les configurations à énergie plus élevée. Si l'énergie de la nouvelle configuration est inférieure à la configuration précédente, alors la nouvelle configuration sera acceptée.
Cette méthode de simulation est très répandue pour simuler l'adsorption/la désorption dans les matériaux poreux.

c) Simulation Hybrid Osmotique Monte Carlo

Dans ce travail, la simulation Hybrid Osmotic Monte Carlo (HOMC) a été adoptée pour étudier l'adsorption et la séparation des gaz d'hydrocarbures dans les MOFs. Les méthodes de simulation introduites précédemment, les simulations de dynamique moléculaire (MD) et de Monte Carlo (MC) ne sont pas capables de suivre une transition de phase structurelle , ni la flexibilité engendrée par l'adsorption des molécules. Parce que dans la simulation MC, le structure de MOFs est considéré rigide, et dans la simulation MD, on travaille dans un ensemble ou le nombre des molécules sont fixes. HOMC permet de franchir ces difficultés en combinant MD et MC.
Une simulation HOMC se compose de plusieurs cycles, chaque cycle contient plusieurs étapes HOMC. Une étape HOMC comprend une simulation MD et une simulation MC. Le programme commence par une simulation MD, la structure atteindra l'équilibre thermodynamique et l'énergie sera convergée. À la fin de la simulation MD, le programme convertit les fichiers de sortie de la simulation MD en fichiers d'entrée pour la simulation MC et ainsi de suite. Comme illustré dans la figure R.3. Ce programme est un code qui est développé au sein de l'IPR de l'université de Rennes 1.

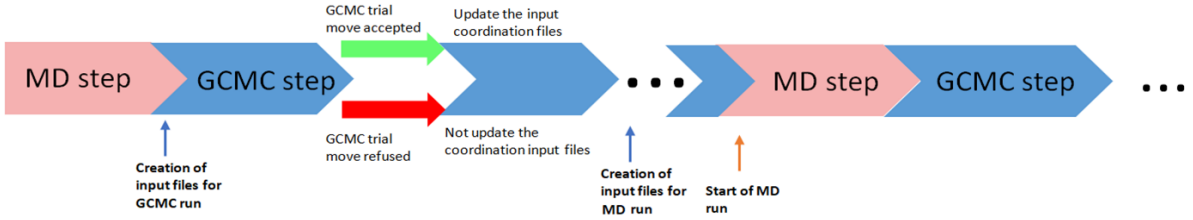

Figure R.3 *Illustration de simulation HOMC.*

III. Séparation des mélanges gazeux avec MOFs

Grâce à la polyvalence structurelle, les MOFs ont montré leur potentiel dans de nombreuses applications, notamment la séparation des gaz, le stockage, la catalyse, les capteurs, le transport de médicaments.[6-9]
Dans ma thèse, on s'intéresse à la séparation des mélanges gazeux industriels. En effet, les procédés conventionnels pour séparer et/ou purifier les produits industriels reposent en grande partie sur des distillations, qui consument beaucoup d'énergie. Pour information, les procèdes de séparation constituent environ 90 à 95 % de toutes les séparations dans les industries chimiques et de raffinage du pétrole.[10]
Nous avons investigué 3 mélanges de gaz, propane/propylène, isomères xylène/éthylbenzène et notamment isomères hexane. Cependant, les propriétés physiques similaires des isomères hexane (*n*C6, 2MP, 3MP, 23DMB et 22DMB) apportent une grande difficulté au processus de séparation.

a) MIL-140B

Malgré les difficultés concernant la séparation des isomères hexanes, le famille MIL-140 (MIL : Les matériaux de l'Institut Lavoisier) Ils sont intéressants pour séparer l'isomère hexanes. MIL-140A, MIL-140B et MIL-140C ont été étudiés par des expériences de percée chromatographique réalisé par notre collaborateurs.[11] MIL-140B présente la sélectivité la plus

élevée, ainsi, notre travail informatique s'est concentré sur MIL-140B. Figure R.4 illustre MIL-140B.

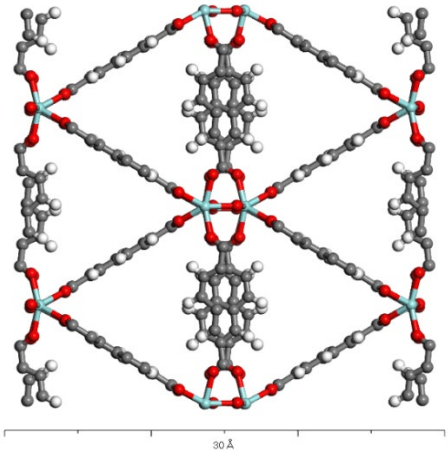

Figure R.4 *MIL-140B 1x2x4 supercell. Les couleurs cyan, grise, rouge et blanche représentent respectivement les atomes de zirconium, de carbone, d'oxygène et d'hydrogène.*

Dans un premier temps, nous avons utilisé la simulation MC pour sonder l'adsorption des corps purs des hexane dans MIL-140B, et puis nous l'avons concomparé avec des données expérimentales. Illustré dans la figure R.5.

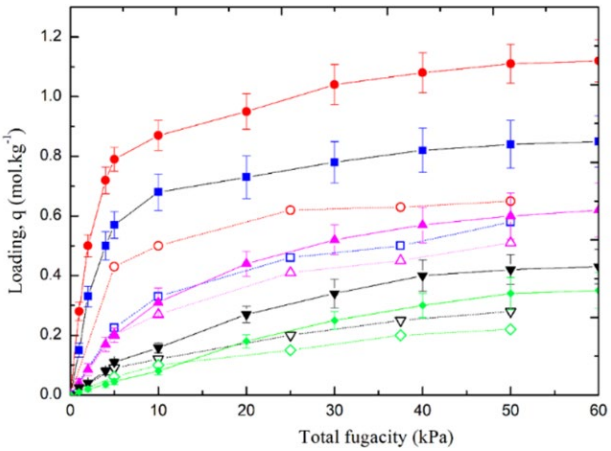

Figure R.5 *Isotherme d'adsorption corp pure VS données expérimentales. GCMC simulations nC6 (●), 2MP (—■—), 3MP, (—▲—) 23DMB (—▼—) and 22DMB (—◆—) and experimental data nC6 (○), 2MP (··□··), 3MP (··△··), 23DMB (··▽··) and 22DMB (··◇··).*

Malgré l'accord qualitatif pour la séquence d'adsorption entre les données de simulation et les données expérimentales, la simulation a surestimé la quantité d'adsorption. D'après l'étude bibliographique, nous suggérons que c'est à cause du manque de la considération de flexibilité de MIL-140B. Toujours avec la simulation Monte Carlo, nous avons effectué des rotations de linkers de manière artificielle pour voir l'effet de la flexibilité. Le résultat de simulation, i.e isotherme d'adsorption relève qu'effectivement la rotation de linker joue un rôle important dans l'adsorption des isomères hexane dans MIL-140B. Prenons exemple de *n*C6 qui est illustré dans la figure R.6.

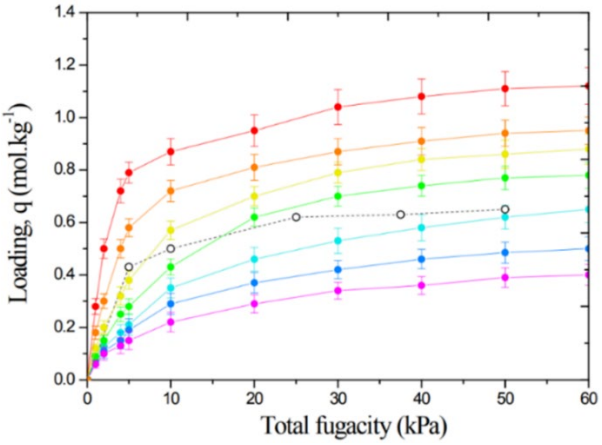

Figure R.6 *isotherme d'adsorption de nC6 vs données expérimentales expérimentales(-- ○ --), 0° linker rotation (—●—), 2° linker rotation (—●—), 5° linker rotation (—●—), 7° linker rotation (—●—), 10° linker rotation (—●—), 12° linker rotation (—●—) and 15° linker rotation (—●—).*

Nous avons ensuite comparé la sélectivité simulée avec expérience. La sélectivité calculée pour une rotation de lieur de 10° et 7° est de 15,5 et 19 et la sélectivité expérimentale est 10. Ces rotations sont artificielles et non physiques parce qu'il s'agit d'une rotation collective et identique pour tous les linkers. Mais comparer à la sélectivité calculée pour la structure origine qui est de 24,7, la considération de linker a déjà amélioré cet écart.

Pour aller plus loin, nous devons utiliser des champs de force pour décrire la flexibilité de MIL-140B pour un résultat plus précis et physique. C'est pour cela que nous avons procédé ensuite à utilisation de la simulation HOMC.

Nous avons commencé par la validation des champs de force, il s'agit de lancer la simulation MD pour MIL-140B vide à la condition expérimentale et en plus avec la pression mécanique, pour pouvoir tester la stabilité de structure. Des analyses structurales ont été faites également pour assurer qu'il ne présente pas de liaison cassée, etc.

Après cette validation des champs de force, nous avons lancé la simulation HOMC. Les isothermes d'adsorption obtenus cette fois-ci, sont en accord avec les expériences. Illustré dans le figure R.7.

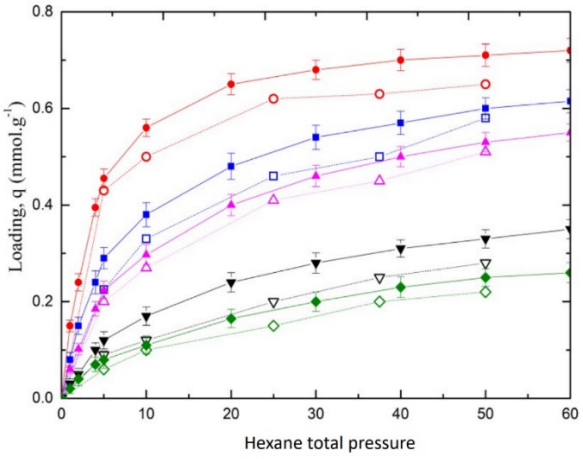

Figure R.7 *Isothermes d'adsorption corp pure VS données expérimentales à 343 K: HOMC simulations nC6 (●), 2MP (—■—), 3MP, (—▲—) 23DMB (—▼—) et 22DMB (—◆—) et expérience nC6 (○), 2MP (--□--), 3MP (-- △--), 23DMB (-- ▽--) et 22DMB (--◇--).*

Les isothermes obtenus pour le mélange quinaire ont montré leur accord avec les données expérimentales comme illustré dans la figure R.8.

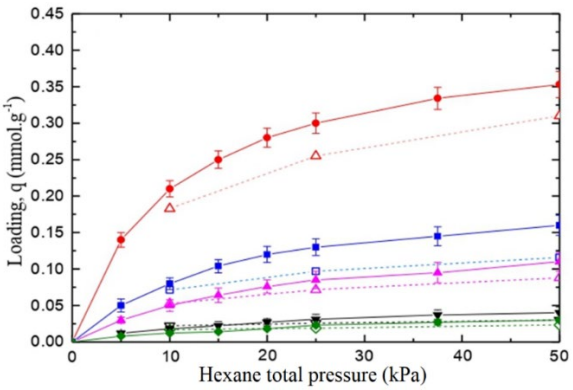

Figure R.8 *Isotherme d'adsorption mélange quinaire VS données expérimentales à 343 K: HOMC simulations nC6 (●), 2MP (—■—), 3MP, (—▲—) 23DMB (—▼—) and 22DMB (—◆—) and experimental data nC6 (○), 2MP (--□--), 3MP (--△--), 23DMB (-- ▽--) and 22DMB (--◇--).*

Le maximum de sélectivité a été trouvé à 10,9 pour une pression totale d'hexane de 10 kPa qui est en cohérence avec la valeur expérimentale de 10,2.
Comparer au MIL-140B rigide, en utilisant le champ de force entièrement flexible, la simulation en accord satisfaisant avec les données expérimentales. Ce résultat a confirmé la précision de la simulation HOMC.
Nous avons ensuite évalué l'impact de la pression mécanique sur les performances de séparation du MIL-140B pour les mélanges quinaires illustré dans la figure R.9.

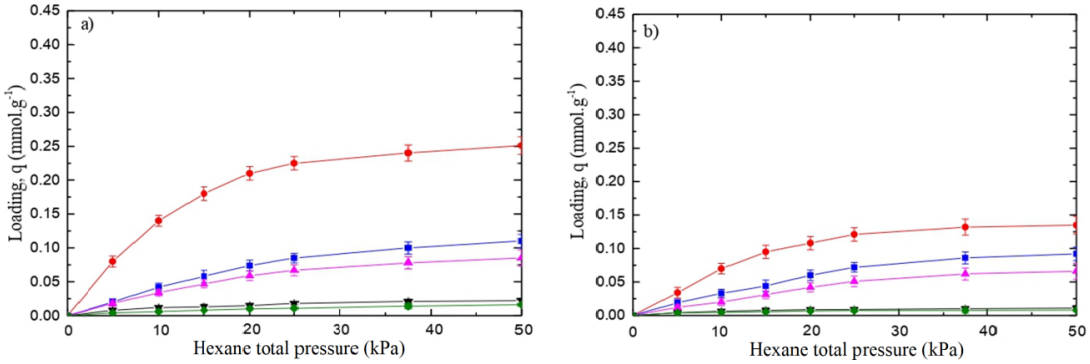

Figure R.9 *Isothermes d'adsorption simulés de mélange quinaire équimolaire des isomères d'hexane dans MIL-140B à 343 K a) 0.7 GPa and b) 1.0 GPa: HOMC simulations nC6 (●), 2MP (—■—), 3MP, (—▲—) 23DMB (—▼—) et 22DMB (—◆—).*

Nous avons constaté que la quantité d'adsorption diminue avec l'augmentation de la pression mécanique, due à la diminution de taille des pores qui est prouvé par des analyses structurales. Cependant, la sélectivité augmente avec l'augmentation de la pression mécanique. Illustré dans la figure R.10 :

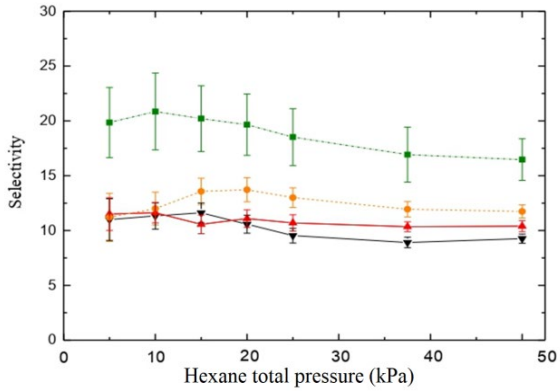

Figure R.10 *Sélectivité calculée à 0.1 MPa (—▼—), 0.5 GPa (—▲—), 0.7 GPa (—●—) and 1.0 GPa (—■—).*

Cette figure montre une augmentation substantielle de la sélectivité globale de 80% (de 10,9 à 21,5) pour une pression totale d'hexane de 10 kPa (maximum de sélectivité). Typiquement, le mélange quinaire d'isomères d'hexane entièrement chargé dans MIL-140B sous une pression mécanique de1 GPa présente un volume de cellule unitaire de 2644 $Å^3$ contre 3034 $Å^3$ à 0,1 MPa. Ce changement de volume de cellule unitaire s'accompagne d'une diminution de taille de pore de 0,5 Å. La rotation de linker est aussi plus prononcée à haute pression mécanique.
Cette étude de simulation moléculaire révèle que la taille des pores du MIL-140B ainsi que la dynamique de ses linkers organiques peuvent être modulées en appliquant une pression mécanique pour augmenter les performances de séparation des isomères de l'hexane dans ce type de MOFs.

b) ZIF-8

Les ZIF (Zeolite imidazolate Frameworks) présentent une diversité chimique/structurelle unique. En effet, ils sont hautement modulable en termes de taille/forme de pores et de fonctionnalité chimique, ce qui les rend attractifs pour la séparation moléculaire non seulement par le tamisage moléculaire mais aussi par la thermodynamique, l'entropie (sélectivité de forme) ou la cinétique. ZIF-8 présente une fenêtre de petite taille (3.4 Å) qui est intéressant pour la séparation des isomères hexane. Illustré dans la figure R. 11.

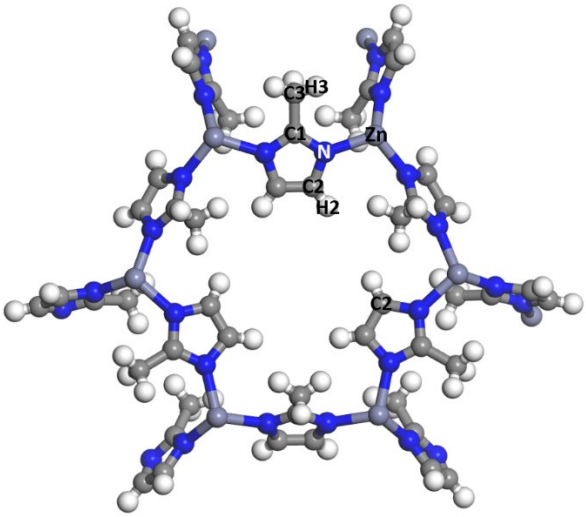

Figure R.11 *Illustration de Fenêtre ZIF-8, avec différents types d'atomes (C2, H2, C1, C3, H3, N et Zn). Les couleurs violet clair, bleu, gris et blanc représentent respectivement les atomes de zinc, d'azote, de carbone et d'hydrogène.*

Après avoir validé les champs de force de ZIF-8. Nous avons effectué des simulations HOMC et comparé avec des données expérimentales.

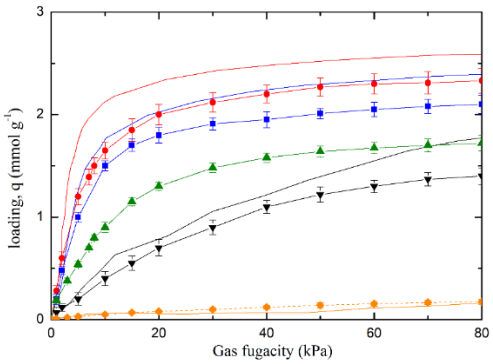

Figure R.12 *Isotherme d'adsorption corp pure calculé VS données expérimentales dans ZIF-8 à 373 K: simulations HOMC. nC6 (—●—), 2MP (—■—), 3MP (—▲—), 23DMB (—▼—), et 22DMB (—◆—) et données expérimentales nC6 (———), 2MP (———), 23DMB (———), and 22DMB (———).*

La séquence d'adsorption simulée nC6 > 2MP > 3MP > 23DMB > 22DMB se trouve en excellent accord avec les données d'adsorption précédentes. L'analyse de la simulation, chaleur d'adsorption isostérique a prouvé que le mécanisme de séparation est piloté par la thermodynamique.

Vu que 22DMB est presque exclus de l'adsorption, donc la séparation pour la mélange quinaire est moins intéressante comparée au cas de MIL-140B. Cela justifie que nous nous sommes intéressés à investiguer la séparation binaire entre *n*C6/2MP, 2MP/23DMB, *n*C6/22DMB qui sont présentées respectivement par les figures R.13, R.14 et R.15.

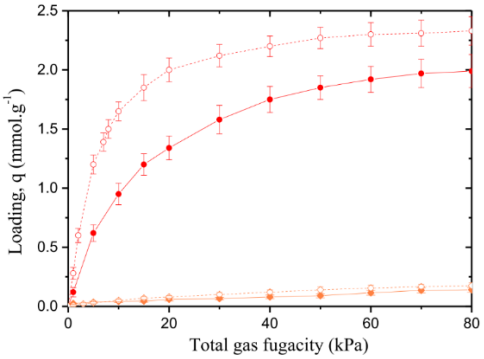

Figure R.13 *Isothermes adsorption pour mélange binaires nC6 (—●—)/22DMB (—◆—) représenté en traits pleins et en symboles pleins. nC6 (—○—)/22DMB (—◇—) représentent les données simulées pour le corp pure pour la comparaison.*

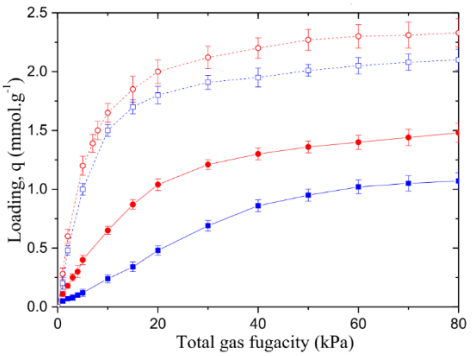

Figure R.14 *Isothermes adsorption pour mélange binaires nC6 (—●—)/2MP (—■—) représenté en traits pleins et en symboles pleins. nC6 (—○—)/2MP (—□—) représentent les données simulées pour le corp pure pour la comparaison.*

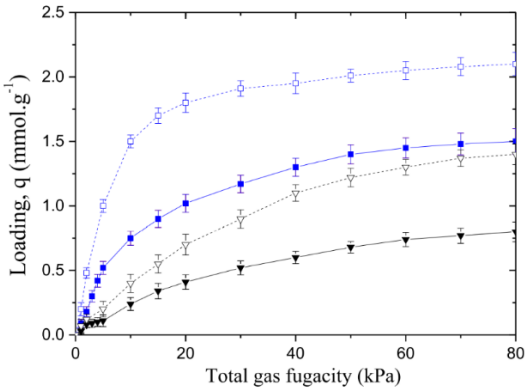

Figure R.15 *Isothermes adsorption pour mélange binaires 2MP (—■—)/23DMB (—▼—) (—■—) représenté en traits pleins et en symboles pleins. 2MP (—□—)/23DMB (—▽—) représentent les données simulées pour le corp pure pour la comparaison.*

Cette observation souligne que ces séparations sont thermodynamiques, cependant la sélectivité est loin d'être optimale, par exemple, S(*n*C6/2MP) = 2,5 et S(2MP/23DMB) = 4,7 pour une fugacité totale du gaz de 10 kPa.
Nous nous sommes intéressés à améliorer le rendement avec l'application de pression mécanique, sur le mélange *n*C6/2MP. Illustré dans la figure R. 16.

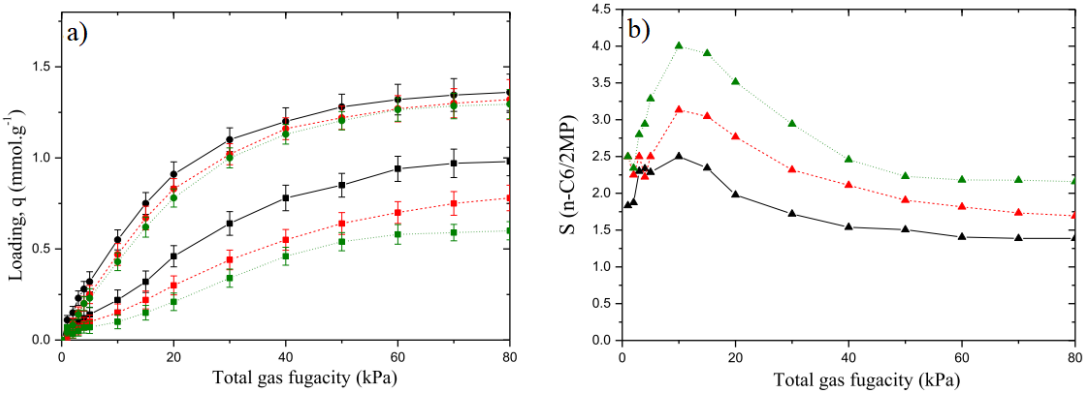

Figure R.16 *Simulation HOMC (a) nC6/2MP isothermes adsorption mélange binaires dans ZIF-8 à 373 K et (b) sélectivité en fonction de la pression de gaz. nC6 (—●—) et 2MP (—■—) à 0.1 MPa; nC6 (---●---) et 2MP (---■---) à 1 GPa; nC6 (···●···) et 2MP (···■···) à 1.5 GPa. (b) nC6/2MP (—▲—) sélectivité à 0.1 MPa; nC6/2MP (---▲---) sélectivité à 1 GPa ; et nC6/2MP (···▲···) sélectivité à 1.5 GPa.*

En résumé, l'impact de la pression mécanique sur l'adsorption des isomères de l'hexane dans le ZIF-8 a été évalué par des simulations HOMC. Nous avons validé le champ de force de ZIF-8 en reproduisant l'isotherme d'adsorption et en le comparant aux données expérimentales. nC6/2MP a été choisi comme mélange binaire de grand intérêt pour simuler le scénario du mélange d'isomères linéaires/mono-branchés. En comparant la sélectivité de nC6/2MP à différentes pressions mécaniques, nous avons obtenu une augmentation de la sélectivité de 30 % de 0,1 MPa à 1,5 GPa.

IV. Conclusions

Dans ce travail de thèse, plusieurs méthodes de simulation moléculaire : la dynamique moléculaire (MD), Monte Carlo (MC) et la simulation Hybrid Osmotic Monte Carlo (HOMC) ont été utilisées pour étudier l'adsorption de molécules dans les MOFs assisté par une pression mécanique externe. On est ainsi capable de moduler simultanément la pression de gaz et la

pression mécanique. L'originalité de ce travail c'est qu'il offre un nouveau concept de processus d'adsorption/séparation des MOFs.
Nous avons mis en évidence que l'application d'une pression mécanique supérieure à 1 GPa engendre une diminution de l'absorption d'adsorption pour tous les isomères d'hexane à un seul composant dans ZIF-8 ainsi que MIL-140B. L'analyse de la distribution de taille des pores (PSD) a souligné que la diminution de la quantité d'adsorption dans ZIF-8 est due à la compression de la cage à haute pression mécanique. La distribution de la rotation de linkers a provoqué la diminution du volume libre dans le MIL-140B. L'effet est renforcé par le désordre local qui conduit à la diminution de la quantité d'adsorption. Nous avons en outre révélé que la pression mécanique apporte une amélioration significative du comportement sélectif sur MIL-140B et ZIF-8. L'augmentation de 70% pour la sélectivité globale du MIL-140B a été enregistrée. Dans ZIF-8, le mélange binaire de nC6/2MP avait une augmentation de sélectivité de 30 %. Cela signifie que certains stimuli externes peuvent améliorer le rendement de séparation, qui ouvre un portail vers une nouvelle conception de séparation utilisant les MOFs. Cette méthode de simulation peut être aussi appliquée sur d'autre matériaux, nous avons utilisé les champs de force généraux pour que la méthode soit transférable.

Références

1. Tomic, E. A. Thermal Stability of Coordination Polymers. *J. Appl. Polym. Sci.* **1965**, *9* (11), 3745–3752. https://doi.org/10.1002/app.1965.070091121.
2. Hoskins, B. F.; Robson, R. Design and Construction of a New Class of Scaffolding-like Materials Comprising Infinite Polymeric Frameworks of 3D-Linked Molecular Rods. A Reappraisal of the Zinc Cyanide and Cadmium Cyanide Structures and the Synthesis and Structure of the Diamond-Related Frameworks [N(CH3)4][CuIZnII(CN)4] and CuI[4,4',4'',4''' Tetracyanotetraphenylmethane]. *J. Am. Chem. Soc.* **1990**, *112* (4), 1546–1554. https://doi.org/10.1021/ja00160a038.
3. Kondo, M.; Yoshitomi, T.; Matsuzaka, H.; Kitagawa, S.; Seki, K. Three-Dimensional Framework with Channeling Cavities for Small Molecules: [M2(4, 4′-Bpy)3(NO3)4]·xH2On (M Co, Ni, Zn). *Angew. Chem. Int. Ed. Engl.* **1997**, *36* (16), 1725–1727. https://doi.org/10.1002/anie.199717251.
4. Li, H.; Eddaoudi, M.; O'Keeffe, M.; Yaghi, O. M. Design and Synthesis of an Exceptionally Stable and Highly Porous Metal-Organic Framework. *Nature* **1999**, *402* (6759), 276–279. https://doi.org/10.1038/46248.
5. Metropolis, N.; Rosenbluth, A. W.; Rosenbluth, M. N.; Teller, A. H.; Teller, E. Equation of State Calculations by Fast Computing Machines. *J. Chem. Phys.* **1953**, *21* (6), 1087–1092. https://doi.org/10.1063/1.1699114.
6. Abánades Lázaro, I.; Forgan, R. S. Application of Zirconium MOFs in Drug Delivery and Biomedicine. *Coord. Chem. Rev.* **2019**, *380*, 230–259. https://doi.org/10.1016/j.ccr.2018.09.009.
7. Wang, Y.; Li, B.; Zhang, B.; Tian, S.; Yang, X.; Ye, H.; Xia, Z.; Zheng, G. Application of MOFs-Derived Mixed Metal Oxides in Energy Storage. *J. Electroanal. Chem.* **2020**, *878*, 114576. https://doi.org/10.1016/j.jelechem.2020.114576.
8. Zhao, X.; Zheng, M.; Gao, X.; Zhang, J.; Wang, E.; Gao, Z. The Application of MOFs-Based Materials for Antibacterials Adsorption. *Coord. Chem. Rev.* **2021**, *440*, 213970. https://doi.org/10.1016/j.ccr.2021.213970.
9. Wiersum, A. D.; Giovannangeli, C.; Vincent, D.; Bloch, E.; Reinsch, H.; Stock, N.; Chang, J.-S.; Llewellyn, P. L. Experimental Screening of Porous Materials for High Pressure Gas Adsorption and Evaluation in Gas Separations: Application to MOFs (MIL-100 and CAU-10). *ACS Comb. Sci.* **2013**, *15* (2), 111–119.

https://doi.org/10.1021/co300128w.

10. Taylor, P. Energy Technology Perspectives 2010. 16.
11. Henrique, A.; Maity, T.; Zhao, H.; Brântuas, P. F.; Rodrigues, A. E.; Nouar, F.; Ghoufi, A.; Maurin, G.; Silva, J. A. C.; Serre, C. Hexane Isomers Separation on an Isoreticular Series of Microporous Zr Carboxylate Metal Organic Frameworks. *J. Mater. Chem. A* **2020**, *8* (34), 17780–17789. https://doi.org/10.1039/D0TA05538G